AERODYNAMIC AND PERFORMANCE CHARACTERIZATION OF SUPERSONIC RETROPROPULSION FOR APPLICATION TO PLANETARY ENTRY AND DESCENT

A Thesis
Presented to
The Academic Faculty

by

Ashley M. Korzun

In Partial Fulfillment
of the Requirements for the Degree
Doctor of Philosophy in the
School of Aerospace Engineering

Georgia Institute of Technology
May 2012

AERODYNAMIC AND PERFORMANCE CHARACTERIZATION OF SUPERSONIC RETROPROPULSION FOR APPLICATION TO PLANETARY ENTRY AND DESCENT

Approved by:

Dr. Robert D. Braun, Advisor
School of Aerospace Engineering
Georgia Institute of Technology

Dr. Ian G. Clark
School of Aerospace Engineering
Georgia Institute of Technology

Mr. Karl T. Edquist
Atmospheric Flight and Entry
Systems Branch
NASA Langley Research Center

Dr. Stephen M. Ruffin
School of Aerospace Engineering
Georgia Institute of Technology

Dr. Jerry M. Seitzman
School of Aerospace Engineering
Georgia Institute of Technology

Date Approved: 27 March 2012

ACKNOWLEDGEMENTS

This dissertation would not have been possible without the support of a number of individuals and organizations during my time at Georgia Tech. First, I would like to thank my advisor, Prof. Robert Braun, for suggesting supersonic retropropulsion as a research topic to me as a new graduate student and for his mentorship, introduction to the EDL community, and support of this research. I would also like to thank Dr. Ian Clark for his guidance on this work during his time as a visiting professor at Georgia Tech.

I would especially like to acknowledge and thank the NASA ETDD Program and the Atmospheric Flight and Entry Systems Branch at NASA Langley Research Center for their support of this work through funding, mentorship, and technical support. Thank you to Karl Edquist (NASA LaRC) and Artem Dyakonov (NASA LaRC) for all of your guidance and for allowing my work to support and be supported by the NASA ETDD Program.

Thank you to the following individuals and groups for their support of the computational and experimental efforts described in this work: Bil Kleb (NASA LaRC, SRP CFD and FUN3D), NASA ETDD CFD Team, FUN3D Development Team (NASA LaRC), Bill Jones (NASA LaRC, GridEx/BatchEx), John Melton (NASA ARC, preliminary CFD), Chris Cordell (Georgia Tech, SRP CFD and FUN3D), ETDD Wind Tunnel Testing Team (SRP test data), and Juan Cruz Ayoroa (Georgia Tech, post-processing of SRP test data). I would also like to acknowledge the NASA Fundamental Aeronautics Program, Hypersonics Project for funding the early years of this work.

I would also like to thank my fellow graduate students in the Space Systems Design Lab. To Mike Grant, Brad Steinfeldt, Richard Otero, Chris Tanner, and Chris Cordell

- thank you for the countless hours we have spent working together, brainstorming ideas, preparing for qualifying exams, and helping each other out over the past several years.

Finally, I would like to thank my family for providing me with the best opportunities possible to succeed and achieve my goals. My accomplishments in completing this dissertation would not have been possible without all of this support.

TABLE OF CONTENTS

LIST OF TABLES

LIST OF FIGURES

NOMENCLATURE

Symbols

α	Angle of attack	[°]
β	Ballistic coefficient	[kg/m^2]
ΔV	Velocity increment	[m/s]
δ	Dimensional thickness	[m]
ϵ	Flow deflection angle	[°]
γ	Ratio of specific heats	
λ	Ratio of parallel and normal elliptical semi-axes	
$\mathcal{M}$	Moment	[N-m]
ν	Flow direction at the nozzle exit plane	
ϕ	Tank-mass factor	[m]
ρ	Density	[kg/m^3]
σ	Standard deviation	
τ	Thrust	[N]
φ	Relative flight path angle	[°]
A	Area	[m^2]
C	Coefficient	
D	Drag	[N]

d	Body diameter	[m]
g	Gravitational acceleration	[m/s^2]
h	Approximate unstructured mesh spacing	
I_{sp}	Specific impulse	[s]
L	Lift	[N]
l	Distance measured from the nozzle exit plane	[m]
L/D	Hypersonic lift-to-drag ratio	
M	Mach number	
m	Mass	[kg]
N	Number of grid nodes	
p	Pressure	[N/m^2]
PMF	Propellant mass fraction	
q	Dynamic pressure	[N/m^2]
R	Gas constant	[J/kg-K]
r	Radius	[m]
Re	Reynolds number	
T	Temperature	[K]
t	Time	[s]
T/W	Vehicle thrust-to-weight ratio	
u	Velocity	[m/s]

V	Volume	[m^3]
W	Weight	[N]
x	Distance along the x-direction	[m]
$\dot{m}$	Mass flow rate	[kg/s]

Superscripts and Subscripts

$*$	Nozzle throat condition
0	Total condition
2	Post-shock condition
∞	Freestream condition
A	Axial direction
a	Local ambient (static) condition
cr	Critical condition
cs	Contact surface
D	Drag
d	Body diameter
da	'Dead air' region condition
e	Nozzle exit condition
f	Forebody
j	Jet flow condition
L	Lift

l	Jet layer condition
m	Moment
n	Nose
p	Pressure
ref	Reference condition
s	Mach disk
T	Thrust

Acronyms

ARC	Ames Research Center
BDF2OPT	Optimized Second Order Backward Difference
BLDT	Balloon Launched Decelerator Test
BPM	Blunt Penetration Mode
CFD	Computational Fluid Dynamics
CG	Center of Gravity
CPU	Central Processing Unit
DGB	Disk-Gap-Band
DOE	Design of Experiments
DOF	Degree of Freedom
EDL	Entry, Descent, and Landing
EDL-SA	Entry, Descent, and Landing Systems Analysis

EFF	Exploration Feed Forward
ESP	Electronically Scanned Pressure
ETDD	Exploration Technology Development and Demonstration
ISRU	In-Situ Resource Utilization
LaRC	Langley Research Center
LDFSS	Low-Diffusion Flux-Splitting Scheme
LPM	Long Penetration Mode
MER	Mars Exploration Rover
MLE	Mars Lander Engine
MOLA	Mars Orbiter Laser Altimeter
MSL	Mars Science Laboratory
MUSCL	Monotone Upstream-Centered Scheme for Conservation Laws
NASA	National Aeronautics and Space Administration
PEPP	Planetary Entry Parachute Program
PLIIF	Planar Laser-Induced Iodine Fluorescence
RANS	Reynolds-Averaged Navier-Stokes
SHAPE	Supersonic High Altitude Parachute Experiment
SPED	Supersonic Planetary Entry Decelerator
SRP	Supersonic Retropropulsion
SST	Shear Stress Transport

TOPSIS	Technique for Order Preference by Similarity to Ideal Solution
TRL	Technology Readiness Level
TVD	Total Variation Diminishing
UPWT	Unitary Plan Wind Tunnel

SUMMARY

The entry, descent, and landing (EDL) systems for the United States' six successful landings on Mars and the 2011 Mars Science Laboratory (MSL) have all relied heavily on extensions of technology developed for the Viking missions of the mid 1970s. Incremental improvements to these technologies, namely rigid 70-deg sphere-cone aeroshells, supersonic disk-gap-band parachutes, and subsonic propulsive terminal descent, have increased payload mass capability to 950 kg (MSL). However, MSL is believed to be near the upper limit for landed mass using a Viking-derived EDL system. To achieve NASA's long-term exploration goals at Mars, technologies are needed that enable more than an order of magnitude increase in landed mass (10s of metric tons), several orders of magnitude increase in landing accuracy (10s or 100s of meters), and landings at higher surface elevations (0+ km). Supersonic deceleration has been identified as a critical deficiency in extending Viking-heritage technologies to high-mass, high-ballistic coefficient systems. As the development and qualification of significantly larger supersonic parachutes is not a viable path forward to increase landed mass capability to 10+ metric tons, alternative approaches must be developed.

Supersonic retropropulsion (SRP), or the use of retropropulsive thrust while an entry vehicle is traveling at supersonic conditions, is one such alternative approach. The concept originated in the 1960s, though only recently has interest in SRP resurfaced. While its presence in the historical literature lends some degree of credibility to the concept of using retropropulsion at supersonic conditions, the overall immaturity of supersonic retropropulsion requires additional evaluation of its potential as a decelerator technology for high-mass Mars entry systems, as well as its comparison

with alternative decelerators.

The supersonic retropropulsion flowfield is typically a complex interaction between highly under-expanded jet flow and the shock layer of a blunt body in supersonic flow. Although numerous wind tunnel tests of relevance to SRP have been conducted, the scope of the work is limited in the freestream conditions and composition, retropropulsion conditions and composition, and configurations and geometries explored. The SRP aerodynamic - propulsive interaction alters the aerodynamic characteristics of the vehicle, and models must be developed that accurately represent the impact of SRP on system mass and performance. Work within this thesis has defined and advanced the state of the art for supersonic retropropulsion. This has been achieved through the application of systems analysis, computational analysis, and analytical methods.

The contributions of this thesis include a detailed performance analysis and exploration of the design space specific to supersonic retropropulsion, establishment of the relationship between vehicle performance and the aerodynamic - propulsive interaction, and an assessment of the required fidelity and computational cost in simulating supersonic retropropulsion flowfields, with emphasis on the effort required to develop aerodynamic databases for conceptual design.

CHAPTER I

INTRODUCTION

1.1 Motivation

The United States has successfully landed six robotic missions on Mars: Viking 1 and 2, Mars Pathfinder, two Mars Exploration Rovers (MERs), and Phoenix. Including prior missions and those launched in 2011, the largest entry mass sent to Mars is Mars Science Laboratory (MSL) at approximately 3300 kg. The entry, descent, and landing (EDL) systems for these missions relied heavily on extensions of Viking-heritage technology, namely rigid 70-deg sphere-cone aeroshells, supersonic disk - gap - band (DGB) parachutes, and subsonic, propulsive terminal descent [1].

MSL is believed to be near the upper limit for landed mass using a Viking-derived EDL system. To land a 950 kg rover within 10 km of the target landing site, the EDL system for MSL will utilize the largest aeroshell (4.5 m-diameter) and largest supersonic DGB parachute (21.5 m-diameter) ever flown at Mars, as well as the highest parachute deployment Mach number (Mach 2.1) and highest L/D (0.24). To achieve NASA's long-term exploration goals at Mars, technologies are needed that enable more than an order of magnitude increase in landed mass, several orders of magnitude increase in landing accuracy, and landings at higher surface elevations [2, 18].

A key parameter used to describe an entry vehicle is the ballistic coefficient, β, or the ratio of entry mass to hypersonic drag area, defined in Eq. 1. At Mars, aeroshell size constraints, high ballistic coefficients, and insufficient atmospheric density often result in unacceptable parachute deployment and operating conditions. Supersonic deceleration has been identified as a critical deficiency in extending Viking-heritage

technologies to the high-mass, high-ballistic coefficient systems required for future Mars exploration missions [1, 2, 19].

$$\beta = \frac{m_{entry}}{C_D A} \tag{1}$$

Figure 1 shows the deployment Mach number and approximate drag area of parachutes tested through the Viking BLDT, PEPP, SPED, and SHAPE test and qualification programs, as well as those used on past Mars missions and on MSL.

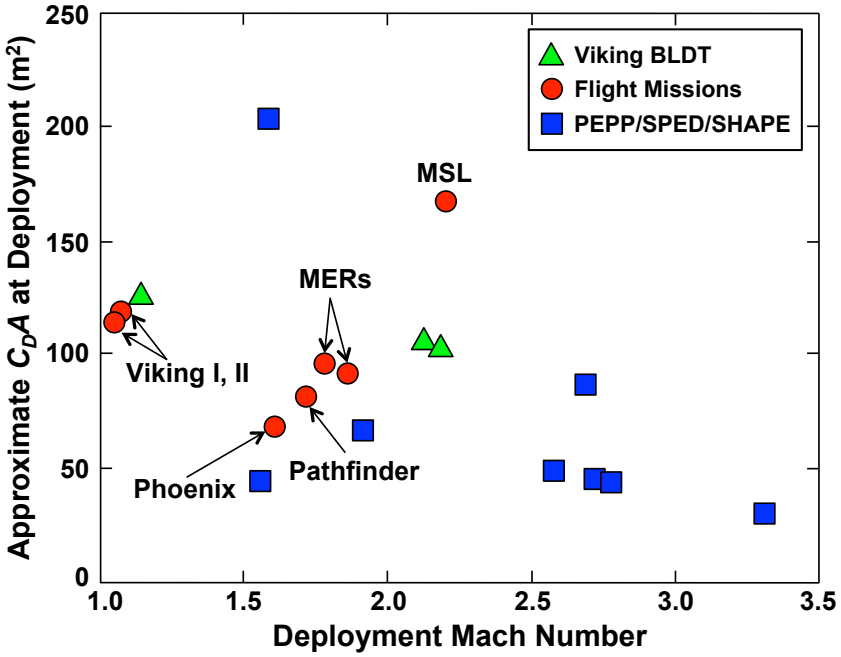

Figure 1: Mach number and dynamic pressure conditions for successful inflation of supersonic DGB parachutes at Mars-relevant conditions. (Adapted from [1]).

Analogously, Fig. 2 illustrates the inability to pass through the supersonic parachute deployment region in altitude - velocity space with increasing ballistic coefficient, with the bounds on the deployment region defined by Mach number, dynamic pressure, and altitude (a function of available timeline). The vehicles required to achieve long-term exploration objectives at Mars will be characterized by large ballistic coefficients and accordingly, will be challenged by the inability to reach conditions that are acceptable

for the deployment of existing supersonic parachute systems. In such applications, supersonic parachutes are challenged by increasingly poor drag performance at higher Mach numbers, longer inflation times as the parachute diameter increases, uncertainties in inflation dynamics for conditions and systems outside of the Viking parachute qualification region (Viking BLDT test cases shown in Fig. 1), and material limits. As a result, developing and qualifying significantly larger supersonic parachutes is not a viable path forward to achieve long-term exploration objectives at Mars, and alternative approaches to supersonic deceleration must be considered. One such alternative deceleration approach is to initiate a retropropulsion phase while the vehicle is traveling at supersonic conditions. Supersonic retropropulsion (SRP) may be an enabling decelerator technology for high-mass systems operating in thin atmospheres, such as Mars'.

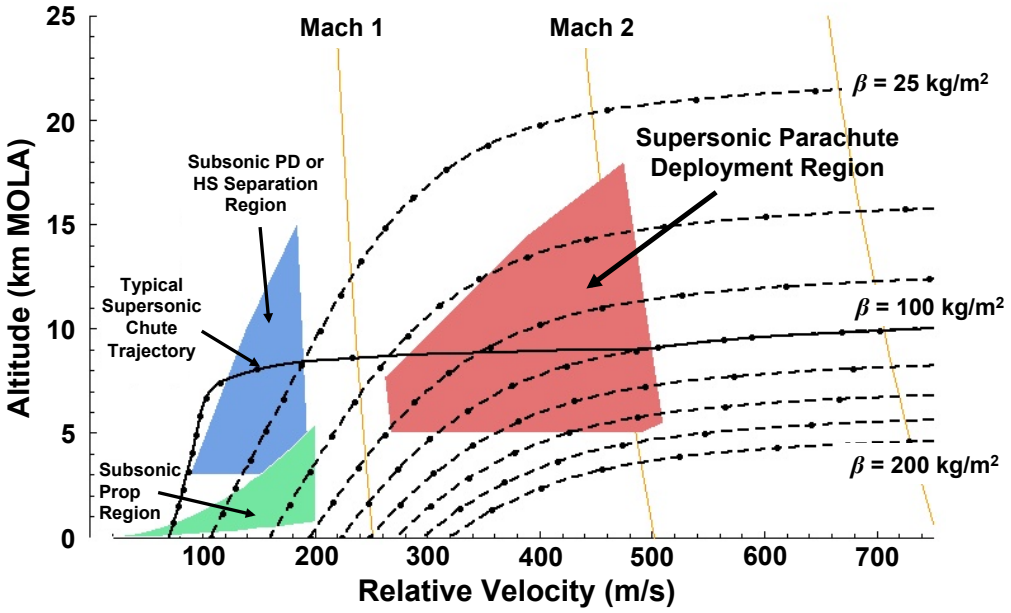

Figure 2: Feasibility limits for supersonic parachute deployment with increasing ballistic coefficient (adapted from [1]).

Technology exploration efforts preceding the Viking missions in the 1960s and 1970s developed supersonic retropropulsion to nearly the level of maturity the concept has today. The focus of these early investigations was on the development of an

all-propulsive configuration for a prototypical Mars lander. The eventual selection of a supersonic DGB parachute system and subsonic, propulsive terminal descent phase for the Viking landers ended much of the research efforts to develop supersonic retropropulsion. Only recently has interest in supersonic retropropulsion resurfaced.

NASA has expended significant effort to define mission architectures for the human exploration of Mars [2, 20, 21, 22]. The objective of NASA's Design Reference Architecture 5.0 [22] was to determine the minimum required technologies to develop a credible EDL concept to land a 40 t payload safely on Mars. Even with a low current technological maturity, SRP was selected for the baseline architecture over alternative inflatable and deployable concepts as a credible solution for supersonic deceleration.

NASA's Entry, Descent, and Landing Systems Analysis (EDL-SA) study [2] was then tasked with opening the design space further to try and identify alternative technology paths. Figure 3 shows eight candidate EDL architectures from this study. Of these candidate architectures, four of the eight rely on the use of supersonic retropropulsion, and all eight transition to subsonic retropropulsion. With the ability to build a measure of redundancy into the EDL system and to provide a propulsive capability to perform any necessary divert maneuvers, supersonic retropropulsion was a key element on the list of recommended EDL technologies [2]. Additionally, liquid bipropellant propulsion systems in the same general thrust class as those required by these candidate architectures have already flown, albeit for different applications, and this was viewed as potentially reducing the development risk for SRP.

NASA's most recent efforts [23] were then focused on determining if the technologies identified in the original EDL-SA study [2] could be combined in a precursor mission scenario to land a payload ≥ 2.5 t on Mars. A scaled monopropellant propulsion system was modeled (including packaging) in this study for supersonic deceleration, and SRP was recommended to NASA as a critical path technology for high-mass

missions to the surface of Mars. While its presence in the historical literature lends some degree of credibility to the concept of using retropropulsion at supersonic conditions, the immaturity of supersonic retropropulsion requires additional evaluation of its potential as a decelerator technology for high-mass Mars entry systems, as well as its comparison with alternative decelerators. The potential for SRP to substantially increase payload capability to the surface of Mars has resulted in its inclusion in NASA's most recent development roadmap for EDL technologies [24] and the initiation of preliminary development efforts [18].

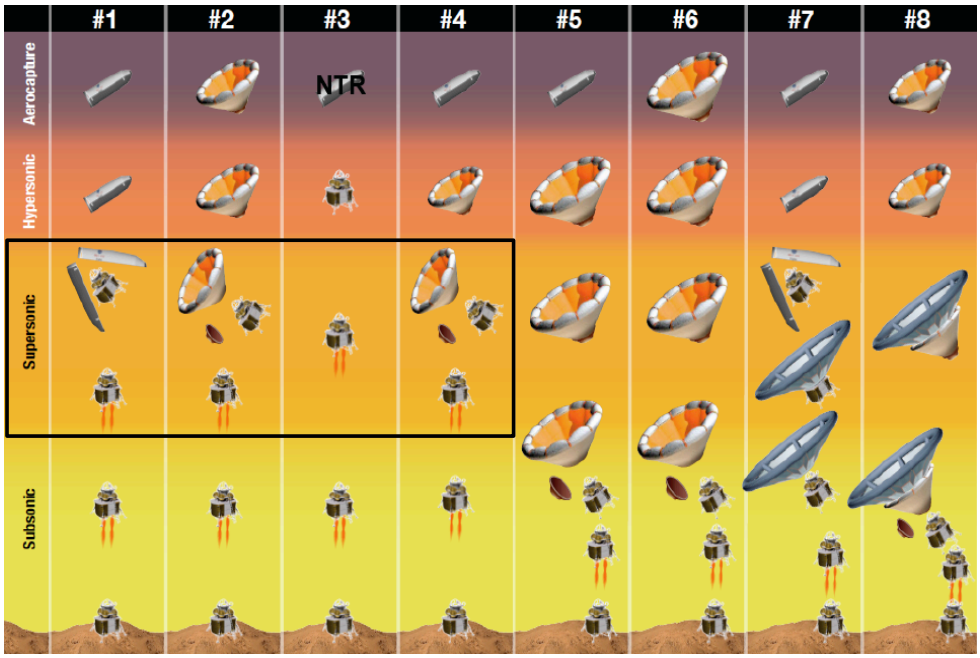

Figure 3: Candidate architectures for high-mass Mars EDL missions. Architectures 1 - 4 use SRP [2].

The supersonic retropropulsion flowfield is a complex interaction between highly under-expanded jet flow and the shock layer of a blunt body in a supersonic freestream. The aerodynamic characteristics of the vehicle are affected by both the retropropulsive thrust and by the SRP interaction [11]. Applying existing computational tools and approaches to SRP flow interactions is computationally expensive if accurate simulation of the many features and behaviors characteristic of SRP flowfields is sought.

This difficulty contributes to a lack of models available for systems analysis.

To date, systems-level analyses of high-mass Mars entry systems utilizing SRP have made a wide range of assumptions, from no preservation of the vehicle's aerodynamics to full preservation of aerodynamics and unaltered control authority during the SRP phase, presenting difficulties in performing a comparative assessment of how and when supersonic retropropulsion might be best utilized within an EDL architecture. Given the expansiveness of the trade space for high-mass Mars EDL architectures, the required fidelity of the aerodynamic databases and other models necessary for exploration at the conceptual design level must be determined.

1.2 Objectives

The knowledge base for supersonic retropropulsion has expanded greatly since interest in sending high-mass missions to Mars resurfaced in the mid-2000s. Significant development effort remains for SRP to be matured from its status today to a flight-viable technology. Many of the largest challenges have been identified through recent efforts in systems analysis, computational analysis, and wind tunnel testing. This thesis addresses some of these challenges by defining the static aerodynamic and system performance for supersonic retropropulsion and by defining the efforts required to move past the conceptual design phase.

The work contained within this dissertation has four primary objectives. The first objective is to define the state of the art for supersonic retropropulsion and to develop a consistent description of SRP flow physics for the community focused on advanced Mars EDL. The concept of supersonic retropropulsion for Mars EDL predates the Viking missions. Current plans to mature SRP into a viable decelerator technology for future Mars missions [18] benefit greatly from an understanding of the past accomplishments in this area. Lessons learned guide the subsequent systems analysis and computational fluid dynamics (CFD) development efforts to advance the

state of the art for supersonic retropropulsion.

The second objective of this work is to characterize the system-level impact of SRP on entry system performance and to identify significant performance trends and relevant operating conditions using models derived from experimental data. This analysis seeks to accurately evaluate the performance of supersonic retropropulsion as a function of vehicle ballistic coefficient and thrust available, defining a range of initiation conditions relevant for future high-mass Mars entry systems. Past experimental work has established trends in static aerodynamics for supersonic retropropulsion as a function of retropropulsion configuration, freestream conditions, and thrust, allowing for the development of an aerodynamic - propulsive interactions model based on these data. Parametric systems analyses with experimentally- and computationally-derived performance models allow for a more complete assessment of the potential benefits of SRP in increasing landed mass capability at Mars. Investigation into the robustness of SRP performance to the variability in SRP static aerodynamics provides insight into the required fidelity of tools used for aerodynamic database development in the context of conceptual design.

The third objective of this work is to assess the capability of modern computational analysis approaches in simulating SRP behavior and aerodynamics. Fully-turbulent, viscous CFD solutions of flowfield structure and behavior, surface pressure distributions, and static aerodynamic characteristics are evaluated against experimental data from the literature. Additionally, unsteady CFD predictions of flowfield structure and surface pressure distributions are compared against experimental data from recent testing in the NASA Langley Research Center (LaRC) Unitary Plan Wind Tunnel (UPWT). The relationship between required fidelity and computational cost in accurately and consistently simulating SRP flowfields is discussed, with applicability to conceptual design of particular interest.

The fourth objective of this work is to establish relationships between design

choices related to vehicle performance and the SRP-induced change in the vehicle's static aerodynamic characteristics. Design choices are then mapped to parameters that influence the SRP aerodynamic - propulsive interaction. The sensitivities of the surface pressures, aerodynamic drag coefficient, and total axial force coefficient to variations in these parameters are determined using an analytical model for the SRP flowfield that is based on a momentum - force balance at the interface between the jet flow and the flow within the shock layer. The results of this analysis are used to draw conclusions about design trades that may require higher fidelity or more detailed analysis.

1.3 Thesis Organization

This thesis is composed of five subsequent chapters detailing the work performed and a final chapter presenting conclusions and recommended directions for forward work. Chapter 2 provides a review of the literature relevant to supersonic retropropulsion and defines the present state of the art. General flowfield characteristics, aerodynamic trends, computational analysis efforts, and a discussion of the composition and limitations of the existing experimental database are given. A preliminary definition of relevant flow physics is also developed as a part of this chapter.

Chapter 3 presents a comprehensive study of entry system performance for vehicles utilizing SRP. Trends in SRP performance across a range of vehicle ballistic coefficients and the definition of relevant initiation conditions are given with consideration to mass and volume constraints, mission requirements, and modeling assumptions. The sensitivity of SRP performance to the fidelity of the aerodynamics models applied is also discussed in this chapter.

Chapter 4 is composed of preliminary CFD solutions for SRP flowfields, prefaced by a discussion on the expected performance of computational approaches in capturing the relevant flow physics. These solutions are compared against experimental

data for flowfield structure and surface pressure distributions for a number of wind tunnel test cases in the literature.

Chapter 5 gives a brief overview of a recent supersonic retropropulsion wind tunnel test and presents CFD solutions for a subset of test runs. The CFD results are compared against experimental data from this test, and the current performance of CFD approaches in predicting the flowfield structure, surface pressure distributions, and integrated aerodynamic force coefficients and computational cost of this performance are discussed.

Chapter 6 discusses the development of a momentum-based flow model and its use in evaluating the sensitivity of parameters governing SRP aerodynamic - propulsive interactions to design choices related to vehicle configuration and system performance. The surface pressures and integrated aerodynamic force coefficients determined from the flow model are determined for parameters directly related to operating conditions, required propulsion system performance, propulsion system composition, nozzle geometry, and vehicle configuration.

Lastly, Chapter 7 summarizes the conclusions of this thesis, with emphasis on the fidelity necessary to develop an aerodynamic database for conceptual design. Recommendations for forward work in the areas of experimental testing, computational analysis, and systems analysis and design are also discussed.

CHAPTER II

OVERVIEW OF SUPERSONIC RETROPROPULSION

This chapter presents a survey of the literature on the aerodynamic effects of retropropulsion on blunt body entry vehicles in an opposing supersonic freestream and describes the state of the art achieved in testing and simulating such flows. The focus is on describing the relevant flow physics and aerodynamic performance effects for application to EDL systems design, computational simulation development, and the definition and support of technology development plans. This chapter does not discuss non-propulsive supersonic decelerators, reaction control system interactions, detailed aerothermodynamic issues, or slender body geometries.

Section 2.1 presents a discussion of the relevant flow physics, building from blunt bodies in supersonic flow and jet flow expansion to the full SRP aerodynamic - propulsive interaction. Section 2.2 compares experimental data trends for different nozzle configurations, and discusses the impact of variations in the environment and design parameters such as nozzle geometry and chemical composition of the freestream and retropropulsion flows. A summary of the existing experimental database is provided in Section 2.3. Section 2.4 provides an overview of the computational simulation of supersonic retropropulsion flowfields and the extensibility and limitations of existing work. Section 2.5 discusses recent development efforts, including work recently completed under NASA's Exploration Technology Development and Demonstration (ETDD) Program and supported by this thesis.

2.1 General Flow Characteristics

The supersonic retropropulsion flowfield is a complex interaction between highly under-expanded jet flow and an opposing supersonic freestream. The jet structure

is immediately recognizable within the SRP flowfield, and the flow physics governing its structure and behavior are strongly similar to those for sonic and supersonic jets exhausting into a quiescent medium. Extensions can also be made from supersonic impinging jets and stagnation flows [25]. Flowfields surrounding blunt bodies with no retropropulsion, bodies with jet flow from the center of the vehicle forebody, and bodies with jet flow from the periphery of the vehicle forebody each exhibit unique behaviors. The flowfield structure and flowfield stability are highly dependent on the jet pressure ratio, defined as the ratio of the pressure of the jet flow to the pressure of the freestream, and the retropropulsion configuration. The exit Mach number, M_e, and composition of the jet flow, γ_j, also influence flowfield structure [7].

For a fixed set of freestream conditions, thrust coefficient is often used as a similarity parameter to gauge the strength of the jet flow relative to the freestream. In the context of supersonic retropropulsion, the thrust coefficient is a force coefficient, defined as the ratio of thrust, τ, to the freestream dynamic pressure, q_∞, and the vehicle reference area, A_{ref}:

$$C_T = \frac{\tau}{q_\infty A_{ref}} \tag{2}$$

Equation 3 gives the relationship between thrust coefficient and the ratio of the static pressure at the nozzle exit to the freestream static pressure (or the jet pressure ratio), assuming an ideal gas and neglecting the ambient pressure contribution to thrust. One-dimensional isentropic flow relations can be used to translate the static pressure ratio to a total pressure ratio, shown subsequently in Eq. 3. The final form of Eq. 3 is the product of five quantities. Each quantity, respectively, is a function of the following:

1. Propulsion system choice, nozzle geometry, and operating environment

2. Nozzle geometry and vehicle configuration

3. Propulsion system choice and nozzle geometry

4. Operating environment

5. Operating conditions

$$C_T = \frac{\tau}{q_\infty A_{ref}} = \frac{2(\dot{m}u_e + A_e(p_e - p_\infty))}{\rho_\infty u_\infty^2 A_{ref}} = \frac{2(\rho_e u_e^2 A_e + A_e p_e - \cancelto{0}{A_e p_\infty})}{\rho_\infty u_\infty^2 A_{ref}}$$

$$= \frac{2A_e(\rho_e M_e^2 \gamma_e R T_e + p_e)}{\rho_\infty u_\infty^2 A_{ref}} = \frac{2p_e A_e(1 + \gamma_e M_e^2)}{\rho_\infty u_\infty^2 A_{ref}}$$

$$= \frac{2(1 + \gamma_e M_e^2)}{\gamma_\infty M_\infty^2} \cdot \frac{A_e}{A_{ref}} \cdot \frac{p_e}{p_\infty} = \frac{2(1 + \gamma_e M_e^2)}{\gamma_\infty M_\infty^2} \cdot \frac{A_e}{A_{ref}} \cdot \frac{p_e}{p_{0,j}} \cdot \frac{p_{0,\infty}}{p_\infty} \cdot \frac{p_{0,j}}{p_{0,\infty}}$$

$$= \frac{2(1 + \gamma_e M_e^2)}{\gamma_\infty M_\infty^2} \cdot \frac{A_e}{A_{ref}} \cdot \left(1 + \frac{\gamma_e - 1}{2} M_e^2\right)^{-\frac{\gamma_e}{\gamma_e - 1}} \cdot \left(1 + \frac{\gamma_\infty - 1}{2} M_\infty^2\right)^{\frac{\gamma_\infty}{\gamma_\infty - 1}} \cdot \frac{p_{0,j}}{p_{0,\infty}} \tag{3}$$

2.1.1 Blunt Bodies in Supersonic Flow

Relevant conditions for SRP are considered to be fully within the continuum flow regime. As shown in Fig. 4, the flowfield surrounding a blunt body entry vehicle at supersonic freestream conditions is characterized by a strong, detached shock [3]. To compare relative thicknesses of the bow shock, boundary layer, and shock layer, Gnoffo [3] defines Re_d to be the post-shock Re based on the body diameter of the entry vehicle. The bow shock is very thin, with a non-dimensional thickness, $\delta_1/d, \simeq Re_d^{-1}$. The boundary layer thickness is greater than the bow shock thickness, with $\delta_2/d \simeq Re_d^{-1/2}$. The shock layer includes the boundary layer and extends to the bow shock.

The dimensionless thickness in the stagnation region, δ_3/d, is nearly independent of Re_d and is instead, controlled by the mass flow rate across the bow shock [3]. For entry vehicles with shallow aftbodies, large flow turning angles, and at small angles of attack, such as some of the geometries under consideration for high-mass Mars entry systems, the boundary layer will separate behind the shoulder. The separated shear layers from the windward and leeward shoulders converge aft of the body, forming a viscous wake cone [3]. The impact of SRP on flow separation and flow in the wake region is discussed further in Chapters 4 and 5.

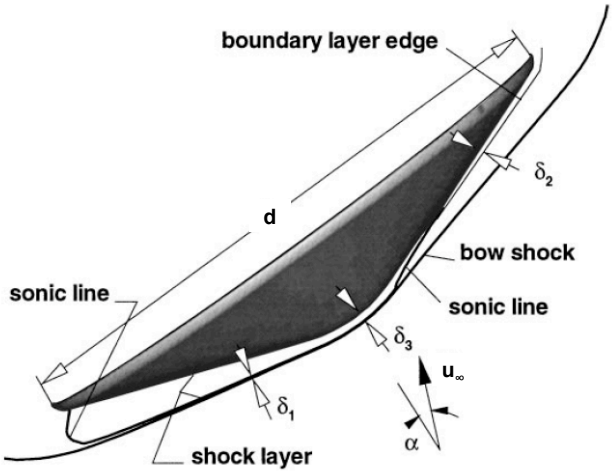

Figure 4: Simplified flowfield over a blunt body entry vehicle [3].

2.1.2 Jet Flows

Three expansion conditions are considered for jet flows: over-expanded, under-expanded, and highly under-expanded (perfectly-expanded jet flows are not separately considered). Figure 5 illustrates the basic structure of over-expanded and under-expanded jets. Over-expanded jet flows have a lower jet static pressure at the nozzle exit, p_e, as compared to the local ambient pressure, p_a, ($p_e < p_a$), with p_a indicated in Fig. 5 for jet flow into a quiescent medium. Compression waves form at the nozzle exit to raise the jet pressure, and these waves intersect and are then reflected off of the jet centerline as another set of compression waves to turn the flow back parallel to

the jet centerline. The compression waves are then reflected off of the jet boundary as expansion waves, and this pattern continues until mixing along the jet boundaries with the ambient fluid causes the jet structure to dissipate. For under-expanded jet flows, the jet static pressure at the nozzle exit is higher than the local ambient pressure ($p_e > p_a$). As a result, Prandtl-Meyer expansion waves form at the nozzle exit to lower the jet pressure. These expansion waves are then reflected off of the opposite jet boundary (across the jet centerline) as compression waves, and a pattern similar to that described for the over-expanded case continues until the jet flow dissipates [4].

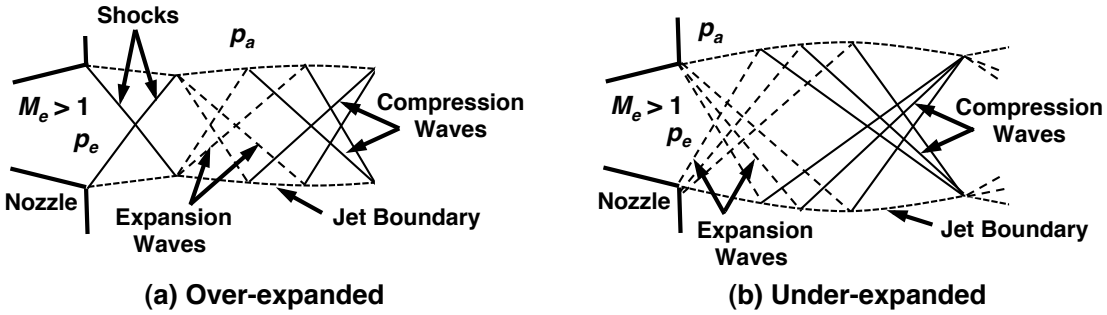

Figure 5: Jet structures for over-expanded and under-expanded conditions. (Adapted from [4]).

In general, highly under-expanded jet flows (p_e is sufficiently greater than p_a) exhausting from a body into a quiescent medium are characterized by an expansion fan at the nozzle lip, an internal (barrel) shock, and termination of the jet structure with a Riemann wave, or Mach disk [5, 6, 26, 27, 28, 29, 30]. At large enough jet pressure ratios, the jet structure has a single cell. Figure 6 illustrates the general jet structure for the highly under-expanded case. From the nozzle exit, the jet flow undergoes Prandtl-Meyer expansion until the jet pressure equals the local ambient pressure, defining the high-velocity jet boundary [5]. At highly under-expanded conditions, a barrel shock is formed in the vicinity of the jet boundary, and a Mach disk forms as a part of a shock intersection away from the jet centerline.

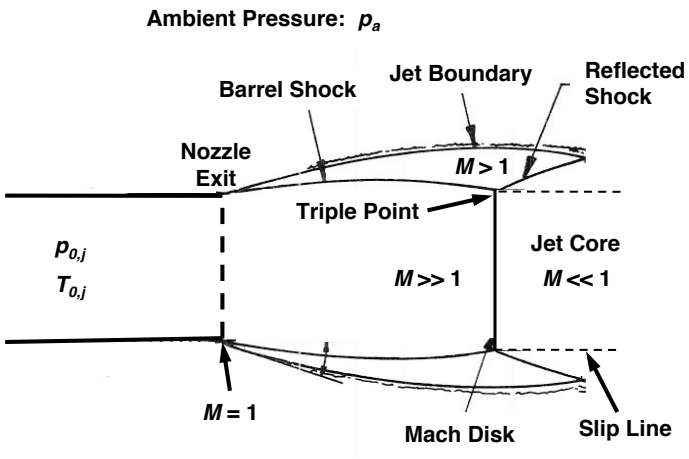

Figure 6: General structure of a highly under-expanded jet flow into a quiescent medium [5, 6].

At the intersection of the Mach disk and the barrel shock, an oblique reflected shock forms. This intersecting structure is thought to arise from the formation of a sonic, throat-like region allowing the subsonic jet core downstream of the Mach disk to be supersonic on the side of the Mach disk nearer the nozzle exit [30, 31]. For jet flows exhausting into static, quiescent mediums, this theory is more accurate than assuming the Mach disk to form where a normal shock has sufficient strength to equate the static pressure behind the shock to the local ambient pressure [26, 30]. Jet flow passing through the Mach disk becomes subsonic, while jet flow passing through the barrel shock and oblique reflected shock remains supersonic, and a slip line forms, defining the boundary between the subsonic jet core and the inner, subsonic shear layer [6].

2.1.3 Supersonic Retropropulsion Flowfields

Investigation into the interaction of retropropulsion with supersonic aerodynamics began in the early 1950s. Experimental work with small-scale wind tunnel models by Huff and Abdalla [32], Love et al. [26, 33, 34], and Moeckel [35, 36] focused on shock - boundary layer phenomena and the effects of retropropulsion nozzle flow on boundary layer separation and transition in both subsonic and supersonic freestreams.

These investigations were among the earliest observations of aerodynamic - propulsive interactions for retropropulsion configurations with a nozzle aligned with the body centerline. They are consistent in observing that increasing the jet pressure ratio decreases aerodynamic drag and shifts boundary layer transition closer to the nose of the body [26, 32, 33, 34, 35, 36].

Additional work on supersonic jet flows and jet - body interactions established the groundwork for future wind tunnel testing of the effects of supersonic jet flows on surface pressure distributions and flowfield stability [26, 32, 37, 38]. Although many of these early body geometries were not the blunted-cone entry vehicle shapes flown in the 1960s and 1970s, these works outlined the fundamental physics of jet - shock interactions and motivated later investigations into the application of such interaction effects to blunt body entry vehicles for planetary exploration.

Work was then extended to blunt body entry geometries, primarily through wind tunnel experiments with small-scale models. Among the concepts investigated were single and multiple nozzle configurations, with the retropropulsion nozzles placed at either the center or the periphery of the vehicle forebody. The majority of the literature is focused on retropropulsion configurations in which a single nozzle is located along the forebody centerline. Prior to June 2010, only two test series [13, 39] had been documented for a configuration with multiple nozzles outboard further than the half radius. Examples of a central configuration and a peripheral configuration are given in Fig. 7(a) and Fig. 7(b), respectively. Flight-relevant SRP concepts are likely to have multiple nozzles with large exit areas and accordingly, are likely to exhibit characteristics of both configurations.

Experimental results for low thrust coefficients ($C_T < 1$) consistently show both aerodynamic drag and thrust contributions to the total axial force coefficient (Eq. 4, valid for $\alpha = 0°$) for peripheral configurations [13, 39, 40]. For higher thrust coefficients ($C_T > 1$), the total axial force is dominated by the thrust contribution

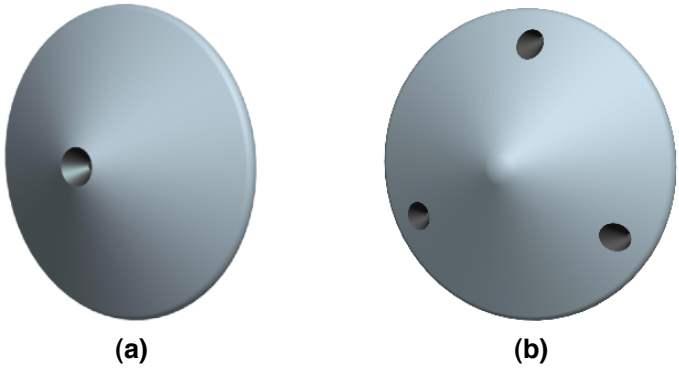

Figure 7: Examples of central (a) and peripheral (b) retropropulsion configurations.

for all forebody nozzle configurations (i.e. there is little or no aerodynamic drag contribution) [7, 8, 9, 12, 13, 39, 41, 42]. Additionally, the stability of the flowfield and resulting static aerodynamic effects were found to be strongly dependent on the ratio of the jet total pressure to the freestream total pressure [7, 8, 9, 12, 13, 39, 40, 41, 42, 43, 44, 45, 46, 47, 48, 49, 50].

$$C_{A,total} = C_T + C_D \tag{4}$$

For supersonic retropropulsion, highly under-expanded jet flow exhausts into the shock layer of a body opposing a supersonic freestream. The aerodynamic characteristics of the body are affected by both the thrust of the jet flow and also by the interaction between the jet flow and the shock layer [7, 27]. Figure 8 illustrates the general structure of a supersonic retropropulsion flowfield. The bow shock is displaced further upstream of the body as a result of the formation of a freestream flow obstruction by the jet flow interaction. The supersonic freestream flow is decelerated to subsonic conditions by the bow shock, and the supersonic jet flow in the jet core is decelerated to subsonic conditions by the jet termination structure, typically a Mach disk. Observations in the literature, however, and also high-speed schlieren video taken during recent experimental testing [51, 52] point out that even in the most

steady flowfields, the jet termination structure often oscillates between a Mach disk and a lambda shock (a weaker reflection). Once highly under-expanded conditions have been reached, no significant changes to the flowfield structure occur; the size and upstream displacement of flowfield structures increases regularly as the jet mass flow increases. Growth of the shear layer along the jet boundaries can significantly affect radial diffusion of the jet flow away from the nozzle exit, challenging attempts at analytical predictions of the location and diameter of the Mach disk.

The interaction region is bounded by two supersonic regions (the freestream and jet flows) and consists of a subsonic region divided by a contact discontinuity [7, 44]. This contact surface is the interface separating the subsonic jet core and the subsonic flow behind the bow shock. For the case of a single, central jet, a free stagnation point forms along the contact surface. The jet flow directly outside of the interaction region is turned outboard into the jet layer [7].

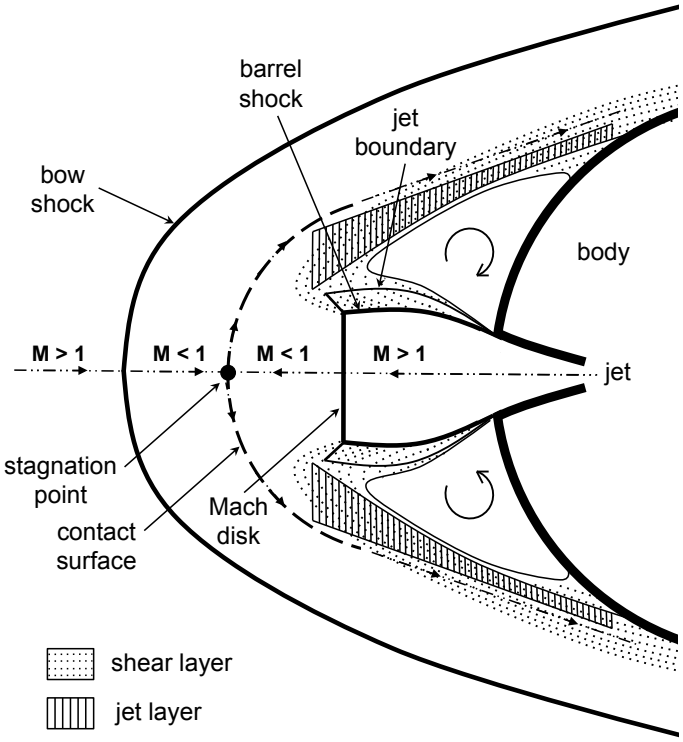

Figure 8: SRP flowfield structure for a single, central jet. (Adapted from [7]).

The flow within the jet layer being swept downstream and the supersonic and

subsonic flow within the shear layer are drawn toward the regions of lower pressure near the nozzle exit, contributing to the formation of recirculation regions over the forebody for configurations with centrally-located nozzles. The shear layer is the parallel-velocity mixing region in the shock layer, between the barrel shock and the aft-swept freestream flow. This mixing region significantly impacts the diffusion of the jet flow away from the nozzle exit [7, 30]. The large velocity gradients between the subsonic flow behind the bow shock and the opposing supersonic jet flow form the supersonic shear layers along the outer jet boundary. The recirculation and high pressure behind the bow shock force significant mixing within the shear layer as the jet flow is turned. The overall effect of the jet - freestream interaction is the shielding of the original flow obstruction (the body) from the freestream, resulting in the blanketing of the body by an annular region of relatively constant pressure below the post-shock freestream stagnation pressure [7].

Experimental and analytical work have shown the jet flow to be unlikely to remain laminar through full expansion, particularly as the flow along the jet boundary reaches an annular mixing region between the Mach disk and the contact surface [28] and with the inherent instabilities associated with tangential, separated flows [53]. Experimental data and observation also suggest that large regions of the SRP flowfield are unsteady at certain conditions, with large, subsonic recirculation regions communicating disturbances and high-velocity shear layers transferring the disturbances along the jet boundary and back into the subsonic recirculation regions.

The wake aft of the body can be significantly larger than the wake for the same body with no opposing jet flow, as the combination of the body and jet flow often creates a larger flow obstruction than the body alone. Recirculation occurring on the forebody for bodies with supersonic retropropulsion, freestream conditions, nozzle exit area, and jet pressure ratio all potentially affect formation of the aft wake.

Although the majority of the literature is concentrated on decelerator applications of supersonic retropropulsion, potential aerothermal effects, test scaling parameters, and the capabilities of modern computational analysis have also been explored. Both experimental and computational work show the aerothermal effects of retropropulsion to be important, with the potential for doubling the local heat transfer to the body when combustion products are injected into the shock layer [8, 43, 44, 45, 46, 47, 49, 50, 54, 55, 56]. Experimental work has produced basic relationships for scaling and developed an initial set of similarity parameters for model and nozzle design. Computational investigations are ongoing, and in many cases, the results show reasonably favorable agreement with experimental data for axisymmetric configurations across a limited set of conditions. This work is discussed in Sections 2.3 and 2.4, respectively, later in this chapter.

2.1.4 Flowfield Stability Transitions

Flowfield stability for supersonic retropropulsion refers to the transitions between blunt, compact flowfields and more oblique flowfields with large upstream displacements as flow conditions change. Flowfield stability is not the same as flowfield steadiness; all SRP flowfields have been observed to exhibit some degree of unsteadiness.

Flowfield stability transitions have been experimentally observed across a variety of SRP configurations, though configuration alone does not drive the transition of the stability of the SRP flowfield [13, 42, 57]. In general, experimental work has found the flowfield stability transition conditions to be a strong function of the ratio of the exit pressure to the local ambient pressure, p_e/p_a or p_e/p_∞ (e.g. the expansion condition of the jet flow), the ratio of the nozzle exit area to the reference (or base) area of the body, A_e/A_{ref}, and the exit Mach number, M_e, or expansion ratio of the nozzle, A_e/A^*, all of which influence the shape of the contact surface formed through the

aerodynamic - propulsive interaction [7, 42, 58].

The flowfield transitions between two primary modes: a blunt penetration mode (BPM) and a long penetration mode (LPM). The blunt penetration mode is characterized by the penetration of the jet flow into the shock layer with a highly under-expanded jet structure. Blunt penetration flowfields typically exhibit local unsteadiness, often at the shock intersections in the jet structure where vortex shedding is occurring. Configurations with multiple jets may exhibit more global unsteadiness in the flowfield as a result of potentially oscillating intersections of the individual jet boundaries but still be in a characteristically blunt penetration mode.

The long penetration mode is characterized by the jet flow penetrating the bow shock, causing a large upstream displacement of the bow shock and visible dissolution/dispersement of the bow shock. The maximum upstream displacement can be substantial; displacements have been observed experimentally to be upwards of 8 - 10 body diameters, depending on the configuration and conditions [42, 51]. SRP flowfields in a long penetration mode typically exhibit global unsteadiness. This unsteadiness is believed to have contributions from oscillatory vortex shedding in the jet, transitions in the jet shear layer, and the dispersed bow shock [57].

Physically, the transition of the flowfield is a function of the jet structure arising from the expansion condition of the jet flow [57]. In the over-expanded case (Fig. 5(a)) ($p_e < p_a$), the jet boundaries collapse toward the jet centerline so sharply in trying to raise the jet pressure to the local ambient pressure that subsequent reflections lack sufficient momentum within the jet flow to significantly disrupt the exterior flow. Over-expanded conditions tend to result in a blunt penetration mode and have been frequently observed experimentally at very low jet pressure ratios [8]. In the moderately under-expanded case (Fig. 5(b)) ($p_e \gtrsim p_a$), expansion waves are reflected off of the opposing jet boundary as compression waves. Several intersecting expansion wave structures are necessary to lower the jet pressure to the local ambient

pressure, creating a more oblique contact surface at an increased displacement from the body. Moderately under-expanded conditions tend to result in a long penetration mode. Highly under-expanded jet flows ($p_e > p_a$) have single-cell structures that terminate with a Mach disk and more blunt contact surfaces, as opposed to a series of intersecting expansion waves and oblique shocks and significantly more slender contact surfaces. Accordingly, highly under-expanded jet flows tend to result in a blunt penetration mode.

These modes are illustrated in Fig. 9 with Mach contours (adapted from [8]) as $p_{0,j}$ is increased from no jet flow to conditions yielding a blunt penetration mode. Note that increasing $p_{0,j}$ increases p_e. As the jet total pressure is increased further, the jet flow becomes increasingly highly under-expanded, and the flowfield remains in a blunt penetration mode.

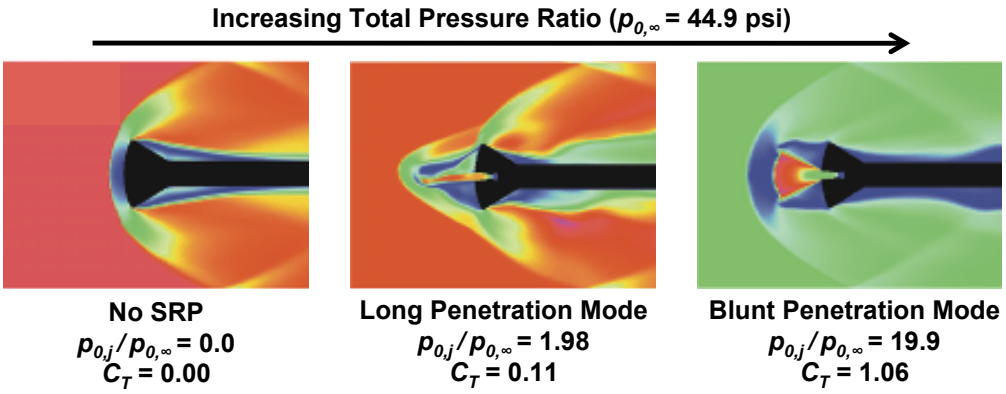

Figure 9: Transition between long and blunt penetration modes. $M_\infty = 3.48$, $M_e = 2.94$. (Adapted from [8]).

Using experimental data from Peterson and McKenzie [9], Fig. 10 illustrates the abruptness with which these mode transitions occur using the non-dimensional bow shock location along the centerline as the total pressure ratio is increased for a model with four nozzles on the forebody at approximately 40% of the model radius. Consistent with other cases in the literature, the bow shock standoff distance increases proportionally with increasing jet total pressure within the blunt penetration mode.

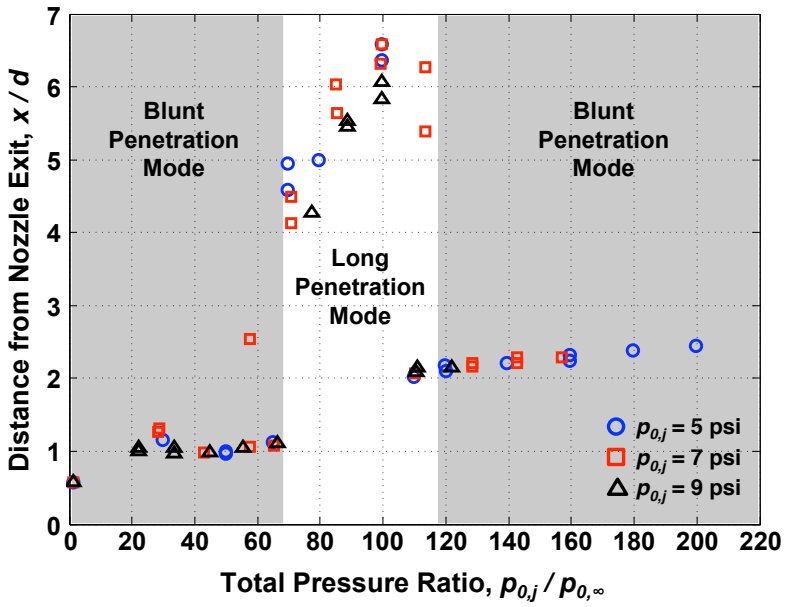

Figure 10: Experimental data illustrating the transition between long and blunt penetration modes. $M_\infty = 1.50$, $M_e = 3.0$. (Adapted from [9]).

Given the complexity of the SRP flowfield along the jet boundary within the shock layer and the dependence on configuration, the conditions at which mode transitions occur have been found to be difficult to predict accurately using analytical and computational methods [57]. During wind tunnel testing by Berry et al. [51, 52], and even earlier in other investigations [9, 13, 42], it was observed that the conditions at which the flowfield transitioned between the long penetration mode and the blunt penetration mode differed depending on whether the point of transition was approached from either a higher or a lower pressure, suggesting a potential for hysteresis in SRP flows. Specifically, the transition from the long penetration mode (and weakly under-expanded jet flow) to the blunt penetration mode (and highly under-expanded jet flow) occurs at higher jet pressure ratios as $p_{0,j}$ is increased than the jet pressure ratios required for the reverse transition as $p_{0,j}$ is decreased. While recent work has examined the mechanisms associated with these transitions [8, 57], this particular phenomena remains poorly understood, and significant work, both experimental and computational, is still needed to fully characterize this behavior. This is particularly

true for different configurations of multiple nozzles, which were observed by Berry et al. [51, 52] to exhibit an additional transition in flowfield stability arising from the interactions between individual jet flows. The work within this thesis has been restricted to conditions resulting in the blunt penetration mode for all SRP configurations.

2.1.5 Configuration Effects

The configuration (location, number, and size) of retropropulsion nozzles on the vehicle forebody affects the structure and behavior of the interaction between the jet flow and the shock layer. Figure 8 (Section 2.1.3) illustrated the primary flow features associated with an aerodynamic - propulsive interaction for a central retropropulsion configuration. Figure 11 illustrates analogous features for a peripheral retropropulsion configuration and a moderately low jet pressure ratio. Clusters of nozzles can have flowfields similar to that described for a central configuration across a large range of jet pressure ratios [9, 17]. A circular arrangement of nozzles, even with the nozzles toward the periphery of the vehicle forebody, has also been observed to produce flowfields strongly resembling the central configuration geometry and structure at conditions still below but approaching flight-relevance [51, 52].

For a central retropropulsion configuration (Fig. 8), the jet flow is directed primarily at the central section of the bow shock. The shape of the contact surface formed between the bow shock and the Mach disk (and extending outboard) is the effective shape of the flow obstruction seen by the freestream. The shape of the contact surface is dependent on the geometry of the body, though the geometry has been shown to be reasonably approximated as spherical [7]. As a result of the displacement of the bow shock upstream and the shielding of the body from the freestream flow by the jet structure, the surface pressures on the body are significantly reduced, as compared to the pressures on the same body with no retropropulsion. This reduction in surface

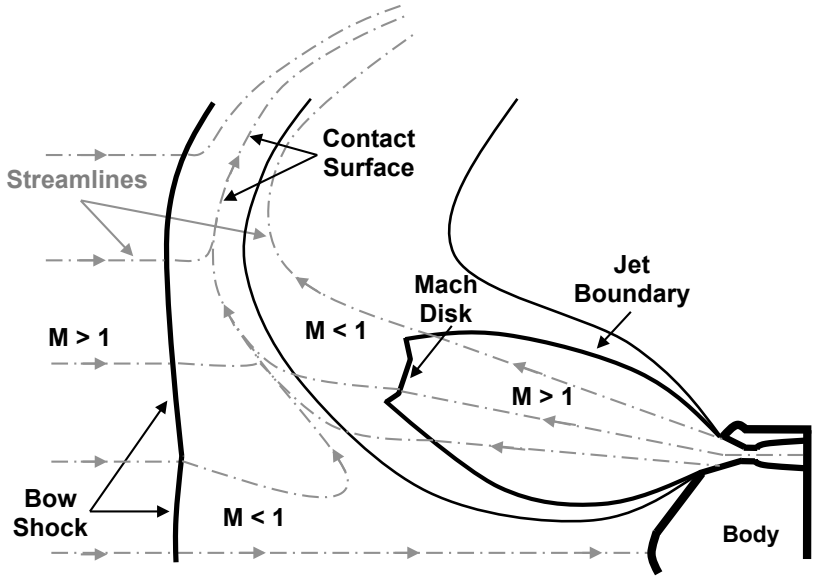

Figure 11: Flowfield characteristics for peripheral retropropulsion configurations. (Adapted from [10, 11]).

pressure corresponds to the observed reduction in aerodynamic drag for central and peripheral SRP configurations, though the conditions at which the pressure begins to be reduced are configuration dependent.

In contrast, the jet flows in a peripheral configuration (Fig. 11) are significantly less disruptive to the bow shock inboard of the nozzles at certain conditions (lower jet pressure ratios). As a result, surface pressures inboard of the nozzles can be preserved at low thrust levels, conditions where the central region of the body is not well shielded from the freestream flow. Figure 12 illustrates the region of high pressure inboard of the nozzle resulting from the relative lack of disturbance of the portion of the bow shock nearest the nose of the blunt body. Peripheral configurations do not typically have significant flow recirculation inboard of the nozzle exits as the freestream and flows are swept primarily outboard and aft of the body. The freestream flow in the stagnation region is turned up to 180° along the jet boundaries, but none of the recirculation over the body characteristic of the central configuration has been observed. The impingement of the jet flow on the outboard portion of the bow shock

generally results in a contact surface projecting a much larger flow obstruction to the freestream than the body alone, yielding a large aft wake.

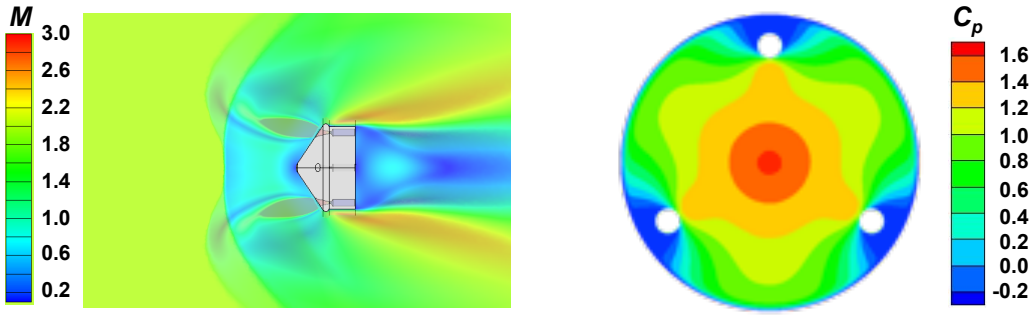

Figure 12: Example of flowfield and inboard surface pressure preservation for a peripheral configuration. $C_{T,total} = 1.66$, $M_\infty = 2.0$ [11].

As the total pressure of the jet flow increases, the individual jets begin to coalesce inboard and form flow structures more characteristic of central configurations [9, 13, 51, 52]. A schematic illustrating this progression is given in Fig. 13. The flowfield is highly unsteady at conditions where intersections of the jet boundaries are occurring. Oscillating intersections between normal and oblique shocks may generate new slip lines, creating additional jet flows and structures within the shock layer.

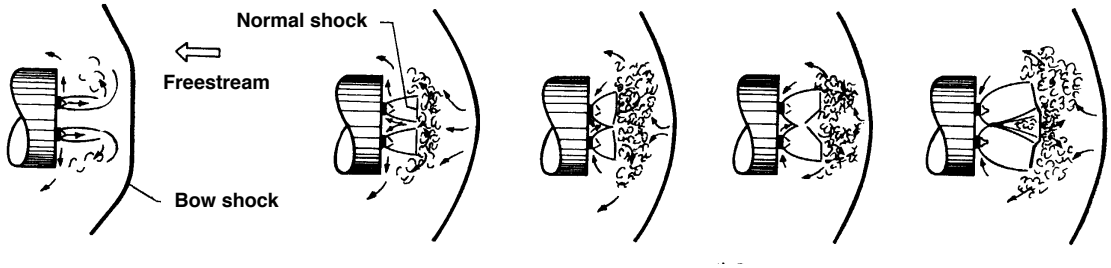

Figure 13: Schematic of individual jet flows coalescing into a larger, single structure. (Adapted from [9]).

For a configuration of multiple nozzles arranged at approximately 40% of the model radius about the body's axis of symmetry, Peterson and McKenzie [9] observed similar transitions in flowfield stability to those observed for an SRP configuration with a single, centrally-located nozzle. Limited data from work by Jarvinen

and Adams [13] for a multiple nozzle configuration with three nozzles at 80% of the body radius also support the notion of a shift in flowfield structure and behavior for peripheral configurations toward structures and behaviors more characteristic of central configurations at higher thrust coefficients. Recent experimental work by NASA's ETDD Program also observed and confirmed the repeatability of these trends in flowfield structure and behavior as jet pressure ratio is increased using a configuration with three nozzles at the model half-radius [51, 52].

A configuration of four nozzles, with a ring of three equally-spaced nozzles as the model half-radius and one nozzle in the forebody center, was also recently explored by NASA's ETDD Program. Remarkably different flowfield structures and behaviors were observed as the jet pressure ratio was increased for this configuration [51, 52]. At low thrust coefficients ($C_{T,total} < 5$), the addition of the central nozzle resulted in a very stable flowfield with only localized unsteadiness from the shedding of the annular vortex from the outboard portions of the jet structure. At the same conditions, without the central nozzle, the flowfield was highly unsteady, with no observable periodic behavior. However, as C_T was increased further for this four nozzle configuration, an abrupt transition to an asymmetric and globally unsteady flowfield occurred. This is the opposite of the change in flowfield structure and behavior observed for the same configuration but without the central nozzle (three nozzles at the model half-radius), where the flowfield became much more steady with an increasingly blunt flowfield structure as C_T increased. The unexpected appearance of this behavior further motivates the need for additional ground testing with parametric variation of flight-relevant SRP configurations.

2.2 Aerodynamic Characteristics

The primary aerodynamic effect of supersonic retropropulsion is to reduce the surface pressures, and subsequently, the aerodynamic drag contribution to the total axial

force decelerating the vehicle. This has been observed for all configurations tested to date, with single and multiple nozzles, both centrally- and peripherally-located on the body, and across all conditions approaching flight-relevance. The precise conditions, or window of conditions, for which this characteristic reduction in surface pressure occurs are a strong function of the relative strength of the retropropulsion exhaust flow as compared to the supersonic freestream environment (i.e. the jet pressure ratio) and the geometry of the SRP configuration. As discussed in the previous section, central and peripheral retropropulsion configurations can exhibit very different flowfield structures and behaviors, particularly at conditions corresponding to low thrust coefficients, resulting in contrasting aerodynamic effects. All force and moment coefficient values and trends discussed in this section have been taken from the literature and are based on the integration of a limited number of experimental pressure measurements to yield force and moment information; to date, no direct measurement of forces and moments has been completed in SRP ground testing.

2.2.1 Central Retropropulsion Configuration

A substantial number of experiments were performed from the late 1950s through the early 1970s on the aerodynamic effects of a centrally-located retronozzle for EDL applications. These experiments used blunted cones, hemispheres, and other simple bodies of revolution over freestream Mach numbers from 1.05 to 9. With increasing thrust coefficient, the aerodynamic drag coefficient decreases rapidly to a minimum value of approximately 5 - 10% of the no-jet value and then remains constant at this minimum value as C_T is increased to its maximum value in each test series. For any appreciable level of thrust, $C_T \geq 0.5$, the total axial force coefficient is dominated by the contribution from thrust. Above a C_T of approximately 0.8, the increment of $C_{A,total}$ above C_T is roughly constant, with this increment due to the minimally preserved aerodynamic drag coefficient. These effects are shown in Fig. 14 (adapted

from Ref. [12]).

With jet flow from a centrally-located nozzle, the high inboard pressure present in the no-jet case is greatly reduced. The jet flow perturbs the bow shock to become more oblique than normal and displaces the bow shock further upstream. This reduction in shock strength, increased displacement from the body, and shielding of the body by the jet structure lead to a reduction in surface pressure. The degree of this surface pressure reduction tends to increase slightly as the freestream Mach number increases [12].

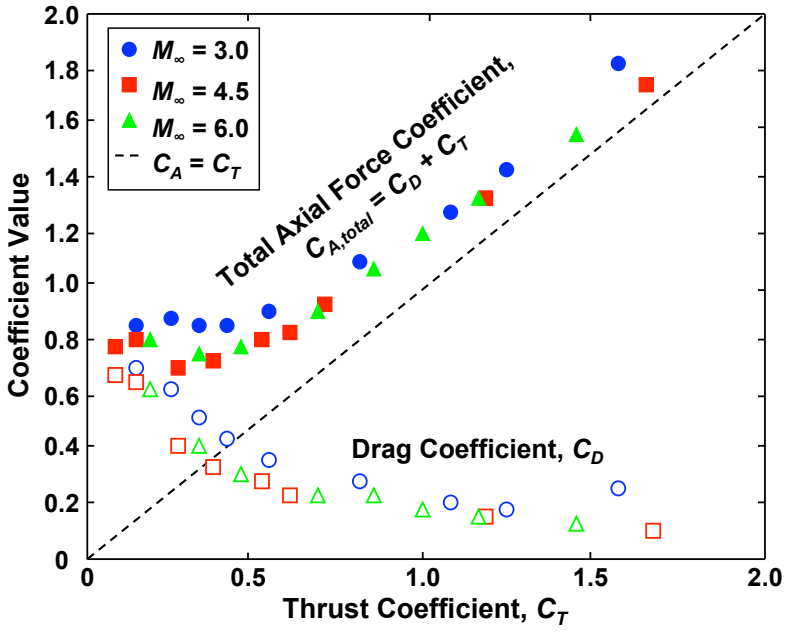

Figure 14: Aerodynamic drag coefficient variation with increasing C_T for a central configuration. (Adapted from [12]).

The jet flow cannot be contained within the boundary layer, and a sharp flow turning angle causes the boundary layer to separate on both sides of the jet over the forebody. Free shear layers form on both sides of the jet, moving the flow within the shock layer towards the vehicle shoulder. Little variation in the surface pressure is seen between different blunt body geometries, indicating a relative independence of aeroshell cone angle on the drag reduction effects of SRP for mid-to-high C_T [7, 8, 9,

12, 13, 41, 58].

Romeo and Sterrett [42] explored flowfield behaviors for a centrally-located nozzle over angles of attack from 0° to 35°. Beyond small angles of attack (> 5°), the structure of the flowfield begins to break down. For conditions where the flow is in a blunt penetration mode with local unsteadiness, at increasing angles of attack, the flowfield becomes asymmetric with significant global unsteadiness. Similar behaviors were recently observed in testing through NASA's ETDD Program; the structure and behavior of the flowfield changes to become less symmetric and more unsteady as the angle of attack increased beyond 8° [51, 52].

The pitching moment coefficient slopes for increasing thrust coefficient at freestream Mach numbers of 0.6, 1.05, and 2.0 are shown in Fig. 15. For this data, the pitching moment is referenced from the apex of a blunted, 60-deg conical aeroshell. The data were taken over angles of attack from -6° to +6°. For the central nozzle configuration, the pitching moment coefficient slope for a given C_T is nearly linear with variation in angle of attack across the range tested (-6° to +6°), with the result that data for a specific angle of attack are not distinguished in Fig. 15. The pitching moment coefficient slope becomes increasingly negative as the thrust coefficient increases to 1, then becomes less negative with additional increases in thrust coefficient, appearing to asymptotically approach a near-zero, though still negative, slope as C_T increases above 4. The pitching moment coefficient slope for these cases is always negative, indicating static stability about the reference point across the range of thrust coefficients tested. This static stability is observed even for cases in which the flowfield itself may be exhibiting global unsteadiness or asymmetric flow structures.

Similarly, work by Hayman [58] found the jet pressure ratio ($p_{0,j}/p_\infty$, from Eq. 3 with requisite isentropic flow relations), M_e, and A_e/A_{ref} to strongly affect the windward surface pressures and negligibly affect the leeward surface pressures as the model pitched through angles of attack from 0° to 90°. The leeward surface pressures

remain approximately equal to the freestream static pressure across the entire angle of attack sweep ($C_p = 0$). Integration of the experimental surface pressure data over a cylinder representative of the original model (aspect ratio of 1:3, referenced about the geometric center of the cylinder) confirms a negative slope for the pitching moment coefficient, varying linearly with angle of attack from 0° to 30° for thrust coefficients up to 12. However, these observations are from a very limited number of test points, and significantly more data is needed before any definitive conclusions can be made about the effect of SRP on the stability characteristics of the vehicle.

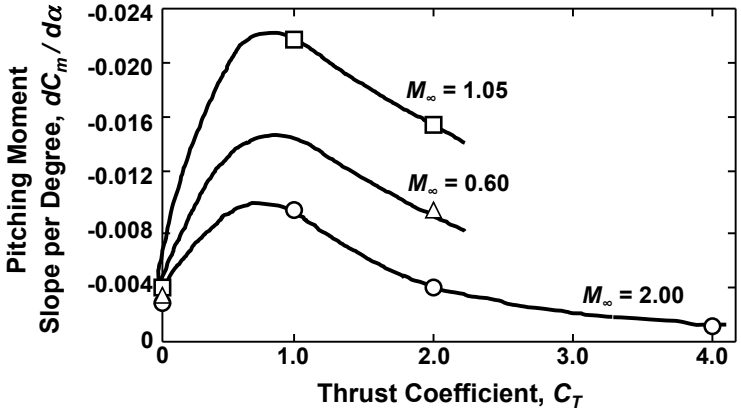

Figure 15: Variation of pitching moment slope with thrust coefficient [13].

2.2.2 Peripheral Retropropulsion Configuration

Prior to June 2010, the only experimental data available for peripheral retropropulsion configurations were for 60-deg sphere-cone aeroshells at freestream Mach numbers of 1.05, 1.50, 2.0, and 6.0, with air for the freestream and jet flow [13, 39]. Jarvinen and Adams [13] and Keyes and Hefner [39] observed a lack of disruption of the center of the bow shock by the peripherally-directed jet flow. The jet flow is swept outboard and downstream, away from the vehicle, resulting in a region of high pressure remaining over portions of the aeroshell inboard of the nozzles. This allows for some degree of preservation of the static aerodynamic drag, as illustrated previously in Fig. 11 and Fig. 12. The bow shock remains sufficiently undisturbed and close to the body for

total thrust coefficients less than approximately 1 for the configurations tested [13].

Experimental work by Jarvinen and Adams [13, 40] also found a range of thrust coefficients over which a peripheral configuration with three scarfed nozzles (see Fig. 7(b)) resulted in a substantially larger total axial force coefficient than that determined for a single, centrally-located nozzle at the same total thrust coefficient. A comparison of the total axial force coefficient between these two extremes in retropropulsion configuration at the same conditions is shown in Fig. 16.

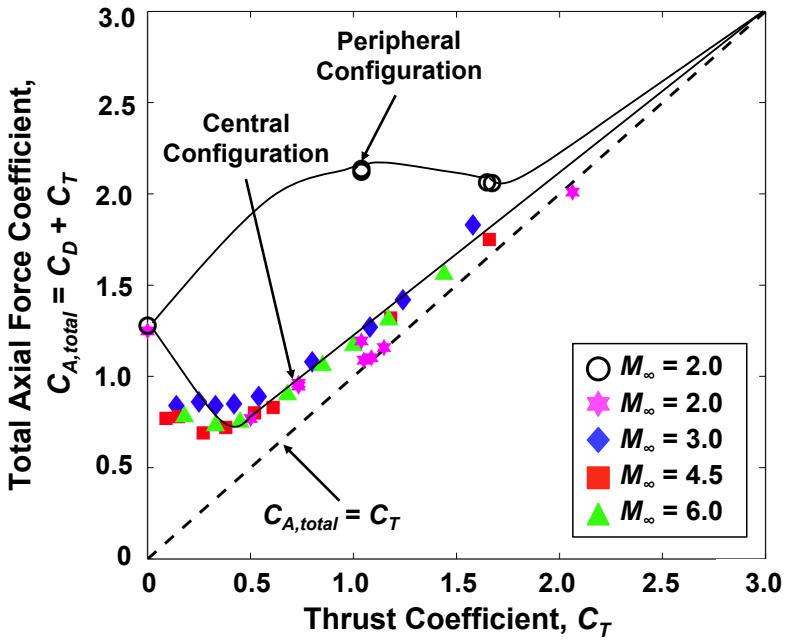

Figure 16: Experimental data for total axial force coefficient as a function of thrust coefficient. (Data from [12, 13]).

A retropropulsion configuration with three nozzles at the body periphery is more aerodynamically efficient than a configuration with a single, central nozzle for low thrust coefficients. This behavior was observed for C_T less than approximately 1.5, meaning that a relatively larger portion of $C_{A,total}$ is composed of C_D for the peripheral configuration than for the central configuration up to these conditions. At thrust coefficients above approximately 3, the total axial force coefficients for both configurations are approximately equal to the thrust coefficient alone, as indicated by

the dashed line in Fig. 16. As discussed in previous sections, this is the result of the body becoming increasingly shielded from the freestream flow by the jet structure.

At lower thrust coefficients, the peripheral jet flow only mildly disturbs the bow shock at the edges (Fig. 11). This perturbation flattens the contact surface outboard of the body, creating a flowfield obstruction nearly equivalent to the area of the body. At higher thrust coefficients, the individual jet flows expand further inboard and eventually coalesce into a more uniform flow structure, reducing the size and strength of the high pressure region inboard of the nozzles [13, 39, 51, 52].

The contribution of aerodynamic pressure to the total axial force coefficient, while strongly dependent on C_T, is less dependent on freestream Mach number. The maximum degree of aerodynamic drag preservation, observed for thrust coefficients up to 1 for retropropulsion configurations with small nozzles at the extreme forebody periphery, remains nearly constant over the freestream Mach numbers tested (2.0 to 6.0) [13], as shown in Fig. 16. In these cases, nearly equal contributions to the total axial force by aerodynamics and thrust are possible. Surface pressure data confirm that the aeroshell is influenced by a nearly uniform region of high pressure, and this surface pressure remains at its highest value up to total thrust coefficients near 1 [13].

Pitching moment data, from integrated pressure measurements, exist for the peripheral configuration and body orientation shown in Fig. 7(b), with a single nozzle at the "top" of the forebody and two nozzles at the "bottom" of the forebody. Variation in angle of attack, from -16° to +16°, causes little change in the total forebody axial force coefficient for freestream Mach numbers of 1.05, 1.50, and 2.0 and thrust coefficients from 0 to 1.9 [13]. However, the pitching moment coefficient exhibits nonlinear behavior for $M_\infty = 2.0$ conditions, as shown in Fig. 17. The pitching moment coefficient is referenced from the apex of a spherically-blunted 60-deg cone. The data given is insufficient to reference the pitching moment coefficient from a more realistic location. For a thrust coefficient of 1.04, the pitching moment coefficient slope is

positive for angles of attack between -2° and -8°.

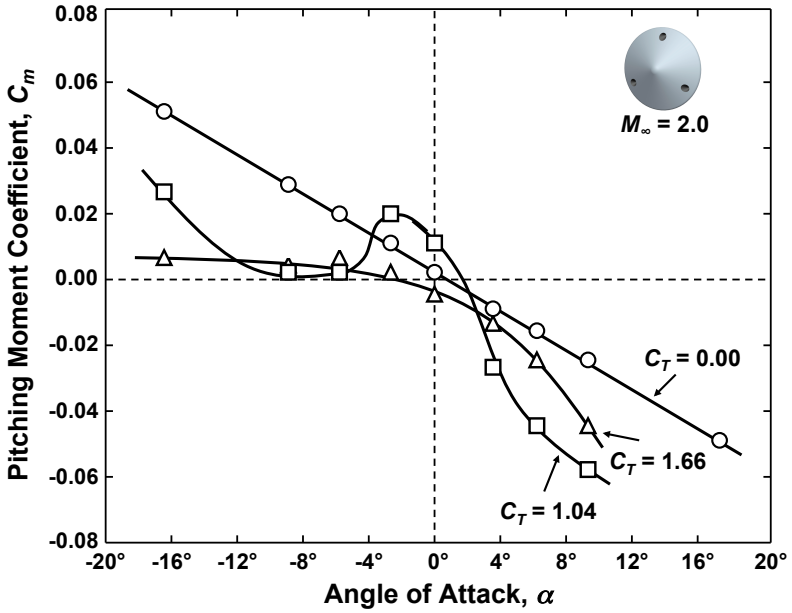

Figure 17: Variation of pitching moment coefficient with thrust coefficient and angle of attack [13].

With the limited data available for this configuration, the nonlinearity and indiscernible dependence on thrust coefficient present difficulty in determining the relationship between the vehicle's static stability about this reference point and C_T. Observations during recent testing in the NASA LaRC UPWT included a strong dependence of flowfield steadiness and structure on the roll orientation of a three nozzle configuration and the total thrust coefficient as the model was pitched through a range of angles of attack [14, 51, 52]. Significant forward work is still required, however, both experimentally and computationally, to establish trends for the static and dynamic stability characteristics of vehicles utilizing SRP across all variations in retropropulsion configuration.

2.2.3 Differential Throttling Effects

Jarvinen and Adams [13, 40] also explored the potential for drag modulation capability by throttling various combinations of three engines in a peripheral configuration.

The variation in $C_{A,total}$ between throttled and unthrottled conditions was observed to increase with increasing freestream Mach number. At $M_\infty = 1.05$, little variation between the unthrottled case and the cases in which one engine was throttled down by either 50% or 75% was observed for thrust coefficients below approximately 3. However, at $M_\infty = 2.0$, more significant variation between the two cases (unthrottled versus throttled down) was observed at total thrust coefficients between 1 and 4.

Similar departures were observed under the same conditions for cases in which two of the three engines (as opposed to just one engine) were throttled down [13]. In the $M_\infty = 1.05$ case, with one engine throttled down by 50% and the total thrust coefficient increased from 0.0 to 4.0, the forebody drag coefficient decreased from 0.9 to approximately -0.6. At the same freestream conditions, with two engines throttled down and the thrust coefficient increased from 0.0 to 4.0, the forebody drag coefficient decreased from 0.9 to approximately -0.8. At higher thrust coefficients, surface pressures were observed to be lower than the freestream static pressure; thus, negative force coefficients are possible at these conditions.

In the $M_\infty = 2.0$ case, with one engine throttled down and the thrust coefficient increased from 0.0 to 4.0, the forebody drag coefficient decreased from 1.2 to approximately -0.1. In the $M_\infty = 2.0$ case, with two engines throttled down and the thrust coefficient increased from 0.0 to 4.0, the forebody drag coefficient decreased from 1.2 to approximately -0.1. Jarvinen and Adams concluded that, as freestream Mach number increased, the same degree of forebody drag coefficient modulation could be realized with decreasing thrust coefficients [13]. Figure 18 shows experimental data for $M_\infty = 1.05$ and $M_\infty = 2.00$, where the reduction in the forebody drag coefficient occurred at lower thrust coefficients for the supersonic freestream condition as compared to the transonic freestream condition.

Not unexpectedly, throttling various combinations of engines at the body periphery alters the static stability characteristics of the vehicle [13]. The total pitching

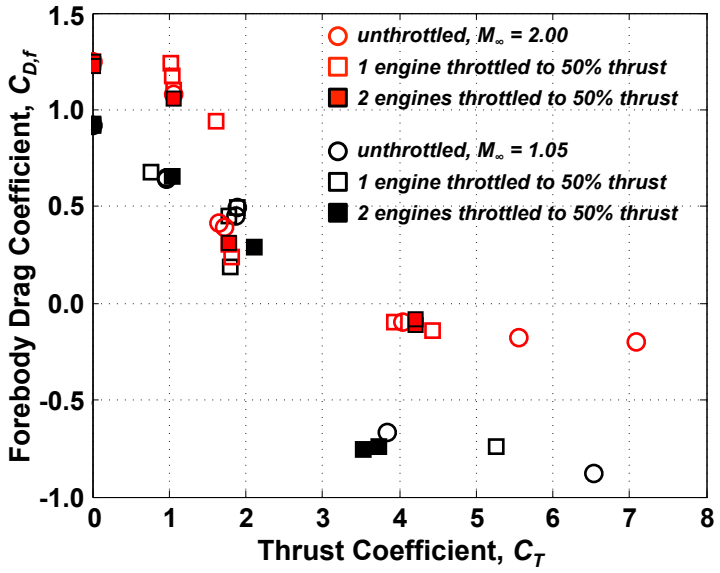

Figure 18: Variation of forebody drag coefficient with thrust coefficient at $\alpha = 0°$. (Adapted from [13]).

moment about the reference point is the sum of the pitching moment due to surface pressure forces and the pitching moment induced by imbalances in thrust. For cases where the body is oriented at a positive angle of attack, throttling down engines on the leeward side of the forebody induces a nose-down pitching moment. In the same orientation, throttling down engines on the windward side of the forebody induces a nose-up pitching moment [13].

These induced pitching moments can be attributed to the non-uniform engine thrust and resulting changes in $C_{A,total}$ at throttled conditions. Schlieren images showed an increase in standoff distance and an increase in the obliqueness of the local section of the bow shock in the region of the unthrottled jet flow [13]. The decrease in shock strength and accompanying increase in obliqueness supports the conclusion that the reduction in the total axial force coefficient with increasing thrust coefficient (as compared to the unthrottled case) is strongly dependent on changes to the surface pressure distribution caused by throttling over the limited range of thrust coefficients explored.

The effectiveness of throttling in controlling pitching moment, defined as the ratio of change in the actual pitching moment (determined from experimental data) to the change in the theoretical pitching moment (due solely to an imbalance in engine thrust), is observed to be reduced by 20% at supersonic freestream conditions as compared with the throttling efficiency at subsonic conditions [13]. The increase in surface pressure with throttling reduces the total pitching moment as compared to the pitching moment arising solely from an imbalance in thrust at supersonic freestream conditions.

The complexity of the internal plumbing required prevented the effects of differential throttling from being explored in recent testing of multiple nozzle configurations by NASA's ETDD Program. However, given that NASA's candidate architectures for landing high-mass payloads on Mars require the throttling of combinations of engines during the SRP phase, future experimental work will likely be required to fully quantify the effects of and develop models for differential throttling.

2.3 Experimental Summary

Technology development programs for planetary exploration missions in the 1960s and early 1970s matured supersonic retropropulsion close to its current level, primarily through experimental investigations. The intent of these experiments was to understand drag effects potentially advantageous to EDL as well as ways to mitigate the severity of the aerothermal environment experienced during entry. Scaling parameters were developed to accurately simulate the larger chemical bipropellant propulsion systems visualized for conceptual Mars landers using subscale models [5]. The freestream Mach number, thrust coefficient, a pressure sensitivity parameter, and an engine scaling parameter are amongst the parameters to be matched for proper simulation of retrorocket flow at subscale in a wind tunnel [5, 13]. The pressure sensitivity and engine scaling parameters are discussed in additional detail below.

The nozzle exhaust flow can be simulated if the nozzle exit to ambient pressure ratio and the pressure sensitivity of the exhaust flow to the flow direction are matched [5]. As discussed in previous sections, the jet flow geometry is dependent on p_e/p_a, as this dictates the expansion condition of the exhaust flow and the location of the jet boundary. For non-SRP flowfields, and in a more limited sense for SRP flowfields, p_a is proportional to p_∞, allowing for the jet boundary and expansion to be simulated if p_e/p_∞ is matched. Recognizing that p_e/p_∞ varies linearly with $M_\infty^2 C_T$ for a given nozzle configuration (from Eq. 3), the engine scaling parameter can be defined as the right hand side of Eq. 5.

$$\frac{p_e}{M_\infty^2 C_T p_\infty} = \frac{\gamma_\infty A_{ref}}{2A_e(1+\gamma_e M_e^2)} \tag{5}$$

Simulation also requires accounting for the differences in the ratio of specific heats between the exhaust gas used in testing and the exhaust gas used in flight to compensate for variation of the flow turning angle with pressure ratio. Pindzola [5] and Jarvinen and Adams [13] suggest this to be achievable by matching the vehicle and model exhaust gas pressure sensitivity with respect to the flow direction, $\frac{1}{p}\frac{dp}{d\nu}$, where ν is the flow direction through the nozzle exit plane. Plotting p versus ν on a semi-log plot for both ratios of specific heats (for the model in a ground test facility and for the full-scale vehicle in flight operation) and translating the axes until the curves are coincident yields the best model exit Mach number for exhaust flow simulation [13].

2.3.1 Pre-2010 Experimental Data Set

Although numerous wind tunnel tests of relevance to supersonic retropropulsion have been conducted, the scope of the work is limited in the freestream conditions, retropropulsion conditions, and configurations and geometries explored. The majority of past efforts focused on blunt bodies with a single, centrally-located nozzle. Prior

to June 2010, only three investigations had been found that used multiple nozzles [9, 13, 39]. An additional limitation of the existing data is the use of compressed air, nitrogen, hydrogen, or helium in all test cases for the nozzle exhaust. No experimental data exist in which combustion products were [intentionally] exhausted, likely due to test scale and the complexity and safety concerns associated with operating a combustion system within a ground test facility. As noted earlier, the primary objectives of many investigations were to explore potential reductions in heat transfer, not supersonic decelerator performance. The flow conditions and geometries comprising the existing experimental database are summarized in Table 1. The maximum model diameter used in any of these experiments was 8.25 in., though the great majority are limited to 4 inch-diameter and below. No supersonic retropropulsion aerodynamic data have been found in support of missions to destinations other than Mars.

Table 1: Existing supersonic retropropulsion experimental database.

Available central nozzle configuration data			
Relevance	M_∞	Freestream	Jet
Static aerodynamics	1.05 - 6.0, 20 - 21	Air	Air, He
Flowfield stability	1.05 - 6.0	Air	Air, He
Flowfield geometry	1.05 - 8.0	Air	Air, He
Effect of nozzle geometry	1.05 - 6.0, 20 - 21	Air	Air, He
Angle of attack variation	1.05 - 6.0	Air	Air, He
Aerothermodynamics	2.0, 6.0 - 8.0, 20 - 21	Air	Air, He, N_2, H_2
Systems-level implications	1.05 - 6.0	Air	Air

Available peripheral nozzle configuration data			
Relevance	M_∞	Freestream	Jet
Static aerodynamics	1.05 - 6.0	Air	Air
Flowfield stability	1.05 - 2.0	Air	Air
Flowfield geometry	1.05 - 2.0	Air	Air
Effect of nozzle geometry	1.05 - 2.0	Air	Air
Angle of attack variation	1.05 - 2.0	Air	Air
Aerothermodynamics	–	–	–
Systems-level implications	1.05 - 2.0	Air	Air

This experimental database will need to be expanded to include additional retropropulsion configurations, geometries, exhaust and freestream species, and combustion retropropulsion systems. A broader range of flow conditions will need to be explored, targeting conditions within the operational envelope for SRP, as discussed in Chapter 3 of this thesis. Additionally, more slender body geometries, such as biconics and ellipsleds, are candidates for entry vehicles in human-scale Mars architectures, and until recently, no experimental data was available to validate computational simulations of SRP systems derived for these geometries.

2.3.2 Recent Experimental Efforts

Two wind tunnel tests of supersonic retropropulsion were completed by NASA's ETDD Program, one in July 2010 in the NASA LaRC 4 $\times$ 4 ft. UPWT and a second in August 2011 in the NASA ARC 9 $\times$ 7 ft. UPWT [14, 51, 52, 59]. These are the first tests targeting conditions approaching flight-relevance for high-mass Mars exploration missions and dedicated to producing a data set for the validation of CFD tools in simulating SRP flowfields. The model was a slender body, with a 5 inch-diameter 70° sphere-cone forebody and a cylindrical aftbody. The configurations tested had no nozzles (baseline), one central nozzle, three nozzles at the forebody half-radius, and four nozzles from the combination of the one- and three-nozzle configurations. This is the first time an SRP configuration with circumferential nozzles and a center nozzle was tested.

Test conditions spanned four freestream Mach numbers (M_∞ = 1.8, 2.4, 3.5, 4.6) [14]. Thrust coefficients up to 6.0 were explored where possible in the first test, depending on the nozzle configuration and observed degree of interference with the tunnel walls. Thrust coefficients up to 10.0 were explored in the second test, again where possible. The model was rolled through 180° and pitched through an angle of attack sweep from -8° to +20°, also depending on the nozzle configuration and

degree of interference with the tunnel walls. Static pressure ports and high-frequency pressure transducers were used to measure surface pressures on the model. Figure 19 shows still images taken from high-speed schlieren test video for each of the three SRP configurations at $M_\infty = 2.4$. The image on the left is at a lower C_T, and the image on the right is at a higher C_T.

While producing the expected highly under-expanded jet flow structures, all configurations and conditions exhibited unsteady flowfield behavior, ranging from localized, periodic unsteadiness due to vortex shedding near the jet termination structure to global, chaotic, and unpredictable unsteadiness throughout the entire flowfield [14]. The one nozzle configuration exhibited only local unsteadiness due to the shedding of an annular vortex from the jet interaction region, even as C_T was increased. The three nozzle configuration exhibited severe unsteadiness throughout the entire flowfield at low thrust coefficients and then rapidly transitioned to a flow structure exhibiting only local unsteadiness, similar to that observed for the one nozzle configuration.

As mentioned in Section 2.1.5, the four nozzle configuration exhibited very different behavior at low C_T and at high C_T conditions. At low C_T, the flowfield was observed to be even more steady than the flowfield for the one nozzle configuration at the same conditions, with the central nozzle flow appearing to significantly reduce or eliminate the unsteadiness observed for the three nozzle configuration at the same conditions. However, at higher C_T conditions, the flowfield was observed to abruptly begin exhibiting global unsteadiness with apparent transitions to a long penetration mode for the individual jet flows around the three jet ring. For all of the configurations, increasing the angle of attack beyond 4° resulted in increased unsteadiness in the jet interaction region on the windward side of the flowfield, with the roll orientation of the model affecting the degree of observed unsteadiness for SRP configurations with multiple nozzles. In ramping the jet total pressure up and down, the flowfield

One Nozzle Configuration

C_T = 1.99
Roll, pitch, and yaw = 0°
M_∞ = 2.4, Re_∞/ft = 1.0 × 10^6

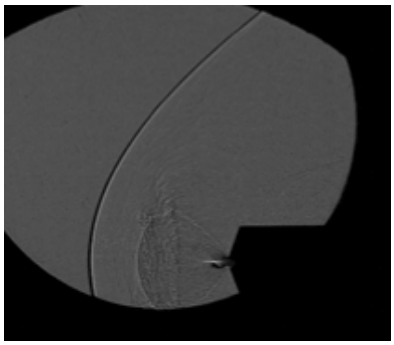

C_T = 4.00
Roll, pitch, and yaw = 0°
M_∞ = 2.4, Re_∞/ft = 1.5 × 10^6

Three Nozzle Configuration

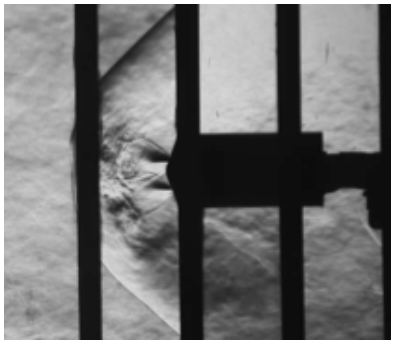

C_T = 1.94
Pitch and yaw = 0°, roll = 180°
M_∞ = 2.4, Re_∞/ft = 1.0 × 10^6

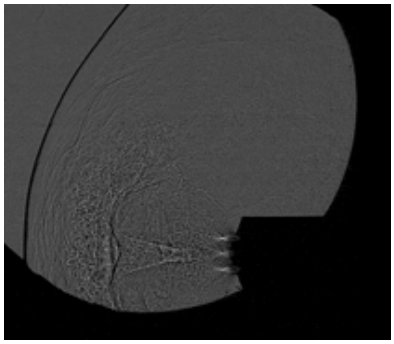

C_T = 10.01
Pitch and yaw = 0°, roll = 180°
M_∞ = 2.4, Re_∞/ft = 1.5 × 10^6

Four Nozzle Configuration

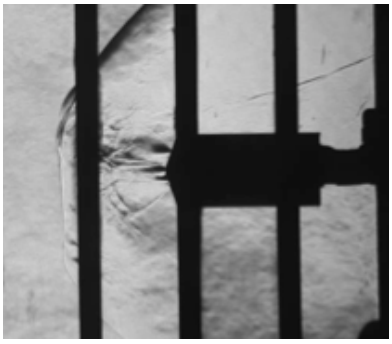

C_T = 2.95
Roll, pitch, and yaw = 0°
M_∞ = 2.4, Re_∞/ft = 1.0 × 10^6

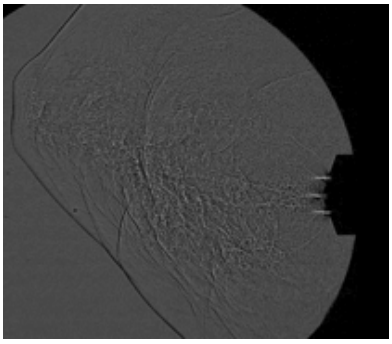

C_T = 5.93
Roll, pitch, and yaw = 0°
M_∞ = 2.4, Re_∞/ft = 1.5 × 10^6

Figure 19: Schlieren still images from SRP testing in the NASA LaRC 4 × 4 ft. UPWT (left) and the NASA ARC 9 × 7 ft. UPWT (right) for one nozzle, three nozzle, and four nozzle configurations. (Video from [14]).

transitions from a long penetration mode to a blunt penetration mode observed previously in other tests [8, 9, 42] were observed across all of the configurations.

The severe reduction in surface pressures observed in past tests of SRP was also observed in these tests across all three SRP configurations. Post-test analysis of the high-frequency pressure data is still in progress, though preliminary results for cases exhibiting a dominant peak frequency have found most frequencies to be in the range of 1 - 3 kHz [14, 51].

This test series has addressed many critical deficiencies in the experimental database from the literature and has increased the understanding of the behaviors and characteristics of SRP flowfields substantially. However, additional testing will still be required for additional multiple nozzle configurations, angles of attack ranging up to 25°, static and dynamic stability, direct force and moment measurements, exhaust composition with combustion products, higher thrust coefficients (and jet pressure ratios), and the exploration of the aerothermal implications of SRP to mature supersonic retropropulsion into a viable decelerator option for high-mass Mars EDL architectures. The data sets from these two tests currently represent the only data available for the validation of CFD tools in simulation SRP flowfields. Additional detail on the instrumentation and data from these tests is given in conjunction with computational results specific to this thesis in Chapter 5.

2.4 Computational Analysis Efforts

The previous sections in this chapter have outlined the flow physics relevant to SRP interactions, discussed the present understanding and implications of integrated aerodynamic characteristics, and summarized the experimental data set in the literature. Computational investigations into flowfields with characteristics similar to SRP flowfields stretch back more than a decade from the present, but much of this work was completed through isolated case studies. Simulations have been completed using both

inviscid and viscous computational approaches applied to a number of problems involving opposing supersonic flows [8, 11, 16, 29, 57, 60, 61, 62, 63, 64, 65, 66, 67, 68, 69, 70, 71, 72, 73, 74, 75, 76]. Much of the early computational work focuses on mitigation of severe aerothermal environments during entry or drag reduction effects, with very little focus on moderate thrust levels and flight-relevant conditions. However, more recent studies, largely in conjunction with NASA's ETDD Program, are focused on the application of SRP to the deceleration of high-mass entry vehicles for Mars exploration. Overall, the literature available on the computational simulation of flowfields resembling those characteristic of supersonic retropropulsion, while still limited in terms of flow conditions and vehicle configurations, is growing rapidly as interest in SRP continues to increase and computational tools are validated against newly available experimental data.

In general, accurate prediction of the static aerodynamics and flowfield stability of supersonic retropropulsion using CFD methods requires the ability to capture:

- Detached shocks
- Highly under-expanded jet flow structures
- Contact surfaces
- Formation and potential turbulent transition of free shear layers
- Fore and aft recirculation
- Boundary layer separation
- Local and global unsteadiness within the flowfield
- Relevant equilibrium chemistry

As mentioned, both inviscid and viscous computational analysis approaches have been applied to SRP flow interactions. The similarities between the flow interactions across these works have been and will continue to be useful in extending the approaches to additional analyses targeting SRP applications. This section reviews the computational approaches and key results for a number of these analyses.

Inviscid computational approaches [66, 70, 71, 73, 74] have shown varying degrees of success in capturing the locations of primary flow features, surface pressure distributions, and integrated force coefficients over the limited range of conditions and configurations considered. Nomura et al. [74] explored the interaction of a sonic jet of air exhausting from a flat-faced cylinder in a Mach 3.0 freestream (also air). This is the earliest computational work found on SRP-related flowfields, published in 1992, and the work is focused on applying a scheme capable of capturing discontinuities without oscillations. The comparisons made with experiment are qualitative only. The work employed a second-order upwind total variation diminishing (TVD) scheme, selected specifically for its ability to capture contact surfaces without smearing, as well as perfect gas chemistry and a Van Leer flux limiter. All solutions are steady-state. The locations of the Mach disk, contact surface, and bow shock agree fairly well with those reported in the original experiment. However, the barrel shock and jet boundary shapes differ from those observed experimentally, a result not entirely unexpected given that the nature of the analysis neglects of viscous dissipation. Such losses along the jet boundary and near the contact surface have been found to be significant under certain conditions.

Fomin et al. [73] performed inviscid analysis in support of experimental work on the pressure effects of a centrally-located, high-temperature, sonic plasma jet at freestream Mach numbers of 2.0, 2.5, and 4.0. The composition of the freestream was air, and the plasma jet was nitrogen at 5000 K, with the plasma jet exhausting from the nose of a truncated 30-deg cone. The analysis was a preliminary effort to

understand the separation existing between fluid dynamics and thermal processes in a supersonic freestream - propulsion interaction. Little information is given on the approach, aside from being a second-order accurate central-differencing scheme with relaxation and all solutions to be steady-state. In comparison with experimental data, the analysis captures the reduction in surface pressures resulting from the transition of the jet flow from a long penetration mode to a blunt penetration mode. The relatively good agreement seen between the inviscid, perfect gas solutions and the experimental plasma jet work for surface pressure distributions suggests that much of the plasma interaction at supersonic freestream conditions resembles retropropulsion gas dynamics, a promising result for future work targeting the inclusion of combustion products [73]. Additional work in which plasma jets are modeled using the assumption of a perfect gas with constant specific heats has been reported with similar conclusions [71].

Bakhtian et al. [70] conducted a parametric investigation into SRP configurations using Cart3D, a Cartesian-based Euler solver with adjoint-based mesh refinement. The configurations and conditions explored are derived from those tested by Jarvinen and Adams [13]: 60-deg sphere-cone aeroshell, $M_\infty = 2.0$ and 1.05, $M_e = 4.3$, central and peripheral nozzle locations on the forebody, and $C_T = 0$ to 3. All solutions utilize a second-order accurate upwind scheme with Van Leer flux vector splitting and are steady-state. The results follow similar trends to those observed in the original experiment for $C_{A,total}$ as a function of C_T, though the comparison becomes slightly less agreeable at higher thrust coefficients for the peripheral configuration. A reduction in surface pressures is achieved for the peripheral configuration but at higher thrust coefficients than observed in the original experiment, suggesting some difficulty simulating the inboard jet flow expansion and interaction of jet boundaries with one another. No flowfield images are given for the cases compared with experimental data, but an apparent lack of grid resolution in the bow shock region, despite

adjoint-based mesh refinement, may be contributing to the difficulties capturing the inboard flowfield structure. In general though, the computational results have favorable agreement with the locations of primary flow features and trends in surface pressure distributions and integrated force coefficients. The parametric configuration study includes tri-nozzle and quad-nozzle configurations, varying nozzle orientation, expansion ratio, and angle of attack.

Both laminar [62, 63, 64, 69, 72] and turbulent, viscous [8, 11, 47, 29, 60, 61, 57, 65, 75, 76] approaches have been applied to SRP-related flowfields, also with varying degrees of success in capturing the locations of primary flow features, surface pressure distributions, integrated force coefficients, and trends for surface heat flux across a broad range of conditions. Daso et al. [72] revisited earlier work by Fomin et al. [73] for a truncated cone with a sonic, nitrogen jet at $M_\infty = 2.0$ conditions (air). CFL3D is used for laminar, steady-state solutions; no additional information is given on the approach. In contrast to the results from Fomin et al. [73], the surface pressure distributions in this investigation do not compare well with experimental data for blunt penetration mode conditions upstream of the expansion corner of the cone. The trends, however, are consistent with the experiment, and the qualitative comparison of flowfield structures for long penetration mode conditions is reasonably good [73].

Under sponsorship from NASA's Fundamental Aeronautics Program, two configurations were tested in a Mach 12 free jet facility at the University of Virginia and examined computationally at the University of Michigan. A 0.22%-scale MSL capsule with either one central nozzle or four nozzles at the forebody half-radius were tested at $M_\infty = 12$ for thrust coefficients from 0 to 2.5 [62, 63, 64, 69]. All flow solutions are obtained using an axisymmetric, steady-state, laminar approach with modified Steger-Warming flux vector splitting applied to the inviscid fluxes. The results show

good qualitative agreement with planar laser-induced iodine fluorescence (PLIIF) visualizations for bow shock location along a stagnation streamline across all thrust coefficients tested. The integrated aerodynamic properties compare well with those given in the literature by McGhee [12], with similar trends and good agreement between $C_{A,total}$ and C_D across a broad freestream Mach number range (McGhee tested at M_∞ = 3.0, 4.5, and 6.0). Overall, the CFD results show a significant improvement in agreement of the shock standoff distance with PLIIF results as C_T increases, with the difference improving from approximately 30% at $C_T = 0.5$ to approximately 1% at $C_T = 2.5$. Qualitative comparisons with species mole fractions show strong agreement along the jet core and also along a cross-sectional cut through the jet [63]. While these cases are for $M_\infty = 12$ conditions, the flowfield structures and aerodynamic trends are the same as those expected for SRP flowfields with similar retropropulsion configurations.

Daso et al. [8] conducted pre-test analyses with a 2.6%-scale Apollo capsule with and without retropropulsion effects. Additional post-test study was completed by Chang et al. [60] and Cheng et al. [61]. In all cases, the analyses were attempting to predict the aerodynamic and aerothermal effects of a centrally-located nozzle exhausting air at freestream Mach numbers of 3.48 and 4.0 (also air). Daso et al. [8] employed half-plane symmetry, perfect gas chemistry, and a pointwise Goldberg one-equation turbulence model to predict the flow rates producing long penetration modes, conditions later validated in testing. As the pressure data from the experiment are not sufficient for quantitative comparison, the analysis is focused on matching experimental heat flux values. At low flow rates, the peak heat fluxes with unsteadiness are significantly higher than the baseline heat flux, though the overall trends are consistent with the experiment and other cases in the literature.

Chang et al. [60] used both laminar and turbulent (k - ϵ turbulence model) approaches to obtain time-accurate solutions for the same conditions as Daso et al.

[8]. The results note significant unsteadiness for all cases with jet flow, and the time histories for drag force and heat flux exhibit low frequency, large amplitude oscillations. Depending on the mass flow rate of the jet, the results either over-predict or under-predict surface heat flux. Cheng et al. [61] extended this work to include a finite-rate chemistry model for air, though no reactions were observed at the relatively low temperature conditions in the experiment ($T_{0,\infty} = T_{0,j} = 300$ K). Quadrilateral and hexahedral meshes are used in an effort to avoid tendencies with triangular and tetrahedral meshes to over-predict the jet spreading rate. In comparing with experimental data, the computational results over-predict heat flux, qualitatively under-predict surface pressures, and do not capture the flow mode transition at the exact conditions reported in the experiment. The work cites a possible explanation for pressure discrepancies as the tendency of two-equation turbulence models to over-predict the jet spreading rate due to compressibility effects, resulting in a smaller, but stronger recirculation zone near the surface. There is qualitatively good agreement with schlieren images in all three sets of analyses.

More recently, Venkatachari et al. [57] revisited their previous work [60, 61] to explore further the nature of the transition for counterflowing jets between a long penetration mode and a blunt penetration mode. Using the same configurations and conditions described previously (2.6%-scale Apollo capsule with a single, central jet at $M_\infty = 3.48$), with additional cases to study flow mode transitions, axisymmetric solutions, both steady-state and time-accurate, are used to study the effect of jet flow rate and jet exit Mach number on flowfield stability, the jet - bow shock interaction, and the impact of integrated aerodynamic and aerothermal loads on the body. An updated procedure to compute spatial derivatives is implemented, improving the ability of their computational approach to handle stretched, unstructured meshes and very strong shocks.

Similar to results observed in the original experiment by Daso et al. [8], both

modes (LPM and BPM) exhibit non-stationary behavior, and the LPM is significantly more unstable than the BPM. In agreement with Romeo and Sterrett [42], as M_e increases, the ratio $p_{0,j}$ / $p_{0,\infty}$ at which maximum shock displacement upstream occurs also increases. Additionally, the computational results give significant evidence for the potential of counterflowing jets to reduce thermal loads on the vehicle forebody, with the surface heat flux decreasing as the mass flow rate of the jet is increased. The study concludes, in conjunction with additional discussions in the literature, that the cause of the instability of the LPM and how the flow transitions to the BPM are very closely related to the behavior of slightly under-expanded free jets. Additional studies are recommended to determine a specific criterion for which SRP flows transition from unstable to stable modes. Though limited to a single, central jet at very low thrust coefficients and $\alpha = 0°$, this analysis is unique as the only known work targeting stability transitions and mechanisms for SRP flows and addresses the physics of flow regimes to be avoided in SRP operation.

Hayashi et al. [47] focused on the numerical prediction of the reduction in aerothermal heating in the stagnation region for a hemisphere with a sonic jet of room-temperature nitrogen in a Mach 3.96 freestream (air). All solutions are axisymmetric and steady-state, obtained using a k - ω turbulence model modified to avoid excessive turbulent energy production. The results show reasonably good agreement with experimental data for the flowfield structure, though the bow shock and Mach disk displacements are slightly greater than those observed experimentally. The strength of the recirculation regions is slightly greater than in the original experiment, resulting in a larger heat flux reduction than expected.

Viti et al. [29] explored the structure of a sonic jet exhausting into a turbulent Mach 4.0 crossflow over a flat plate. All solutions are steady-state and obtained using Roe flux-vector splitting and a min-mod limiter, with a flux correction included to prevent the carbuncle effect in the stagnation region. The approach uses Wilcox's

1998 k - ω turbulence model, chosen for its ability to handle adverse pressure gradients and separated flows successfully more often than other two-equation turbulence models (namely Menter's shear stress transport model) and Wilcox's Reynolds-stress transport model. The results correctly capture the location and shape of the primary flow features. The results also compare reasonably well with the experimental pressure distribution on the flat plate, though the work admits a lack of appropriate data from the experiment to fully validate the computational approach.

Viti et al. [76] conducted a comparative study of the one-equation Spalart-Allmaras and Wilcox's 1998 one-equation k - ω eddy viscosity turbulence models for a normal, sonic jet exhausting from a ramp in Mach 4.0 turbulent flow. The objective of the investigation was to compare the performance of these two models for a flowfield with a number of physical phenomena that are characteristically difficult for turbulence models to simulate: compressible flows in strong adverse pressure gradients, separation, compressible mixing layers, steep pressure gradients associated with expansion fans and compressible shocks, and shock-boundary layer interactions. All solutions are steady-state and obtained using half-plane symmetry and Roe flux-vector splitting of the inviscid fluxes with a min-mod limiter. The Roe flux is replaced with a Van Leer flux in one computational direction to avoid the carbuncle effect. The k - ω model agrees best with experimental pressure coefficient data, with a smaller but stronger recirculation region than predicted by the Spalart-Allmaras model. The two models are in better agreement in the regions of the flowfield aft of the jet, likely due to the reduced steepness of the pressure gradients in this region as compared to the regions ahead of and at the jet. As a result of the better C_p agreement, the k - ω model predicted the highest normal force, drag force, and nose-up pitching moment. There is generally favorable agreement between the two turbulence models for the resolution and location of primary flow features; the barrel shock, bow shock, and reflected shock have the same location and inclination to the freestream flow. Of the

two models considered, Viti et al. [76] suggest Wilcox's 1998 k - ω turbulence model to perform better than the Spalart-Allmaras turbulence model in simulating complex flows with jet flow interactions.

NASA's ETDD Program has also contributed to the literature on SRP computational analysis. Three NASA-developed CFD codes have been applied to cases from the recent wind tunnel tests described in Section 2.3.2, as well as two additional cases from the literature. Emphasis was placed on demonstrating the strengths and weaknesses of existing modeling capabilities and initiating the validation of CFD codes for supersonic retropropulsion flowfields. The three codes are: FUN3D (with Edwards' LDFSS flux function with a Van Albada limiter, Menter's SST model for turbulence, local time stepping to reach steady-state, and Mach Hessian gradient-based mesh adaptation), OVERFLOW (with HLLE++ with a Van Albada limiter, strain-based SST turbulence model, global time stepping, and 3rd-order accurate MUSCL extrapolation for inviscid flux terms), and DPLR (with perfect gas chemistry, modified Steger-Warming flux-vector splitting with a min-mod limiter, and Menter's SST turbulence model).

The single nozzle and three nozzle configurations from Jarvinen and Adams [13] and the scaled Apollo capsule with a single, central nozzle from Daso et al. [8] were the initial cases explored by NASA's ETDD Program [11, 75]. For the single, central nozzle configuration from Jarvinen and Adams [13], all three codes over-predict the location of primary flow features (bow shock, free stagnation point, Mach disk), with FUN3D and OVERFLOW results showing a pressure rise at the shoulder that was not reported in the experimental data. For the three nozzle, peripheral configuration from Jarvinen and Adams [13], FUN3D and OVERFLOW predict much higher pressures at the nose than are reported in the original experiment for conditions of $C_T = 4.04$ and $C_T = 7.0$. Both qualitative and quantitative comparisons are reasonably good for $C_T = 1.00$ conditions. All three codes show favorable qualitative agreement

with experimental schlieren for the case taken from Daso et al. [8]. In all of these cases, and also in similar work by Cordell et al. [65] with the configurations and conditions from Jarvinen and Adams [13], grid resolution was found to be extremely important, with under-resolving the barrel shock - shear layer region often leading to a jet termination structure with a Mach reflection, and under-resolving the region for the jet termination shock often resulting in a completely different jet boundary shape than expected with no jet termination structure.

Numerical studies in support of the wind tunnel tests described in Section 2.3.2 included determination of the order-of-accuracy, code-to-code comparisons, and comparison of results with experimental data [16]. Physical modeling studies included wind tunnel wall and sting mount interference and turbulence modeling. All three CFD codes mentioned above were used to simulate unsteady, fully-turbulent flow for all four configurations at $M_\infty = 4.6$, angles of attack of 0°, 12°, 16°, and 20°, roll angles of 0° and 180°, and C_T of 2 and 3. In order of decreasing turbulent eddy viscosity levels, the turbulence models considered included two versions of Menter's SST Reynolds-averaged Navier-Stokes (RANS) model, Spalart's DES model (SA-DES), and an SST-based DES model [16]. The RANS models were found to dampen or entirely dissipate the inherent unsteadiness of the flow unless both sufficient grid resolution and realizability constraints are used. While these investigations found tunnel wall interference to be minimal for the conditions considered, they also found the boundary layer thickness to be nearly one-third of the test section height and depth, illustrating one of the challenges of testing SRP in ground facilities [67].

The trends in forebody and aftbody surface pressures agreed reasonably well with the experimental data, to nearly within the uncertainty bounds on the experimental data for all three CFD codes and across all of the experimental cases considered. The amount of pressure recovered was found to be a strong function of the grid resolution and turbulence modeling approach applied [68]. The characteristic highly

under-expanded jet structure and unsteady behavior for the shedding of the annular vortex from the jet interaction region were also captured by each code, with favorable qualitative agreement with the high-speed schlieren test video.

Bakhtian et al. applied the same inviscid approach (with Cart3D) described earlier in this section to a number of cases examined by NASA's ETDD Program to explore the applicability of a rapid, steady, inviscid approach in investigating the preliminary design space for supersonic retropropulsion [66]. Comparisons were made with NASA's ETDD CFD results for all four configurations tested. The flowfield structure, particularly the jet structure, does differ between the inviscid solutions and the Navier-Stokes solutions, but these differences appear to be no more significant than the differences in flowfield structure between the three different Navier-Stokes solutions. Overall, the steady, inviscid simulations compared well with the flowfield features and surface pressure distributions from the experiment and, in limited circumstances, with the time-averaged results from unsteady, Navier-Stokes solutions. It is highly undesirable to use exclusively three-dimensional, unsteady, Navier-Stokes analyses for design space exploration, given the high computational expense of generating solutions. While the approach used by Bakhtian et al. is likely limited to high-level design trades, their results demonstrate that an inviscid, and more significantly, fast analysis approach may be applicable to the simulation of supersonic retropropulsion flowfields.

Overall, the computational analysis efforts by the NASA ETDD Program have led to the development of capabilities and improvements to existing capabilities in the areas of grid generation/adaptation, turbulence modeling, and flowfield visualization. The analysis and results presented in Chapter 5 of this thesis work exercise these capabilities and provide a set of solutions complementary to those generated through NASA ETDD SRP efforts.

More focused computational simulation of the interactions between highly underexpanded retropropulsion exhaust flows and shock layers at supersonic conditions is the next step required to continue maturing supersonic retropropulsion from a potentially feasible concept to a viable alternative for advanced EDL architectures. Much of the physics relevant to the flowfield behavior is coupled and viscous in nature, though inviscid approaches have demonstrated some success in capturing the primary discontinuities in the flowfield and resulting surface pressure distributions. Flow separation, recirculation, boundary layer transition, and oscillation of the primary flow features, such as the bow shock, stagnation region, contact surface, barrel shock, jet flow boundary, and reflected jet termination structures, are relevant characteristics of supersonic retropropulsion flowfields. Computational solutions that accurately capture these characteristics exist under a limited range of conditions at this point.

2.5 Recent Development Efforts

Supersonic retropropulsion has been assessed to currently be at TRL 2 (technology concept and/or application formulated) [18], and candidate EDL architectures utilizing SRP to enable human-scale Mars exploration and the requisite robotic precursor missions have been developed [2, 23]. However, the models required to evaluate SRP as an alternative supersonic decelerator technology are either unvalidated or do not yet exist. Despite redefinition of the state of the art for supersonic retropropulsion through major contributions and progress by NASA's Exploration Technology Development and Demonstration Program, significant challenges remain in maturing supersonic retropropulsion to a level at which it can be viably considered for an actual mission at Mars. These challenges span analytical, experimental, and computational disciplines.

Following early work completed as a part of this thesis, and then continuing in parallel and with collaboration over the next two years, NASA's ETDD Program,

EDL Project, Supersonic Retropropulsion Task has begun to address many of the challenges faced in maturing SRP from a potentially enabling concept to a viable technology option for high-mass missions to Mars. Efforts under NASA's ETDD Program included:

- Development of a technology roadmap for SRP from TRL 2 to TRL 6
- Design, planning, and execution of two wind tunnel tests of SRP
- Computational analysis and code validation activities for three NASA-developed CFD tools using historical and new wind tunnel test data
- Definition of objectives, mission requirements, and concepts for SRP flight tests using a sounding rocket platform

Much of this work was planned and completed collaboratively with the efforts presented in this thesis.

2.6 Summary

Interactions between retropropulsion exhaust flows and blunt body aerodynamics have been investigated since the early 1950s. A significant number of wind tunnel experiments in the 1960s and early 1970s developed supersonic retropropulsion to nearly the level of maturity the technology has today. The flowfield arising from an interaction between highly under-expanded jet flow and the shock layer of a blunt body is characterized by a strong bow shock and a barrel shock - Mach disk - triple point - reflected shock jet structure, with a contact surface separating the jet and freestream flows. The degree of formation of flow structures and the stability of the SRP flowfield have been found to depend on the differences in the momentum of the opposing flows. This is reflected through the significance of the following parameters: jet pressure ratio (or thrust coefficient), the ratio of the nozzle exit area

to the reference area of the body, freestream and jet flow composition, and the nozzle expansion ratio.

In general, the aerodynamic - propulsive interaction for SRP results in an inability to preserve forebody surface pressures, reducing the static aerodynamic drag of the vehicle as compared to the static aerodynamic drag of the vehicle at the same conditions with no SRP. Only a configuration with multiple nozzles at the periphery of the forebody has demonstrated a degree of surface pressure preservation, though only for very low thrust coefficients. The existing experimental database is limited in the configurations, conditions, and compositions explored, and many of the historical cases are missing critical details on test conditions, configurations, instrumentation, and accuracy. This information is required for subsequent computational validation. Two recent wind tunnel tests by NASA's Exploration Technology Development and Demonstration Program have addressed a number of deficiencies in the experimental database, particularly for multiple nozzle configurations and conditions approaching flight-relevance ($C_T >$ than 6). Chapters 4 and 5 of this thesis use results from this test series and additional cases in the literature to support the validation of an existing CFD tool in simulating supersonic retropropulsion flowfields.

The most significant challenges in maturing supersonic retropropulsion span analytical, computational, and experimental disciplines and are related to a lack of knowledge in the following areas:

- Required fidelity to develop analytical models to assess the systems-level impact of SRP on aerodynamic performance, control authority, and vehicle integration
- Validated computational fluid dynamics approaches
- Aerodynamic and stability trends (static and dynamic) for configurations with multiple nozzles and/or differential throttling
- Integrated aerodynamic effects for more slender body geometries

- Aerothermal effects from exhausting combustion products into the shock layer
- Uncertainties in scaling wind tunnel results to full-scale flight systems

Building from the contents of this chapter, the remainder of this thesis is focused on developing analysis and results to address the first two of these challenges.

CHAPTER III

MARS SUPERSONIC RETROPROPULSION SYSTEMS ANALYSIS

Past experimental work has demonstrated supersonic retropropulsion on a small scale, establishing basic trends in static aerodynamics as a function of retropropulsion configuration, freestream conditions, and thrust [10]. Most prior high-mass Mars EDL systems studies [1, 2, 19, 22] have neglected aerodynamic - propulsive interactions and the associated performance impacts during the supersonic phase of descent. The results of this chapter demonstrate mass-optimal trajectory performance to be insensitive to SRP aerodynamic - propulsive interactions across a range of mission scales. The applicability, limitations, and performance implications of supersonic retropropulsion technology in the context of future human and robotic Mars exploration missions are also addressed.

The objectives of these analyses are to characterize the performance of supersonic retropropulsion with increasing vehicle ballistic coefficient and to define a range of relevant initiation and operating conditions. The maximum allowable vehicle T/W is determined through multi-objective optimization to minimize both the total mass and total volume required for the propulsion system. Additional treatment is given to the accuracy of SRP modeling assumptions in the context of experimentally observed trends for SRP aerodynamics and the sensitivity of the results of this study to I_{sp}. Mass-optimal performance for vehicles ranging from robotic- to human-scale is determined using a blunt body configuration similar to the one used on all past and present Mars missions. Additionally, pitching moment characteristics during the SRP phase are examined with a mid-L/D configuration more representative of the

vehicles assumed in recent EDL systems studies.

3.1 Overview of Systems Study

The hypersonic and supersonic phases of a Mars entry trajectory are modeled and simulated, utilizing supersonic retropropulsion to decelerate the vehicle to the desired terminal state. Vehicle ballistic coefficients of 200, 400, and 600 kg/m^2 are considered for human-scale cases, and an MSL-derived case (β = 185 kg/m^2) is considered for comparison to future robotic-scale missions. All cases are constrained by the same initial and final altitude and velocity conditions (those conditions at the atmospheric interface and retropropulsion termination).

3.1.1 Analysis Methods

The three-dimensional, translational equations of motion are integrated from a specified set of initial conditions (altitude, mass, and velocity) to minimize the ΔV required from the propulsion system and to simultaneously target Mach 0.9 and 3 km altitude, the chosen subsonic terminal conditions. These terminal conditions are considered to be conservative with respect to available timeline and mission constraints. The Program to Optimize Simulated Trajectories (POST II) [77] is used to model and simulate both the hypersonic lifting entry phase and the ballistic SRP phase. Optimization and targeting use 17 design variables (relative entry flight path angle, 7 bank angle settings, the time of SRP initiation, and eight throttle settings) to maximize final vehicle mass.

Gravity, thrust, and aerodynamic drag forces are modeled over the trajectory, with thrust modeled from a throttle profile as a function of relative velocity. Relative velocity was chosen to allow for adequate resolution within the thrust profile across the conditions of interest for each case. Aerodynamic force coefficients are interpolated between tabulated points as a function of Mach number (hypersonically) and Mach

number and thrust coefficient (supersonically). A nominal tabulated atmosphere (-2.5 km to 128 km altitude) based on a reconstructed Mars Pathfinder entry mission scenario is used for all density, pressure, and temperature values as functions of altitude [78]. Mars and its atmosphere are assumed to rotate with constant angular velocity. All cases assume a direct entry, with a relative velocity at the atmospheric interface of 5400 m/s.

3.1.2 Vehicle Configurations

Three vehicle configurations are considered: a human-scale blunt body, a robotic-scale blunt body, and a human-scale mid-L/D body. The human-scale blunt body configuration is used to characterize the performance of SRP with increasing vehicle ballistic coefficient and to define a range of relevant initiation and operating conditions. The robotic-scale blunt body is used to compare SRP mass-optimal performance between the two mission scales. The human-scale mid-L/D body is used to examine pitching moment characteristics during the SRP phase with a vehicle more representative of those assumed in recent EDL systems studies.

3.1.2.1 Blunt Body Vehicle Configurations

The human-scale blunt body vehicle is assumed to be a 70-deg sphere-cone with three axially-aligned, bipropellant engines at the periphery of the forebody. Past work by Christian et al. [19] showed that for a blunt entry vehicle, a propulsive configuration with the engines towards the forebody periphery provides more useful volume for payload and propellant tanks than a cluster of engines at the center. The aeroshell outer mold line geometry is given in Fig. 20. The retropropulsion configuration is assumed to be similar to the peripheral configuration shown in Fig. 7(b). The total volume of this 10 m-diameter aeroshell is 247.2 m^3.

Table 2 gives approximate entry masses corresponding to the ballistic coefficients used in this investigation for 10 m-diameter, 70-deg sphere-cone aeroshells. This entry

mass range is consistent with those assumed in NASA Design Reference Architecture 5.0 [22], the NASA EDL-SA study [2], and other studies of future human-scale Mars exploration systems [10, 19, 79, 80, 81].

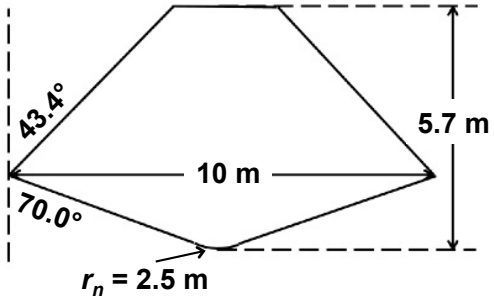

Figure 20: 70-deg sphere-cone aeroshell.

Table 2: Entry masses (kg) for a 10 m-diameter, 70-deg sphere-cone aeroshell.

Hypersonic Phase	m_{entry}, kg
$\beta = 200$ kg/m^2	26611
$\beta = 400$ kg/m^2	53222
$\beta = 600$ kg/m^2	79833

The robotic-scale configuration is based on the Mars Science Laboratory EDL architecture, with an entry mass of 5 t, a 4.5 m-diameter, 70-deg sphere-cone aeroshell ($\beta \approx 200$ kg/m^2), and use of the MSL Mars Lander Engines (MLEs). A single MLE is assumed to have a maximum thrust of 3000 N and an I_{sp} of 225 seconds (hydrazine propellant) [82]. A descent stage with 12 MLEs is used for all deceleration not derived from the vehicle's aerodynamic drag. The MSL descent stage has 8 MLEs; the use of 12 MLEs increases the vehicle $(T/W)_{max}$ from 1.23 to 1.94 (Mars-relative) for a 5 t vehicle.

3.1.2.2 Mid-L/D Vehicle Configuration

The human-scale mid-L/D vehicle is assumed to be a cylindrical section with a hemispherical nose cap measuring 10 m $\times$ 30 m, shown in Fig. 21. The propulsion system

is located on the flat-faced end of the vehicle in Fig. 21. The vehicle is sized to have a hypersonic ballistic coefficient of 400 kg/m^2. Note that this vehicle configuration is the same configuration used in a previous study by Steinfeldt et al. [81]. Table 3 summarizes the characteristics of the mid-L/D vehicle.

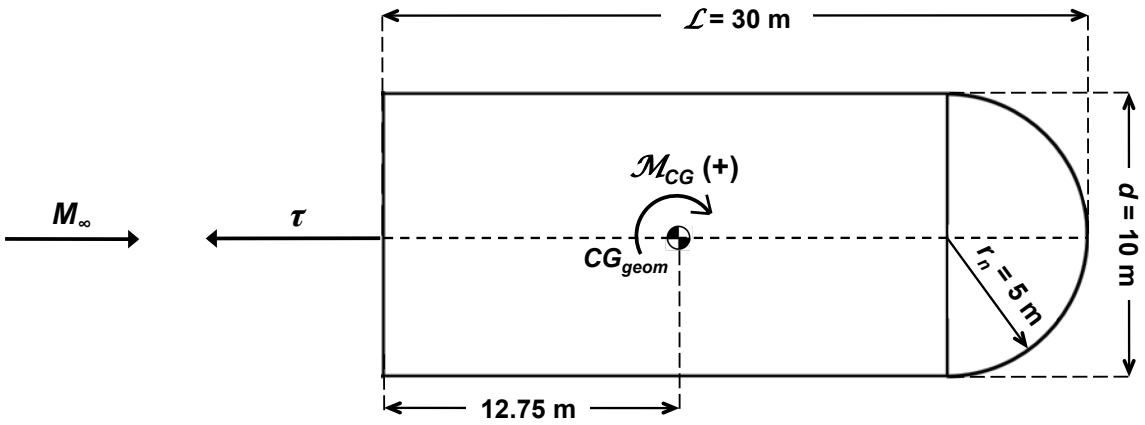

Figure 21: Mid-L/D aeroshell geometry showing the geometric center of gravity location. Moment convention is positive for "pitch-up". All thrust is applied in a normal direction from the flat-faced end of the vehicle.

Table 3: Summary of mid-L/D vehicle characteristics.

β, kg/m^2	m_{entry}, kg	$(T/W)_{max}$	τ_{max}, kN	ΔV_{prop}, m/s	PMF
400	53815	3.5	694.4	509.5	0.1379

The pitching moment induced by SRP about the vehicle's center of gravity is calculated along the SRP phase of the trajectory. Two CG locations are considered: $CG_{hyp\ trim}$ is the location that trims the vehicle at $\alpha = 35°$ (required α for $L/D = 0.69$, located 15.85 m from the aft end) during the hypersonic phase, and CG_{geom} is the location of the geometric centroid (12.75 m from the aft end). The reference length in this analysis is taken to be the vehicle length, or 30 m. The model used for the pitching moment coefficient as a function of angle of attack and C_T is based on experimental data and described in Section 3.1.3.2. All thrust is assumed to act along the vehicle centerline through the CG; there is no separate thrust contribution in the

calculation of $\mathcal{M}_{CG}$. Prior to SRP initiation, the vehicle undergoes a transition from a hypersonic configuration trimmed at $\alpha = 35°$ to a descent configuration at $\alpha = 0°$.

3.1.3 Aerodynamic - Propulsive Interactions (SRP) Models

3.1.3.1 Blunt Body Aerodynamic Drag Model

The aerodynamic - propulsive interactions model used during the supersonic retropropulsion phase is based on experimental work by Jarvinen and Adams [13] for a peripheral retropropulsion configuration, similar to the one shown in Fig. 7(b). The experimental data used to construct the model, as well as a comparison between peripheral and central retropropulsion configurations, are given in Chapter 2 in Fig. 16. All experimental data shown are for zero angle of attack; $C_{A,total}$ is equivalent to the sum of C_D and C_T for such conditions.

For a given vehicle T/W and real-time trajectory conditions, the aerodynamic - propulsive interactions model is referenced to determine the total axial force. While the current form of the model does not include variations with Mach number, McGhee [12], with Jarvinen and Adams [13] and Keyes and Hefner [39], observed only minor variations in axial force coefficient with C_T across initiation Mach numbers of 2.0 to 6.0 (see Fig. 16). The trajectory conditions require a deceleration force greater than the aerodynamic drag provided by the blunt body for the model to be active. For thrust coefficients above 3.0, the deceleration force coefficient ($C_{A,total}$) is equivalent to the thrust coefficient, and no aerodynamic contribution to the deceleration is applied. Figure 22 illustrates the multiplier applied in this investigation to the supersonic C_D as a function of C_T for both a peripheral and a central retropropulsion configuration. The sharp slope changes in Fig. 22 are a result of the limited data available to construct the model. This model is applied to all cases using a blunt-body vehicle configuration.

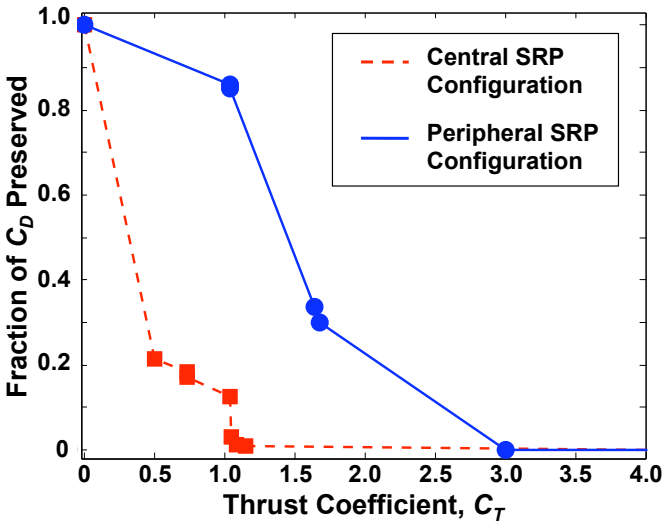

Figure 22: Aerodynamic - propulsive interactions model. Filled points are experimental data from Jarvinen [13].

3.1.3.2 Mid-L/D Body Pitching Moment Coefficient Model

The mid-L/D body pitching moment model for the SRP phase is based on data from a historical wind tunnel test completed by Peterson and McKenzie [9]. At the time of this work, experimental data exist for only two SRP configurations with multiple nozzles. One configuration, from work by Jarvinen and Adams [13], has three nozzles near the forebody periphery of a blunt body. The other configuration, from work by Peterson and McKenzie [9], has four nozzles near the half-radius of a semi-ellipsoid. This configuration, illustrated in Fig. 23, most resembles current SRP vehicle concepts, and the original experiment produced a data set useful for developing a pitching moment model. In both Fig. 21 and Fig. 23, the flat-faced end of the body is facing forward during the SRP phase. The model developed is intended to be a notional model and allow for sensitivity studies of the modeling of SRP-induced pitching moments. A higher-fidelity and/or more detailed model can be exchanged and integrated within the simulation framework as better data becomes available.

The data from the experiment are for $M_\infty = 0.8$, 1.5, and 1.9 and $\alpha = 0°$, 5°,

and 10°. The pitching moment coefficient was determined in the original experiment through the integration of measured surface pressures on both the model face and model body. The pitching moment coefficient data have been translated from a reference at the end of the model to a reference at the desired center of gravity location.

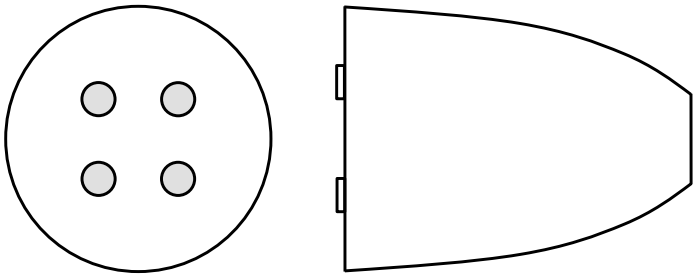

Figure 23: SRP configuration and body shape from the original experiment completed by Peterson and McKenzie [9].

Figure 24 shows the experimental data and model fits for each angle of attack and freestream Mach number condition. The original data was reported as a function of jet pressure ratio; jet pressure ratio has been converted to C_T on the x-axis of Fig. 24. Little variation in C_m is seen with freestream Mach number; accordingly, the model for C_m is a function of C_T and angle of attack only. MATLAB is used to estimate the coefficients for a nonlinear regression using a Weibull function. Figure 24 includes the generic Weibull function form of the model, as well as parameter estimates for the model for each angle of attack (0°, 5°, and 10°).

Figure 25 shows the predicted C_m for the angles of attack considered in both the original experiment and the analysis in this section across thrust coefficients from 0 to 8. At low thrust coefficients (C_T less than approximately 3), the vehicle is statically unstable. At higher thrust coefficients (C_T greater than approximately 3), the vehicle is increasingly statically stable with increasing C_T between $\alpha = 0°$ and 5°. However, the trend reverses between $\alpha = 5°$ and 10°, where the vehicle is statically unstable across the entire range of thrust coefficients considered in the original experiment.

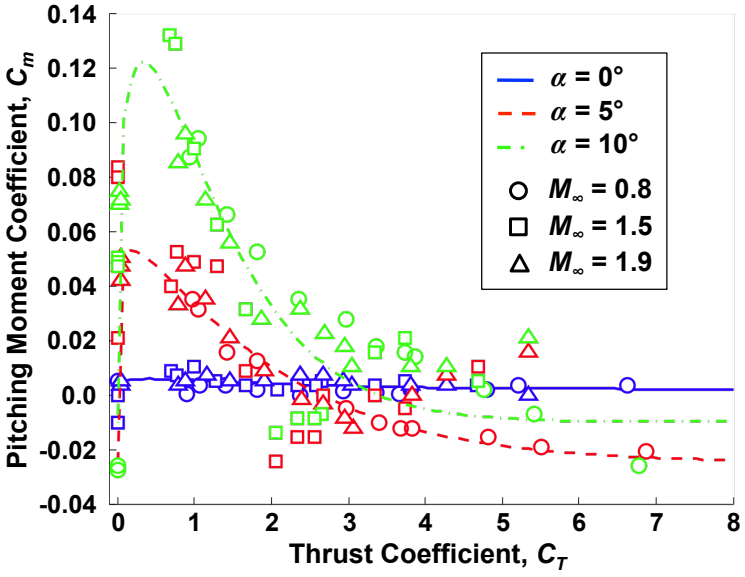

$$C_m = c\left(\frac{C_T}{a}\right)^{b-1} e^{-(C_T/a)^b}$$

α	a	b	c
0°	1.916	1.180	0.006
5°	1.889	1.080	0.102
10°	1.276	1.232	0.218

Figure 24: Model for the SRP-induced pitching moment coefficient (based on experimental data from [9]). The general Weibull function form and estimates of the model parameters for each α are given on the right.

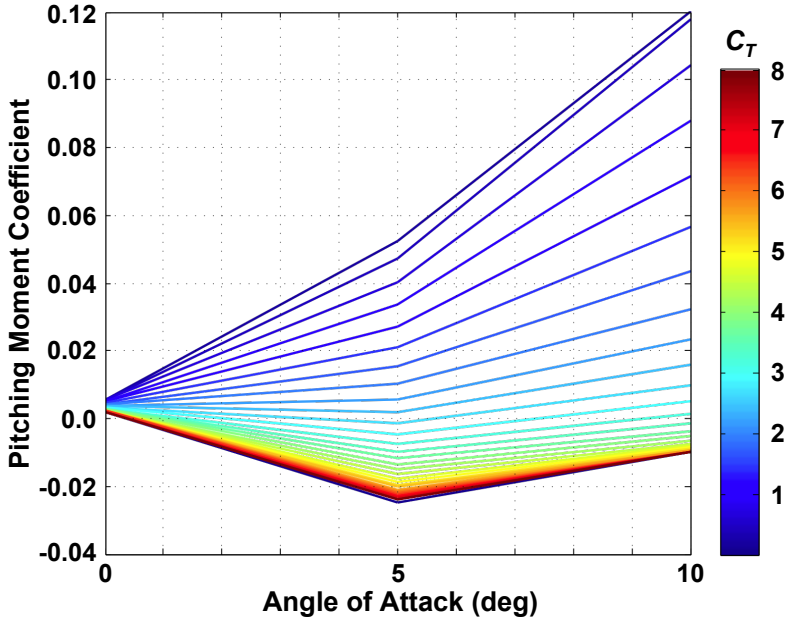

Figure 25: SRP-induced pitching moment coefficient vs. angle of attack for C_T from 0 to 8 (based on experimental data from [9]).

3.1.4 Determination of Maximum Allowable Thrust

The results of this investigation, specifically the range of SRP initiation and operating conditions, are dependent on the maximum allowable system T/W. For each ballistic coefficient (200, 400, 600 kg/m^2), the selection of $(T/W)_{max}$ is considered as a multi-objective optimization problem. The two objectives are (1) to minimize total propulsion system mass (engines, tanks, and propellant) and (2) to minimize the total volume required for the propulsion system. Plotting these two objectives against one another for a range of $(T/W)_{max}$ yields a collection of Pareto-optimal points, or points for which improvement in one objective leads to degradation in the other objective. Minimizing the total volume occupied by the propulsion system and also minimizing the total mass of the propulsion system requires a trade-off between mass-efficient performance and available volume within the aeroshell. For example, maximizing the performance of the propulsion system to minimize the total propulsive ΔV requires increasing the available thrust; increasing the available thrust increases the size of the engines but lowers the propellant mass and reduces the size of the propellant tanks. In the supersonic descent phase, the total vehicle mass is updated as a part of the vehicle state at each time step by the relation given in Eq. 6. All T/W values given in this analysis are relative to Martian gravity.

$$\frac{dm}{dt} = \frac{-\tau}{I_{sp} g_{ref}} \tag{6}$$

The propulsion system is defined to be the propellant, engines, and tanks. The propulsion system is assumed to use LOX/CH$_4$ ($\rho_{LOX} = 1140.1$ kg/m^3, $\rho_{CH_4} = 422.6$ kg/m^3) with an I_{sp} of 350 seconds and a mixture ratio of 3.5 [19, 81]. This propulsion system choice is consistent with other human-scale Mars EDL studies [19, 79, 80, 81] and reflects consideration of in-situ resource utilization (ISRU) compatibility requirements [2, 22]. Additional discussion on the impact of this assumption is presented in

Section 3.2.3. The engine mass is scaled with thrust using Eq. 7, a relation developed by Christian et al. [19] through a regression analysis of data for conceptual LOX/CH_4 engines, where τ is thrust in N, and m_{engine} is the engine mass in kg. Engine volume is conservatively estimated through a regression analysis in which a cylindrical volume of equivalent height and diameter for 14 different liquid bipropellant systems [83] is analyzed against the maximum thrust (in kN) of the engine.

$$m_{engine} = 0.00144\tau + 49.6 \tag{7}$$

The engines, physical dimensions, and thrust characteristics are provided in Table 4, with the resulting regression shown in Fig. 26 and given by Eq. 8. Sea-level thrust is given for first-stage engines, and vacuum thrust is given for upper-stage engines and engines used over a full trajectory. This is done to compensate for variations in expansion ratio across the range of propulsion systems used to develop the relationship for engine volume as a function of maximum thrust applied in this analysis.

Table 4: Summary of liquid bipropellant engines used to develop a relation for engine volume as a function of maximum thrust.

Engine	Oxidizer / Fuel	Thrust, kN	Height, m	Diameter, m	Volume, m^3
RL-10	LOX/LH_2	67	1.73	0.99	5.381
RL-10B2	LOX/LH_2	110	4.14	2.21	28.74
H-1	LOX/RP-1	890	2.68	1.49	12.59
J-2	LOX/LH_2	1033	3.38	2.01	21.34
RS-27A	LOX/RP-1	1050	3.78	1.70	20.19
J-2S	LOX/LH_2	1139	3.38	2.01	21.34
J-2X	LOX/LH_2	1310	4.70	3.05	45.03
RD-253	N_2O_4/UDMH	1670	3.00	1.50	14.14
SSME	LOX/LH_2	1817	4.24	1.63	21.71
RS-68	LOX/LH_2	3312	5.21	2.44	39.89
RD-180	LOX/RP-1	3840	3.56	3.15	35.23
RD-270	N_2O_4/UDMH	6270	4.90	3.40	52.34
F-1	LOX/RP-1	6670	5.79	3.76	68.39
RD-170	LOX/RP-1	7550	3.78	4.02	47.74

$$V_{engine} = 0.0058\tau + 15.755 \tag{8}$$

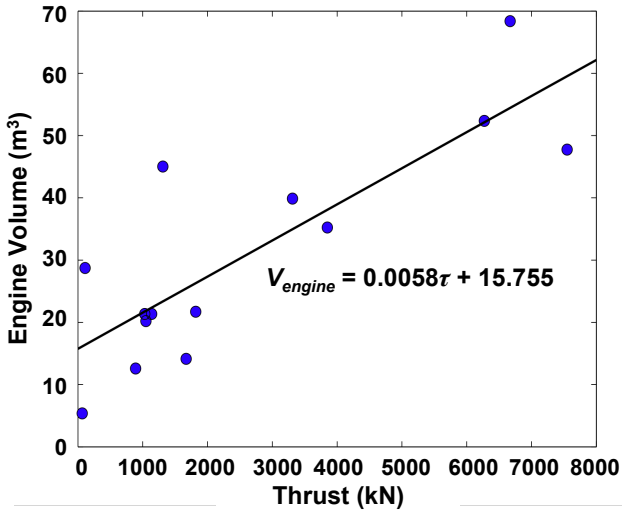

Figure 26: Regression of engine volume against engine thrust.

The propellant tanks are assumed to be spherical and made of titanium, with an operating pressure of approximately 1.4 MPa (burst pressure of approximately 2.8 MPa) [19, 81]. The tank mass is given by Eq. 9, where m_{tank} is the tank mass in kg, p is the operating pressure in Pa, V is the volume of the propellant in m^3, and ϕ is the tank-mass factor (assumed to be 5000 m for titanium) [19, 81].

$$m_{tank} = \frac{pV}{9.81\phi} \tag{9}$$

All of the human-scale blunt body cases in this chapter use a 70-deg sphere-cone aeroshell, scaled to 10 m-diameter (shown in Fig. 20). While increasing thrust available increases the mass delivered to the surface by reducing the propellant mass required, the corresponding increase in volume required for the engine results in a net increase in the total volume required for the propulsion system. This net increase in the volume required for the propulsion system reduces the volume available for other systems and increases the overall aeroshell packaging density. For consistency with the Apollo and Soyuz capsules [19, 81], a 65% usable pressurized volume is assumed in this investigation. Considering that a number of other systems share the remaining unpressurized volume (e.g. thermal protection system, aeroshell support structure), it

is desirable that the propulsion system not exceed 15% of the total aeroshell volume. Fig. 27 shows plots of the two objectives for each ballistic coefficient case, with the Pareto-optimal points indicated and increased resolution in the regions of interest.

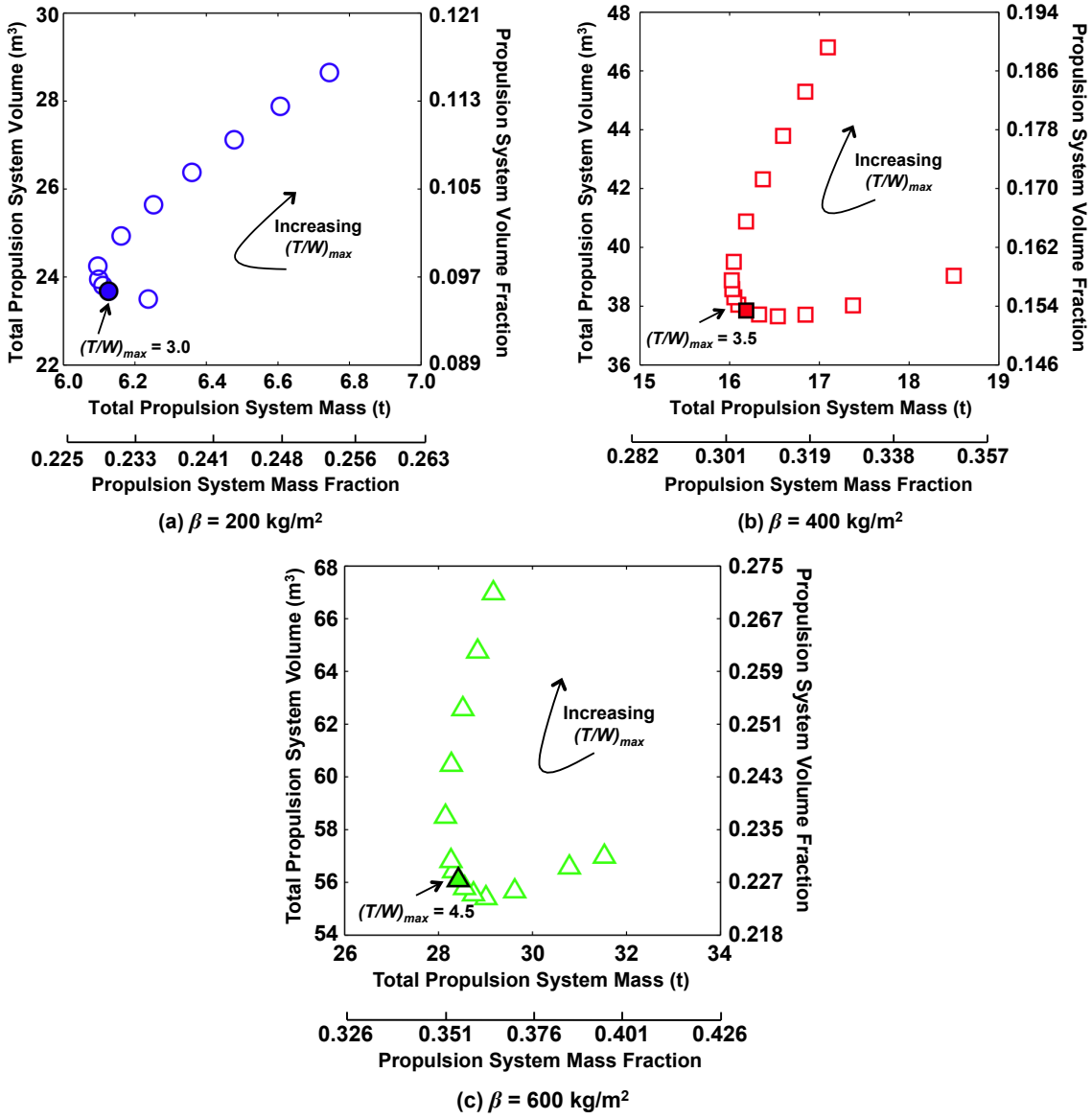

Figure 27: Pareto-optimal design points for $\beta = 200$ (a), 400 (b), 600 (c) kg/m^2 (indicated by arrow).

The Technique for Order Preference by Similarity to Ideal Solution (TOPSIS [84]) is used to select the maximum allowable vehicle T/W based on an ideal solution that minimizes both total propulsion system mass and total propulsion system volume. As

seen in Fig. 27, there is no clear choice of $(T/W)_{max}$ that minimizes both objectives across the range of ballistic coefficients considered. The Euclidean distance of each alternative (the maximum allowable vehicle T/W) to the ideal solution (the minimum mass and volume for each ballistic coefficient across all $(T/W)_{max}$ considered) and the relative closeness of each alternative to the ideal solution are used to develop a preferred order of the alternatives. Total propulsion system mass and total propulsion system volume are assumed to have equal weight (50-50) in this analysis.

The assumption of equally-weighted objectives may not be accurate for a full-scale flight vehicle; the constraint on allowable volume is likely to be more stringent than the constraint on allowable mass, given the expansion ratios and nozzle lengths of typical high-thrust, liquid bipropellant rocket engines. Table 5 summarizes the outcome of the TOPSIS analysis for each ballistic coefficient and illustrates the impact of weighting minimum total propulsion system volume more heavily than total propulsion system mass (60-40). As seen in Fig. 27, more $(T/W)_{max}$ values are considered in the region of the Pareto front to increase resolution; not every $(T/W)_{max}$ listed in Table 5 is considered for each ballistic coefficient. The columns of Table 5 provide the relative closeness of each alternative to the ideal solution, scaled between 0 and 1. The preferred alternative is the one that is closest to 1, indicated in bold in Table 5. The preferred $(T/W)_{max}$ for the equal weighting case is used for all subsequent analyses in this chapter. This same value of $(T/W)_{max}$ is optimal for the volume-favored weighting in the cases of $\beta = 200$ kg/m^2 and 400 kg/m^2. Note that in all cases, this value of $(T/W)_{max}$ is in the range of 3.0 to 4.5 (relative to Martian gravity).

Table 6 summarizes the outcome of the selection of the maximum allowable vehicle T/W. The final selected maximum allowable vehicle T/W values are 3.0, 3.5, and 4.5 for $\beta = 200$, 400, and 600 kg/m^2, respectively. These T/W correspond to the shaded points in Fig. 27. The maximum thrust magnitude for each β is roughly equivalent to 1/4 of a J-2X engine, 1/2 of a J-2X engine, and 1 J2-X engine, respectively.

Table 5: TOPSIS results for selection of $(T/W)_{max}$.

T/W_{max}	$\beta = 200$ kg/m^2		$\beta = 400$ kg/m^2		$\beta = 600$ kg/m^2	
	Equal Weighting	Volume Favored	Equal Weighting	Volume Favored	Equal Weighting	Volume Favored
2.25	–	–	0.5585	0.6479	–	–
2.5	0.9003	0.9287	0.7365	0.8023	–	–
2.75	–	–	0.8332	0.8772	–	–
3.0	**0.9583**	**0.9619**	0.8925	0.9212	0.5880	0.6749
3.25	0.9442	0.9423	0.9344	0.9518	0.6587	0.7368
3.5	0.9228	0.9180	**0.9605**	**0.9677**	0.8002	0.8351
3.75	0.9008	0.8938	0.9604	0.9587	0.8791	0.9123
4.0	0.8726	0.8637	0.9409	0.9352	0.9130	0.9365
4.25	–	–	0.9166	0.9081	0.9336	**0.9470**
4.5	–	–	0.8905	0.8790	**0.9348**	0.9378
4.75	–	–	–	–	0.9198	0.9159
5.0	0.7503	0.7362	0.8352	0.8173	0.8946	0.8866
6.0	0.6157	0.5998	0.7148	0.6837	0.7787	0.7567
7.0	0.4717	0.4567	0.5906	0.5463	0.6463	0.6080
8.0	0.3208	0.3089	0.4666	0.4093	0.5101	0.4544
9.0	0.1631	0.1563	0.3517	0.2835	0.3834	0.3115
10.0	0.0000	0.0000	0.2631	0.1956	0.2884	0.2142

Table 6: Mass and volume summary for Pareto-optimal $(T/W)_{max}$.

	$\beta = 200$ kg/m^2		$\beta = 400$ kg/m^2		$\beta = 600$ kg/m^2	
	Pareto-optimal	PMF_{min}	Pareto-optimal	PMF_{min}	Pareto-optimal	PMF_{min}
Propulsion system mass, kg	5659	6276	15249	16159	27018	27764
Propellant, kg	5008	4638	13726	12811	24205	22648
LOX, kg	3895	3607	10676	9964	18826	17615
CH_4, kg	1113	1031	3050	2847	5379	5033
Engines, kg	478.2	1478	1050	2907	1978	4335
Tanks, kg	172.7	159.9	473.3	441.7	834.6	780.9
Propulsion system volume, m^3	23.53	27.11	36.76	42.74	52.76	60.38
Propellant, m^3	6.050	5.603	16.58	15.48	29.24	27.36
LOX, m^3	3.417	3.164	9.364	8.739	16.51	15.45
CH_4, m^3	2.633	2.439	7.218	6.736	12.73	11.91
Engines, m^3	17.48	21.51	20.17	27.26	23.52	33.02
Fraction of aeroshell volume	**0.095**	0.110	**0.149**	0.173	**0.213**	0.244
SRP PMF	**0.068**	0.054	**0.138**	0.121	**0.183**	0.164
τ_{max}, kN	297.6	992.1	694.4	1984	1339	2976
$(T/W)_{max}$ (Mars)	**3.0**	10.0	**3.5**	10.0	**4.5**	10.0

The propellant mass fraction (PMF), defined in Eq. 10, for a constant-thrust gravity turn from Mach 0.9, 3 km conditions is included in the propellant masses in Table 6. Bounded by extremes in relative flight path angle at the start of the gravity turn, the propellant mass fraction required for the gravity turn is between 0.137 and 0.169. The $(T/W)_{max}$ corresponding to each Pareto-optimal point in Fig. 27 does not change as the gravity turn PMF is varied within this given range; however, the total propulsion system mass and volumes do change by the linear relationships given above. The minimum gravity turn PMF (0.137) has been used for the results shown in Fig. 27. No margin has been applied to either wet or dry masses in this investigation. Similar to the effect of varying the subsonic, terminal descent PMF, the application of margin to all sizing results does not affect the Pareto-optimal $(T/W)_{max}$.

$$PMF = \frac{m_{prop}}{m_{entry}} \tag{10}$$

Supersonic descent PMF is defined to be the ratio of the required propellant mass to reach Mach 0.9 conditions at 3 km altitude to the vehicle mass at SRP initiation (m_{entry}). It is significant to notice the difference in Table 6 between the Pareto-optimal results and the minimum supersonic descent PMF results (PMF_{min}). For each ballistic coefficient considered, the vehicle $(T/W)_{max}$ that yields the lowest SRP propellant mass fraction is the upper limit of the T/W range considered ($(T/W)_{max} = 10.0$). However, the PMF_{min} results occupy a larger fraction of the aeroshell volume and require a larger total propulsion system mass than that required for the Pareto-optimal results. The consideration of volume and total system mass as two objectives results in a more realistic vehicle $(T/W)_{max}$ than if total system mass alone had been considered. Note that the goal of achieving a total propulsion system volume below 15% of the aeroshell volume (247.2 m^3) is achievable only for the β = 200 and 400 kg/m^2 cases, and only then for the Pareto-optimal results.

3.2 Mass-Optimal Trajectory Performance

This section presents the results of a systems-level performance assessment of supersonic retropropulsion. Defined are: relevant SRP initiation and operating conditions and propulsion system and overall system performance requirements for nominal operation (e.g. excluding start up, shut down, engine out, or throttled conditions). A brief study of the sensitivity of supersonic PMF to I_{sp} is presented, the pitching moment characteristics of a mid-L/D vehicle during the SRP phase are examined, and the modeling assumptions used in prior studies are assessed. Lastly, the effect of scale on these trends is illustrated through a sample robotic-scale case. All cases require the ability to fly a lifting hypersonic portion of the trajectory ($L/D_{max} = 0.24$) and unless noted otherwise, terminate the SRP phase at Mach 0.9 and 3 km altitude.

3.2.1 Bounding Conditions for Initiation and Nominal Operation

The determination of bounding conditions for initiation and nominal operation of SRP is approached in two ways: by targeting specific conditions and then by optimizing the initiation condition using the targeted conditions as initial guesses. The most mass-efficient trajectories utilizing SRP will minimize the ΔV provided by the propulsion system (ΔV_{req}), an expression for which is given by Eq. 11. Off-axis thrust losses (ΔV_{thrust}) are assumed to be negligible in this analysis.

$$\begin{aligned} \Delta V_{req} &= \Delta V_{ideal} + \Delta V_{gravity} - \Delta V_{drag} + \Delta V_{thrust} \\ &= I_{sp} g_{ref}\, ln \frac{m_{entry}}{(m_{entry} - m_{prop})} + \int g sin\varphi \, dt - \int \frac{D}{m}\, dt + (\approx 0) \end{aligned} \quad (11)$$

For EDL application and the assumption of a constant I_{sp}, the mass delivered to the surface is maximized for integrated trajectories that minimize gravity losses ($\Delta V_{gravity}$) and maximize drag losses (ΔV_{drag}). Provided there is sufficient thrust available and the drag force is not significant, the retropropulsion phase will begin

as late as possible (i.e., at the lowest altitude and lowest velocities permitted by the system T/W and other mission constraints), where the thrusting time is the least to minimize the propellant mass required (from Eq. 6). Considering no additional constraints, these mass-optimal SRP trajectories will be characterized by relatively shallow flight path angles at SRP initiation, extended phases of constant-altitude deceleration deep within the atmosphere, and thrust profiles of minimal duration.

Because the SRP aerodynamic - propulsive interaction provides the greatest degree of drag preservation at low thrust coefficients (see Fig. 22), it is possible that the optimal propulsive phase may initiate earlier and decelerate at a reduced thrust level in circumstances where the drag contribution to deceleration is significant. Understanding this trade between thrust required, velocity losses, and available timeline is necessary to bound conditions for initiation and nominal operation for SRP.

To parametrically assess the effect of drag preservation on SRP PMF, initiation velocity and thrust coefficient are decoupled, and specific SRP initiation conditions are targeted. These initial cases provide valid starting solutions for the mass-optimal trajectory cases with the full set of design variables. From experimental data, operating conditions for which there is some degree of drag preservation can be used to define a "drag-affected" region as a function of the hypersonic vehicle ballistic coefficient in altitude - velocity space. Using Eq. 1 and Eq. 2, the dependency of dynamic pressure on vehicle parameters and thrust coefficient can be determined. This relationship is given in Eq. 12, where C_D is the vehicle's hypersonic drag coefficient, g_{Mars} is the gravitational acceleration at the surface of Mars, and T/W is the Pareto-optimal $(T/W)_{max}$ determined in Section 3.1.4.

$$q_\infty = \frac{\tau}{C_T A} = \frac{(T/W)_{max} m g_{Mars}}{C_T A} = \frac{(T/W)_{max} \beta C_D g_{Mars}}{C_T} \tag{12}$$

From the relationship given in Eq. 12, a range of initiation conditions for the

supersonic retropropulsion phase can be determined in altitude - velocity space. This range of conditions is not the operational envelope for SRP; however, it is useful in understanding the role of drag preservation in overall EDL system performance by parameterizing initiation conditions. These conditions are constrained by the altitude at which the vehicle reaches Mach 0.9 (with subsequent timeline constraints), Mach number, and dynamic pressure. The dynamic pressure bounds are determined from conditions of nearly full aerodynamic drag preservation ($C_T = 1.0$) and no aerodynamic drag preservation ($C_T = 3.0$). Note that these bounds are based on the limited experimental data available and can be shifted as the assumed retropropulsion configuration changes.

Figure 28 illustrates trajectory bounds for aerodynamic drag preservation during the SRP phase. Table 7 gives the dynamic pressure bounds for these two thrust coefficients and β = 200, 400, and 600 kg/m^2. In Fig. 28, an upper bound on SRP initiation Mach number is defined to be the minimum whole Mach number (5 or greater) for which four distinct corner points can be found along the dynamic pressure bounds in altitude - velocity space [85].

The four corner points of each aerodynamic drag preservation region can be used to confirm that lower initiation velocities are preferable, and that for the same initiation velocity, a lower thrust coefficient yields a lower PMF. The hypersonic lifting trajectories utilize bank angle profiles and atmospheric entry flight path angles that minimize (yield a near-zero) flight path angle at the target altitude and velocity conditions (the corner points defined in Fig. 28) to minimize gravity losses in the subsequent SRP phase. For these targeted cases, the SRP thrust profile and maximum vehicle T/W are determined to minimize the PMF required to reach the target terminal conditions of Mach 0.9 at 3 km altitude. The resulting trajectories for ballistic coefficients of 200, 400, and 600 kg/m^2 are shown in Figs. 29 - 31, with a summary of the initiation conditions and required PMF given in Table 8. While the

SRP initiation boxes are bounded by Mach number, dynamic pressure, and altitude, a small offset of Corner B from the Mach number boundary is made to allow for an assessment of initiation velocity, and not initiation Mach number, effects.

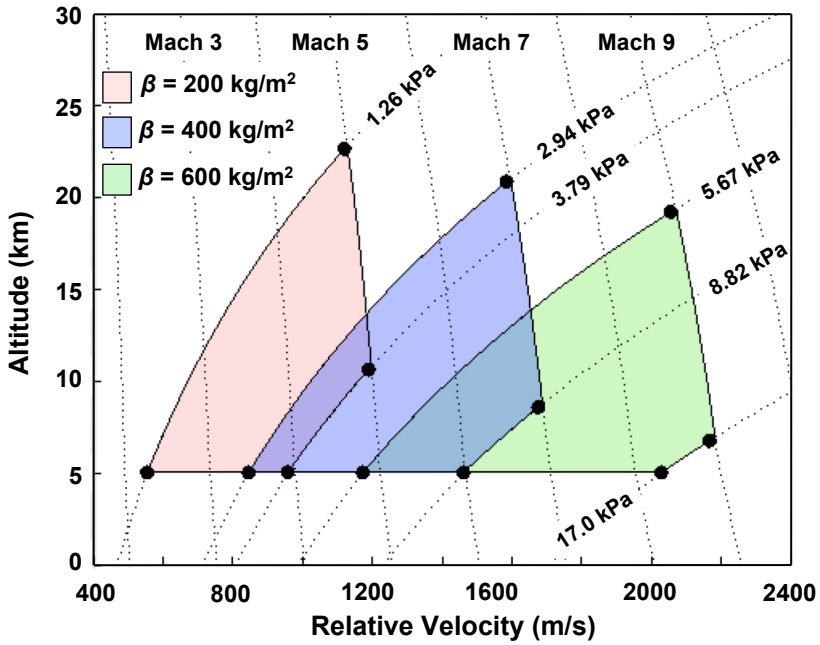

Figure 28: Trajectory bounds for aerodynamic drag preservation during the retropropulsion phase.

Table 7: Dynamic pressure bounds of a "drag affected" region.

	$C_T = 1.0$	$C_T = 3.0$
$\beta = 200$ kg/m^2	3.79 kPa	1.26 kPa
$\beta = 400$ kg/m^2	8.82 kPa	2.94 kPa
$\beta = 600$ kg/m^2	17.0 kPa	5.67 kPa

Between Corners B and C, which have the same initiation velocity, Corner B has a consistently higher PMF required to reach the target conditions. Corner B corresponds to the $C_T = 3.0$ boundary, and Corner C corresponds to the $C_T = 1.0$ boundary. As expected, for the same required velocity change, lower thrust coefficients enable more aerodynamic drag preservation and yield a lower PMF. While

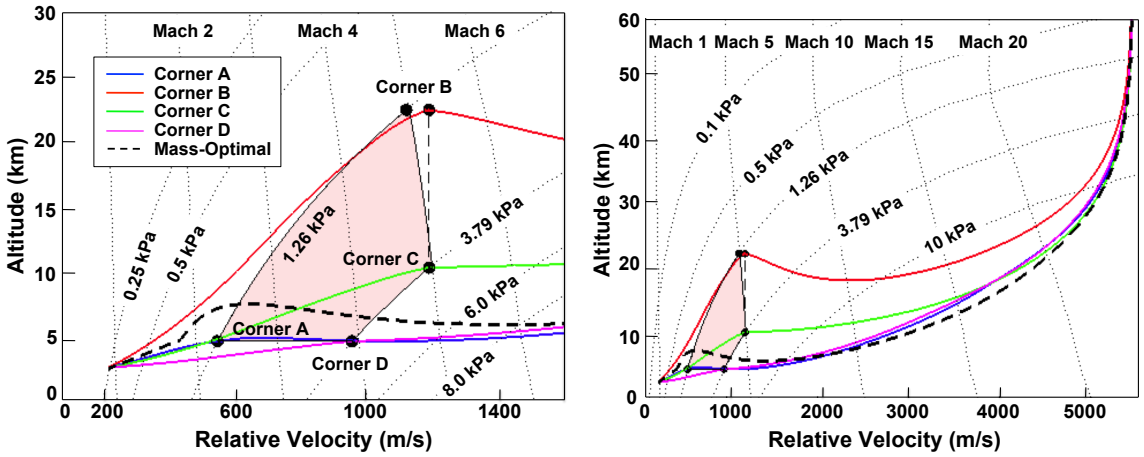

Figure 29: $\beta = 200$ kg/m^2.

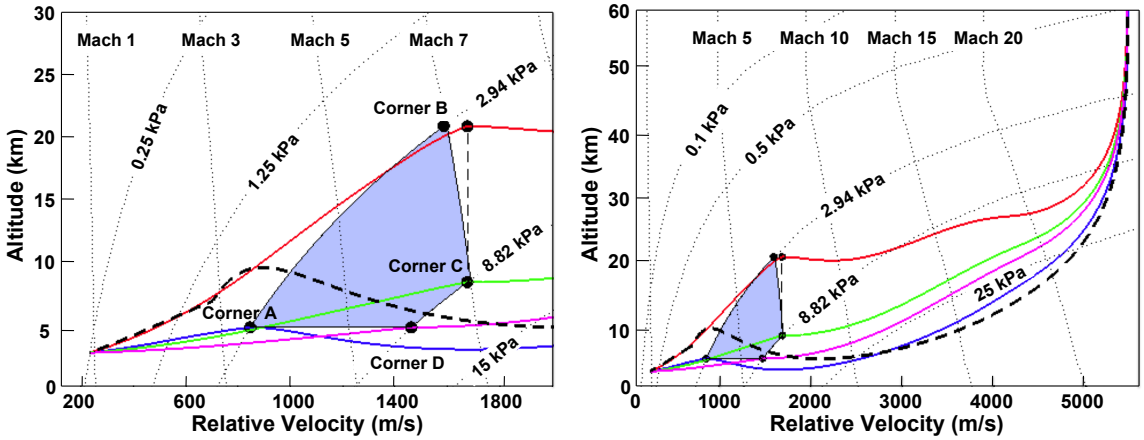

Figure 30: $\beta = 400$ kg/m^2.

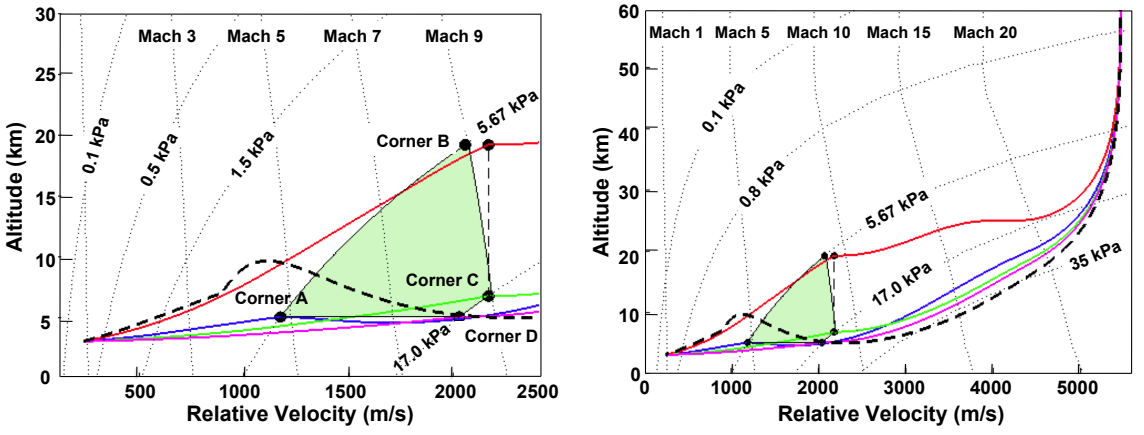

Figure 31: $\beta = 600$ kg/m^2.

Table 8: SRP phase initiation conditions and PMF results.

	Altitude, km	$u_{relative}$, m/s	Mach Number	$\varphi_{relative}$, deg	Maximum $(T/W)_{max}$	τ_{max}, kN	SRP PMF	ΔV_{prop}, m/s
$\beta = 200$ kg/m^2								
Pareto-optimal	5.124	441.35	1.80	-13.45	3.0	297.6	0.0683	242.9
Corner A	5.000	549.8	2.24	0.0	3.27	324.4	0.0962	347.3
Corner B	22.54	1183	5.21	0.0	2.59	256.6	0.2699	1080
Corner C	10.58	1183	4.91	0.0	4.16	413.1	0.2538	1005
Corner D	5.000	952.2	3.87	0.0	6.87	681.7	0.1945	742.6
$\beta = 400$ kg/m^2								
Pareto-optimal	7.049	697.5	2.86	-8.44	3.5	694.4	0.1379	509.5
Corner A	5.000	839.8	3.42	0.0	5.76	1143	0.1681	631.9
Corner B	20.75	1668	7.27	0.0	3.59	711.7	0.3589	1526
Corner C	8.537	1668	6.87	0.0	7.01	1390	0.3481	1469
Corner D	5.000	1455	5.92	0.0	11.18	2117	0.3033	1241
$\beta = 600$ kg/m^2								
Pareto-optimal	6.966	889.1	3.64	-6.396	4.5	1339	0.1832	694.8
Corner A	5.000	1166	4.75	0.0	8.45	2515	0.2427	954.5
Corner B	19.11	2158	9.32	0.0	4.63	1377	0.4403	1993
Corner C	6.711	2158	8.83	0.0	10.93	3252	0.4329	1948
Corner D	5.000	2020	8.22	0.0	15.23	4533	0.4087	1804

there is also a potential energy effect, since Corner B is always significantly higher in altitude than Corner C, this effect is small in comparison to the difference between the degrees of C_D preservation for $C_T = 1.0$ (Corner C) and $C_T = 3.0$ (Corner B).

Considering pairings of Corners A and B and Corners C and D, which each have the same C_T constraining their initiation conditions, the corners with the lower initiation velocities have a lower PMF. This result is expected, as the PMF should be lower if the velocity at initiation is lower. The large difference between Corner A and the other three corners for the $\beta = 200$ kg/m^2 case, as compared to the higher ballistic coefficient cases, is due primarily to the thrust requirements under the constraints of constant thrust and fixed initiation conditions.

Balancing the above two corner comparisons, the impact of initiation velocity is more significant than thrust coefficient at initiation, evidenced by the larger differences in PMF with variation in initiation velocity than with variation in C_T at

initiation. In all of the cases examined, Corner A has the lowest PMF, indicating that the optimal initiation conditions are likely to be weighted heavily towards this minimum velocity point (which will occur on the minimum altitude boundary defined by the timeline considerations of the subsequent EDL events).

3.2.2 Mass-Optimal Results

Mass-optimal trajectories are shown as dashed lines in Figs. 29 - 31, and the results are included in Table 8 as "Pareto-optimal" (in the previous section). These results are based on the use of the $(T/W)_{max}$ determined in Section 3.1.4. Note that a minimum altitude constraint of 5 km is applied during the hypersonic phase to prevent solutions with unrealistic minimum altitudes prior to SRP initiation.

Figures 29 - 31 illustrate the characteristics of the hypersonic phase of Mars entry trajectories for vehicles utilizing supersonic retropropulsion across ballistic coefficients from 200 to 600 kg/m^2. For all three ballistic coefficients considered, the vehicle initially dives deeply into the atmosphere and then banks to fly an extended, near-constant altitude deceleration profile until SRP initiation at low-to-mid supersonic conditions. All three cases show a 3-to-5 km loft at supersonic conditions, prior to SRP initiation. Additional details on the hypersonic phases of these trajectories can be found in Ref. [85].

Figure 32 shows the thrust, C_T, and dynamic pressure histories for each ballistic coefficient. Table 8 (in the previous section) summarizes the SRP initiation conditions for the three Pareto-optimal cases. Initiation occurs between Mach 1.80 and Mach 3.64 and at altitudes ranging from 5.12 km to 7.05 km. In all cases, initiation occurs on the downside of a 3-to-5 km loft, outside of the aerodynamic drag preservation region. This loft allows the vehicle to gain timeline and helps reduce the propulsive ΔV by delivering the vehicle to initiation conditions that minimize the amount of time required for the SRP phase as a function of the thrust available. The thrust

history (see Fig. 32) shows little or no throttling required, though a throttle range from 0 to 100% was permitted during optimization.

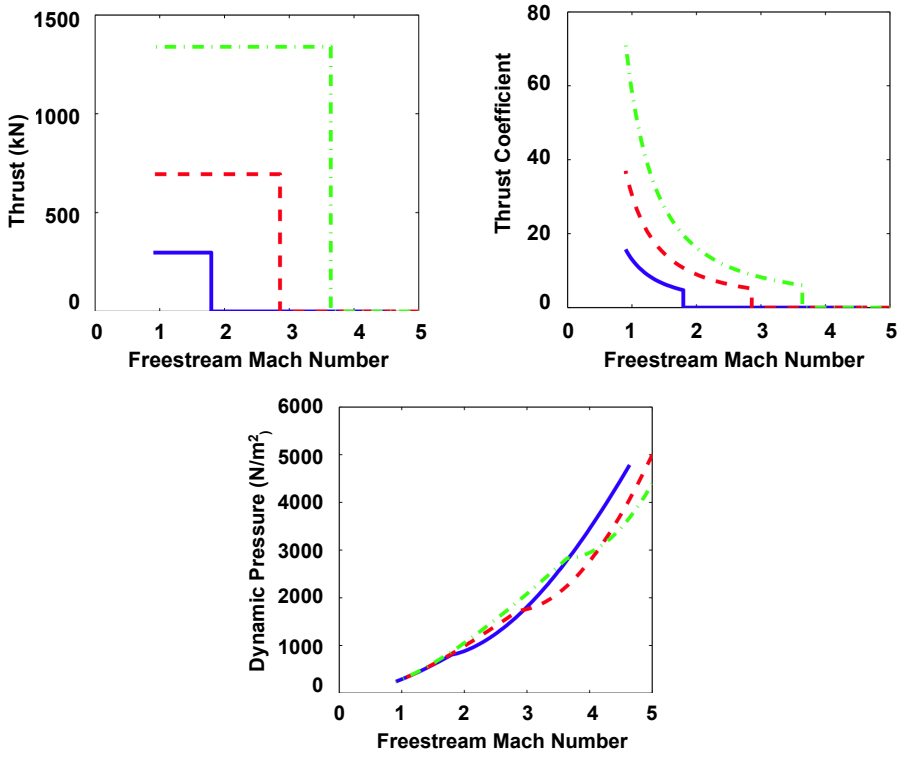

Figure 32: Comparison of SRP trajectory histories with vehicle ballistic coefficient.

For $\beta = 200$, 400, and 600 kg/m^2, the minimum thrust coefficients are 4.72, 5.11, and 6.03, respectively. The minimum C_T occurs at SRP initiation. Experimental data [9, 10, 12, 13, 39, 42] show no C_D preservation above C_T of approximately 3, confirming that analytic models that consider thrust as the only contributor to axial force are valid for high ballistic coefficient Mars entries with SRP.

Comparing the Pareto-optimal trajectories to the targeted corner point trajectories in Section 3.2.1, the Pareto-optimal trajectories all require less propulsive ΔV, comparatively lower thrust magnitudes, lower initiation Mach numbers, higher thrust coefficients, and steeper initiation flight path angles. A critical feature of the most mass-efficient, targeted corner point trajectories and the Pareto-optimal trajectories is the supersonic loft prior to initiation, delivering the vehicle to the conditions most

suitable for minimizing the propellant mass required as a function of the thrust available.

For high ballistic coefficient Mars entry, maximum drag preservation during SRP ($C_T \leq 1$) results in thrust conditions that are sub-optimal with respect to the PMF required to achieve Mach 0.9 conditions at 3 km altitude. Preservation of aerodynamic drag during the SRP phase, which has been suggested by experimental work from Jarvinen et al. [13] to be possible (see Section 2.2), could potentially result in a departure from the "maximum available thrust for the minimum time" trend described in Section 3.2.1 and reduce the propellant mass required. For human-scale vehicles, however, this departure requires an ability to preserve drag at levels that have not been demonstrated experimentally or computationally. Even if possible, theoretically preserving 100% of the vehicle's aerodynamic drag during the SRP phase only reduces the required propellant mass by 2.3% [85].

3.2.3 Sensitivity to Specific Impulse

The results presented in Section 3.2.1 and Section 3.2.2 all assume a constant I_{sp} of 350 seconds, with the maximum thrust magnitude constrained by the Pareto-optimal $(T/W)_{max}$ at SRP initiation. Varying I_{sp} will change the total propulsion system volume and total propulsion system mass; however, the sensitivity of the Pareto-optimal $(T/W)_{max}$ to I_{sp} is negligible. In consideration of propellant combinations other than LOX/CH_4, a sweep of I_{sp} for the $\beta = 400$ kg/m^2 case is completed. As expected, the trend shown in Fig. 33 is consistent with Eqn. 6. Between 250 sec and 550 sec, there is a 70.2% difference in PMF, or approximately 5045 kg of propellant.

Table 9 compares the impact of I_{sp} on system performance and sizing using sample LOX/RP-1, LOX/CH_4, and LOX/LH_2 propulsion systems. The sample systems all have a maximum thrust magnitude comparable to 694.4 kN, τ_{max} for the $\beta = 400$ kg/m^2 case. The propulsive ΔV is assumed to be equal for all three propulsion

systems compared. The LOX/CH_4 propulsion system is the same system used in all other trades presented in this chapter. The propellant densities for LOX, RP-1, CH_4, and LH_2 are 1140.1 kg/m^3, 820 kg/m^3, 422.6 kg/m^3, and 70 kg/m^3, respectively.

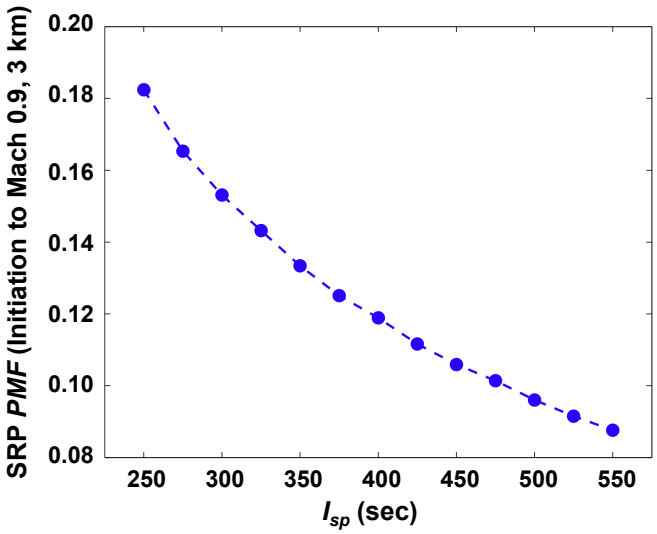

Figure 33: Variation in SRP PMF with I_{sp}.

Table 9: Effect of I_{sp} (vacuum) on system performance and sizing.

I_{sp}, sec	289	350	421
Engine	H-1	Theoretical	J2-X
Ox/Fuel	LOX/RP-1	LOX/CH_4	LOX/LH_2
Mixture Ratio	2.25	3.50	5.50
ΔV, m/s	490.8	490.8	490.8
Propellant Mass, kg	8447	7089	5963
Oxidizer Mass, kg	5848	5514	5046
Fuel Mass, kg	2599	1575	917.4
Propellant Volume, m^3	**8.30**	**8.56**	**17.53**
Oxidizer Volume, m^3	5.13	4.84	4.43
Fuel Volume, m^3	3.17	3.73	13.12
PMF	**0.1587**	**0.1332**	**0.1120**

Figure 33 and Table 9 illustrate that increasing I_{sp} reduces the required propellant mass. As discussed earlier, the volume occupied by the propulsion system is likely to be of equal or more importance than the overall system mass. While using significantly less propellant overall, the LOX/LH_2 system requires more than twice the propellant volume required for each of the LOX/RP-1 and LOX/CH_4 systems to

yield the same propulsive ΔV. Provided that a LOX/CH_4 propulsion system can be developed that satisfies the thrust, control, and throttling requirements of both SRP and terminal descent, a LOX/CH_4 propulsion system is likely advantageous to the overall EDL system sizing and performance.

3.2.4 Pitching Moment Characteristics

Many high-mass Mars EDL systems studies use more slender aeroshell geometries to deliver payloads on the order of tens of metric tons to the surface [2, 22, 81]. Such a geometry can provide substantial improvements over blunt, sphere-cone configurations in hypersonic aerodynamic performance and packaging volume. Work from the NASA EDL-SA study [2] has assumed an ability to fly at angles of attack up to 20° during the SRP phase to satisfy targeting and divert maneuver requirements (0 km MOLA landing site, landing precision to within 50 m of the target, and the capability to execute divert maneuvers to prevent any shed drag devices, e.g. aeroshell and/or deployable decelerators, from passing within 2 km of the target). While the results of Section 3.2 demonstrate the ability of a 70-deg sphere-cone aeroshell (L/D = 0.24) to deliver a β = 200 - 600 kg/m^2 vehicle to a wide range of SRP initiation conditions, such a blunt configuration may not be able to satisfy such targeting and divert requirements or carry the payload volume required for such a mission. As an alternative to a scaled, Viking-heritage, blunt vehicle geometry, a mid-L/D aeroshell geometry is considered in this section.

The results of Section 3.2.2 demonstrate the optimal trajectories for a vehicle utilizing supersonic retropropulsion to be dominated by the available thrust. If the primary objective is to maximize the mass delivered to a particular subsonic condition, SRP initiation conditions are governed by the desire to use the maximum thrust available for the minimum amount of time (subject to any additional constraints,

such as acceleration), largely independent of any changes in the vehicle's static aerodynamic force characteristics arising from the use of SRP. Based on these results, the analysis presented in this section focuses on the pitching moment during the SRP phase only. The vehicle is assumed to have a mid-L/D geometry ($L/D = 0.69$), as described in Section 3.1.2.2. The Pareto-optimal SRP initiation conditions from the $\beta = 400$ kg/m^2 blunt body case are used as the initial conditions (see Table 8), and the terminal conditions are also the same as those used in the previous section ($M_\infty = 0.9$ at 3 km altitude).

The objectives of this analysis are to estimate the magnitude and sign of the pitching moment induced by SRP about the vehicle's center of gravity and to understand the sensitivity of the resulting pitching moment to the model applied in the analysis. The pitching moment model developed for the SRP phase provides C_m as a function of α and M_∞ and is described in detail in Section 3.1.3.2. Given the flight-relevant operating conditions for SRP to be thrust coefficients greater than 10 and angles of attack up to 20° [2], the likelihood of SRP resulting in static instability leads to the conclusion that a dedicated system (e.g. on-board attitude control) or approach (e.g. engine gimbaling or throttling) to attenuate this instability will be required on a full-scale flight system. In this analysis, thrust deflection (or engine gimbaling) is used to counteract the moment generated about the vehicle's CG in the pitch plane during the SRP phase. Both the magnitude of the SRP-induced pitching moment and the required thrust deflection angle to counteract the moment are discussed in the following section.

3.2.4.1 Determination of Required Restoring Moment

Figure 34 shows the moment about the CG in the pitch plane and C_m over the SRP phase of the trajectory for fixed angles of attack of 0°, 5°, and 10°. The solid lines represent $\mathcal{M}_{CG}$, and the dashed lines represent C_m. The standard convention

is followed, with a positive moment resulting in "pitch-up" for the thrusting end of the vehicle. Recalling from Fig. 32, C_T increases rapidly as the vehicle decelerates through the SRP phase. In the model developed as a part of this analysis, C_m begins to asymptotically level off as C_T increases beyond 4. This effect is illustrated by the C_m results in Fig. 34.

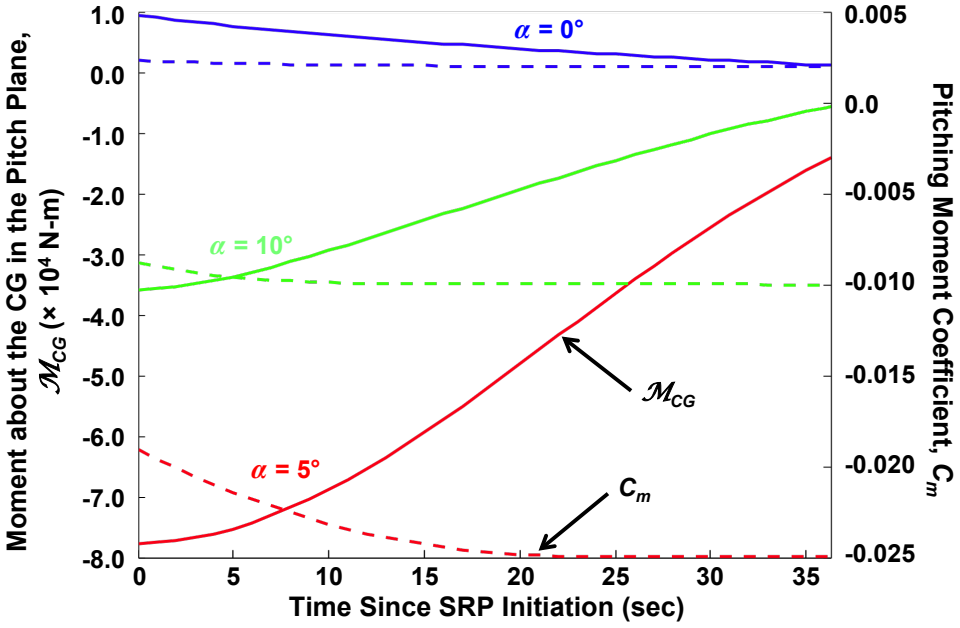

Figure 34: Moment about the CG in the pitch plane and pitching moment coefficient during the SRP phase of the trajectory for fixed angles of attack of 0°, 5°, and 10°.

In Fig. 34, which covers only the SRP phase of the trajectory, the magnitude of $\mathcal{M}_{CG}$ is greatest at SRP initiation for all three angle of attack cases. The slope appears to lessen as the vehicle decelerates to subsonic conditions, a direct result of the decreasing dynamic pressure and lack of significant variation in C_m across these conditions. For $\alpha = 0°$, the maximum moment is a "pitch-up" moment of approximately 9350 N-m, with the pitching moment decreasing asymptotically as the vehicle approaches subsonic conditions. As dynamic pressure decreases to zero, the pitching moment should also approach zero. For $\alpha = 5°$, the maximum moment is a "pitch-down" moment of approximately 77,700 N-m, with this moment decreasing

in magnitude throughout the SRP phase to approximately 14,000 N-m by Mach 0.9 conditions. The $\alpha = 10°$ case shows similar, though less severe, behavior for $\mathcal{M}_{CG}$ as the $\alpha = 5°$ case. The maximum moment is a "pitch-down" moment of approximately 35,800 N-m, decreasing to approximately 5630 N-m by Mach 0.9 conditions. Given the lack of experimental data at high C_T, it is possible that the pitching moment may change sign in the lower subsonic portion of the trajectory as C_T continues to increase and dynamic pressure continues to decrease as the vehicle decelerates to zero velocity. These results are consistent with conclusions given in the original experiment [9], that the moment in the pitch plane for a fixed angle of attack decreases in magnitude as thrust coefficient increases.

3.2.4.2 Sensitivity of Results to Pitching Moment Model

The results of Section 3.2.4.1 demonstrate the requirement for a strategy or system to attenuate the pitching moment about the vehicle's center of gravity during the SRP phase of a high-mass Mars EDL trajectory. As prior systems analysis work has not employed any aerodynamic models for SRP, understanding the degree of effort required to counteract changes in the vehicle's static stability arising from SRP is a necessary step in improving the fidelity of the analysis of these systems. The severe reduction of surface pressures from SRP may prohibit the effective use of aerodynamic surfaces, such as body flaps or trim tabs, in maintaining the vehicle's attitude during SRP; alternative approaches, such as use of an independent attitude control system or thrust vector modulation through engine gimbaling or engine throttling may be more suitable. This section presents the results from determination of the required thrust deflection angle to counteract the pitching moment about the vehicle's center of gravity using the main SRP engines during the SRP phase for fixed angles of attack of 0°, 5° and 10°.

Current systems analysis efforts to assess the static (and dynamic) stability characteristics of vehicles utilizing supersonic retropropulsion are challenged by a lack of available experimental data from which force and moment models can be constructed. The lack of a capability to directly measure aerodynamic forces and moments requires a limited number of surface pressure measurements to be integrated to obtain force and moment coefficients. The small magnitudes of the pressures being measured introduces additional uncertainty and further reduces confidence in the aerodynamic force and moment coefficient models developed for SRP using existing experimental data.

Figure 35 shows the change in the thrust deflection angle required to counteract moments about the CG during the SRP phase as a function of a multiplicative factor applied to $\mathcal{M}_{CG}$ for fixed angles of attack of 0°, 5° and 10° and two different CG locations. This multiplicative factor ranges from 1 to 100, where 1 represents $\mathcal{M}_{CG}$ as determined directly from the C_m model, and 100 represents a moment about the CG that is two orders of magnitude greater than the moment prescribed from the model. Figure 35(a) shows the results for a CG location that trims the vehicle at $\alpha = 35°$ during the hypersonic phase of the trajectory. This is the CG location used in a prior study with this vehicle configuration by Steinfeldt et al. [81] and assumes that there is no significant transition in vehicle configuration or jettison of the aeroshell prior to SRP initiation. Figure 35(b) shows the results for a CG location that is coincident with the geometric centroid. This CG location may be a more realistic assumption for the SRP phase of the trajectory. Table 10 summarizes the maximum required thrust deflection angle.

In Figs. 35(a) and 35(b), the required thrust deflection angle is most sensitive to large errors in the magnitude of the pitching moment at the beginning of the SRP phase, where $\mathcal{M}_{CG}$ and dynamic pressure are greatest. The range of thrust deflection angles is greatest for the $\alpha = 5°$ cases. This is unsurprising, given the experimental

data trend for C_m as a function of C_T shown previously in Fig. 24. As expected, the required thrust deflection angle is increasingly less sensitive to errors in $\mathcal{M}_{CG}$ as the vehicle decelerates to subsonic conditions.

Liquid propellant rocket propulsion systems with proven technology have demonstrated a maximum range of $\pm$ 12° of engine gimbaling [83]. For the $\alpha = 0°$ cases, even a pitching moment two orders of magnitude greater than that prescribed by the C_m model applied in this analysis can be attenuated by thrust deflection angles less than 7°. For the $\alpha = 5°$ cases, the pitching moment magnitude needs to be 24 to 30 times greater than that prescribed by the current model to exceed a 12° required thrust deflection angle. For the $\alpha = 10°$ cases, the maximum allowable thrust deflection angle is not exceeded until the pitching moment is 51 to 63 times greater than that prescribed by the current model. Assuming conservatively that state of the art computational fluid dynamics analyses can predict C_m at relevant conditions within 30% of the actual value of C_m during the SRP phase, minimal thrust vector control through engine gimbaling can be used to maintain vehicle attitude and, as such, should prevent static stability concerns from being a driving requirement for SRP.

This analysis demonstrates that thrust vector control through engine gimbaling is a feasible and potentially viable strategy for countering pitching moments during the SRP phase of a high-mass Mars EDL trajectory. Such an ability provides confidence in modeling SRP, even with significant uncertainties in the force and moment coefficients predicted through computational analysis and ground testing. It should be noted that all of these results are dependent on the experimental data set used to construct the model for C_m as a function of α and C_T and also on the specified performance of the SRP propulsion system, CG location, and vehicle configuration during the SRP phase.

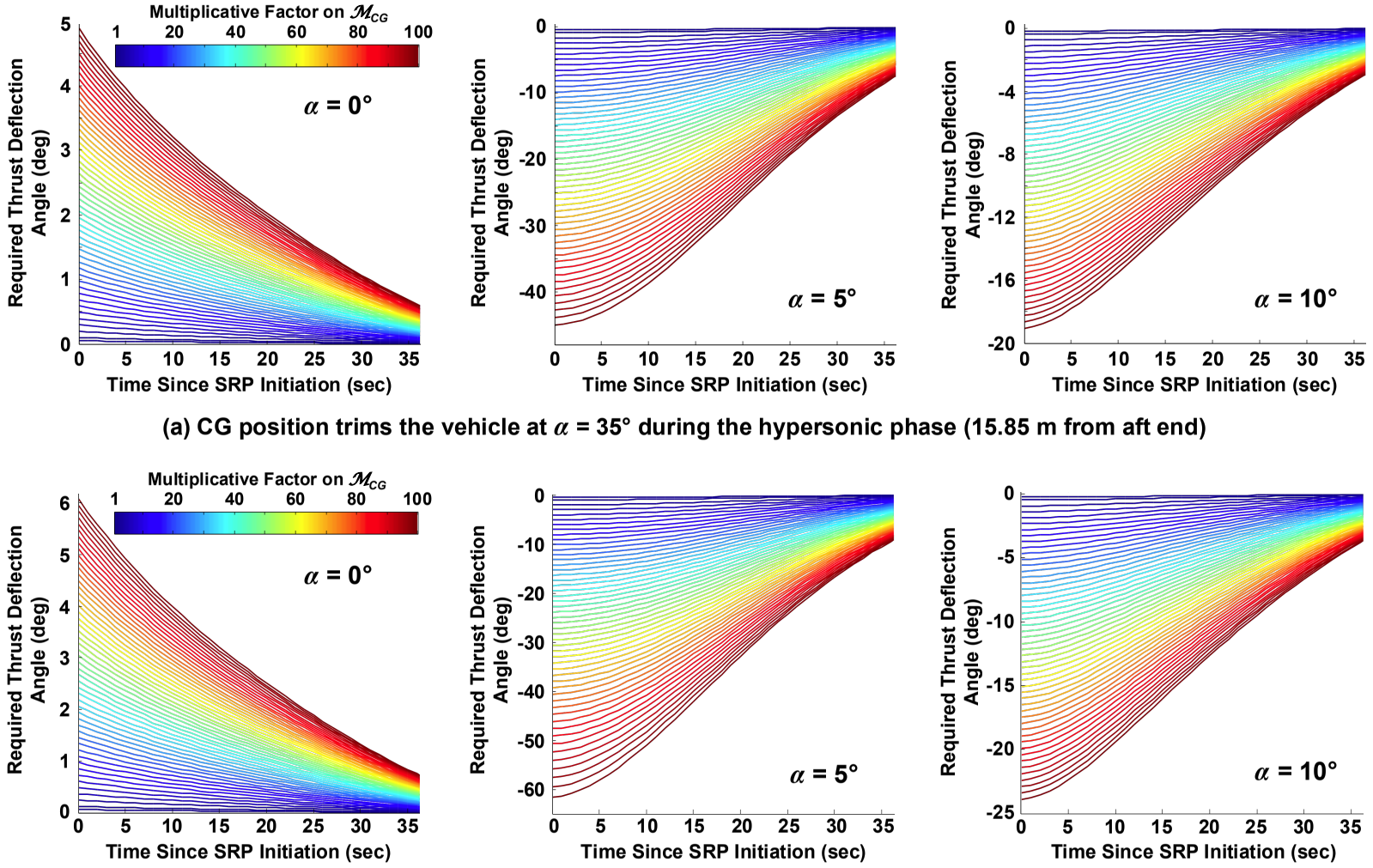

(a) CG position trims the vehicle at α = 35° during the hypersonic phase (15.85 m from aft end)

(b) CG position at the vehicle's geometric centroid location (12.75 m from aft end)

Figure 35: Change in the thrust deflection angle required to counteract moments about the CG during the SRP phase as a multiplicative factor on $\mathcal{M}_{CG}$ increases from 1x ($\mathcal{M}_{CG}$ as determined from the experimentally-derived C_m model) to 100x ($\mathcal{M}_{CG}$ is two orders of magnitude greater than that prescribed from the experimentally-derived C_m model).

Table 10: Summary of the thrust deflection angle required to counteract moments about the CG during the SRP phase.

Multiplicative	$\alpha = 0°$		$\alpha = 5°$		$\alpha = 10°$	
Factor	$CG_{hyp\ trim}$	CG_{geom}	$CG_{hyp\ trim}$	CG_{geom}	$CG_{hyp\ trim}$	CG_{geom}
1x	0.05°	0.06°	-0.41°	-0.50°	-0.19°	-0.23°
2x	0.10°	0.12°	-0.81°	-1.01°	-0.37°	-0.46°
10x	0.49°	0.61°	-4.06°	-5.05°	-1.87°	-2.32°
100x	4.89°	6.08°	-45.07°	-61.62°	-19.04°	-23.92°

3.2.5 Assessment of SRP Modeling Assumptions

A comparison with a prior human-scale Mars EDL study by Christian et al. [19] is completed in this section to illustrate the potential impact of assuming C_D preservation during the SRP phase. The prior study assumed the SRP phase to be modeled by a constant-thrust gravity turn control law with the aerodynamic drag fully preserved. The vehicle followed a constant thrust trajectory to a zero-velocity terminal condition 50 m above the surface. The gravity turn control law requires the thrust vector to be maintained in the direction opposite the vehicle's relative velocity vector and the thrust magnitude to be constant. The SRP initiation time is varied to minimize the sum of the propellant and propulsion system masses.

For consistency with the prior study, the vehicle configuration is assumed to be a 15 m-diameter Apollo aeroshell with a LOX/CH_4 propulsion system. All trajectories start from orbit (4 km/s) with an inertial entry flight path angle of -14.5°. The trajectories are constrained to a $5g$ (Earth) limit. The design points for this comparison are for pure lift-up and lift-down trajectories. For consistency, the design points from this study assume a constant thrust magnitude, constrained to be no larger than 1 MN. The thrust magnitude and initiation conditions are varied to minimize the total propulsion system mass; however, a condition-dependent model for C_D preservation is active during the SRP phase.

Figure 36 shows the difference between the three C_D preservation assumptions as vehicle ballistic coefficient increases for the $L/D = 0.3$ cases. The complete results are summarized in Table 11. The data in Table 11 include results for both 10 m- and 15 m-diameter aeroshells. Table rows with no data are cases that were unable to satisfy the desired terminal conditions without violating the maximum allowable thrust or $5g$ deceleration constraints.

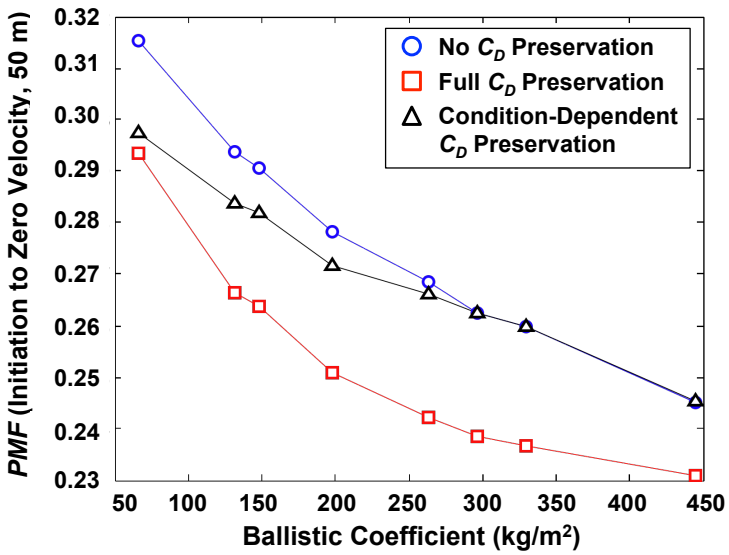

Figure 36: Comparison of C_D preservation assumptions during SRP.

Figure 36 illustrates that the condition-dependent drag preservation model is better aligned with the assumption of full drag preservation at very low vehicle ballistic coefficients (< 100 kg/m^2) and better aligned with the assumption of no drag preservation for ballistic coefficients above approximately 300 kg/m^2. Since most human-scale Mars exploration missions utilize entry vehicles that are characterized by large ballistic coefficients [19, 80, 81], these systems-level analyses would be more accurately performed by assuming no aerodynamic drag preservation (or by assuming the aerodynamic - propulsive interactions model defined in this investigation) than full drag preservation.

In addition, Fig. 36 demonstrates that human-scale Mars exploration missions

Table 11: Results from comparison of SRP modeling assumptions.

	m_{init}, kg	No C_D Preservation	Thrust, kN	Condition-Dependent C_D Preservation	Thrust, kN	Full C_D Preservation	Thrust, kN	% Diff. (Between Cond. and No C_D)	% Diff. (Between Cond. and Full C_D)
$L/D = 0.3$		PMF		PMF		PMF			
$\beta = 65.94$ kg/m^2	18411	0.315	102.8	0.297	85.57	0.294	70.90	5.90	1.27
$\beta = 131.9$ kg/m^2	36823	0.294	240.1	0.284	221.1	0.266	176.7	3.49	6.30
$\beta = 148.4$ kg/m^2	18411	0.291	121.7	0.282	113.0	0.264	91.10	3.07	6.65
$\beta = 197.8$ kg/m^2	55234	0.278	417.7	0.272	396.9	0.251	319.5	2.43	7.93
$\beta = 263.8$ kg/m^2	73645	0.268	660.6	0.266	651.5	0.242	523.6	0.83	8.44
$\beta = 296.7$ kg/m^2	36823	0.262	358.2	0.262	358.2	0.238	290.0	0.00	9.58
$\beta = 329.7$ kg/m^2	92057	0.260	976.0	0.260	976.0	0.237	805.6	0.00	9.33
$\beta = 445.1$ kg/m^2	55234	0.245	1026.5	0.245	1026.5	0.231	916.3	0.03	6.03
$\beta = 593.5$ kg/m^2	73645	–	–	–	–	–	–	–	–
$\beta = 741.8$ kg/m^2	92057	–	–	–	–	–	–	–	–
$L/D = 0.5$		PMF		PMF		PMF			
$\beta = 65.94$ kg/m^2	18411	0.308	108.9	0.283	77.30	0.284	72.40	8.55	0.41
$\beta = 131.9$ kg/m^2	36823	0.285	263.9	0.270	233.0	0.253	186.9	5.33	6.48
$\beta = 148.4$ kg/m^2	18411	0.281	139.2	–	–	0.248	99.90	–	–
$\beta = 197.8$ kg/m^2	55234	0.271	477.3	0.263	447.5	0.240	356.8	2.93	8.90
$\beta = 263.8$ kg/m^2	73645	0.260	813.6	0.259	806.0	0.233	643.3	0.31	10.4
$\beta = 296.7$ kg/m^2	36823	0.255	454.3	0.256	454.3	0.232	369.4	0.38	9.74
$\beta = 329.7$ kg/m^2	92057	0.250	1407.8	0.250	1407.8	0.229	1184.7	0.00	8.67
$\beta = 445.1$ kg/m^2	55234	–	–	–	–	–	–	–	–
$\beta = 593.5$ kg/m^2	73645	–	–	–	–	–	–	–	–
$\beta = 741.8$ kg/m^2	92057	–	–	–	–	–	–	–	–

that utilize slender body aeroshells (generally characterized by lower ballistic coefficients than blunt body aeroshells) may be more suited to the application of supersonic retropropulsion technology. To make definitive statements in this regard, an SRP aerodynamic interactions model for a slender body entry configuration must be developed.

3.2.6 Application to Future Robotic Mission

In this section, the robotic-scale vehicle configuration described in Section 3.1.2.1 is used to investigate the impact of vehicle scale on mass-optimal trajectory performance. Two cases are compared: (1) no C_D preservation is allowed during SRP, and (2) a fraction of the no thrust C_D is preserved as a function of the thrust magnitude and current dynamic pressure (based on Eq. 12). A relative entry flight path angle of -13.65° is assumed, and a variable bank angle profile is utilized during the hypersonic phase of flight. The conditions at SRP initiation and the thrust profile are allowed to

vary to minimize the propellant mass required to decelerate to a terminal condition of 2.5 m/s at 50 m above the ground. From these two optimizations, a summary of the differences in the required SRP initiation conditions and propellant mass is given in Table 12.

A third case is considered, with a vehicle $(T/W)_{max}$ of 5.0 for comparison; the results are included in Table 12. Increasing the available thrust (by increasing $(T/W)_{max}$) allows the vehicle to initiate the SRP phase later in the trajectory, using the vehicle's aerodynamic drag to reduce the total propulsive ΔV. The increase in $(T/W)_{max}$ from 1.94 to 5.0 reduces the required ΔV by 230 m/s as compared to the original case with condition-dependent C_D preservation and by 251 m/s as compared to the original case with no C_D preservation.

Table 12: SRP performance for a 5 t robotic case.

	SRP C_D Preserved	No C_D Preserved	Delayed Initiation
Initiation			
M_∞	2.85	2.96	1.82
C_T	2.20	2.16	5.87
Altitude, km	12.95	13.67	2.76
q_∞, Pa	1032	1046	996.2
Performance			
$(T/W)_{max}$	1.94	1.94	5.0
m_{prop}, kg	1594	1664	1010
PMF	**0.319**	**0.333**	**0.202**

For these cases, the maximum thrust available from the 12 MLEs is low enough for C_T to be less than 3.0 until the vehicle has decelerated to approximately Mach 2. For the $(T/W)_{max} = 1.94$ case with no C_D preservation, this translates into SRP initiation earlier in the trajectory (at a higher altitude and Mach number) as compared to the case with condition-dependent C_D preservation. Though the thrust profile was not constrained to be constant, the final profiles were of near-constant thrust magnitude in both cases, similar to the characteristics of mass-optimal thrust profiles for human-scale vehicles.

3.3 Summary

As vehicle mass requirements increase for missions involving atmospheric entry, descent, and landing at Mars, supersonic deceleration will continue to challenge the qualifications and capabilities of Viking-heritage EDL technology. At Mars, high entry masses and insufficient atmospheric density often result in unacceptable parachute deployment and operating conditions, requiring the exploration of alternative approaches to supersonic deceleration. Supersonic retropropulsion may be an enabling technology for systems that aim to decelerate large masses in a thin atmosphere, such as at Mars.

Across a wide range of ballistic coefficients, mass-optimal Mars entry trajectories for vehicles utilizing supersonic retropropulsion are characterized by extended phases of near-constant altitude deceleration deep within the atmosphere, shallow flight path angles at SRP initiation to minimize gravity losses, and initiation conditions that minimize the required propulsive ΔV. These conditions generally imply SRP initiation at a minimum altitude boundary defined by the timeline considerations of subsequent EDL events. Overall, a lower initiation velocity is strongly preferable over a lower C_T at initiation. SRP initiation conditions are a strong function of the thrust available, and for all high-β cases considered in this chapter, the SRP phase relies on no drag preservation to reach subsonic conditions with timeline margin. The 70-deg sphere-cone aeroshell ($L/D_{max} = 0.24$) is capable of delivering the vehicle to a significant range of SRP initiation conditions across the ballistic coefficients considered.

While minimizing the propulsion system mass increases the mass delivered to the surface, the increased volume required for the propulsion system increases aeroshell packaging density significantly. Considering the minimization of total propulsion system volume as an equally important objective to minimizing propulsion system mass results in a lower $(T/W)_{max}$ than if the minimization of propulsion system mass is considered alone.

For blunt body entry systems and a constant thrust profile, assuming no C_D preservation during SRP is conservative for hypersonic $\beta < 250$ kg/m^2. For entry systems with a hypersonic $\beta > 300$ kg/m^2, the required thrust coefficients imply that aerodynamic drag cannot be preserved. As such, entry systems studies for human-scale Mars exploration are most accurately performed by assuming no aerodynamic drag preservation (or by assuming the condition-dependent aerodynamic-propulsive interactions model defined in this chapter) as opposed to full drag preservation. In addition, while analysis of a 5 t robotic-scale mission ($\beta \approx 200$ kg/m^2) demonstrated a 4.5% PMF advantage for drag preservation during SRP, the T/W limitations of the propulsion system assumed in the analysis constrain SRP initiation to a high altitude, high velocity condition that was shown to be relatively inefficient in comparison to a design with a higher system T/W.

Using a mid-L/D vehicle configuration, thrust vector control through engine gimbaling was demonstrated to be a feasible and potentially viable strategy for controlling pitching moment during the SRP phase of a high-mass Mars EDL trajectory. Moments about the vehicle's center of gravity in the pitch plane are greatest near SRP initiation and decrease in magnitude rapidly as the vehicle decelerates to subsonic conditions, even at small (up to 10°) angles of attack. The actual moments would need to exceed the predicted moments by more than a full order of magnitude before the required thrust deflection angles are greater than those already proven for liquid bipropellant propulsion systems. These results provide confidence in modeling SRP, even if there are significant uncertainties in the force and moment coefficients predicted through computational analysis and ground testing. For conceptual design, support from high-fidelity computational analysis is not required to assess SRP performance. Rather, aerodynamic forces and moments during the SRP phase can be estimated using trends in the existing experimental database.

CHAPTER IV

PRELIMINARY COMPUTATIONAL SOLUTIONS

System-level analyses beyond the conceptual design phase will be challenged by a lack of available empirical models and will look to computational fluid dynamics analyses for databases representing the aerodynamic - propulsive interactions inherent to supersonic retropropulsion. Given the limitations of existing experimental data (see Ref. [10]) and the inability to fully simulate Mars-relevant conditions and configurations in ground-based facilities, the development of these models will likely depend on the use of validated computational fluid dynamics tools.

In the most general sense, supersonic retropropulsion flowfields are characterized by the interaction between the shock layer of the entry vehicle and the retropropulsion exhaust flow. Investigation into the capabilities of modern computational analysis tools in simulating similar flow interactions has been completed [8, 11, 29, 47, 60, 61, 69, 70, 71, 72, 73, 74, 75, 76]. These works are reviewed briefly in Chapter 2, Section 2.4. Most of this computational work focuses on the mitigation of severe aerothermal environments during entry or drag reduction effects, with little focus on moderate thrust levels and flight-relevant conditions. The similarities between the flow interactions across these works are, however, useful for extending past work to analyses targeting conditions, configurations, and applications that are flight-relevant for SRP. In general, accurate prediction of the static aerodynamics and flowfield stability of aeroshells with supersonic retropropulsion using computational fluid dynamics methods requires the ability to capture detached shocks, highly under-expanded jet flow structures, contact surfaces, shock - shock interactions, recirculation, and the formation and turbulent transition of free shear layers.

This chapter investigates the ability of computational analysis approaches to consistently and accurately capture the relevant flow physics and changes in the vehicle's static aerodynamic characteristics arising from supersonic retropropulsion. Complimenting the discussion on supersonic retropropulsion flow physics in Chapter 2, computational results for a central and a peripheral retropropulsion configuration are compared with data from a wind tunnel test series completed by Jarvinen and Adams [13, 40] in 1970, the only work available (prior to 2010) with data from an experimental investigation of a peripheral SRP configuration. An additional qualitative comparison is made with experimental results from a more recent test by Daso et al. [8]. This assessment is completed by comparing the location and formation of primary flowfield features and surface pressure distributions with experimental data. This chapter seeks to serve as a starting point for understanding the challenges facing the computational simulation of SRP flowfields and presents preliminary FUN3D solutions at relevant conditions. The following chapter builds upon this work to support the validation of FUN3D in simulating SRP flowfields with data from a recent NASA wind tunnel test. This chapter is focused on steady-state solutions; Chapter 5 is focused on time-accurate solutions.

4.1 Expected Results for Inviscid and Viscous Analysis Approaches

The relevant flow physics provide insight into the expected results of applying inviscid and viscous computational approaches to SRP flowfields. Given the significance of shear layer interactions and dissipation mechanisms on the formation of the jet structure, it is expected that inviscid approaches may be unable to fully capture the correct SRP flowfield structures and interactions, particularly in the radial direction, and accordingly, be unable to consistently capture the resultant forebody surface pressure distribution across a broad range of conditions. However, in the vicinity of the nozzle exit, the boundary layer at the initial jet expansion is very thin, and inviscid

theory has been shown to describe the resulting jet flow reasonably well by capturing the jet expansion angle, jet boundary, and jet termination structure [5, 30]. Further from the nozzle exit, the thickening shear layer and recirculation region require the addition of boundary layer approximations to inviscid theory to capture the jet structure fully [5]. Inviscid approaches should also perform well in capturing the locations of discontinuities (e.g. bow shock, contact surface, Mach disk, barrel shock) along and near stagnation streamlines. Work by Bahktian et al. [66, 70] has demonstrated the ability of a Cartesian Euler flow solver to capture the general flowfield structure, flowfield behavior, and integrated surface quantities for supersonic retropropulsion flowfields over a limited range of configurations and conditions, supporting the hypothesis that SRP flowfields are generally characterized by inviscid flow phenomena within the subset of configurations and conditions explored.

The presence of supersonic and subsonic free shear layers within SRP flowfields suggests viscous dissipation of both the jet and freestream play a secondary, though important role in the formation of the flowfield structure away from the nozzle exit. Work has been completed on the transition from laminar to turbulent flow along supersonic free shear layers and on the differences in transition behavior between subsonic and supersonic free and wall-bounded shear layers [86]. However, much of this work is experimental and/or analytical, and current models in use may not reflect such transition behaviors. Experimental observation of flow transition for jets exhausting into quiescent mediums and supersonic crossflows [6, 29, 76] and the formation of large mixing regions suggest a strong potential for transition in SRP flowfields. Appropriate turbulence modeling is likely to be a significant contributor to the ability to consistently capture the true flowfield structure and resulting pressure distributions.

Based on the complexity of the SRP flowfield, with subsonic recirculation and

supersonic and subsonic shear layers, a steady flowfield is not expected. Experimental observation and data have shown that SRP flowfields are unsteady under certain conditions [14, 51]. The degree to which viscous dissipation lessens the potential for unsteadiness is unclear, but flow solutions obtained using viscous approaches are expected to be more steady than flow solutions obtained using otherwise equivalent inviscid approaches as a result of the added dissipation. Similarly, flow solutions obtained using turbulent approaches are expected to be more steady than those obtained using otherwise equivalent laminar approaches due to the addition of turbulent dissipation. The effectiveness of any computational approach will be highly dependent on the specific models applied and how certain models (e.g. turbulence and turbulent transition) are coupled to the flow solver.

Independent of the analysis approach, solutions for SRP flowfields will be computationally expensive. The complexity and expanse of the interaction between the jet flow and shock layer, and also between the resulting flow structures, at relevant conditions require a high degree of grid resolution over a large volume. Additionally, the increased size of the freestream flow obstruction caused by the jet flow interaction requires a much larger computational domain, particularly for the downstream location of the outflow boundary, than would be sufficient for the same blunt body with no SRP. If steady-state solutions are unable to capture critical flow behavior, the computational cost will increase further for conditions requiring time-accurate solutions.

4.2 Approach and Models

The general approach taken in this chapter is to generate flow solutions for several retropropulsion configurations at conditions that span experimental data from historical references and extend toward flight-relevant operation. Cart3D (described briefly in Section 2.4) is used for a subset of cases as an initial, exploratory effort with

a Cartesian Euler flow solver. All Cart3D solutions are discussed in Section 4.2.1. FUN3D is used to generate all flow solutions in the other sections in this chapter and also in all sections of Chapter 5. FUN3D is used for turbulent, viscous analyses, with all cases run to a steady-state solution. Steady-state solutions are obtained with FUN3D using local time stepping to drive a second-order accurate spatial residual to steady state. Steady-state convergence is considered to be achieved by a three order of magnitude drop in the x-momentum residual and maintenance of this drop through several hundred additional iterations. All run conditions are determined assuming one-dimensional isentropic flow through the nozzle, with stagnation conditions defined for the nozzle plenum face.

4.2.1 Initial Exploration

The models and approach applied to produce the computational results presented in this chapter are initial, exploratory efforts aimed at uncovering some of the challenges of simulating supersonic retropropulsion flowfields and gaining experience in starting and establishing solutions using configurations tested in the 1960s and early 1970s. These configurations included a single nozzle case consistent with work by McGhee [12], a configuration of three nozzles on the forebody periphery consistent with work by Jarvinen and Adams [13] (see Section 4.2.3.3), and a configuration of four nozzles consistent with work by Peterson and McKenzie [9]. As mentioned, Cart3D [87], a NASA-developed, Cartesian-based Euler flow solver is used for the majority of the work in this section.

Figure 37 shows Mach number contours obtained for the peripheral nozzle configuration from Jarvinen and Adams [13]. In these initial solutions, the bow shock and barrel shock are clearly visible, and with sufficient grid resolution in the interaction regions, the jet structure begins to form. Even for converged, steady-state solutions, the jet flow structures do not appear to be well formed. The jet shapes

are highly elliptical, and there is no distinct jet termination structure or Mach disk. Little disruption of the portions of the bow shock over the nose allows for a degree of preservation of post-shock stagnation pressures on the body. This result is consistent with the trends observed in the original experiment.

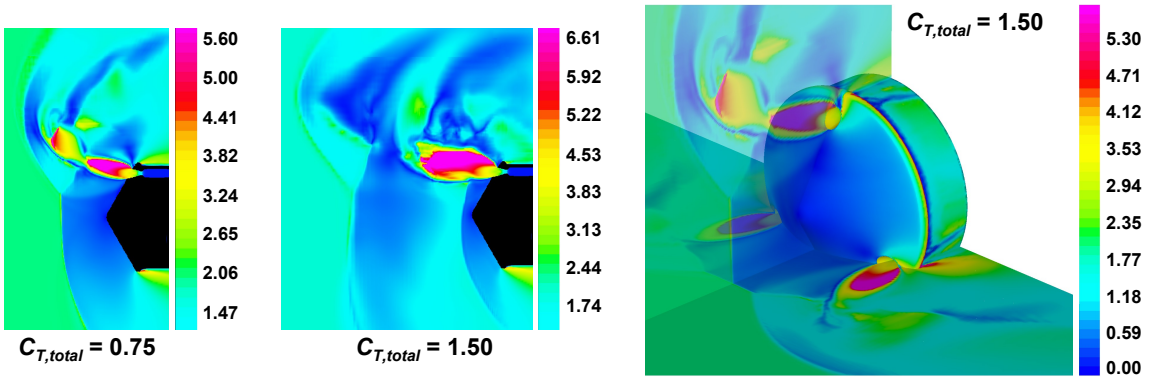

Figure 37: Mach number contours from initial inviscid solutions for a peripheral configuration.

The solutions for this configuration (three peripheral nozzles) are highly sensitive to the approach used to start the solution. If the pressure in the plenum is ramped up to the desired condition too rapidly, the jet structure does not properly form (as compared to the expected flow structure from observations by Jarvinen and Adams [13]) and lacks a clear termination structure.

In general, starting solutions was found to be tedious and difficult, even with the implementation of an iteration-based schedule for increasing the plenum pressure. The most stable and efficient approach for starting solutions was initializing the computational domain at supersonic freestream conditions and, where possible, also initializing the entire plenum to the total conditions corresponding to the desired thrust coefficient.

Figure 38 shows Mach number contours and the bow shock standoff distance with increasing total pressure ratio for a configuration investigated by Peterson and McKenzie in 1962 [9]. This configuration has four nozzles, equally spaced at a distance

of approximately $0.4r$ from the center of a flat-faced semi-ellipsoid. The semi-ellipsoid geometry is visible in the two leftmost images in Fig. 38. Mach number contours, with the total pressure ratio increasing from left to right, illustrate the progressive formation of the jet structures and coalescence of the individual jets into a single structure for $M_\infty = 1.5$ conditions. The bow shock standoff distance from these solutions is compared with the locations observed in the original experiment in Fig. 38. The predictions for the bow shock standoff distance agree well with the experimental locations for total pressure ratios below approximately 70 and above approximately 120. In the original experiment, a large upstream displacement of the bow shock was observed prior to the coalescence of the individual jet structures. This displacement was not captured by the inviscid solver.

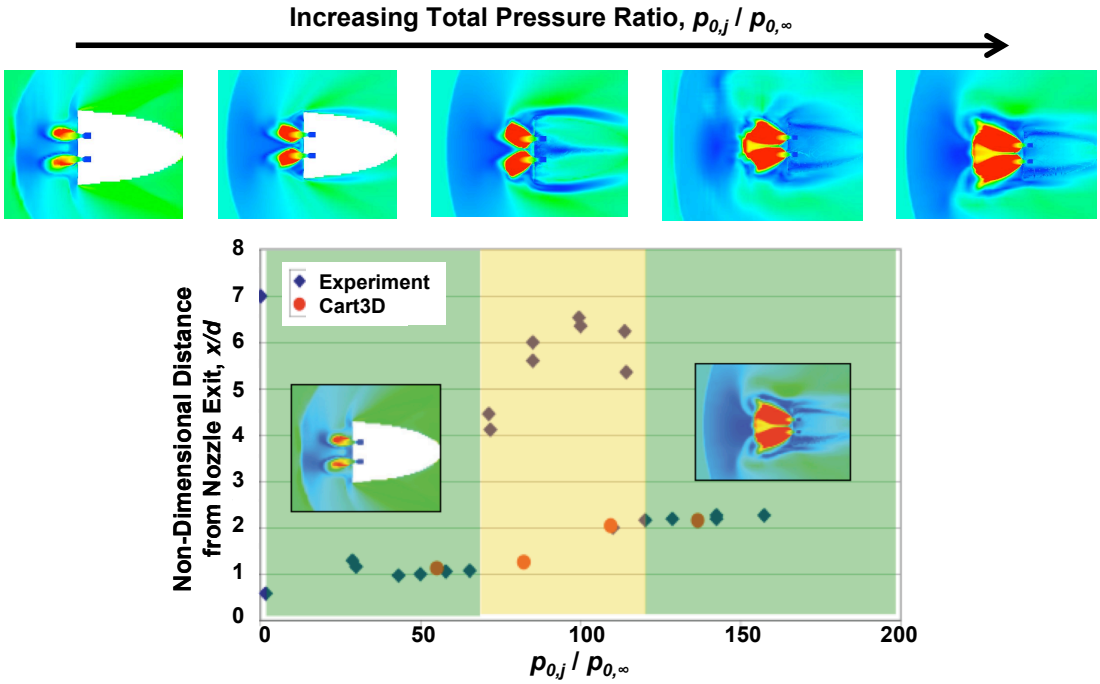

Figure 38: Mach number contours from initial inviscid solutions showing bow shock standoff distance for a four nozzle configuration. Contours on the body are blanked out for the two lowest total pressure ratio cases.

Not unexpectedly, all of these initial solutions were found to be very sensitive to the grid applied and required substantial grid resolution in the regions surrounding

the initial jet expansion (nozzle exit) and jet termination structures. Though only exploratory, the results obtained through this initial work uncovered some of the challenges to be faced in simulating SRP flowfields and confirmed that over a limited range of conditions and configurations, an inviscid analysis approach can perform well in predicting the structure of the SRP flowfield and associated surface pressure distributions. Considering some of the inconsistencies in these initial results and that viscous analysis was also to be completed, FUN3D was selected as the computational tool to be used for all of the remaining computational analyses in this thesis; the code is described in the following section.

4.2.2 Computational Tool – FUN3D

FUN3D is the computational tool used for all viscous CFD analyses completed in this thesis. FUN3D is a fully-unstructured, NASA-developed CFD code capable of solving the Euler and Reynolds-averaged Navier-Stokes equations through perfect gas simulation [88, 89, 90]. The flow solver is based on second-order, node-centered, finite-volume discretization. Local time stepping is applied for steady flows, and second-order time accuracy is applied for unsteady flows. The scheme utilizes implicit upwind-differencing and, similar to recent work [16, 65, 75], Edwards' dissipative LDFSS flux function [91] with a Van Albada limiter [92]. The RANS flow solver is loosely coupled to Menter's SST turbulence model [93], with no compressibility correction. All solutions in this chapter are steady-state and generated using version 11.2 of the FUN3D code.

Generation of unstructured, tetrahedral grids is completed through a multi-step workflow using GridEx/BatchEx [94] and VGRID/PostGRID [95]. The geometry is initially read into GridEx/BatchEx in parasolid format, and boundary conditions are then assigned. Nodal, linear, and volume VGRID sources are defined to control the characteristics of the resulting grids. Increased resolution in the vicinity of the model

surface is specified at the nozzle exit, nozzle throat, converging section of the nozzle, model shoulder, and aft end of the model. A conical volume source is applied to increase grid density in the jet flow interaction region upstream of the model. An example of the GridEx setup illustrating these sources on a model geometry is shown in Fig. 39.

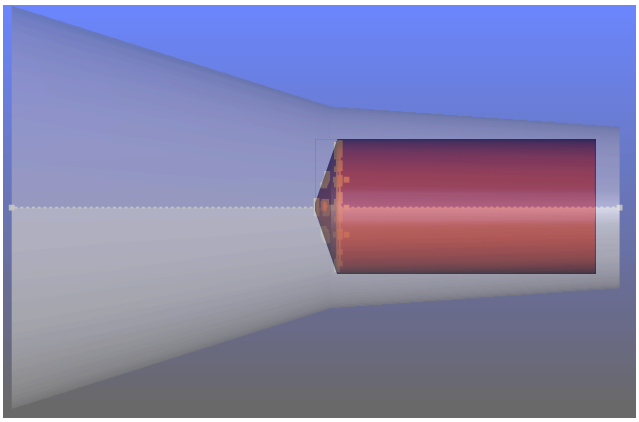

Figure 39: Example GridEx setup illustrating conical volume sources and linear edge sources. Conical volume sources extend beyond the anticipated jet flow interaction region.

Additionally, a cylindrical volume source spanning the length of the computational domain is specified with a spacing gradient to assist with the convergence of the advancing front algorithm used by VGRID in generating the volume grid. The final grids are processed by first generating the surface mesh. VGRID then generates the viscous mesh, and finally, the inviscid mesh. This entire process, from reading the original geometry through final grid generation can be executed either manually or automatically. The fully processed VGRID grids are then read directly into FUN3D. The specific geometries, configurations, and conditions used are given in the following section (4.2.3). The unstructured, tetrahedral meshes used for each case are also shown.

4.2.3 Experimental Data Set and Conditions Summary

This section provides an overview of the geometries, configurations, conditions, and original wind tunnel test series and associated experimental data sets used in this preliminary assessment. These cases encompass three different model geometries, three different retropropulsion configurations, freestream Mach numbers from 2.0 to 3.48, and thrust coefficients from 0 to 10.

4.2.3.1 2.6% Scale Apollo Capsule with a Single, Central Nozzle

A comparatively recent (mid-2000s) test series was completed in the Trisonic Wind Tunnel at NASA Marshall Space Flight Center using a 2.6%-scale Apollo capsule with a single, central nozzle. The objectives of the test were to explore the use of counterflowing jets as a form of active flow control for reducing the severity of the aerothermal environment experienced during atmospheric entry. Five different nozzle geometries were run at five different mass flow rates for freestream Mach numbers of 3.48 and 4.0. Static aerodynamic and aerothermal data were collected from 56 static pressure ports and 15 heat flux transducers/thermocouples on the model. Schlieren still images and bow shock standoff distances are available for the 0.5 inch-diameter sonic nozzle cases at $M_\infty = 3.48$ and $\alpha = 0°$. Figure 40 gives the dimensions of the model and nozzle.

The objectives of the test, as well as the size of test section (14 $\times$ 14 inch cross-section), restricted the thrust coefficients tested with the 0.5 inch-diameter sonic nozzle to $C_T = 0.4$ and below. Even though the conditions are not flight-relevant, this test series is used as a simplified starting point with modern experimental data and for the availability of complimentary computational solutions in the literature [8, 60, 61, 75]. The composition of both the freestream and jet flow is air ($\gamma_\infty = \gamma_j = 1.4$). Table 13 summarizes the freestream and jet conditions.

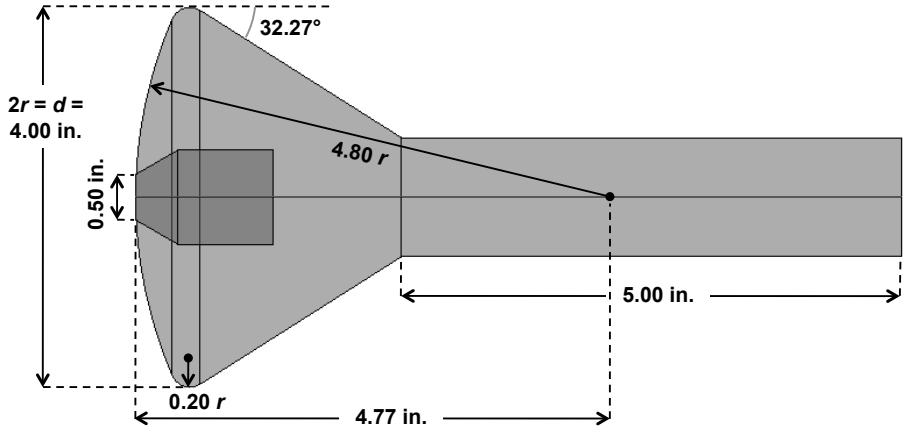

Figure 40: 2.6%-scale Apollo capsule and sonic nozzle dimensions.

Table 13: Conditions summary for the 2.6%-scale Apollo capsule.

Freestream conditions					
M_∞	$p_{0,\infty}$ (psi)	p_∞ (psi)	$T_{0,\infty}$ (K)	T_∞ (K)	Re_∞ $(1/d)$
3.48	44.9	0.607	322.2	94.6	1.63×10^6
Nozzle conditions					
$\dot{m}$ (lb_m/s)	C_T	M_e	$p_{0,j}$ (psi)	$T_{0,j}$ (K)	
0.00	0.00	–	–	–	
0.05	0.05	1.0	12.5	273.9	
0.10	0.09	1.0	22.7	270.6	
0.25	0.21	1.0	54.8	262.8	
0.35	0.29	1.0	75.9	263.9	
0.50	0.40	1.0	104.3	266.1	

A quarter-model grid is used for all cases to reduce the computational cost associated with a single run. Figure 41 shows the grid in the vicinity of the nozzle exit and the model forebody, with portions of the linear and cylindrical shell sources used to generate the inviscid volume mesh visible. The full domain spans $2.5d$ upstream, $4.5d$ downstream, and $1.75d$ cross-stream from the nozzle exit. This quarter-model grid has 8.95 million nodes.

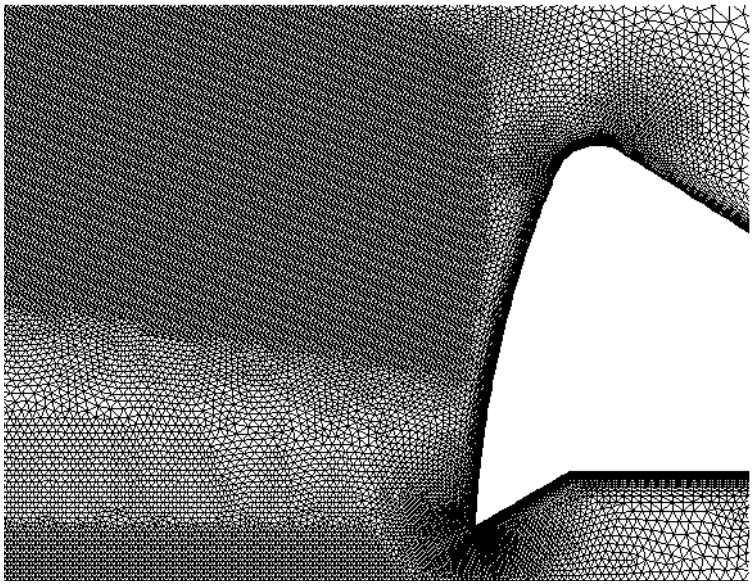

Figure 41: Cut plane showing grid resolution in the vicinity of the nozzle exit.

4.2.3.2 60-deg Sphere-cone Aeroshell with a Single, Central Nozzle

The primary experimental data set used for this preliminary investigation is from a wind tunnel test series completed by Jarvinen and Adams [13] from 1968 - 1970. This work is the only historical (pre-2010) reference available for a parametric test series spanning both central and peripheral retropropulsion configurations [10]. The test series was conducted in the NASA Ames Research Center 6 ft. $\times$ 6 ft. supersonic wind tunnel across freestream Mach numbers of 0.4 to 2.0. In total, the test series explored the effects of aeroshell geometry (45° and 60° sphere-cones), retropropulsion configuration (one central nozzle vs. three peripheral nozzles), exhaust gas composition (air and helium), angle of attack (-18° to +9°), thrust coefficient (0 to 7, at supersonic freestream conditions), and differential throttling for the peripheral configuration. Of interest in this investigation are the data for the 60° sphere-cone at $M_\infty = 2.0$ and $\alpha = 0°$, for all thrust coefficients tested with air as the exhaust gas ($\gamma_\infty = \gamma_j = 1.4$).

The experimental data set includes surface pressure distributions, integrated force and moment coefficients, and flowfield geometry information as a function of thrust

coefficient. The 4 inch-diameter models were instrumented with concentric rings of pressure taps on the forebody: 30 taps on the single nozzle model and 45 taps on the three nozzle model. Force and moment data were generated by integrating these pressure measurements over the model. All cases were run with $p_{0,\infty} = 2.0$ psi, varying C_T by changing the jet total pressure. The experimental data set does not provide information on the freestream total temperature or the plenum total temperature. As such, $T_{0,j}$ is assumed to be 294 K for consistency with other SRP investigations completed in the 1960s using compressed, dry air. $T_{0,\infty}$ is assumed to be 311.67 K to be consistent with the operating envelope of the NASA Ames Research Center 6 ft. $\times$ 6 ft. supersonic wind tunnel [96]. In addition to an absence of total temperature information, the experimental data set does not provide information on data collection or reduction methods, resulting in only an approximate knowledge of the test conditions and data presented in the original test report.

Though not reported in the original experiment, the model geometry and test conditions likely yielded very low temperatures in the jet flow and now raise questions on the possibility of liquefaction during expansion. It is unknown if the plenum air could have been heated during the test; no consideration of the possibility of phase change within the jet flow is mentioned in the test documentation. Complimentary work [75] with the same experimental data set observed single-digit Kelvin temperatures in the jet flow with the assumption of no phase change at the same test conditions as those used in this chapter. No special treatment is applied here concerning the potential phase change in the jet flow, as no other work has been found (experimental or computational) that was concerned with liquefaction at similar conditions.

The central retropropulsion configuration has a single, central nozzle aligned with the body's axis of symmetry. Figure 42 shows the geometry of the aeroshell model, and Fig. 43 shows the dimensions of the nozzle and plenum. The nozzle is a 15-deg conical nozzle with a 0.5 inch-diameter exit. The nozzle has an area ratio, $A_e/A^\star$,

of 13.95, corresponding to an exit Mach number of 4.3, assuming one-dimensional isentropic expansion. A sting (length: 4 in., diameter: 1 in.) has been added to the aft face of the original model.

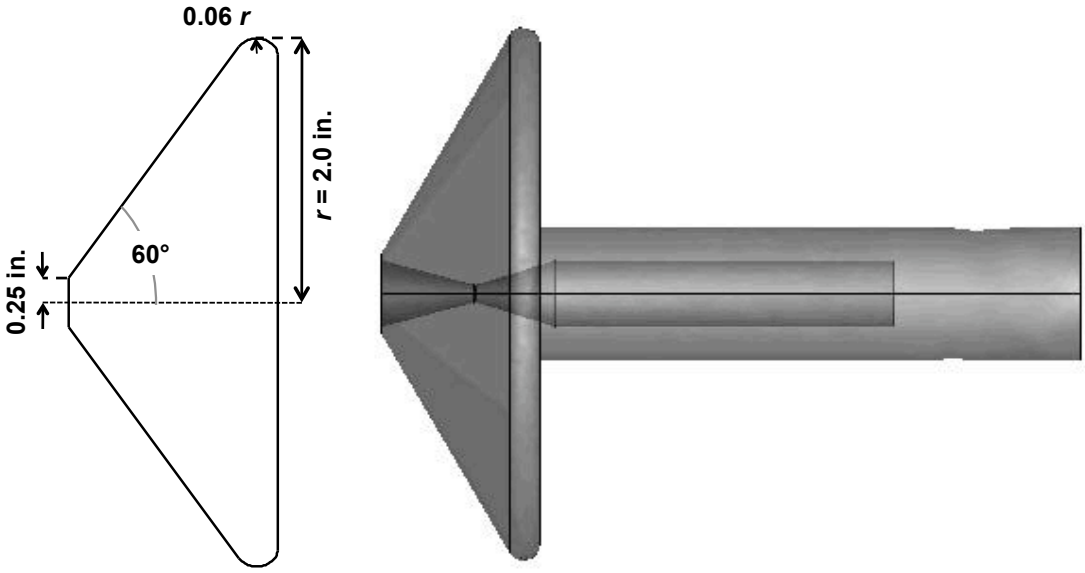

Figure 42: Aeroshell geometry and nozzle location.

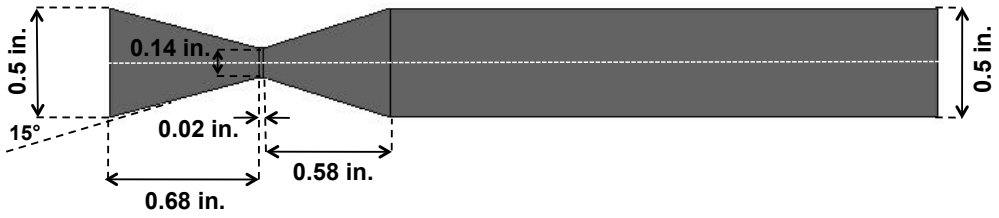

Figure 43: Nozzle dimensions for the central retropropulsion configuration.

Table 14 provides a summary of the freestream and nozzle conditions for the central configuration cases. Recall from Fig. 32 in Chapter 3 that C_T is lowest at initiation and increases rapidly as the vehicle decelerates. As such, only the $C_T = 4.04$ and $C_T = 7.00$ conditions are considered to be flight-relevant for Mars exploration missions. An additional run at $C_T = 10.0$ is included as a more flight-relevant case. Experimental data at flight-relevant conditions are extremely limited in the current SRP database.

Table 14: Conditions summary for the central retropropulsion configuration.

Freestream conditions

M_∞	$p_{0,\infty}$ (psi)	p_∞ (psi)	$T_{0,\infty}$ (K)	T_∞ (K)	Re_∞ $(1/d)$
2.0	2.0	0.256	311.7	172.4	1.624×10^5

Nozzle conditions

Run	C_T	M_e	$p_{0,j}$ (psi)	$T_{0,j}$ (K)
1	0.00	–	–	–
2	2.00	4.3	767.9	294.0
3	4.04	4.3	1549.0	294.0
4	7.00	4.3	2682.3	294.0
5	10.0	4.3	3831.0	294.0

Figure 44 shows the grid used for the central configuration cases in the vicinity of the nozzle exit. The grid is fully three-dimensional. The boundaries of the computational domain are $8d$ upstream, $15d$ downstream, and $5d$ cross-stream of the model. The effective flow obstruction resulting from the SRP interaction at higher thrust coefficients produces a significantly larger wake region than the model with no SRP, requiring large downstream distances for the wake to close fully and permit supersonic flow at the outflow boundary. This grid has 10.3 million nodes.

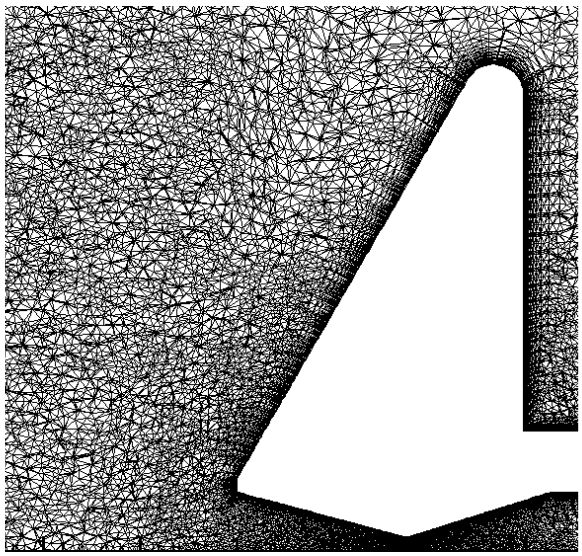

Figure 44: Cut plane showing grid resolution in the vicinity of the nozzle exit.

4.2.3.3 60-deg Sphere-cone Aeroshell with Three Peripheral Nozzles

The peripheral retropropulsion configuration tested by Jarvinen and Adams [13] has three nozzles, spaced 120° apart on a circle at 80% of the model radius. The nozzles are 15° conical nozzles, each scarfed at 30° to be flush with the model forebody. Figure 45 and Fig. 46 show the location of the nozzles on the aeroshell forebody and the nozzle dimensions. The three nozzles were designed to collectively have the same total thrust coefficient as the single, central nozzle. In the original experiment, the model did not have an aft section; all plumbing behind the forebody was exposed. A 1 inch-long cylindrical aft section has been added past the shoulder in this investigation to simplify the flowfield aft of the model.

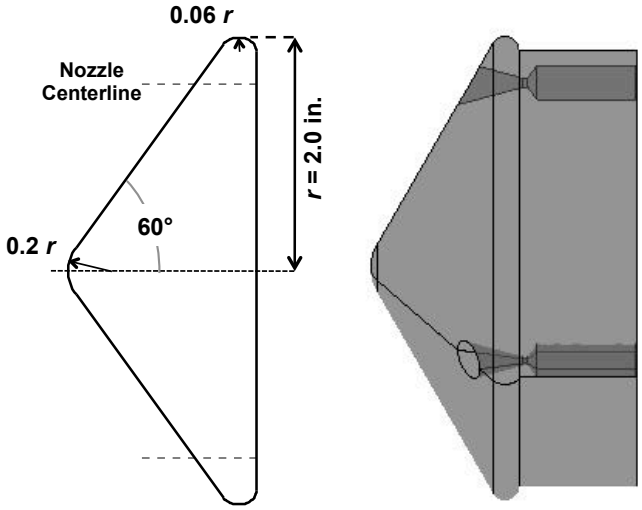

Figure 45: Aeroshell geometry and nozzle locations.

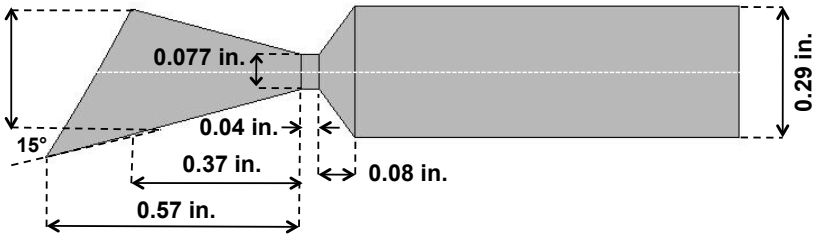

Figure 46: Nozzle dimensions for the peripheral retropropulsion configuration.

The nozzle conditions for the peripheral configuration cases are given in Table 15,

with the total pressure, $p_{0,j}$, given per nozzle to yield the total C_T. The freestream conditions are the same as those used for the central configuration.

Table 15: Conditions summary for the peripheral retropropulsion configuration.

Freestream conditions					
M_∞	$p_{0,\infty}$ (psi)	p_∞ (psi)	$T_{0,\infty}$ (K)	T_∞ (K)	Re_∞ $(1/d)$
2.0	2.0	0.256	311.7	172.4	1.624×10^5
Nozzle conditions					
Run	C_T	M_e	$p_{0,j}$ (psi)	$T_{0,j}$ (K)	
1	0.00	–	–	–	
2	1.00	4.3	384.4	294.0	
3	1.66	4.3	638.2	294.0	
4	4.04	4.3	1553.1	294.0	
5	7.00	4.3	2691.0	294.0	

Figure 47 shows the grid used for the peripheral configuration cases in the vicinity of one nozzle exit. A full three-dimensional grid is used for all cases to avoid disruption of the interactions between jet flows by symmetry planes. The boundaries of the computational domain are $5d$ upstream, $20d$ downstream, and $5d$ cross-stream of the model.

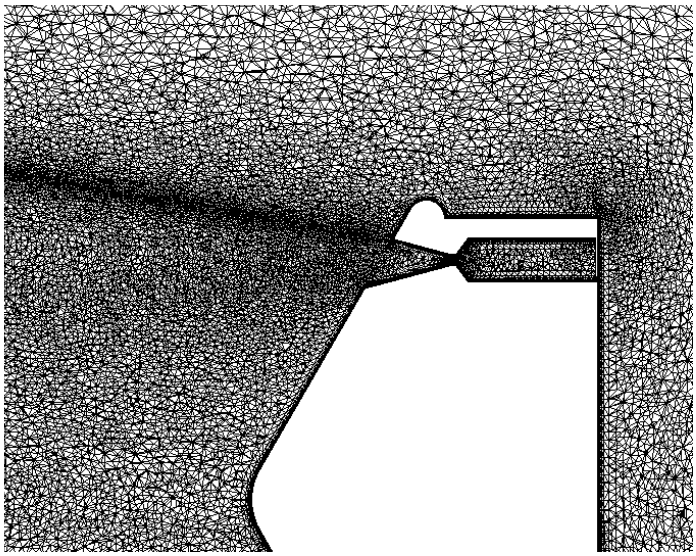

Figure 47: Cut plane showing grid resolution in the vicinity of one nozzle exit.

Even more so than for the central retropropulsion configuration, the effective flow obstruction resulting from the SRP interaction at higher thrust coefficients produces

a significantly larger wake region than the model with no SRP, requiring large downstream distances for the wake to close fully and permit supersonic flow at the outflow boundary. Difficulties with post-processing limited this grid to 3.26 million nodes.

4.3 Results – Preliminary Computational Cases

For the three retropropulsion configurations described in Section 4.2, preliminary FUN3D solutions have been generated for each case listed in Tables 13, 14, and 15 using a steady-state, turbulent approach (Menter's SST model). Mach number contours are shown to illustrate the SRP flowfield structure, with streamlines generated to highlight critical flow features. For the cases based on experimental data from Jarvinen and Adams [13], distributions of C_p as a function of radial distance on the forebody are also provided at three angular locations. No integrated force coefficients are given, as the coefficients given in the experimental data set were originally integrated from a very limited number of surface pressure measurements, and no information regarding the uncertainty in these measurements is given in the test report.

4.3.1 2.6%-Scale Apollo Capsule with a Single, Central Nozzle

Schlieren data are compared with the Mach number contours for FUN3D solutions in Fig. 48 for the five thrust coefficients examined in the original experiment, as well as a $C_T = 0.00$ baseline case. Qualitatively, the resulting flowfield structures agree well with those observed in experiment. In the $C_T = 0.05$ and $C_T = 0.09$ cases, the jet flow is marginally under-expanded, and the intersecting shock structures are visible within the jet flows. For the three cases with the largest thrust coefficients, the jet flow is highly under-expanded, and the jet structure changes; the bow shock, Mach disk, reflected Mach wave intersection, and barrel shock are all clearly resolved at these conditions. Figure 49 shows Mach number contours and streamlines for the $C_T = 0.40$ case, with streamlines indicating the turning of the flow at the free stagnation

point and recirculation over the forebody outboard of the nozzle. The data set from this test series [8] did not include quantitative pressure data. All solutions converged to steady-state, though small oscillations remained in the residual histories.

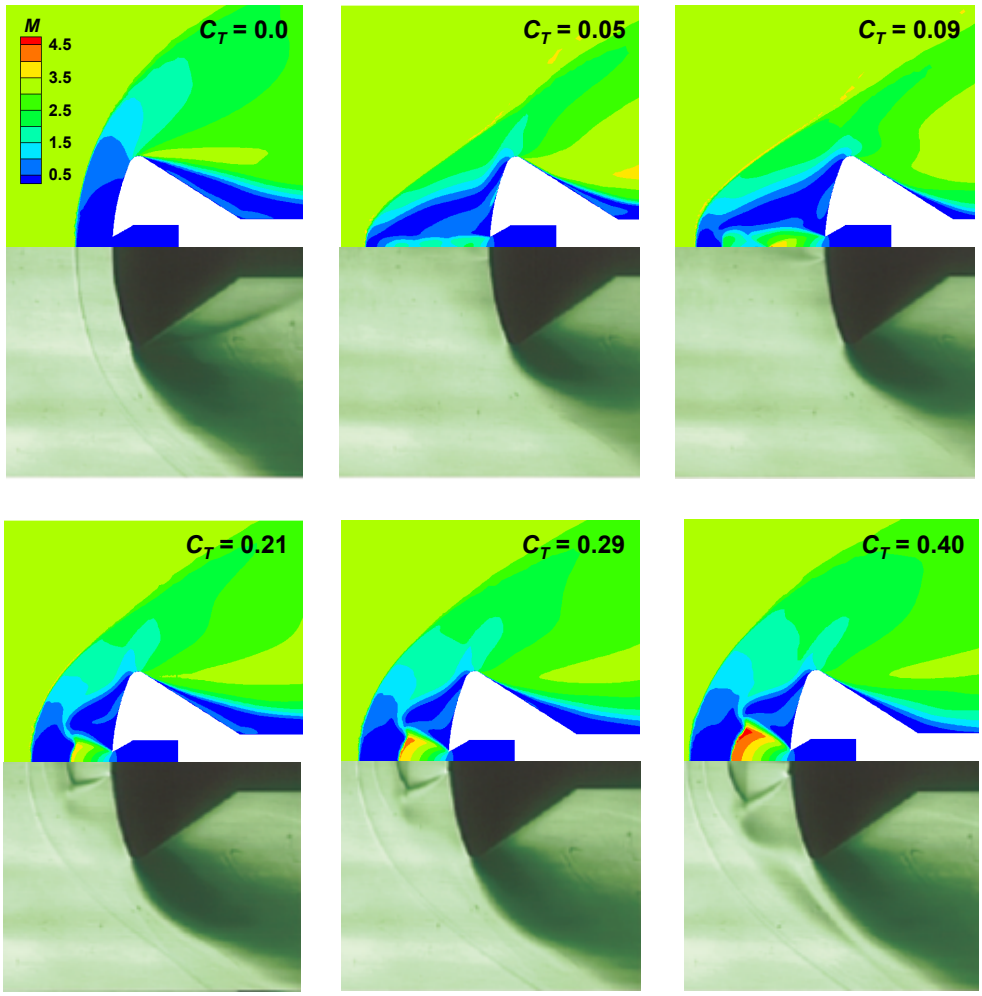

Figure 48: Comparison of FUN3D solutions with experimental schlieren images.

As the jet total pressure increases, the jet flow becomes more highly under-expanded, and the overall flowfield structure becomes both more stable and more steady. Table 16 gives experimental and computational solution values for the bow shock standoff distance for the cases where the jet flow is highly under-expanded. The experimental values are given in the literature [8], though no additional information is provided on the uncertainty or original determination of these values. In

all cases, the FUN3D solution slightly under-predicts the bow shock standoff distance, possibly indicating over-dissipation within the models applied. The absolute difference between the bow shock standoff distances observed in the experiment and those predicted by CFD remains constant as the overall flowfield stabilizes at thrust coefficients corresponding to highly under-expanded jet flow.

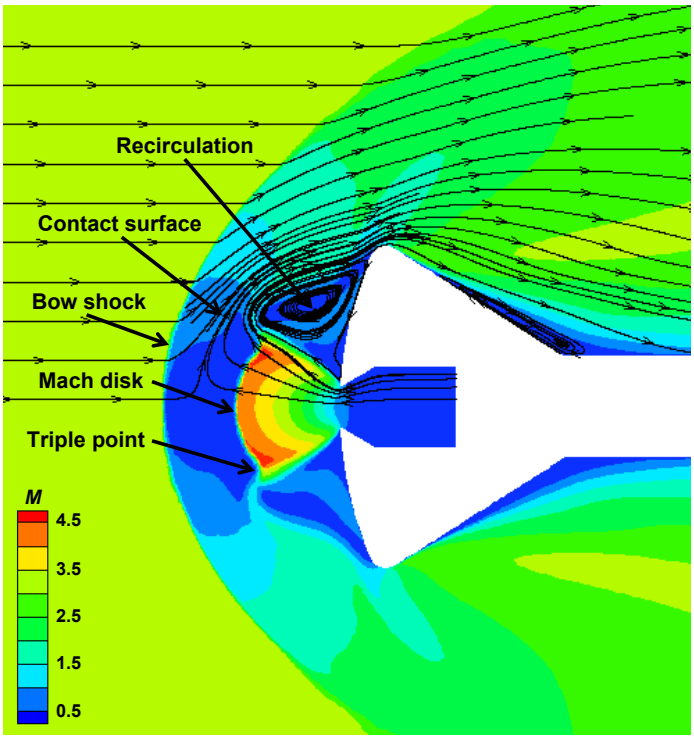

Figure 49: Streamlines and Mach contours for $C_T = 0.40$ conditions.

Table 16: Comparison of bow shock standoff distances.

$\dot{m}$ (lb_m/s)	C_T	CFD x/d	Exp. x/d	% Difference
0.00	0.00	0.19	0.20	6.17
0.25	0.21	0.43	0.44	3.26
0.35	0.29	0.48	0.49	2.08
0.50	0.40	0.54	0.55	1.10

4.3.2 60-deg Sphere-cone Aeroshell with a Single, Central Nozzle

As discussed in Chapter 2, a central SRP configuration at $\alpha = 0°$ should yield a symmetric jet structure defined along a constant-pressure boundary, with a barrel shock

and a terminal Mach disk at highly under-expanded conditions. A free stagnation point should form on the contact surface along the body axis in the subsonic region between the bow shock and the Mach disk. A comparison of the axial locations of the Mach disk, stagnation point, and bow shock for the FUN3D solutions and experimental data is given in Fig. 50. Reasonable agreement is demonstrated with the trends in the experimental data as C_T increases, with the best agreement seen at low thrust coefficients. The FUN3D results and experimental data points begin to diverge for $C_T > 2$, a trend likely contributed to by insufficient grid resolution in the jet interaction region. The axial locations for the flight-relevant cases follow an apparently linear trend with increasing C_T for $C_T > 4$. Once the highly under-expanded jet structure is established, increases in thrust coefficient increase the momentum of the jet flow in fixed increments, supporting this linear trend.

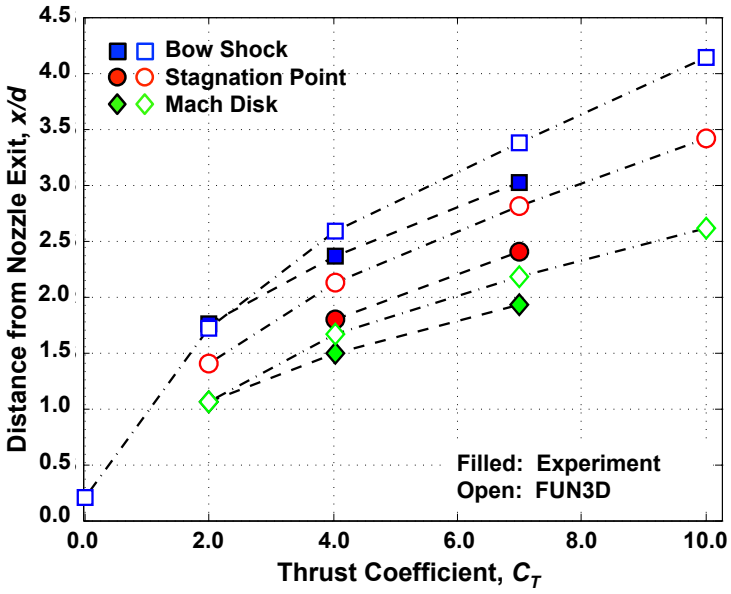

Figure 50: Non-dimensional axial location of flow features with increasing C_T.

The locations of the Mach disk agree more closely with the experiment than the locations of the stagnation point and bow shock. This is not unexpected, as small discrepancies in the formation of the jet structure are amplified in the stagnation region through changes in both the magnitude and dissipation of momentum, both

in this region and in the shear layer. The degree to which this alters the shape and location of the contact surface is dependent on the implemented approach.

The over-prediction of the bow shock, free stagnation point, and Mach disk locations agrees very well with the results given by Trumble et al. [75] for the C_T = 7.00 condition (the only case given). As discussed in Section 4.2.3.2, a number of assumptions were made for the test conditions and no information is available to assign error bars to the experimental values. While a freestream total pressure of 2.0 psi is given in the test report [13] and also used here, this condition is outside of the operational envelope for the original test facility [96], potentially contributing to this disagreement in flow feature locations.

Mach number contours for the central configuration cases are shown in Fig. 51 for each C_T. The solution for $C_T = 0.00$ shows the bow shock located near the body as expected. Flow separation occurs around the shoulder, creating a wake region aft of the vehicle. As C_T increases, the subsonic wake region expands further aft of the vehicle, indicating that the area of the effective freestream flow obstruction is increasing with C_T. The Mach disk is clearly visible at each "jet-on" condition in Fig. 51, and the increase in the area of the effective freestream flow obstruction can be attributed to the progressive increase in the area of the Mach disk with C_T. The triple point is visible at the location of the intersection between the Mach disk and the barrel shock and represents the intersection of the structures required to turn the jet flow. These flow features are marked on Mach number contours in Fig. 52, with streamlines illustrating the contact surface, stagnation region, and recirculation. The shear layer also exists in this region, as seen in the Mach number contours, as well as in the streamlines showing the flow path along the outer boundary of the barrel shock, where supersonic jet flow is mixing with parallel subsonic recirculation flow.

Streamlines also indicate the location of the contact surface and free stagnation point between the bow shock and Mach disk. After passing through the bow shock,

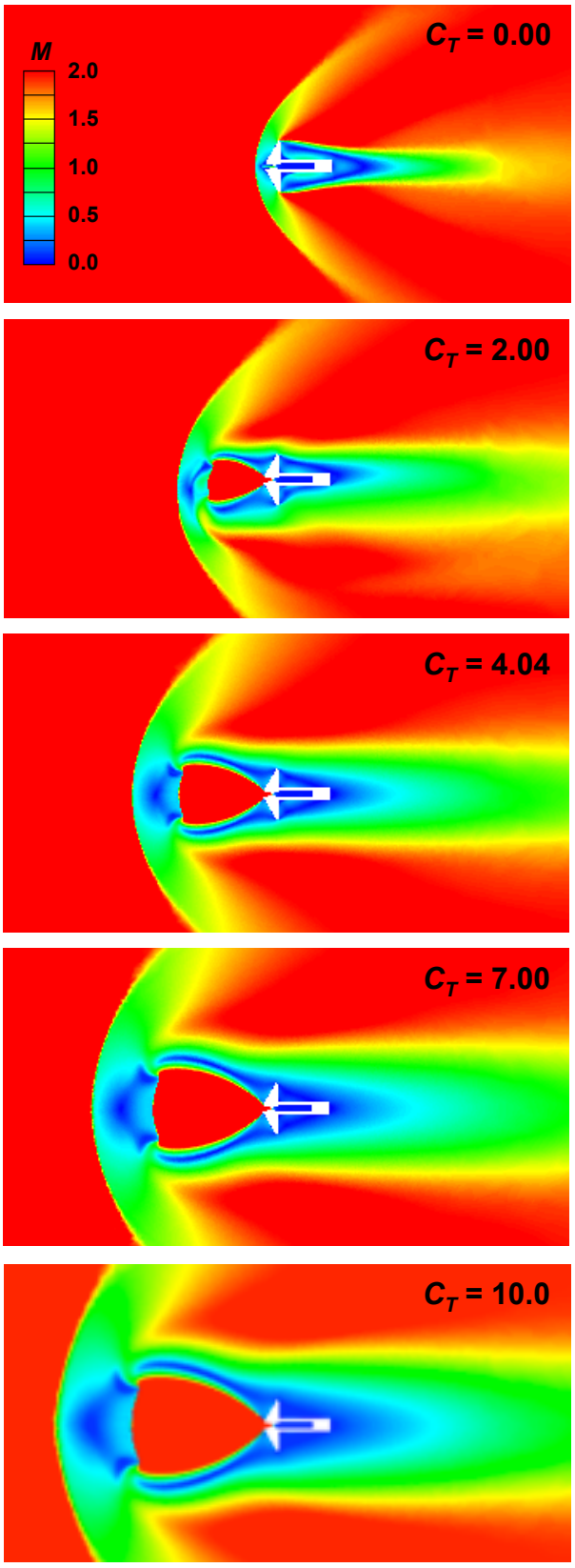

Figure 51: Mach number contours for the central configuration.

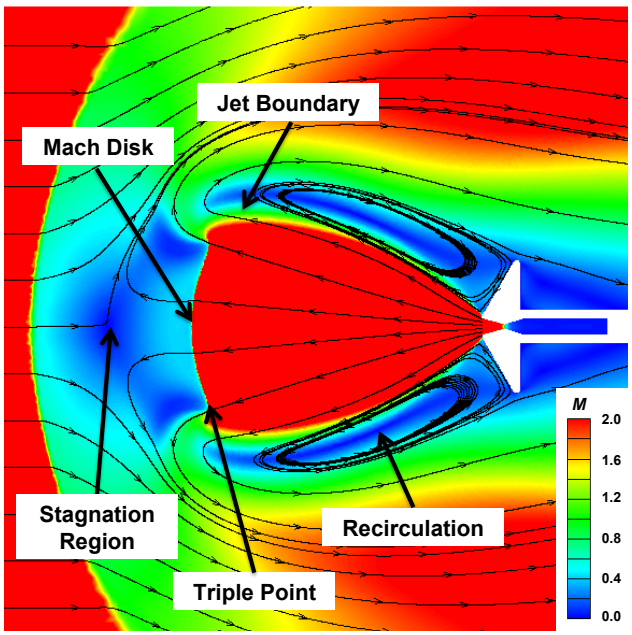

Figure 52: Mach number contours and streamlines illustrating the location of primary flow features ($C_T = 7.00$).

the freestream streamlines are turned to run parallel to the turning streamlines of the jet flow. This interface where the streamlines intersect is the contact surface, apparent in Fig. 52. The free stagnation point exists where the streamlines change the direction in which they pass around the contact surface and is located along the body axis for $\alpha = 0°$. The recirculation regions between the supersonic jet flow boundary and the freestream flow being swept aft of the body are also apparent from the streamlines in Fig. 52 for $C_T = 7.00$ conditions.

Figure 53 compares experimental C_p data with the pressure distributions obtained from FUN3D. A baseline $C_T = 0.0$ case (not included in Fig. 53) compares well with the experimental C_p distribution. The FUN3D C_p data are taken along three different radial lines from steady-state solutions. The differences in the $C_T = 2.0$ condition data reflect the asymmetry in the steady-state solution. The experimental results show a negligible change in pressure near the shoulder for all cases with the jets active, while the CFD solutions show a larger rise in surface pressure in this region. The pressure rise at the shoulder is not necessarily caused by re-attachment of the flow,

as re-attachment is not observed at every condition. While there is no information available on the uncertainty of the pressure measurements in the experimental data, particularly at the low pressures observed, the maintenance of the reduction in surface pressure towards the shoulder is consistent with similar test series [10].

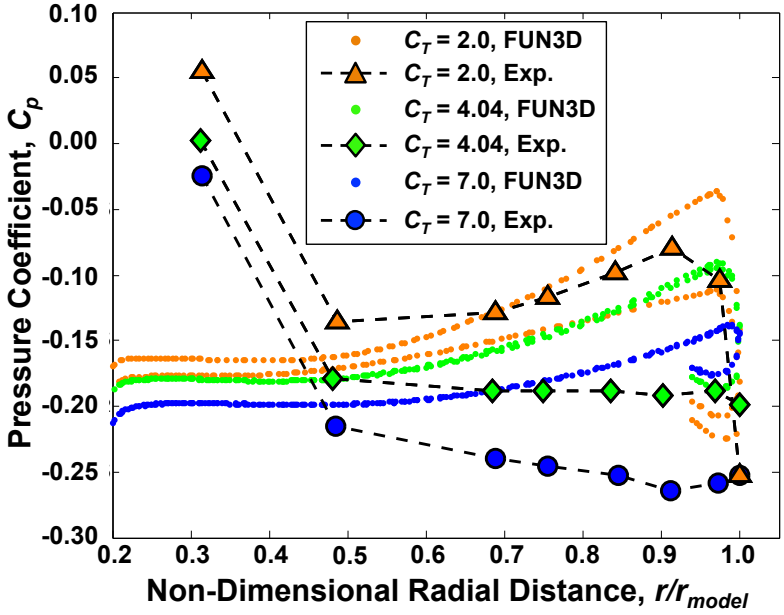

Figure 53: Comparison of radial C_p data with experimental data.

In Fig. 53, the pressure at the port on the forebody closest to the nozzle exit is not captured at all by the FUN3D solution. The expansion of the jet flow at the nozzle exit affects the pressure distribution in the region near the nozzle exit. The experimental data shows a significant rise in C_p near the nozzle exit, while the CFD solution shows a relatively constant C_p value across the forebody in this region for each C_T value. This appears to indicate that the CFD solution may not be capturing the proper expansion angle at the nozzle exit. No data are provided in the original experiment with regard to the jet structure near the nozzle exit to verify that this is the cause of the difference in surface pressure at this location. Modeling effects, such as grid resolution and the computational approach (inviscid, laminar, turbulent), can also change the jet angle.

Figure 54 compares experimental $C_{D,f}$ and $C_{A,f}$ values with the same force coefficients obtained from FUN3D. The corresponding coefficient values are given in Table 17. The dashed line represents the condition that the forebody axial force is composed entirely of thrust ($C_{A,f} = C_T$). Recall that each case is at zero angle of attack, $C_{A,f}$ is the sum of $C_{D,f}$ and C_T, and that negative force coefficients are possible as a result of forebody surface pressures below the freestream static pressure. Note that the original experimental conditions are only approximate, due to the lack of complete information in the test report.

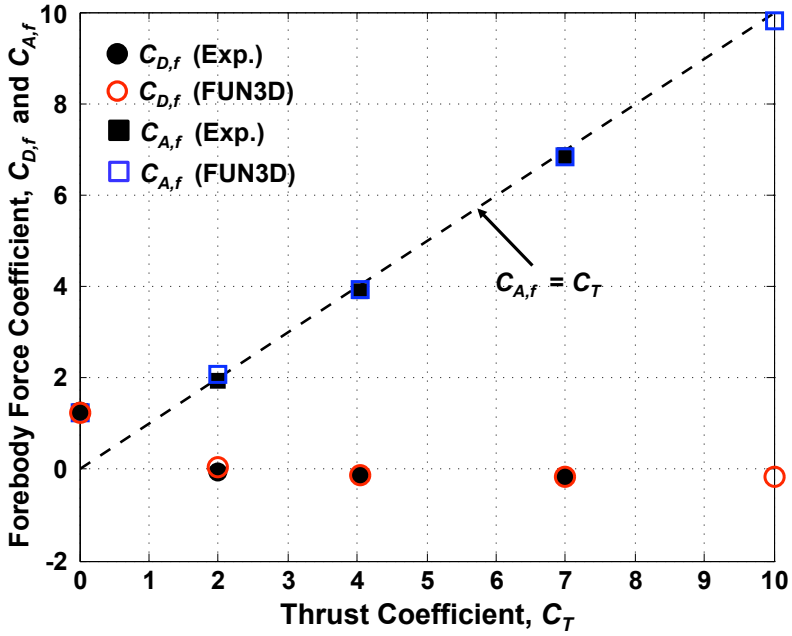

Figure 54: Comparison of integrated forebody drag and axial force coefficients with experimental data.

Even with the disagreement in pressure coefficient, particularly near the shoulder (see Fig. 53), the integrated forebody drag and axial force coefficients agree well with those reported in the original experiment. The expected reduction in forebody drag coefficient as thrust coefficient is increased is apparent in Fig. 54. The close proximity of the $C_{A,f}$ data to the dashed line, indicates a dominant thrust contribution to the forebody axial force as compared to static aerodynamic drag, also as expected.

Table 17: Comparison of integrated forebody drag and axial force coefficients.

	CFD		Exp.		% Difference	
C_T	$C_{D,f}$	$C_{A,f}$	$C_{D,f}$	$C_{A,f}$	$C_{D,f}$	$C_{A,f}$
0.00	1.251	1.251	1.254	1.254	0.24	0.24
2.00	0.059	2.059	-0.047	1.953	22.6	4.98
4.04	-0.113	3.927	-0.142	3.898	22.2	0.74
7.00	-0.157	6.843	-0.148	6.852	5.98	0.13
7.00	-0.157	6.843	-0.167	6.833	6.05	0.14
10.0	-0.176	9.824	–	–	–	

It is interesting to note that prior work by the author [11] using the same computational approach, but on a coarser grid, found much better agreement of primary flow feature locations with experimental data by effectively increasing the jet spreading in the radial direction through poor grid resolution. The agreement of the surface pressure distributions is nearly equivalent, with both sets of FUN3D solutions exhibiting a pressure rise towards the shoulder. Grid refinement studies will be required to separate modeling effects from those driven by the computational grid. The turbulent flow solutions all converge to a steady-state condition with the jet flow geometry agreeing reasonably well with the measured locations in the experimental data and qualitatively well with the theoretical flow physics.

4.3.2.1 60-deg Sphere-cone Aeroshell with Three Peripheral Nozzles

For a peripheral configuration, the interactions from multiple jet flows results in a different flowfield structure than that observed for a central configuration, while the structures for the individual jets retain similar characteristics. The jet flows develop a shear layer along the jet boundary, and a Mach disk and barrel shock form to terminate the supersonic jet flow for highly under-expanded conditions. The nozzle geometry for the peripheral configuration is such that the total C_T for the three nozzles in the peripheral configuration is equal to the C_T for the single nozzle in the central configuration. As compared to the central configuration, the peripheral configuration

requires a higher total C_T to be at highly under-expanded conditions as a result of the lower total pressures required for the individual jet flows. This delays the formation of the Mach disk - intersecting shock structure to higher thrust coefficients. The subsonic region inboard of the jet flows in the peripheral configuration does not contain recirculation and retains higher pressures than the central configuration at the same conditions.

The preliminary solutions for the peripheral configuration are shown in Fig. 55 for the thrust coefficients listed in Table 15. Mach number contours are shown, scaled to Mach 3 to highlight different flow features. The Mach number contours are for two transparent, planar slices to show the three-dimensional flowfield structure. Each slice passes through the center of a nozzle, making two jet plumes visible in this orientation. C_p contours for the forebody are also shown for each C_T in Fig. 55. Analogous to Fig. 52, Fig. 56 and Fig. 57 highlight the Mach disk, triple point, and jet boundary for the peripheral configuration using Mach number contours for $C_T =$ 7.00 conditions. The streamlines in Fig. 57 illustrate qualitative agreement with the expected flowfield for a peripheral configuration. The flow inboard of the nozzles is not contained within a recirculation region, but instead the flow is turned to follow the jet flow and eventually moves outboard and downstream of the body. The contact surface that forms between the decelerated freestream flow and the subsonic jet flow extends outboard beyond the true body diameter. The larger effective obstruction to the freestream results in a larger wake region aft of the body than has been observed for the central configuration.

For the $C_T = 0.00$ case, the flowfield structure agrees well with the similar solution for the central configuration. The difference in geometry between the two configurations is the spherical nose cap on the peripheral configuration, which results in a slightly different pressure distribution near the body axis as compared to the central configuration, which has the nozzle exit plane open to the freestream. Each case with

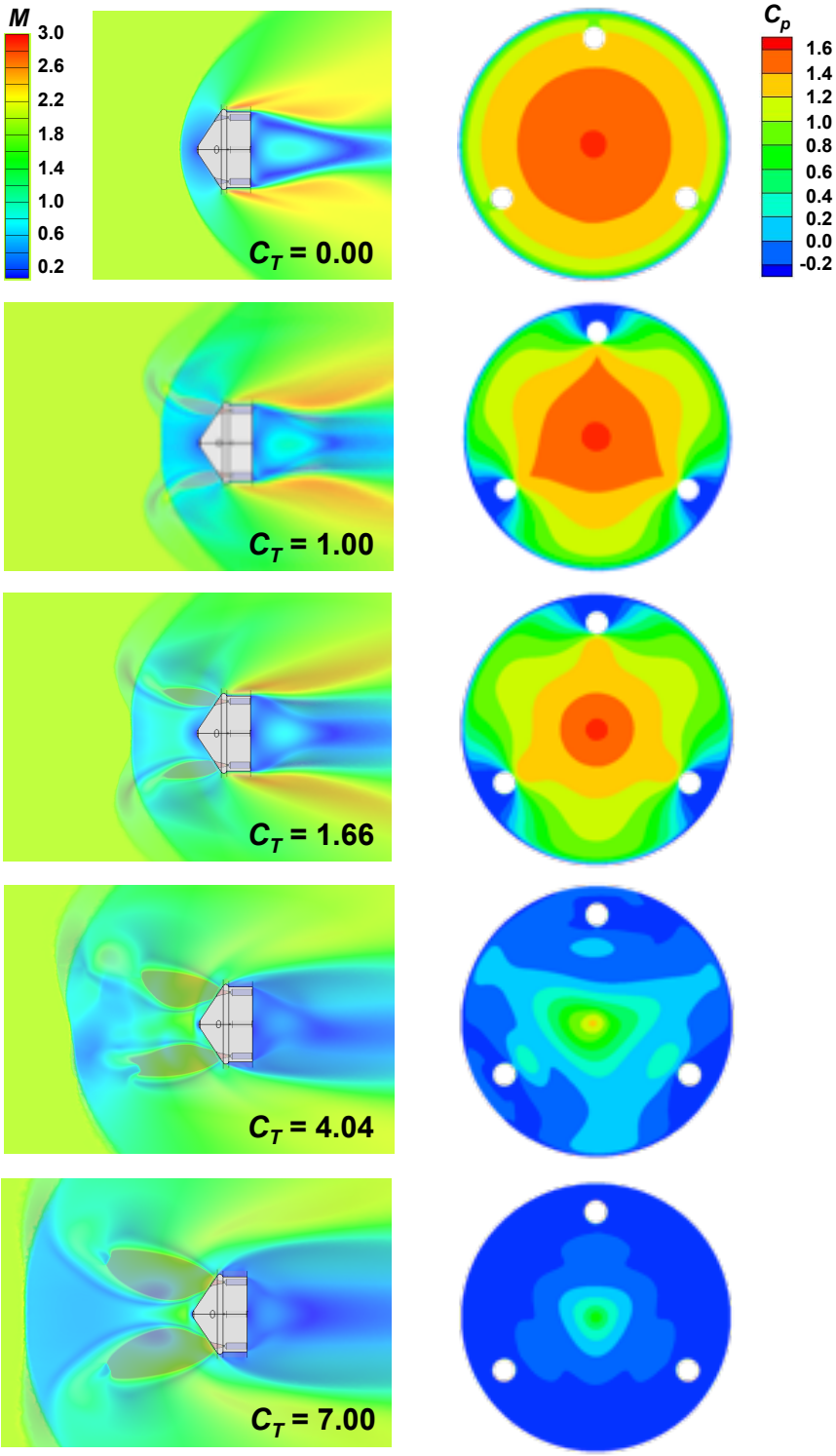

Figure 55: Mach number contours and C_p contours for the peripheral configuration with increasing C_T [11].

jet flow exhibits a different jet structure and, subsequently, a different contact surface is formed. The $C_T = 1.66$ case presents a weakly under-expanded jet and exhibits steady behavior in the solution residual history. As shown in the Mach number contours in Fig. 55, the jet structures are symmetric, resulting in a symmetric pressure distribution. The pressures inboard of the nozzles remain near those seen for the $C_T = 0.00$ case, indicating that surface pressure, and accordingly, the static aerodynamic drag is being preserved inboard of the nozzles at $C_T = 1.66$ conditions.

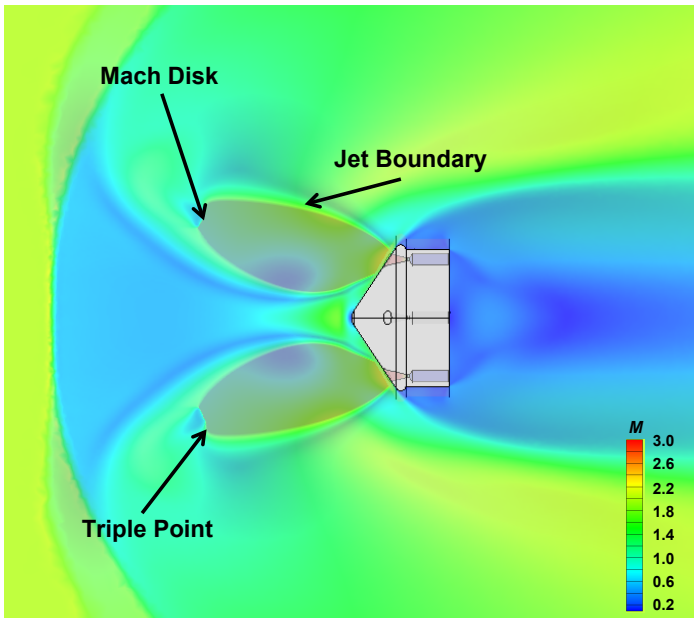

Figure 56: Mach number contours and locations of primary flow features ($C_T = 7.00$) [11].

However, as shown in Fig. 58, the pressure distribution from the CFD solution is not in agreement with the experimental C_p distribution at these conditions ($C_T = 1.66$), a contrast to the agreement seen for $C_T = 1.00$. Along circles of constant radius, the pressure coefficient at radii near that of the nozzles ($0.8\ r_{model}$) shows a noticeable variation in the experimental data, depending on the proximity to the nozzle exits. The general shape for these radii is in agreement, but the CFD solution consistently shows a higher pressure than the experimental data at all angular locations. At radii inboard of the nozzles, the pressure should be more constant with variation in

angular location; this is consistent between the CFD solution and the experimental data. Again, the actual value of C_p in this region is higher for the CFD solution.

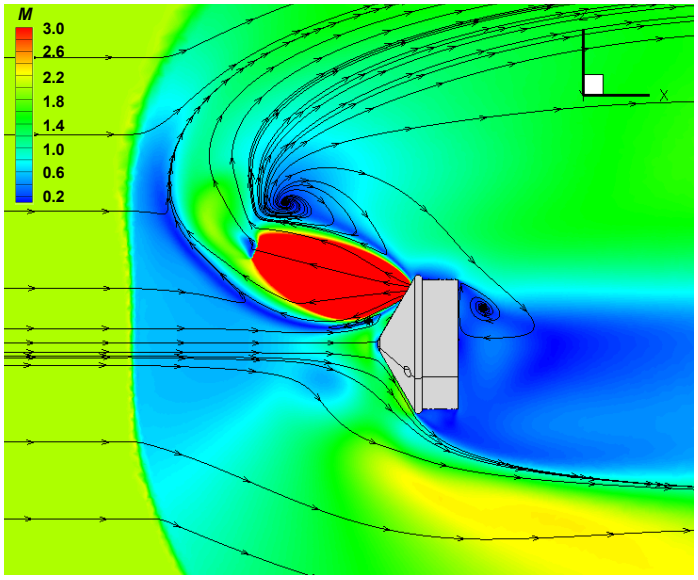

Figure 57: Mach number contours and streamlines ($C_T = 7.00$) [11].

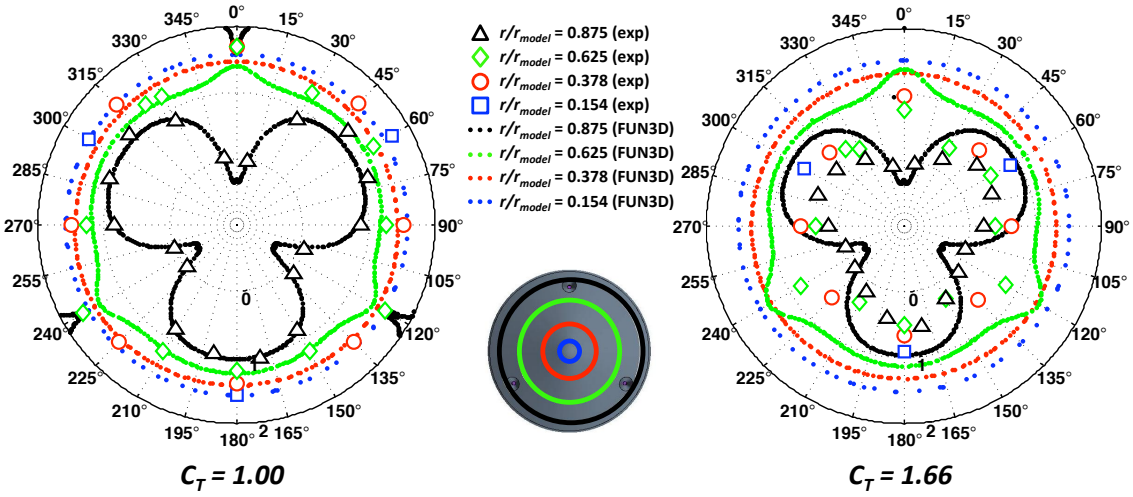

Figure 58: Circumferential C_p distributions for the peripheral configuration [11].

Since preservation of the forebody surface pressure decreases with increasing C_T, and the jet expansion from the nozzle increases with increasing C_T, it is possible that the CFD solution is under-predicting the jet expansion in the inboard vicinity of the

nozzle exit and not capturing the interaction between the individual jet flows. If the CFD solution was to predict a larger jet expansion inboard for this C_T condition, then the pressure values along the forebody would be reduced and agree more closely with the experimental results. As these are exploratory solutions, no formal grid resolution studies or turbulence modeling trades have been completed. It is acknowledged that grid resolution and computational approach can significantly affect the resulting flow structures for SRP flowfields. The impact of grid resolution, specifically, is addressed in Chapter 5.

The conditions corresponding to $C_T = 4.04$ yield an asymmetric flowfield structure as the degree of under-expansion of the jet flow increases as compared to the flowfield structures for lower thrust coefficients. In the Mach number contours shown in Fig. 55, a secondary plume cell is visible after the jet flow passes through the terminal shock structure. The C_p distribution is also asymmetric, a result of the pressure around each nozzle varying independently. Both the residual history and asymmetries in the flowfield and C_p distribution suggest the flowfield behavior to be unsteady at $C_T = 4.04$ conditions. As discussed previously, this reduction in pressure can be attributed to the jet structure shielding the body from the freestream flow through the establishment of a contact surface between the two flows. Even with the unsteadiness in the flow solution, the pressure inboard of the nozzles is not preserved to the same degree as seen at the lower C_T conditions. As the jet structures become larger, contributing to the formation of a larger contact surface, less pressure is preserved on the forebody as a result of this shielding.

Figure 59 shows a comparison of radial C_p trends for the $C_T = 7.00$ case. At these conditions, the solution is once again exhibiting steady behavior similar to that observed for the $C_T = 1.66$ case. The data at the $\phi = 0°$ position is taken along a line that passes directly through a nozzle exit, and the points between $r/r_m = 0.7$ and 0.9 show the increase in C_p across the nozzle exit.

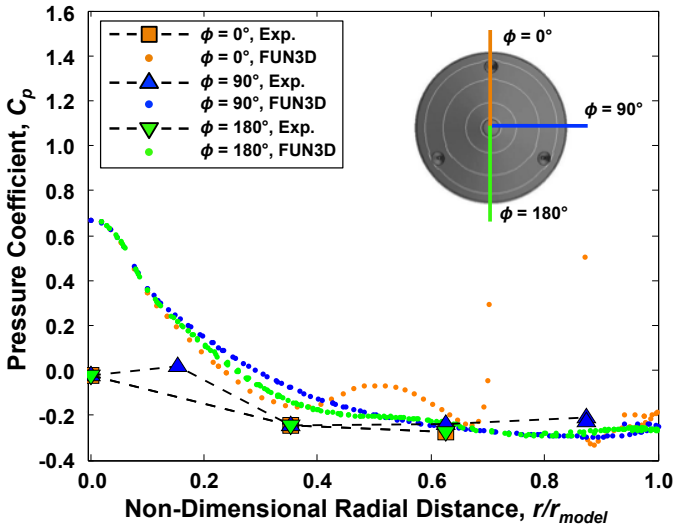

Figure 59: Radial C_p distribution for the peripheral configuration ($C_T = 7.00$) [11].

For $C_T = 7.00$ conditions, each jet more clearly resembles the expected flow structure, shown previously in Fig. 11. Figure 55 shows a significant improvement over the $C_T = 4.04$ case in the symmetry between the two visible jet structures. The jet boundaries have expanded well inboard of the nozzle exits at these conditions, further decreasing the forebody pressure near the body axis. However, the degree of pressure preservation is still greater than that given in the experimental data at the nose. This is also similar to the $C_T = 1.66$ case, where the CFD solution is likely not capturing the jet expansion and interaction between the individual jet flows and, as a result, preserving higher pressures along the forebody than those observed in the original experiment.

4.4 Summary

Supersonic retropropulsion flowfields are the result of a complex interaction between typically highly under-expanded jets and the shock layer of a blunt body. The jet flows are characterized by a constant-pressure jet boundary, thick shear layers along the jet boundary away from the nozzle exit, and a Mach disk - reflected shock - barrel shock jet structure. This interaction forms a contact surface within the shock

layer. The shape of this contact surface is the effective flow obstruction seen by the freestream, and the resulting change in surface pressure significantly alters the static aerodynamic characteristics of the body as compared to the same body with no SRP.

Accurate and consistent simulation of SRP flowfields is of significant interest to the NASA technology development community. A lack of experimental data at relevant conditions and the incompleteness of existing data sets challenge efforts to validate existing computational tools and approaches. This chapter discussed the potential effectiveness of inviscid and viscous computational analysis approaches in consistently and accurately capturing the relevant flow physics. Preliminary computational results for three blunt body SRP configurations were compared with experimental data for the locations of prominent flow features and surface pressure distributions. This chapter is intended to be an initial discussion of the challenges facing the computational simulation of supersonic retropropulsion flowfields and also a preliminary exercise of FUN3D for turbulent CFD analysis. The next chapter extends the application of FUN3D to the validation of this computational approach in simulating SRP flowfields based on comparison with data from a recent NASA wind tunnel test.

The results obtained from the turbulent analysis employed here agree reasonably well with experimental data for the axial locations of the bow shock, free stagnation point, and Mach disk for a central retropropulsion configuration with a single nozzle. A small, but consistent over-prediction of the standoff distances is seen, and this result is consistent with similar work in the literature for these cases [75]. The surface pressure distributions agree less favorably, showing a pressure rise towards the shoulder that was not observed in the original experiment. The flowfield structures for a peripheral retropropulsion configuration agree qualitatively with the expected structures, but proper inboard jet flow expansion and interactions between individual jet flows are likely not being captured; accordingly, pressure is preserved inboard of

the nozzles to higher thrust coefficients than was observed experimentally. Time-accurate simulation, grid convergence, and the subsequent sensitivity to time step size are addressed in the following chapter.

CHAPTER V

SUPERSONIC RETROPROPULSION WIND TUNNEL TESTING AND COMPUTATIONAL ANALYSIS

The validation of computational tools in simulating supersonic retropropulsion flowfields requires an experimental data set containing fully defined information for the geometry and configuration of the model, test conditions, and uncertainties associated with the measured data. Reports from prior SRP experiments are missing much of this information, limiting the usefulness of such data sets in validation exercises. Understanding the relationship between the performance of high fidelity computational approaches in predicting the aerodynamic - propulsive interactions inherent to SRP and the computational cost associated with achieving such performance is critical to defining the computational requirements for progressive phases of development and design.

The work presented in this chapter uses a Reynolds-averaged Navier-Stokes approach to predict the flowfield structure, surface pressure distributions, and integrated aerodynamic force coefficients for four configurations recently tested in the NASA Langley Research Center Unitary Plan Wind Tunnel. These configurations have zero, one, three, and four nozzles integrated with the model forebody. This wind tunnel test series was explicitly designed to provide a data set suitable for the validation of computational fluid dynamics tools in simulating supersonic retropropulsion flowfields. Comparisons are made with experimental data for static pressure distributions on the forebody and aftbody. Computational schlieren images illustrating the resulting flowfields have also been generated. Where available, high-speed schlieren images have been included for qualitative comparison. This work is built upon the

results presented in the previous chapter and seeks to evaluate the performance of a high-fidelity computational approach in predicting flowfield structure, surface pressure distributions, and integrated aerodynamic quantities for SRP. It is also intended to compliment recent efforts within NASA's Exploration Technology Development and Demonstration Program, EDL Project to validate existing CFD tools for use in developing an aerodynamic modeling capability for supersonic retropropulsion.

5.1 Wind Tunnel Test Summary

The experimental data used in this chapter are from a supersonic retropropulsion test completed under NASA's ETDD Program in the NASA LaRC 4 ft. $\times$ 4 ft. UPWT in July 2010 [15]. This test was explicitly designed to provide experimental data for concurrent CFD validation efforts and uncertainty analyses. Additionally, it was the first test in nearly 40 years targeting flight-relevant conditions and applications of SRP and represents a significant step forward in addressing the limitations of existing historical data sets [10]. Only a brief overview of the model, instrumentation, test data, and test conditions is given here; publications dedicated to the design of the test [15, 67] and post-test data analysis [14, 16, 51, 59] are available in the literature.

5.1.1 Model Dimensions and Configurations

The 5 inch-diameter model, shown in Fig. 60, was a 70-deg sphere-cone forebody with a 10 inch-long cylindrical aft housing. Four nozzle configurations were tested with this model: no nozzles, one central nozzle, three nozzles spaced 120° apart at the forebody half-radius, and four nozzles from the combination of the one and three nozzle configurations. Figure 60 also shows the three nozzle configuration of the model installed in the wind tunnel test section. The nozzles were conical, with an exit diameter, d_e, of 0.5 inch and an expansion ratio, A_e/A^*, of 4 ($M_{e,ideal} = 2.94$). The nozzles were axially-aligned; the three nozzles at the forebody half-radius were scarfed to have the exit plane of the nozzle flush with the model forebody. The

composition of both the freestream and the nozzle flow was air ($\gamma_\infty = \gamma_j = 1.4$).

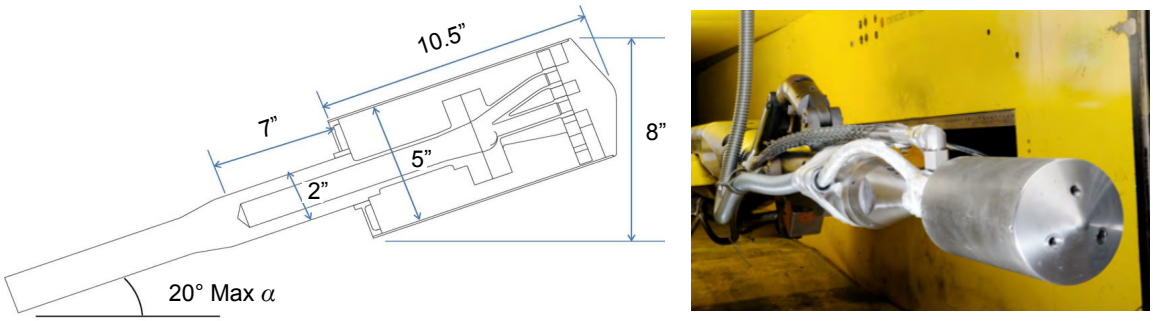

Figure 60: Model dimensions and a view of the model installed in the wind tunnel test section. [15].

5.1.2 Description of Available Data

Test conditions spanned three freestream Mach numbers (M_∞ = 2.4, 3.5, 4.6) and thrust coefficients up to 3.0 for each configuration. Thrust coefficients up to 6.0 were explored where possible, depending on the nozzle configuration and observed degree of interference with the tunnel walls. (Thrust coefficients up to 10.0 were explored in August 2011 in the NASA ARC 9 ft. $\times$ 7 ft. UPWT; however, this test was completed too recently for comparison cases and experimental data to be included here.) The model was rolled through 180° (in 60° increments) and pitched through an angle of attack sweep from -8° to +20°, also depending on the nozzle configuration and degree of interference with the tunnel walls.

The run matrix was defined from an uncertainty methodology based on sampling principles from Design of Experiments (DOE). The implementation of this methodology stemmed from earlier work directed toward the improvement of CFD model validation using experimental data by Oberkampf et al. [97, 98]. The DOE method is based entirely on comparisons of multiple measurements of the same quantity. The traditional method for quantifying error in wind tunnel test measurements is based on error propagation (see [99]). The DOE method has been found to yield similar results to the traditional error propagation method for one component of uncertainty;

however, the traditional method has been found to typically under-predict total uncertainty [97]. The SRP test described in this section was designed to acquire information allowing for the assessment of three components of the total uncertainty (repeatability, flowfield non-uniformity, and model geometry/instrumentation) [14, 59].

The model was instrumented with static pressure taps on the forebody and aft housing, Kulite pressure transducers (40 kHz) on the forebody for both time-averaged and unsteady pressure measurements, and internal pressure and temperature sensors. The static pressure measurements were taken at a 10 Hz sampling rate over a 2.5 sec test point interval. Figure 61 shows the pressure port layout on the model. The ports that have been filled in with red are the port locations to be compared with CFD results in Section 5.4. There were 167 total surface pressure ports: 104 ports on the forebody, 49 ports on the aft housing, and 14 additional ports between three of the four nozzle plugs.

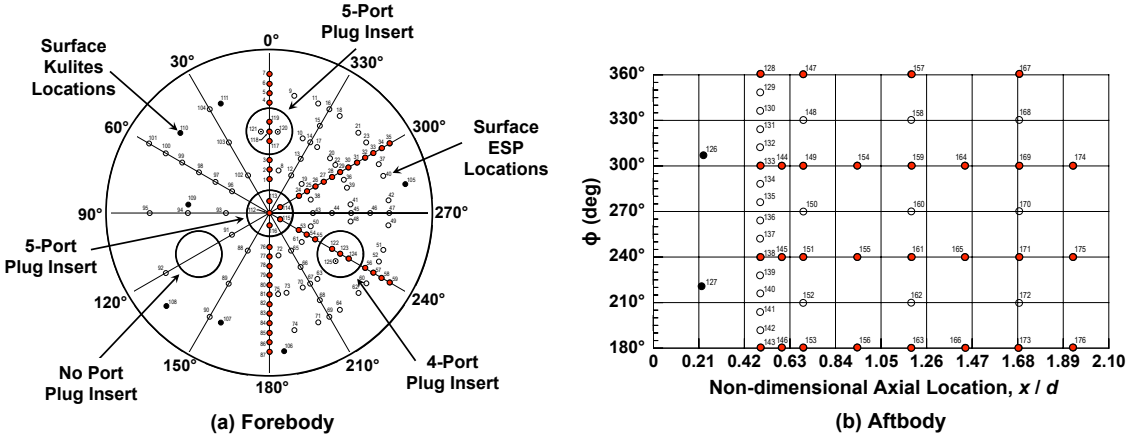

Figure 61: Pressure port locations and nozzle configurations. Ports of interest are filled in red. Kulite locations are filled in black.

As reported by Berry et al. [14, 51], static pressure data was collected using two 64-channel ($0 - 5 \pm 0.005$ psid, 118 forebody ports and 4 aftbody ports) and one 48-channel ($0 - 2.5 \pm 0.003$ psid, 45 aftbody ports) electronically scanned pressure (ESP) transducer modules. The three modules were pulled to vacuum to provide absolute pressure measurements. Three separate reference pressures were supplied

from pressure gages ($0 - 38 \pm 0.004$ psia) to transducers on the ESP modules and monitored for drift. In-situ ESP calibrations were performed using the system pressure calibration unit ($0 - 15 \pm 0.003$) when drift exceeded 0.0175 psi. The seven Kulite pressure transducers on the model were rated for $0 - 5 \pm 0.013$ psia [51].

Internal pressures and temperatures were measured using four Kulite pressure transducers ($0 - 2000 \pm 2$ psia) along the high-pressure airflow path and a platinum resistance temperature detector probe ($132 - 910 \pm 1$ °R) in the plenum, respectively. Inside the two instrumented nozzles, additional temperature measurements were taken using a Type K thermocouple opposite the plenum pressure port [14]. Additional instrumentation included:

- A Q-Flex accelerometer (calibration accuracy $\pm 0.01°$) mounted inside the model to directly measure model pitch angle during the test
- Eight Type J thermocouples ($492 - 1842 \pm 4$ °R) to monitor temperatures inside the model for the ESP modules and accelerometer
- A subsonic venturi flow meter installed in the high-pressure air line outside of the test section to measure nozzle mass flow rate with an uncertainty estimate of ± 0.07 lb_m/s

Quantification of the total uncertainty in the static pressure measurements from the ESP modules was completed using the zero nozzle, baseline configuration [59]. The analysis found the uncertainty contributions due to flowfield non-uniformity to be 70% of the total variance, with additional contributions due to repeatability at 19% and model geometry/instrumentation at 11%. The σ_{total} values for pressure coefficient were found to be 0.0040, 0.0059, and 0.0074 for $M_\infty = 2.4$, 3.5, and 4.6, respectively. These σ_{total} values define the total uncertainties for the baseline, zero nozzle configuration for the given freestream Mach numbers. It is expected that the total uncertainty would be higher for the cases with nozzle flow; however, no analysis

has been done to explore this. References [14, 59] provide additional detail on the instrumentation used during the test and the uncertainty analysis, respectively.

For qualitative data, high-speed schlieren video was taken at frame rates up to 10,000 frames per second during the test. Still images taken from the high-speed schlieren video are available for a subset of the "jet-on" cases described in Section 5.1.3. These images are given in Section 5.4 for qualitative comparison with the computational results.

5.1.3 Cases for Computational Analysis

Table 18 gives a summary of the cases explored in this chapter.

Table 18: Conditions summary for CFD comparison cases.

Zero nozzle configuration – Run 283

Freestream conditions					Nozzle conditions			
M_∞	$p_{0,\infty}$ (psi)	p_∞ (psi)	$T_{0,\infty}$ (K)	T_∞ (K)	$p_{0,j}$ (psi)	$T_{0,j}$ (K)	$\dot{m}$ (lb_m/s)	$C_{T,total}$
4.600	25.40	0.0775	338.9	64.77	–	–	–	–

One nozzle configuration – Run 165

Freestream conditions					Nozzle conditions			
M_∞	$p_{0,\infty}$ (psi)	p_∞ (psi)	$T_{0,\infty}$ (K)	T_∞ (K)	$p_{0,j}$ (psi)	$T_{0,j}$ (K)	$\dot{m}$ (lb_m/s)	$C_{T,total}$
4.600	25.40	0.0775	338.7	64.73	598.9	345.6	0.620	1.968

Three nozzle configuration – Run 247

Freestream conditions					Nozzle conditions (per nozzle)			
M_∞	$p_{0,\infty}$ (psi)	p_∞ (psi)	$T_{0,\infty}$ (K)	T_∞ (K)	$p_{0,j}$ (psi)	$T_{0,j}$ (K)	$\dot{m}$ (lb_m/s)	$C_{T,total}$
4.600	25.40	0.0775	339.1	64.81	201.2	346.4	0.272	1.919

Four nozzle configuration – Run 307

Freestream conditions					Nozzle conditions (per nozzle)			
M_∞	$p_{0,\infty}$ (psi)	p_∞ (psi)	$T_{0,\infty}$ (K)	T_∞ (K)	$p_{0,j}$ (psi)	$T_{0,j}$ (K)	$\dot{m}$ (lb_m/s)	$C_{T,total}$
4.600	25.40	0.0775	338.7	64.74	151.9	343.5	0.273	1.923

A baseline zero nozzle case and a "jet-on" case for each nozzle configuration were considered, at angles of attack of 0° and 8°. Similar cases at an angle of attack of 12° have been run as a part of the NASA ETDD Program [16]. The conditions for the cases in this chapter were selected based on the apparent steadiness of the flowfield and lack of wall interaction observed in the high-speed schlieren video. The

SRP flowfield was most steady (i.e. exhibited primarily local unsteadiness) at higher thrust coefficients and smaller angles of attack, and the wall interactions were less significant at higher freestream Mach numbers. These observations were consistent across all three SRP configurations. With these considerations, the flow conditions selected correspond to $M_\infty = 4.6$ (Re_∞/ft $= 1.5 \times 10^6$) and $C_T \approx 2.0$.

5.2 Computational Approach and Modeling

Verification, or the rigorous process of checking that the mathematical equations are being solved correctly, has been completed previously in the development of the FUN3D flow solver [100]. The work in this chapter is, instead, focused on validation by comparing computational results with experimental data. The same Reynolds-averaged Navier-Stokes approach described in Chapter 4 is applied to all cases here to predict the flowfield structure, surface pressure distributions, and integrated aerodynamic force coefficients for the four configurations discussed in Section 5.1. Force and moment coefficients are determined through integration of surface pressures over all surfaces of the model, including plenum wall faces, unless otherwise specified. All pitching moment coefficients are referenced from the nose of the model. Comparisons have been made with experimental data for static pressure on both the forebody and the aftbody of the model. A description of FUN3D and the grid generation process can be found in Section 4.2.2. The final grid spacing specifications were based on a grid resolution study, described in Section 5.3.1, but were limited by available computational resources due the computationally intensive nature of unsteady SRP problems. All of the "jet-on" cases in this chapter were run using a time-accurate approach and were generated using version 11.4 of the FUN3D code.

Iterative convergence was determined previously (see Chapter 4) through a three order of magnitude drop in the residuals of conservative quantities and maintenance of this drop through several hundred additional iterations. The results in this chapter

similarly determined iterative convergence through tracking residuals with iteration (mass, momentum, energy, turbulence) and terminating after the residuals reached and maintained a plateau or periodic oscillations for several hundred iterations.

As mentioned, a spatial convergence, or grid refinement, study was also completed. FUN3D does not currently include adjoint-based mesh refinement capability for use with Menter's SST turbulence model, and no direct quantities reflecting spatial discretization errors are available. As such, an alternative approach that uses a sequence of grids and shows the sensitivity of important dependent variables as the grid resolution becomes increasingly more fine was applied [101]. The quantities tracked were the integrated drag and integrated lift of the forebody. Additional discussion and results of this study are given in Section 5.3.1.

Unsteady solutions were computed using the BDF2OPT scheme, theoretically second-order accurate [102]. To assess temporal accuracy, a temporal error controller [90, 101] was employed to run subiterations until the subiteration residual was one full order of magnitude lower than the estimated temporal error for the x-momentum and turbulent kinetic energy residuals. The maximum number of subiterations per time step was set to 40; this limit was used in cases where the turbulent kinetic energy residual was not decreasing quickly enough. A non-dimensional time step of 0.0004 (dimensionally, 2.5×10^{-6} sec) was specified for the one nozzle cases, yielding approximately 200 time steps per cycle in the force history. The time step was reduced by half to 1.25×10^{-6} sec for the three and four nozzle configurations. The $\alpha = 0^{\circ}$ and $\alpha = 8^{\circ}$ cases for the three nozzle configuration converged to steady-state for both this time step and a time step of 6.25×10^{-7} sec. The axial force oscillation frequency was determined from this information for the cases that did not converge to steady-state.

Kleb et al. [16] examined the aspects of physical modeling related to tunnel wall interference and the complicated sting and high pressure feedline structure aft of the

model (see Fig. 60). Comparing the effect of modeling the tunnel walls as inviscid or neglecting the walls altogether, they found the effect on the pressure distribution to be significant for cases at an angle of attack of 12° and negligible for cases at zero angle of attack. The tunnel walls in this investigation were modeled as inviscid, as all cases here were restricted to $\alpha = 0°$ and $\alpha = 8°$.

As visible in Fig. 60, the geometry of the support hardware aft of the model is complex and protrudes into large areas of the subsonic wake flow. Kleb et al. [16] explored the impact of modeling the sting hardware at multiple angles of attack for both the one nozzle and three nozzle configurations. They found sting effects to be limited to the base and the three furthest aft pressure ports on the model and concluded that, for pressure comparisons over the rest of the body, modeling the complex sting hardware was not necessary. Accordingly, the outer mold line of the model used here consists of the forebody, aftbody, and aft face.

5.3 Spatial and Temporal Resolution

5.3.1 Grid Resolution Study and Final Grids

A grid refinement study was completed using the one nozzle case at $\alpha = 0°$ (and associated Run 165 conditions) to understand the sensitivity of solutions to grid spacing and to assess the spatial accuracy of the numerical scheme applied (FUN3D is spatially second-order accurate). This study was also used to establish grid generation guidelines for the other three configurations. A baseline grid was generated with a medium-fine grid density, and three coarser grids were then generated from this baseline grid. While the unstructured grid generation process used cannot be scaled linearly, the background grid spacing and surface grid spacing were scaled to approximate grid densities of 75%, 50%, and 25% (as compared to the grid density of the baseline grid). The approximate spacings for the baseline grid are given in Table 19, non-dimensionalized by model diameter. Each grid has additional volume and line

sources specified to increase grid resolution in the jet interaction region, at the nozzle exit, nozzle throat, converging section of the nozzle, model shoulder, and aft end of the model.

Table 19: Approximate baseline grid spacing.

	Far field	Interaction region	Nozzle exit	Shoulder
Grid spacing (in model diameters)	0.32	0.0055 to 0.0063	0.0031	0.0047

Equation 13 gives an assumed form of the relationship between the exact solution and the approximate numerical solution, where A is a constant, p corresponds to the order of accuracy, and h is the mesh spacing [103]. For an unstructured mesh, a representative mesh spacing, h, is approximated by the cube root of the total number of nodes, $N^{-1/3}$. Equation 14 gives the result of taking the logarithm of both sides of Eq. 13. The order of accuracy can be evaluated graphically, where on a log-log plot, the slope reflects the order of accuracy. If $\log(N^{-1/3})$ vs. $\log E(h)$ is plotted, the slope corresponds to the spatial order of accuracy. A slope of one corresponds to first-order spatial accuracy, and so forth.

$$\begin{aligned} f_{exact} &= f(h) + Ah^p + \text{higher order terms} \\ E(h) &= f_{exact} - f(h) \approx A(N^{-1/3})^p \end{aligned} \tag{13}$$

$$\log E(h) \approx \log A + p \log(N^{-1/3}) \tag{14}$$

Following the recommendations of Kleb et al. [16], two error quantities were tracked in this study: $C_{L,f}$ and a derived error quantity based on $C_{D,f}$ for the finest grid. Run 165 is a single nozzle case at zero angle of attack; accordingly, $C_{L,f}$ should be zero. The second error quantity was computed as the difference between $C_{D,f}$ of the finest grid (Grid A, 55.2M nodes) and $C_{D,f}$ of the current grid. Table 20 summarizes the grid characteristics and error quantities for each case. Both error

quantities are plotted against a representative mesh spacing based on the number of nodes, $N^{-1/3}$, in Fig. 62. The axial force oscillation frequency was observed to increase with increasing grid resolution, though it did not demonstrate convergence through the four grids considered. The high-frequency pressure transducers reported frequencies between 1.7 and 2.3 kHz for this configuration at $\alpha = 0°$ and $C_T = 2$ [14]. All NASA ETDD Program CFD solutions for this case found the dominant oscillation frequency to be within this range [14, 16, 68].

Table 20: Summary of grid refinement study.

	Approximate grid density (as % of baseline grid density)	No. of surface nodes	Total no. of grid nodes	Oscillation frequency (kHz)	$C_{L,f}$	$C_{D,f(finest)}$ - $C_{D,f}$
Grid A	100%	2.839M	55.21M	2.036	6.46×10^{-4}	–
Grid B	75%	2.338M	29.15M	1.858	3.08×10^{-4}	0.0012
Grid C	50%	1.791M	17.19M	1.761	1.18×10^{-4}	0.0011
Grid D	25%	1.140M	10.90M	1.673	2.67×10^{-4}	0.0008

FUN3D is spatially second-order accurate for smooth flows, and in Fig. 62, the dashed line indicates a unity slope for second-order accuracy. Figure 62(a) shows the lift error to be noisy but tracking reasonably well with the second-order trend line. Computational resources limited the number of cases able to be run, and with the noisy behavior of the error quantities, results for the drag-based error quantity (Fig. 62(b)) were inconclusive. The increased resolution of additional flow features and sources of unsteadiness with increasing grid resolution also likely contributed to the noisy behaviors observed. Kleb et al. [16] were able to run this same case using FUN3D for a family of 7 grids and observed noisy behavior in the same error quantities. Their results are given in Fig. 63 for comparison to the results of this study (Fig. 62).

Supersonic retropropulsion flowfields cannot be characterized as smooth flows as there are discontinuities within the flowfield, namely shock waves. For upwind numerical schemes, such as the second-order method used here, use of a flux limiter is

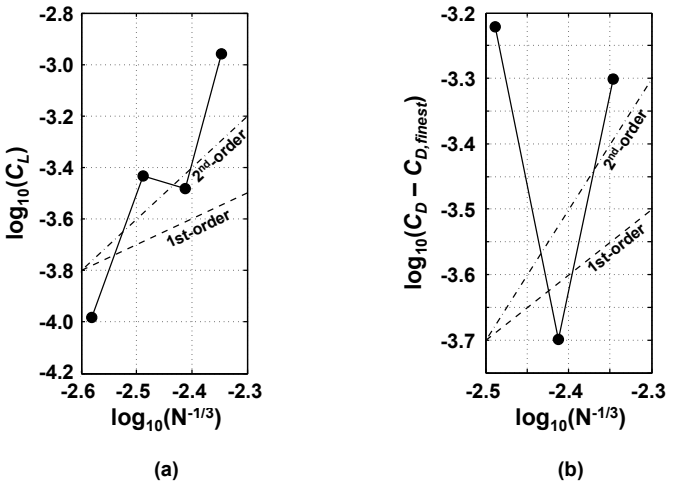

Figure 62: Error quantities related to lift and drag as functions of grid resolution for Run 165, $\alpha = 0°$.

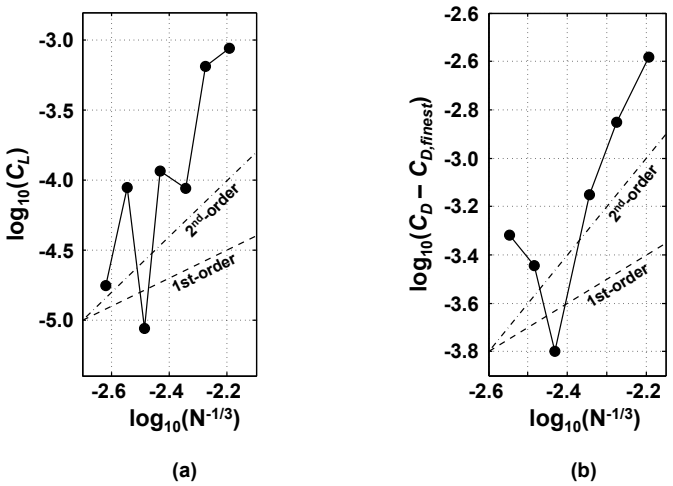

Figure 63: Results from the grid resolution study completed by Kleb et al. for Run 165 ($\alpha = 0°$) with FUN3D and a family of 7 grids [16].

required to prevent non-physical oscillations [104]. The limiter reduces the spatial order of accuracy to first order at the discontinuity. Godunov demonstrated that the ability to capture a discontinuity without oscillation requires the spatial order of accuracy of the numerical scheme to reduce to first order [105]. Roy [103], in examining grid convergence error for mixed-order numerical schemes applied to flows with shock waves, surmised that the local truncation error reduces to first order at the discontinuity in shock-containing flows, regardless of the use of a flux limiter, citing a number

of other works with similar observations. As a result, the spatial variation in the order of the truncation error (here, from second-order to first-order) leads to first-order asymptotic behavior as the cell size approaches zero. Kleb et al. [16] also observed an approach toward a change in the spatial accuracy with increasing grid refinement, a result consistent with shock-containing flows. The noise in the data and transition in order of accuracy for shock-containing flows complicate the determination of the spatial order of accuracy for this case.

Figure 64 illustrates the effect of grid resolution more qualitatively using Mach number contours in the interaction region of the flowfield. As grid resolution increased, flow features sharpened as expected, particularly the shocks, shear layers, and jet boundaries. Additionally, the Mach number in the jet increased more rapidly and to a higher value away from the nozzle exit with increasing grid resolution.

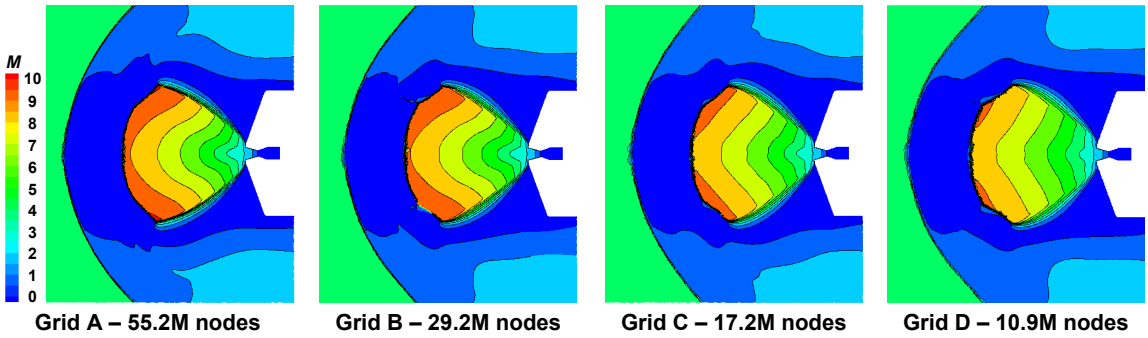

Figure 64: Mach number contours illustrating the effect of grid resolution on SRP flowfield structure.

The desired grid resolution for the cases in this chapter was limited by available computational resources. As a result, the grids used were scaled to be as fine as possible in the jet interaction region and still have workable run times (limited to approximately 25M - 30M total nodes). To this end, grids for the zero, three, and four nozzle configurations were constructed to have approximately 65% of the baseline grid density. The axial force oscillation frequencies for the two finest grids considered agreed well with those determined by several other CFD codes for this case [16, 51],

lending additional support to the grid resolution selected.

In each of the grids for the four configurations, the maximum y^+ value is less than 1 for all surfaces except those for the nozzle(s). For the nozzle surfaces, y^+ is greatest at the throat ($y^+_{max} = 23.0$). Figure 65 shows the surface mesh and y^+ distribution within the center nozzle. While no differences between the expected nozzle thrust and the computational nozzle thrust have been observed in this analysis, future grids should use finer grid resolution within the nozzle. Slices showing the final grid spacing in the pitch plane (focused on the jet interaction region), as well as views of the surface meshes, are given for each of the four configurations in Fig. 66. Note that for the one nozzle configuration, a conical shell source was specified in place of a full cone for the jet interaction region.

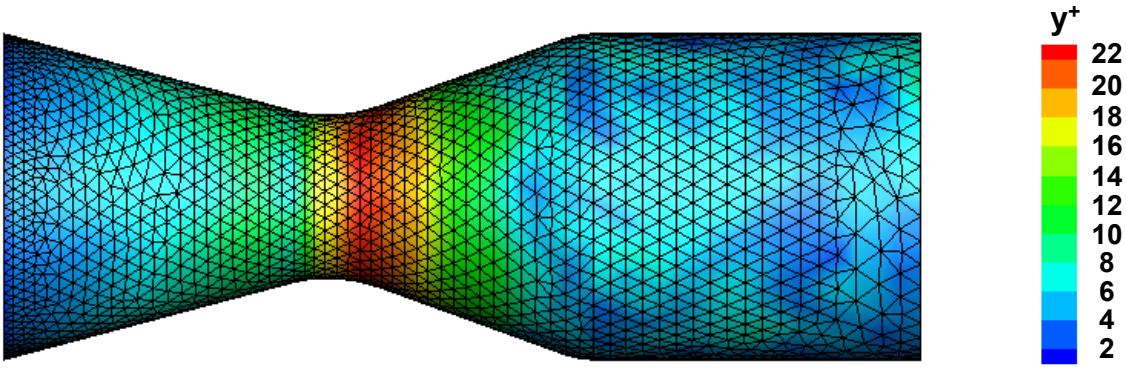

Figure 65: Surface mesh and y^+ distribution for the center nozzle.

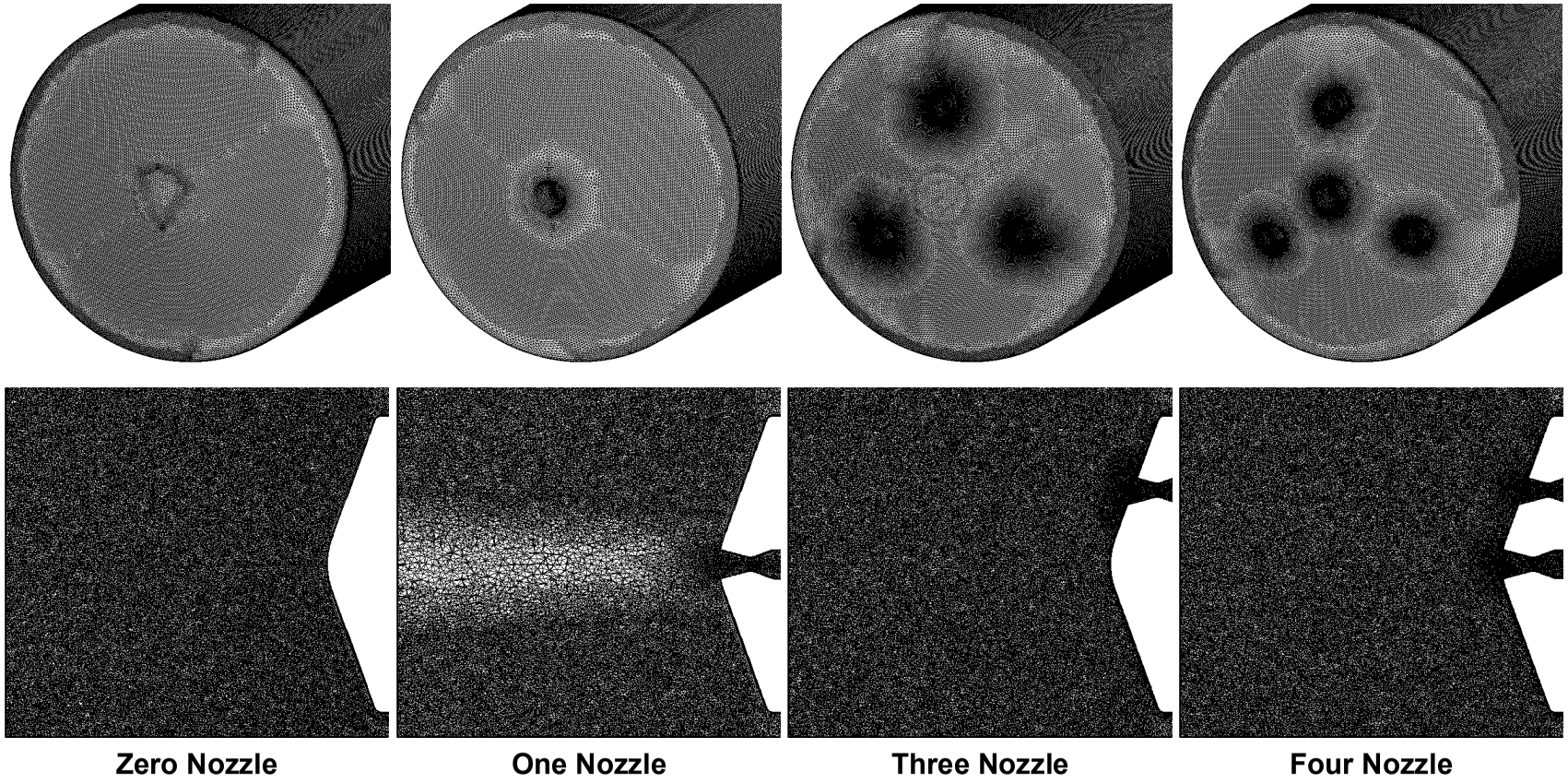

Figure 66: Final grids (surface − top, near-field jet interaction region − bottom) for each configuration.

5.3.2 Discussion of Temporal Resolution and Accuracy

All "jet-on" solutions in this chapter were obtained using an unsteady approach (BDF2OPT scheme) with a formal accuracy between second and third order. Implementation of this scheme can be thought of as solving a steady-state problem at each time step, with some number of subiterations required in pseudo-time to converge the steady-state problem [106]. In practice, convergence of the subiteration residual at each time step to machine zero is prohibitively expensive. As such, a temporal error controller was used to monitor subiteration convergence and a maximum number of subiterations specified.

The temporal error controller in FUN3D monitors the difference between the subiteration residual and an estimate of the temporal error norm. The estimate of the temporal error norm at each time step is determined from the difference in residual contribution, assuming two different levels of approximation of the time derivatives [106]. The exit criterion for the subiteration process in pseudo-time is a user-specified fraction [90]. For all cases in this chapter, this fraction was specified to be 0.1, or to have the solution advance to the next time step after the subiteration residual dropped one full order of magnitude below the estimated temporal error for the x-momentum and turbulent kinetic energy residuals. One full order of magnitude difference is the minimum required to achieve the formal order of accuracy of the scheme [90]. Alternatively, the solution advances to the next time step once the specified maximum number of subiterations is reached. Advancement of the solution to the next time step by reaching the maximum number of subiterations occurred in approximately half of the cases. In these cases, the mean flow residual dropped sufficiently, and the turbulence residual also dropped, but not to a sufficient level prior to reaching the subiteration limit.

Knowing that all solutions were not going to be grid converged, no dedicated temporal resolution study was completed. In addition to monitoring subiteration

residual histories, the time steps for each case were chosen to yield approximately 200 (or more) time steps per cycle in the axial force history. In most of the cases presented in this chapter, both the mean flow (x-momentum) and turbulence (turbulent kinetic energy) residuals fell to sufficient levels within the maximum number of subiterations specified. As an additional note, it is recognized that the determination of convergence in space and time cannot be entirely decoupled. As discussed, however, the computationally intensive nature of these cases limited the depth to which spatial and temporal resolution studies could be completed.

5.4 Computational Results

The results in this section have been compared directly with pressure data from the wind tunnel test described in Section 5.1. Error bars representing $\pm\ 3\sigma$ are given on all experimental data. For the $M_\infty = 4.6$ condition, $\pm\ 3\sigma_{C_p} = \pm\ 0.0222$. Computational flowfield schlieren images, C_p contours, and C_p as a function of location on the body are given for each case at two angles of attack: $\alpha = 0°$ and $8°$. Where available, representative still images from the high-speed schlieren test video are given for qualitative comparison. The one, three, and four nozzle results were all generated using a time-accurate approach. Time-averaged results are presented for each case. During the experiment, the model position was not adjusted to correct for an approximately $1°$ tunnel flow angle, potentially explaining some of the asymmetry in the pressure data with the model at zero angle of attack [16].

5.4.1 Zero Nozzle Configuration

5.4.1.1 0-deg Angle of Attack

The baseline case was the zero nozzle configuration at $\alpha = 0°$. Figure 67 shows the forebody C_p contours and computational flowfield schlieren for the zero nozzle configuration. Figures 68(a) and 68(b) compare FUN3D results with experimental data for pressure coefficient (see Fig. 61 for specification of angular locations on the

model). The C_p contours and flowfield features in Fig. 67 are as expected for a 70-deg sphere-cone forebody at zero angle of attack: axisymmetric with the highest pressure at the nose and decreasing outboard toward the shoulder and the position of the bow shock close to the body. The FUN3D results agree well with the experimental data on both the forebody and the aftbody for the four radial locations compared.

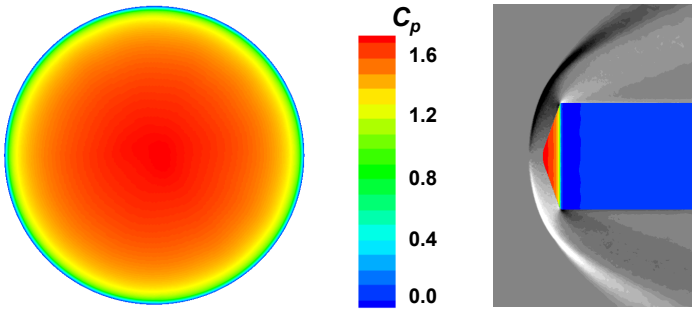

Figure 67: Forebody C_p contours and computational flowfield schlieren for the zero nozzle configuration ($\alpha = 0°$).

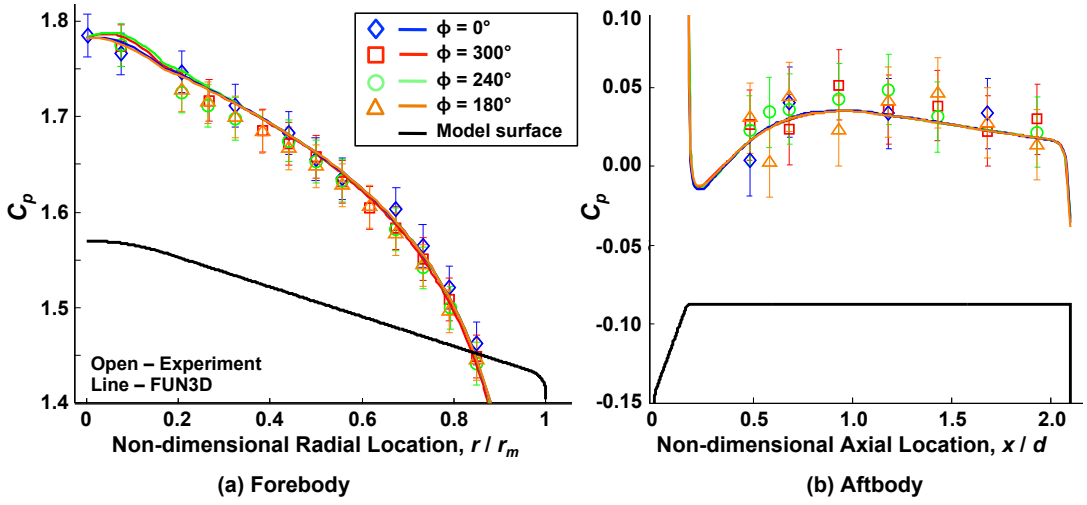

Figure 68: Comparison of C_p for the zero nozzle configuration ($\alpha = 0°$).

5.4.1.2 8-deg Angle of Attack

The zero nozzle configuration at $\alpha = 8°$ was also analyzed. Figure 69 gives C_p contours and computational flowfield schlieren for this case. Figures 70(a) and 70(b)

compare computational results with experimental data for pressure coefficient. With the model pitched to an 8° angle of attack, as expected, the highest pressures are on the windward side of the body and decreasing toward the leeward side. On the forebody (Fig. 70(a)), the FUN3D results agree well with the experimental data along each of the four rays considered. On the aftbody (Fig. 70(b)), the FUN3D C_p results follow similar trends to the experimental data, though the agreement is not as strong as on the forebody.

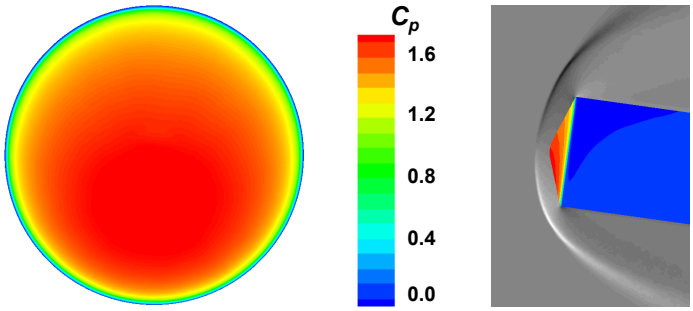

Figure 69: Forebody C_p contours and computational flowfield schlieren for the zero nozzle configuration ($\alpha = 8°$).

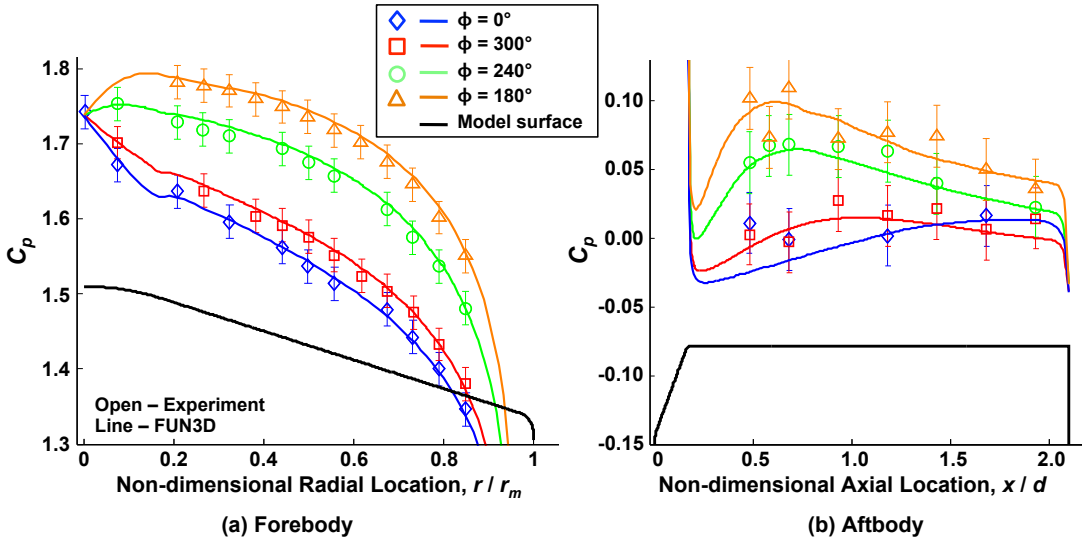

Figure 70: Comparison of C_p for the zero nozzle configuration ($\alpha = 8°$).

5.4.2 One Nozzle Configuration

5.4.2.1 0-deg Angle of Attack

Figure 71 shows the progression of forebody C_p contours and computational flowfield schlieren images through one complete cycle in the axial force history for the one nozzle case at $\alpha = 0°$. Also given in Fig. 71 are Mach number contours and streamtraces, illustrating the vortex shedding from the subsonic region. All of the prominent flow features are visible; the bow shock is displaced upstream by a highly under-expanded jet (Mach disk, reflected shock intersection, barrel shock). The progression illustrates the unsteady nature of the flowfield, with the dominant oscillation frequency being that of the shedding of the annular vortex in the subsonic region. This shedding is communicated through the subsonic shear layer and recirculation regions over the forebody to the nozzle exit and back up along the supersonic shear layer along the jet boundary. The shedding of this annular vortex follows a change in the expansion condition at the nozzle exit due to a change in the local static pressure arising from the previous disturbance traveling through the flowfield. This feedback mechanism has been shown to be a predominantly inviscid phenomena related to local flow times [66]. Figure 72 is a video showing the unsteady behavior for this case using computational schlieren for the flowfield and C_p contours for the body (click to play).

Figure 73 shows representative still images from the high-speed schlieren test video for this case (click to play). The behavior and flowfield structure from the high-speed test schlieren agree qualitatively well with the FUN3D results shown in Figs. 71 and 72.

As discussed in Section 5.3.1, the dominant oscillation frequency was found to depend strongly on grid resolution, and for the medium-density grid applied here, the oscillation frequency of the axial force for the one nozzle configuration with C_T = 1.968 is 1.86 kHz. The finest grid for this case has a frequency of 2.04 kHz. The Kulite data from the test show a peak frequency near 2.0 kHz [14].

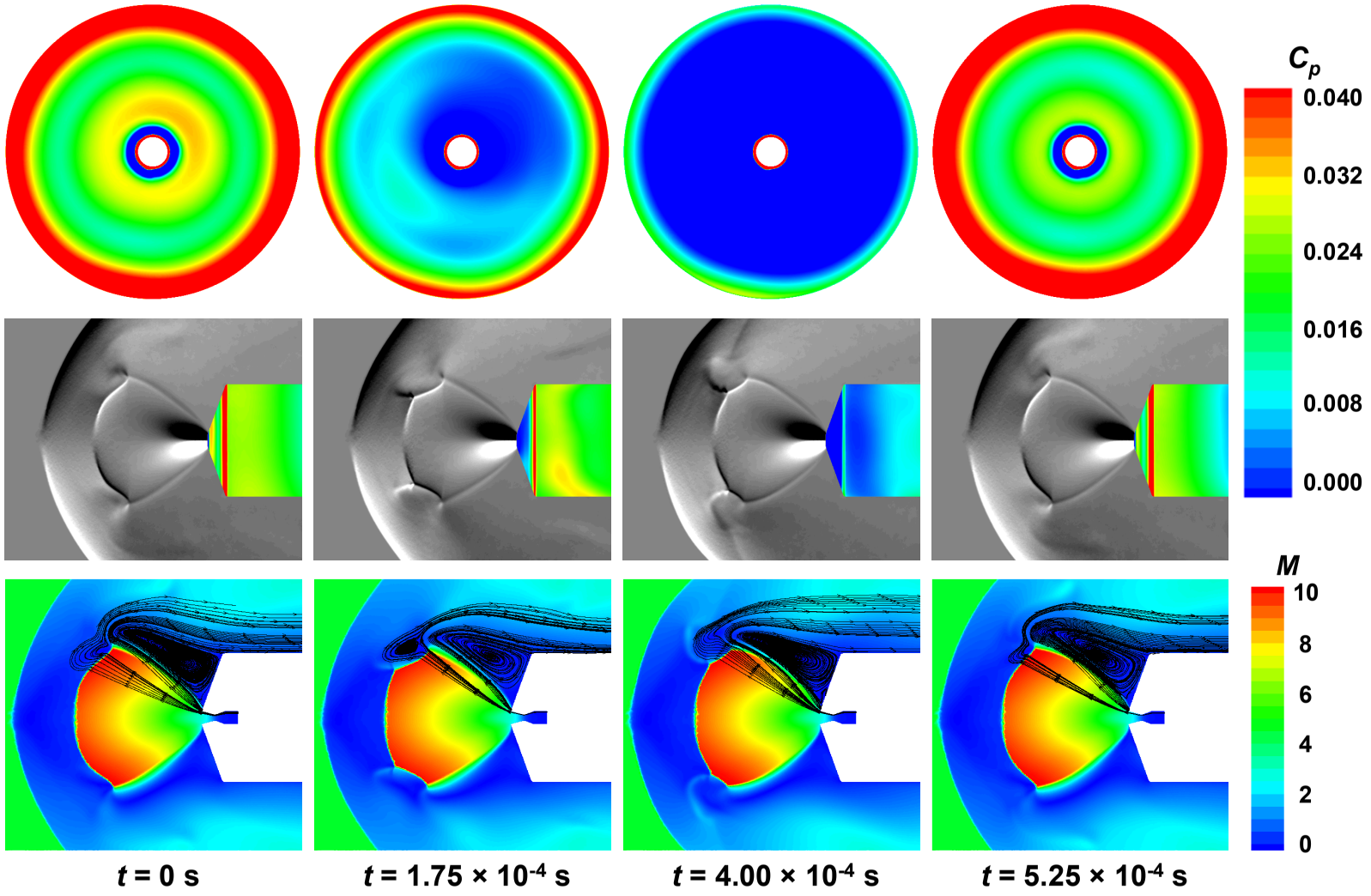

Figure 71: Forebody C_p contours, computational flowfield schlieren, and Mach number contours for the one nozzle configuration through one complete axial force oscillation cycle, depicting the shedding of the annular vortex ($\alpha = 0°$).

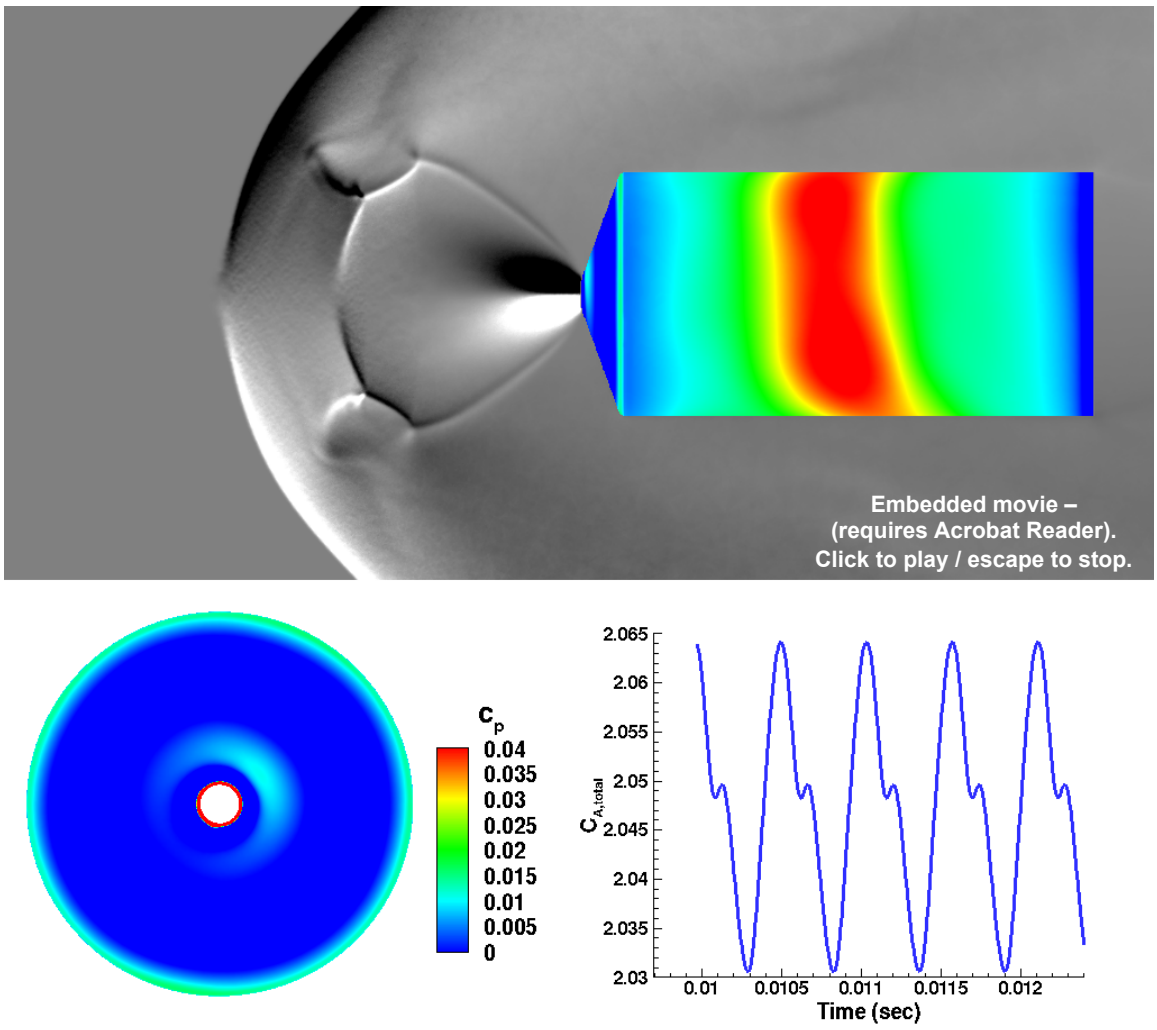

Figure 72: Unsteady flow solution for the one nozzle configuration ($\alpha = 0°$) using computational flowfield schlieren and C_p contours. (Click to play).

The steady-state convergence histories for the x-momentum and turbulent kinetic energy residuals are given in Fig. 74. As the flow solution is established, the turbulent kinetic energy residual increases by approximately an order of magnitude from its initial value before leveling out. The time histories for the forebody axial force coefficient, normal force coefficient, and pitching moment coefficient across 0.01 seconds are given in Fig. 75. The contribution of the jet flow is not included in these results. Note that the range on the y-axis for $C_{A,f}$ is one order of magnitude greater than the y-axis ranges for $C_{N,f}$ and C_m. Periodic, unsteady behavior is visible in the

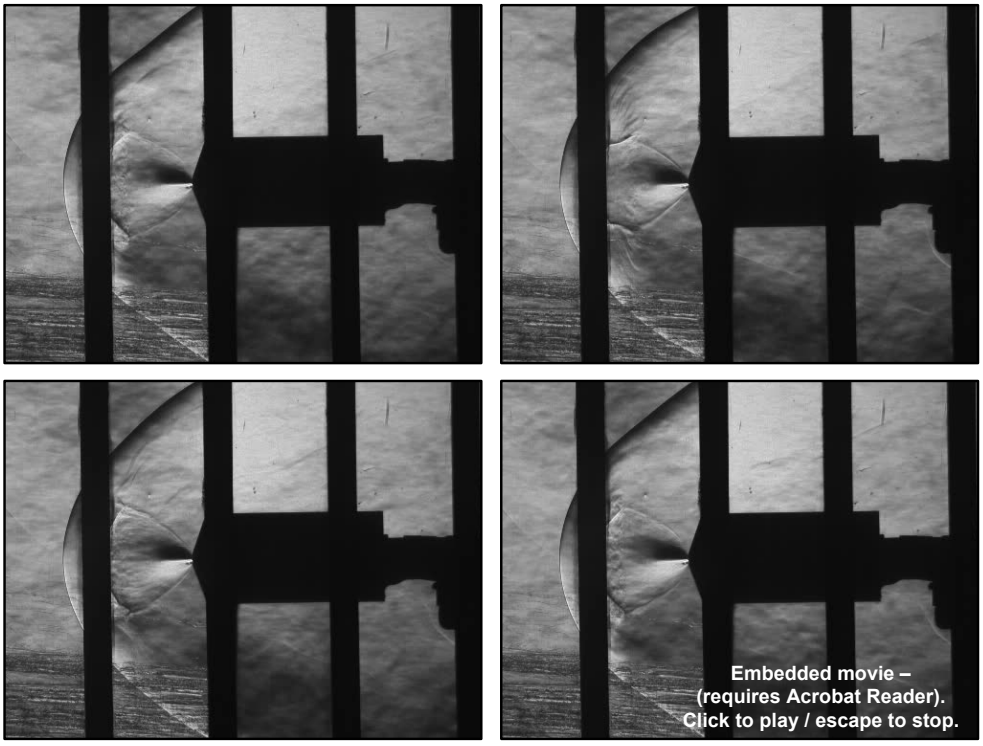

Figure 73: High-speed schlieren test images for Run 165, $\alpha = 0°$. (Click to play, 6,245 frames/sec).

time histories of $C_{A,f}$, $C_{N,f}$, and C_m for this case.

Figure 76(a) and 76(b) compare FUN3D results with the experimental data (see Fig. 61 for specification of angular locations on the model). On the forebody, the pressure taps show the pressure coefficient dropped outboard of the nozzle exit (r/r_m = 0.1 corresponds to the nozzle exit lip) and then remained nearly constant over much of the forebody, with the exception of a slight rise toward the shoulder. This pressure drop is substantial as compared to the zero nozzle configuration at the same conditions and is the direct result of the shielding of the body by the jet structure ($C_{p,0N} > 1.4$ vs. $C_{p,1N} < 0.04$, as measured on the forebody). The pressure taps on the aftbody show some asymmetry, though this may be due to the aforementioned 1° tunnel flow angle. The majority of this noise in the aftbody pressure data, however, still falls within $\pm\ 3\sigma$ bounds on the data.

On the forebody, FUN3D captured the pressure drop outboard of the nozzle,

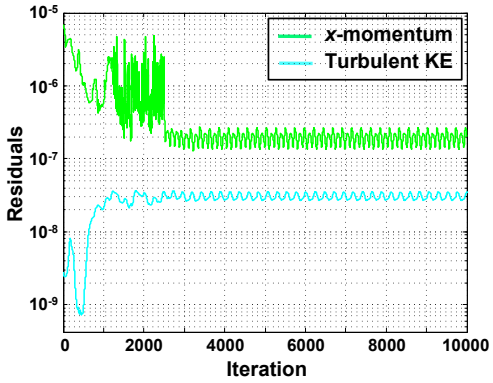

Figure 74: Steady-state histories of x-momentum and turbulent kinetic energy residuals for the one nozzle configuration ($\alpha = 0°$).

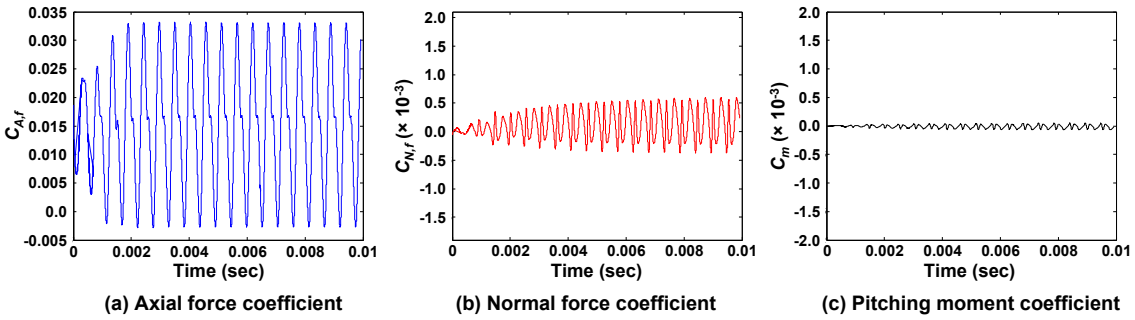

Figure 75: Axial force, normal force, and pitching moment coefficient time histories for the forebody, excluding nozzle surfaces. One nozzle configuration ($\alpha = 0°$).

including the rise toward the shoulder. With the exception of the pressure port closest to the nozzle exit, the FUN3D results are all within $\pm 3\sigma$ bounds on the experimental data. The FUN3D results along four separate rays show good symmetry in the time-averaged C_p distributions, though FUN3D appears to be slightly under-predicting C_p across the entire forebody as compared to the experimental data. The same trends are seen in the FUN3D aftbody C_p distributions. It is interesting to note that a slight pressure rise toward the shoulder was seen here in both the experimental data and the FUN3D results. Prior works [11, 75] have shown a slight pressure rise toward the shoulder for CFD results based on the configuration and conditions from Jarvinen and Adams [13] (60° sphere-cone forebody with a single, central nozzle and $C_T \approx 2$). However, the experimental data given for the Jarvinen and Adams [13] cases did not

show the same pressure rise.

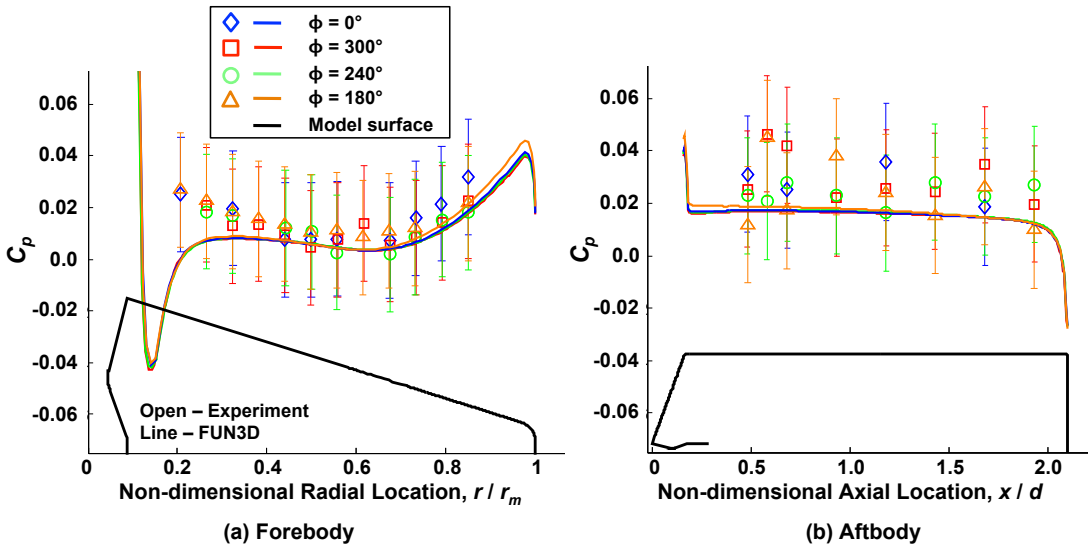

Figure 76: Comparison of C_p for the one nozzle configuration ($\alpha = 0°$).

5.4.2.2 8-deg Angle of Attack

Figure 77 gives forebody C_p contours, computational flowfield schlieren, and Mach number contours with streamtraces for the one nozzle configuration at an angle of attack of 8°. The progression of images in Fig. 77 are for one complete cycle in the axial force history. The dominant oscillation frequency of the total axial force for this case ($C_T = 1.968$) is 1.80 kHz. This frequency is similar to the frequency for the $\alpha = 0°$ case (1.80 kHz vs. 1.86 kHz) and is also associated with vortex shedding in the subsonic region. However, even at 8° angle of attack, the vortex shedding and jet structure variations are apparent only on the windward side. Figure 78 is a video showing the unsteady behavior for this case using computational schlieren for the flowfield and C_p contours for the body (click to play).

No high-speed schlieren video was taken for this case during the test; however, video was taken during a repeat run at the same conditions. Figure 79 shows representative still images from the high-speed schlieren test video for this repeat run

(click to play). The asymmetry in the flowfield structure and vortex shedding behavior from the high-speed test schlieren agree qualitatively well with the FUN3D results shown in Figs. 77 and 78.

The steady-state convergence histories for the x-momentum and turbulent kinetic energy residuals are given in Fig. 80. The time histories for the forebody axial force coefficient, normal force coefficient, and pitching moment coefficient across 0.01 seconds are given in Fig. 81. The contribution of the jet flow is not included in these results. Note that the y-axis span is the same for $C_{A,f}$, $C_{N,f}$ and C_m in Fig. 81. Though less periodic than in the $\alpha = 0°$ case, $C_{A,f}$, $C_{N,f}$ and C_m all exhibit unsteady behavior.

Figures 82(a) and 82(b) show the comparison between the experimental data and FUN3D results for pressure coefficient along four rays on the body. As in the $\alpha = 0°$ case, the pressure dropped immediately outboard of the nozzle exit. However, in contrast to the $\alpha = 0°$ case, only the pressures on the windward surfaces of the body showed a pressure rise toward the shoulder ($\phi = 180°$ and $240°$). Pressures measured along the $\phi = 0°$ and $300°$ locations remained nearly constant at values slightly below freestream conditions from the nozzle exit outboard to the shoulder. As the body pitches in angle of attack, the behavior of the jet and its structure begins to change, with differences appearing in the flowfield and C_p for the windward and leeward sides. The windward surfaces of the body are less shielded from the freestream and have higher surface pressures than the leeward surfaces, which are shielded from the freestream by the jet structure as well as the body at an angle of attack.

On the forebody, FUN3D agrees reasonably well with the trends in the experimental data while predicting slightly higher pressures. The pressure drop immediately outboard of the nozzle exit, minimum pressure near the half-radius, and pressure rise toward the shoulder are captured along all four rays ($\phi = 0°$, $180°$, $240°$, $300°$). Only along the $180°$ ray, beyond $r/r_m \approx 0.6$, do the FUN3D results fall outside the $\pm\ 3\sigma$

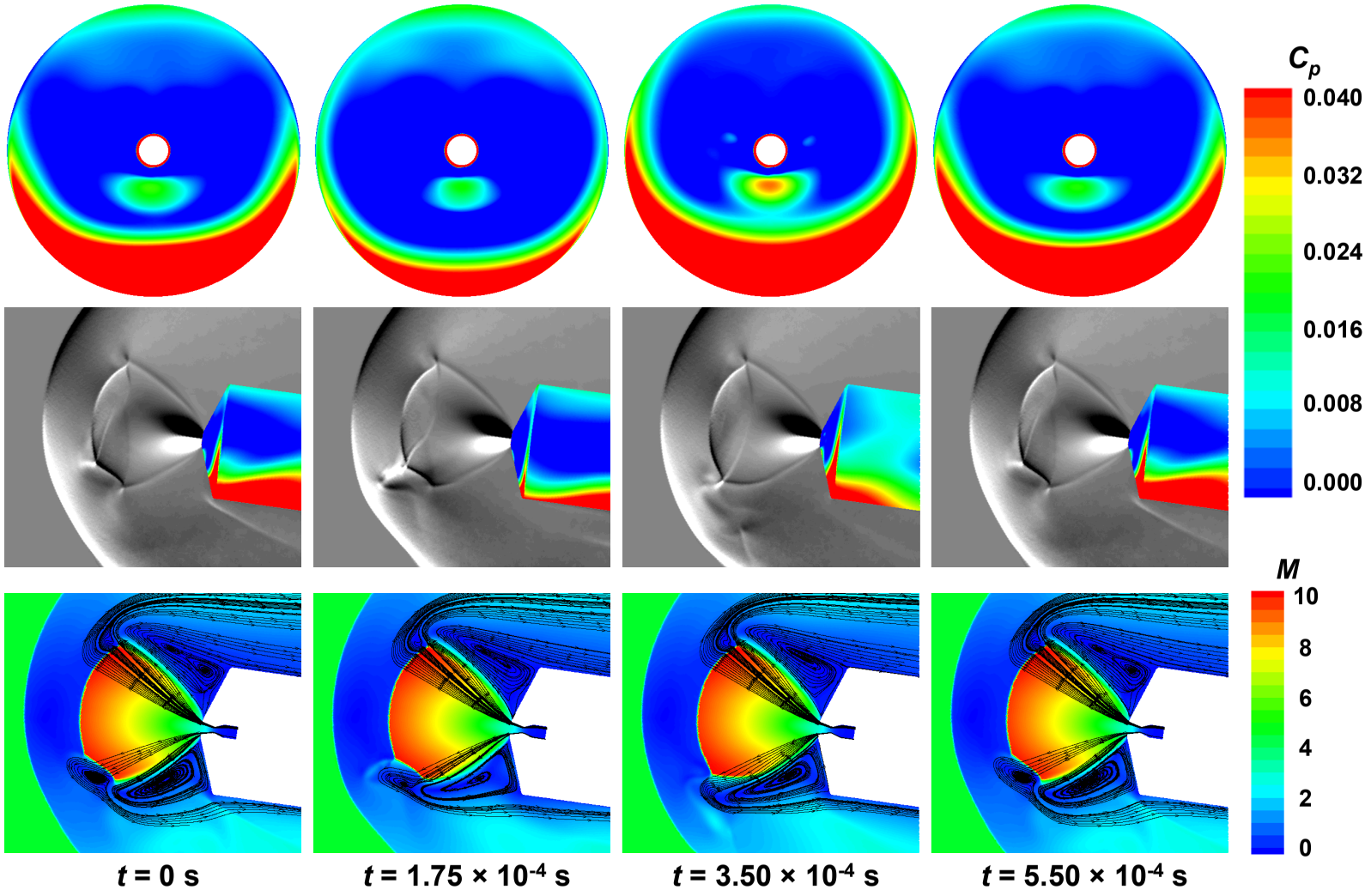

Figure 77: Forebody C_p contours, computational flowfield schlieren, and Mach number contours for the one nozzle configuration through one complete axial force oscillation cycle, depicting the asymmetric shedding of the annular vortex ($\alpha = 8°$).

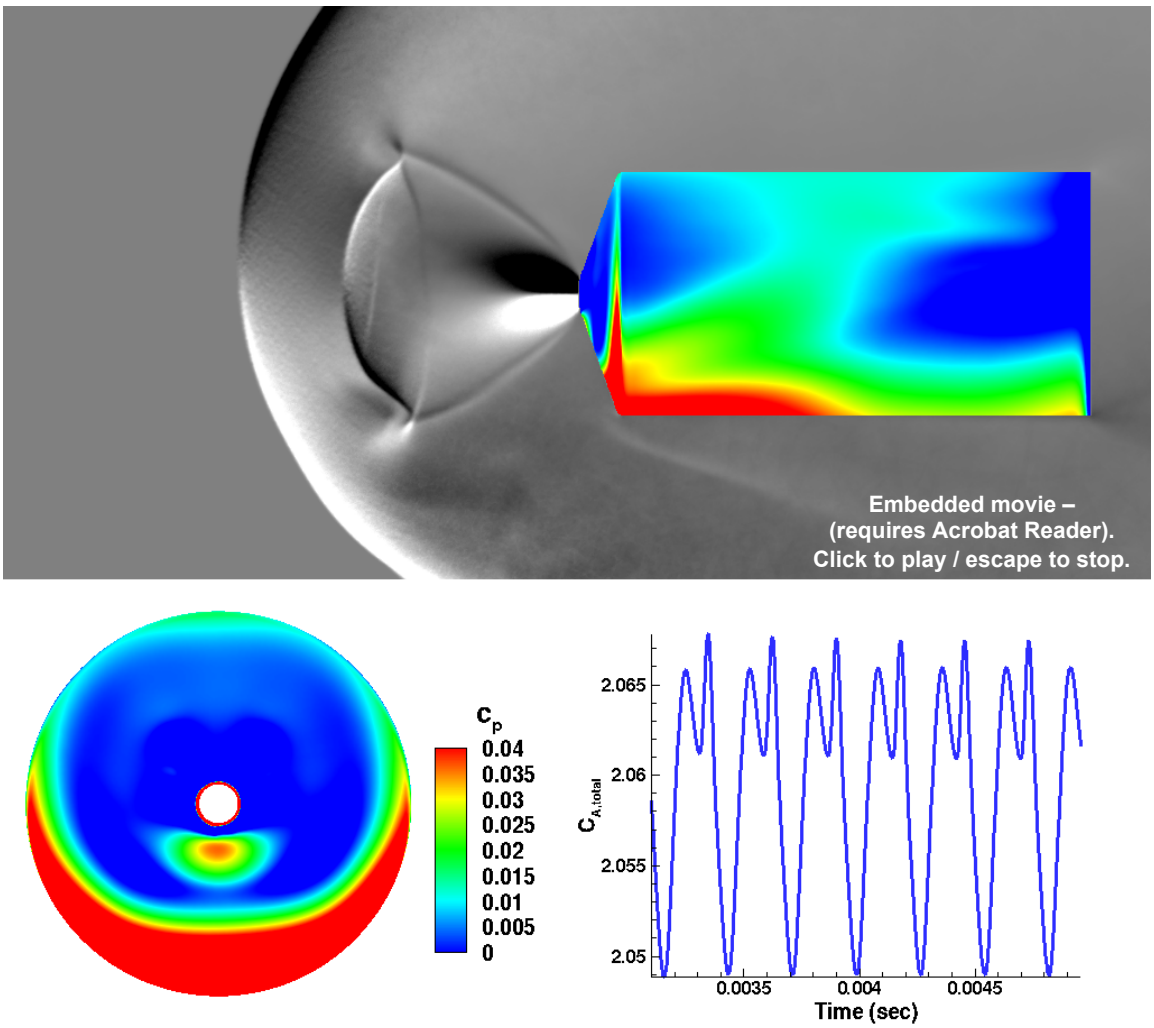

Figure 78: Unsteady flow solution for the one nozzle configuration ($\alpha = 8°$) using computational flowfield schlieren and C_p contours. (Click to play).

bounds on the experimental data. On the aftbody, there is a significant spread in the experimental data. FUN3D agrees with the experimental data that the highest pressures are on the windward surfaces and the lowest pressures are on the leeward surfaces, though FUN3D appears to be slightly under-predicting the aftbody pressure coefficient along all four rays examined.

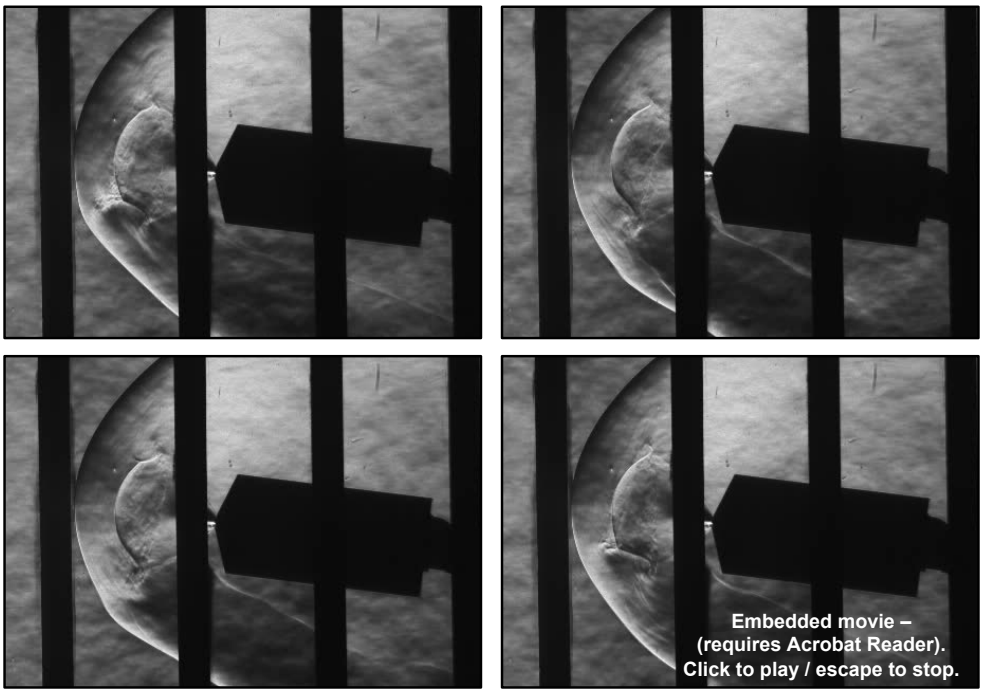

Figure 79: High-speed schlieren test images for Run 321, $\alpha = 8°$. (Click to play, 10,000 frames/sec).

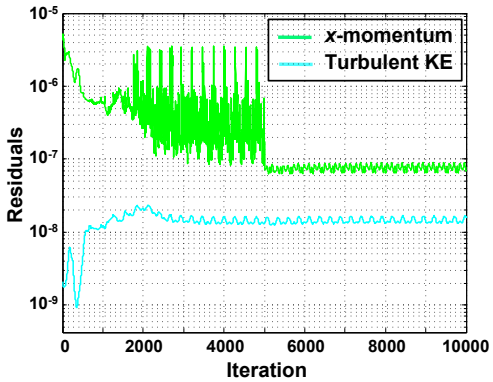

Figure 80: Steady-state histories of x-momentum and turbulent kinetic energy residuals for the one nozzle configuration ($\alpha = 8°$).

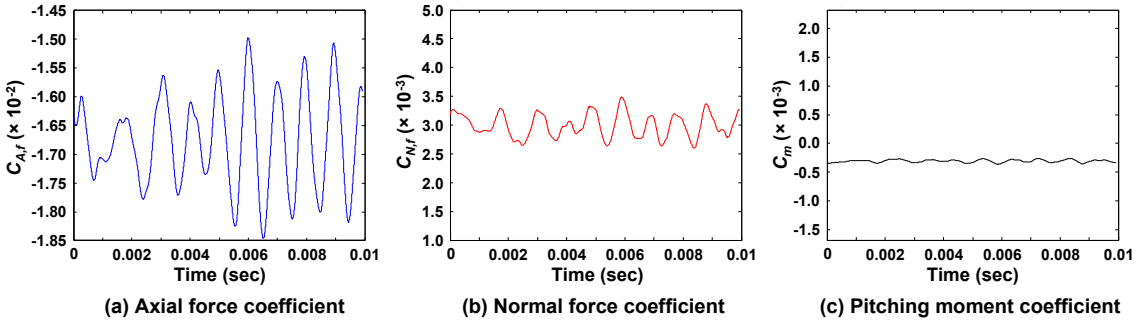

Figure 81: Axial force, normal force, and pitching moment coefficient time histories for the forebody, excluding nozzle surfaces. One nozzle configuration ($\alpha = 8°$).

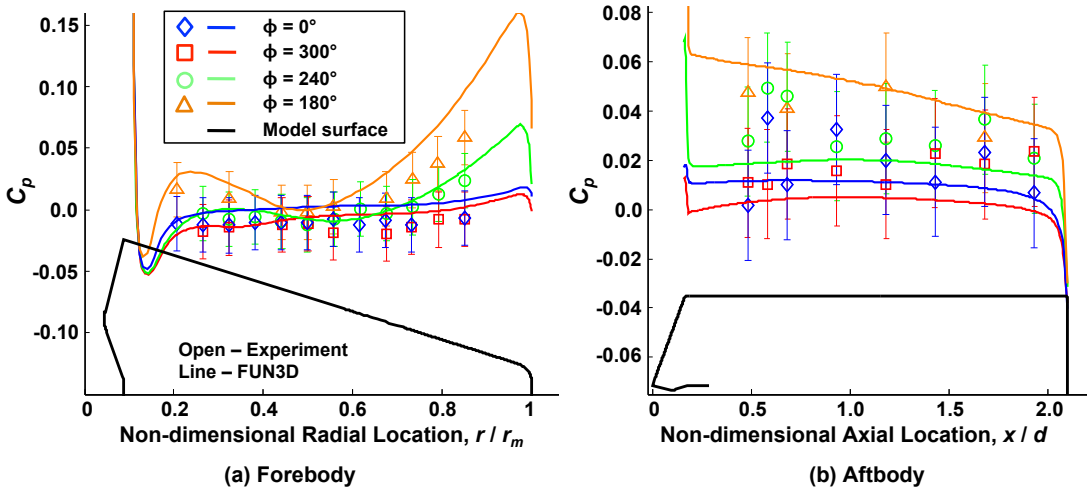

Figure 82: Comparison of C_p for the one nozzle configuration ($\alpha = 8°$).

5.4.3 Three Nozzle Configuration

5.4.3.1 0-deg Angle of Attack

The three nozzle case at $\alpha = 0°$, though run as time-accurate, converged to steady-state, even after the time step was reduced from 2.5×10^{-6} seconds to 6.25×10^{-7} seconds. The results below are for the steady-state converged case. The high-speed schlieren video taken during the experiment for this case, even at zero angle of attack, showed the flowfield to be highly unsteady. For this case, the use of Menter's SST turbulence model may be over-dampening the unsteadiness.

Figure 83 shows forebody C_p contours, computational flowfield schlieren, and Mach contours with streamtraces for the three nozzle configuration with a total C_T of 1.919. The forebody C_p contours are symmetric, as is consistent with the convergence of the solution to steady-state at an angle of attack of 0°. The pressure in between the nozzles drops from the nose to approximately the 2/3 r location on the forebody before rising again toward the shoulder. The flowfield schlieren with surface C_p contours illustrates the impact of the jet interaction structure on the surface pressure distribution. Visible in the schlieren are two of the three jets, each with distinct highly under-expanded jet structure. In these FUN3D results, the interaction between the jets inboard of the nozzle exits maintains significant pressure at the nose (C_p at the nose is 0.38), with lower, though still elevated, pressures out to the nozzle exits from the half-radius. Also visible is a recompression wave off of the body shoulder.

Figure 84 shows representative still images from the high-speed schlieren test video (click to play). The behavior observed in the high-speed schlieren video is highly unsteady for this case and does not appear to be periodic, unlike the one nozzle configuration at the same total C_T and angle of attack. Vortex shedding from the barrel shock - Mach disk intersection region is still occurring, but the process is highly asymmetric and disrupts much of the flowfield structure in the jet interaction region within the shock layer.

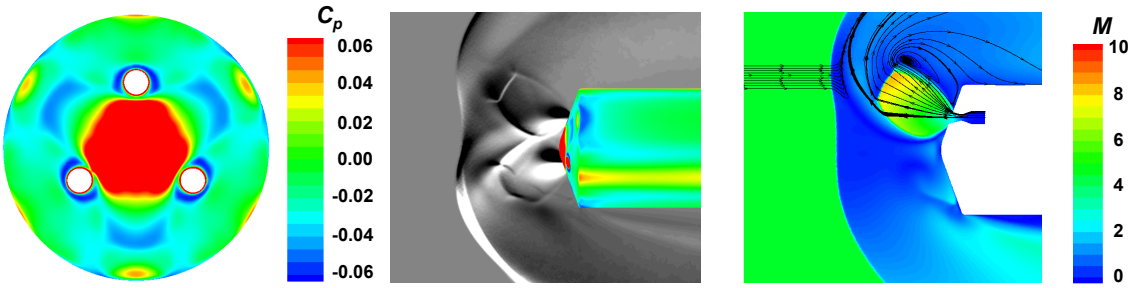

Figure 83: Forebody C_p contours and computational flowfield schlieren for the three nozzle configuration (converged to steady-state) ($\alpha = 0°$).

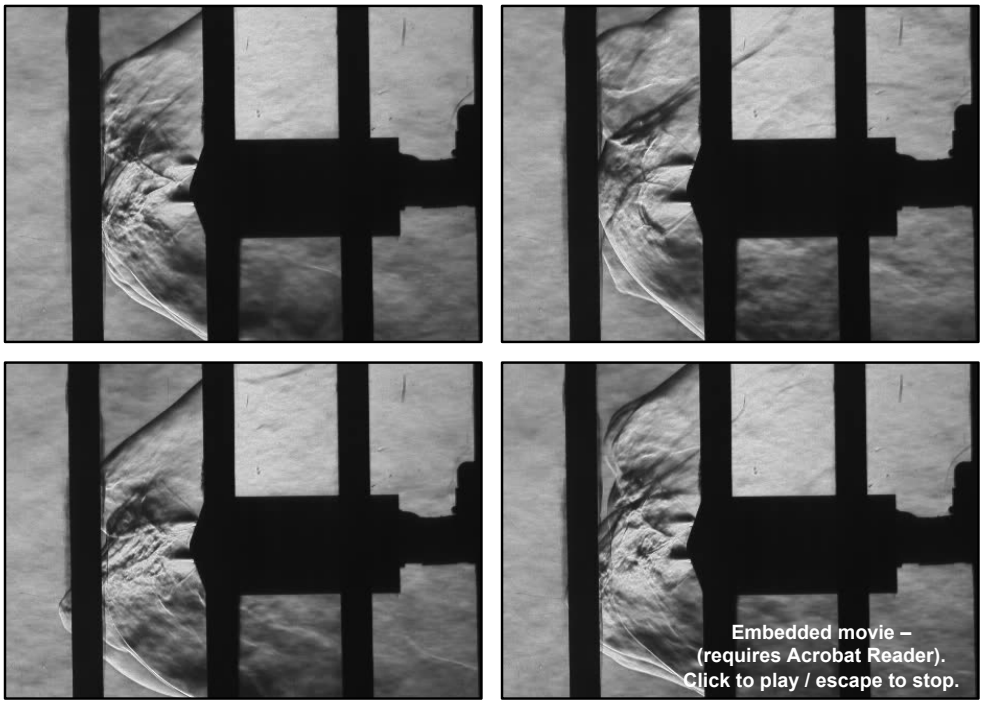

Figure 84: High-speed schlieren test images for Run 247, $\alpha = 0°$. (Click to play, 10,000 frames/sec).

The steady-state convergence histories for the x-momentum and turbulent kinetic energy residuals are given in Fig. 85. The time histories for the forebody axial force coefficient, normal force coefficient, and pitching moment coefficient across 0.01 seconds are given in Fig. 86. The contribution of the jet flow is not included in these results. Note the differences in the y-axis scales in Fig. 86. The span of the y-axis for $C_{A,f}$ is one order of magnitude greater than that for $C_{N,f}$ and two orders of magnitude greater than that for C_m. This case is converging to steady-state, even

though the solution is generated using a time-accurate approach.

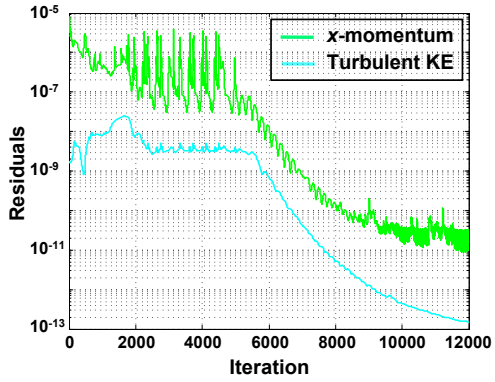

Figure 85: Steady-state histories of x-momentum and turbulent kinetic energy residuals for the three nozzle configuration ($\alpha = 0°$).

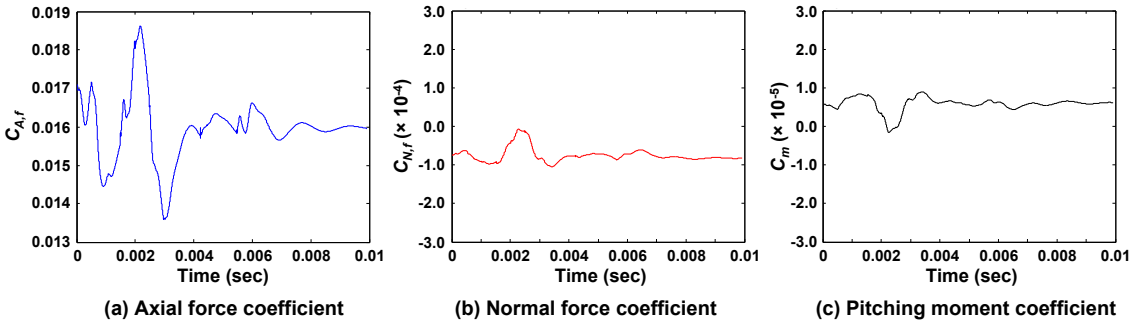

Figure 86: Axial force, normal force, and pitching moment coefficient time histories for the forebody, excluding nozzle surfaces. Three nozzle configuration ($\alpha = 0°$).

Figure 87(a) and 87(b) compare FUN3D results with the experimental data. The experimental data for the forebody show higher pressures at the nose, with a gradual decrease in pressure toward the shoulder for the 0° and 240° rays. Recalling the pressure tap layout shown in Fig. 61, the 0° and 240° rays run through nozzles, and the 180° and 300° rays run through the midpoint between two nozzles. The experimental data show a rise in pressure toward the shoulder for the 180° and 300° rays, behavior similar to though more pronounced than that observed for the one nozzle configuration.

FUN3D is over-predicting the pressure at the nose as compared to the experimental data ($C_{p,FUN3D} = 0.81$ vs. $C_{p,Exp} = 0.38$), a result observed previously in

CFD solutions for SRP flowfields with multiple nozzles [11, 65, 70, 75]. Along the 0° and 240° rays, FUN3D follows the trend of the experimental data, though with values slightly lower than the experimental values outboard between the nozzle exit and the shoulder. However, the pressure rise observed experimentally along the rays between the nozzles beginning near $r/r_m = 0.4$ appears to be only minimally captured by FUN3D. FUN3D predicts higher pressures at the nose and lower pressures in between nozzles than were observed in the experimental data, indicating that the interaction between the individual jets may not be fully captured. The flowfield structure implies that the FUN3D solutions do not have sufficient inboard jet expansion at these conditions. The aftbody C_p distributions agree more favorably than the forebody C_p distributions as the pressure drops past the shoulder and remains approximately constant at a level near that of the freestream static pressure.

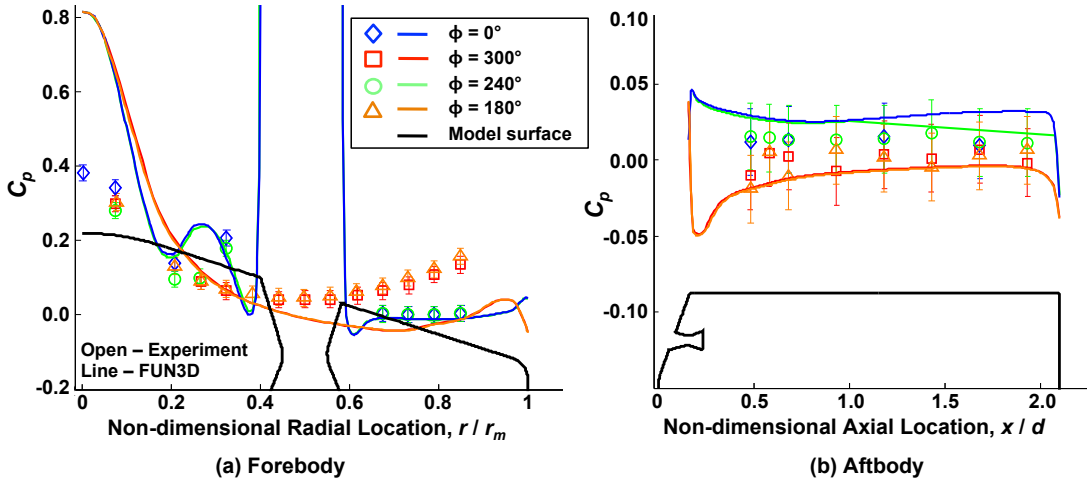

Figure 87: Comparison of C_p for the three nozzle configuration ($\alpha = 0°$).

This over-prediction of inboard pressures seems to be consistent across several CFD codes that have been applied to SRP configurations of concentrically arranged nozzles. One cause may be related to the tendency of two-equation turbulence models to over-predict the jet spreading rate as a result of compressibility effects. The SST turbulence model applied here does not include any compressibility correction.

5.4.3.2 8-deg Angle of Attack

Figure 88 gives forebody C_p contours, computational flowfield schlieren, and Mach number contours with streamtraces for the three nozzle configuration at an angle of attack of 8°. Similar to the three nozzle case at $\alpha = 0°$, this case converged to steady-state while the high-speed schlieren video taken during the experiment showed significant unsteady behavior. In the computational schlieren image in Fig. 88, two of the three jets are visible. The structure of the leeward jet (top) strongly resembles that from the $\alpha = 0°$ case, while the structure of the windward jet is asymmetric. Pressure is still being preserved inboard of the nozzle exits on the forebody, though the pressure coefficient at the nose has dropped slightly, from 0.38 for the $\alpha = 0°$ case to 0.26 for this case at $\alpha = 8°$. In this orientation, with the model at a roll angle of 0° (two nozzles "down"), a region of higher pressure forms on the forebody near the windward shoulder.

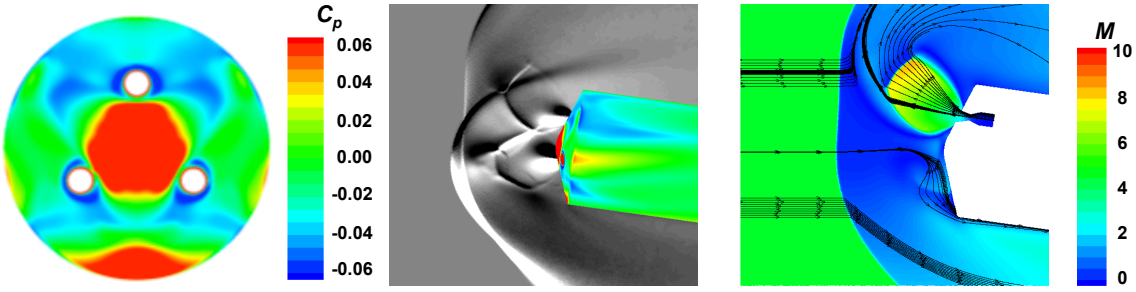

Figure 88: Forebody C_p contours, computational flowfield schlieren, and Mach number contours for the three nozzle configuration (converged to steady-state) ($\alpha = 8°$).

Figure 89 shows representative still images from the high-speed schlieren test video (click to play). Similar to the same case at $\alpha = 0°$, the behavior observed in the high-speed schlieren is highly unsteady at $\alpha = 8°$. Stronger variation in the jet structure is visible on the windward side than on the leeward side, and none of the periodic behavior observed for the one nozzle configuration is visible for the three nozzle configuration.

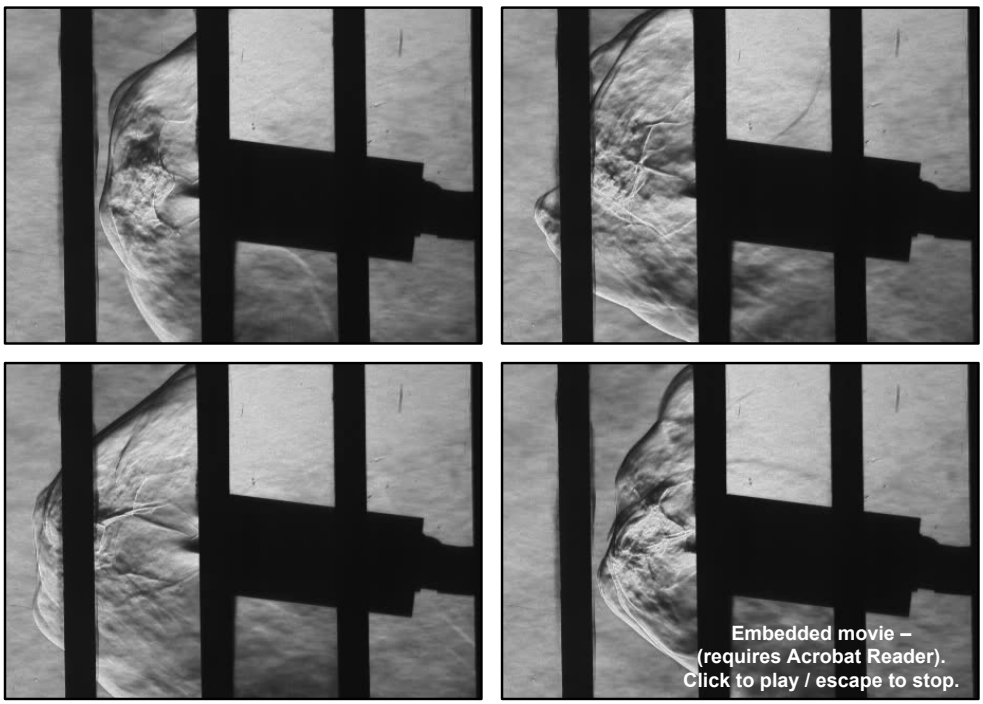

Figure 89: High-speed schlieren test images for Run 247, $\alpha = 8°$. (Click to play, 10,000 frames/sec).

The steady-state convergence histories for the x-momentum and turbulent kinetic energy residuals are given in Fig. 90. The time histories for the forebody axial force coefficient, normal force coefficient, and pitching moment coefficient across 0.01 seconds are given in Fig. 91. The contribution of the jet flow is not included in these results. Note the differences in the y-axis scales in Fig. 91. The span of the y-axis for $C_{A,f}$ is one order of magnitude greater than that for $C_{N,f}$ and two orders of magnitude greater than that for C_m. Similar to the three nozzle configuration at $\alpha = 0°$, this case is converging to steady-state, even though the solution is generated using a time-accurate approach.

Figures 92(a) and 92(b) compare FUN3D results with the experimental data for pressure coefficient on the forebody and aftbody, respectively. The 0° and 240° rays run through nozzles, and the 180° and 300° rays run through the midpoint between two nozzles (see the pressure tap layout shown in Fig. 61). The rays for $\phi = 0°$ and 300° are on the leeward surface, and the rays for $\phi = 180°$ and 240° are on the

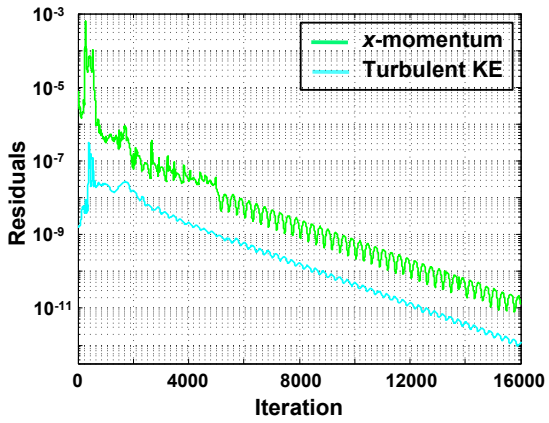

Figure 90: Steady-state histories of x-momentum and turbulent kinetic energy residuals for the three nozzle configuration ($\alpha = 8°$).

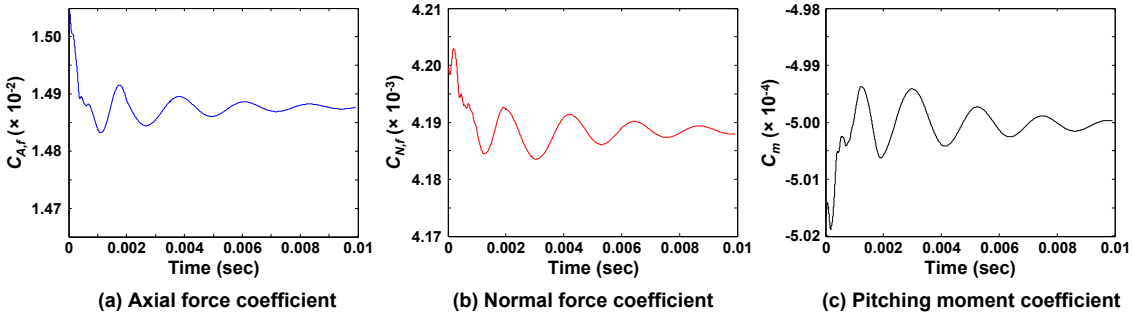

Figure 91: Axial force, normal force, and pitching moment coefficient time histories for the forebody, excluding nozzle surfaces. Three nozzle configuration ($\alpha = 8°$).

windward surface.

The experimental data show the highest pressures to be at the nose, with the exception of the windward shoulder region on the forebody. Along the two rays that run through nozzles at the half-radius ($\phi = 0°$ and $\phi = 240°$), the pressure dropped from the nose to the nozzle exit and then remained nearly constant from the outboard nozzle exit to the shoulder on both the windward and leeward surfaces. Along the two rays that run through the midpoint between two nozzles at the half-radius ($\phi = 180°$ and $\phi = 300°$), the pressure dropped from the nose to approximately the half-radius and then began increasing toward the shoulder. The pressure increase from the half-radius to the shoulder was significantly greater on the windward surface

than on the leeward surface. These trends are similar to those observed for the one nozzle configuration at angle of attack. On the aftbody, the pressures were relatively constant down the length of the body, with the windward surface pressures higher than the leeward surface pressures.

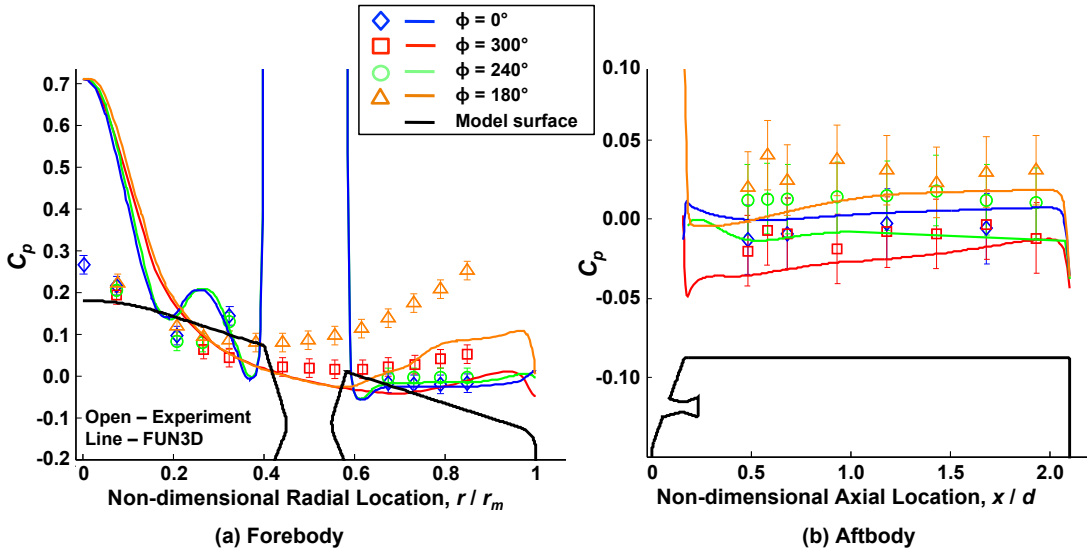

Figure 92: Comparison of C_p for the three nozzle configuration ($\alpha = 8°$).

As in the $\alpha = 0°$ case, FUN3D is over-predicting the pressure at the nose, with the pressure decreasing rapidly to approximately $r/r_m = 0.3$. On the forebody, from $r/r_m \approx 0.2$ to the shoulder, the FUN3D results agree well along the $\phi = 0°$ and $\phi = 240°$ rays, both of which run through a nozzle at the half-radius. Along the $\phi = 180°$ and $\phi = 300°$ rays, FUN3D is under-predicting pressures from $r/r_m \approx 0.4$ to the shoulder, though the outboard pressure rise on both the windward and leeward surfaces is somewhat captured. This may be due to insufficient jet expansion in the radial direction. FUN3D agrees well with the near-constant pressures on the aftbody, though slightly under-predicting pressures on both the windward and leeward surfaces.

5.4.4 Four Nozzle Configuration

5.4.4.1 0-deg Angle of Attack

Figure 93 shows forebody C_p contours, computational flowfield schlieren, and Mach number contours with streamtraces for the four nozzle case at $\alpha = 0°$. Figure 94 is a video showing the unsteady behavior for this case using computational schlieren for the flowfield and C_p contours for the body (click to play).

Similar to the three nozzle case at $\alpha = 0°$, the case for the four nozzle configuration was also run initially as time-accurate and converged to steady-state. Reduction of the time step from 2.5×10^{-6} sec to 1.25×10^{-6} sec resulted in capturing the expected unsteady behavior. The addition of the center nozzle eliminated all significant pressure inboard of the concentric nozzles and evened out the pressure distribution over much of the forebody as compared to the three nozzle configuration.

Figure 95 shows representative still images from the high-speed schlieren test video (click to play). Vortex shedding in the jet interaction region is visible, but only from the outboard regions of the combined four-jet structure. The outboard and downstream portions of the bow shock do respond to the vortex shedding, but the inboard region of the bow shock remains stable and more normal than in cases for the other retropropulsion configurations. The FUN3D results shown in Figs. 93 and 94 qualitatively capture these behaviors.

At these conditions ($C_{T,total} \approx 2$, $M_\infty = 4.6$), the center nozzle also reduced the unsteadiness in the intersecting shear layers and jet boundaries observed experimentally for the three nozzle configuration. In comparing the computational flowfield schlieren images in Fig. 93, the bow shock resembles that of the baseline zero nozzle configuration (Fig. 67) but for a flow obstruction with a larger area. The displacement of the bow shock by the individual jets seen for the three nozzle configuration (Fig. 83) is no longer seen with the addition of the center jet.

The steady-state convergence histories for the x-momentum and turbulent kinetic

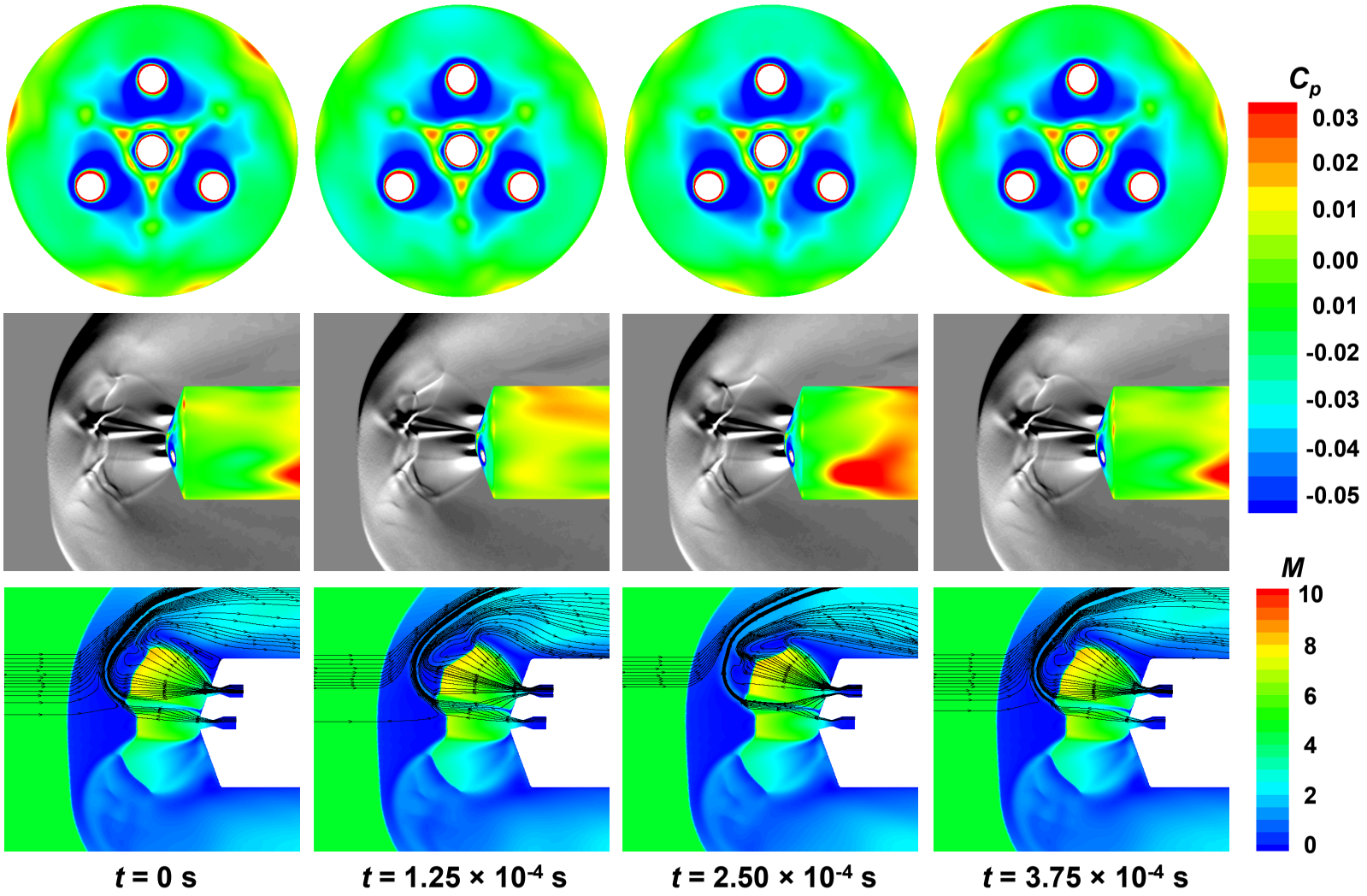

Figure 93: Forebody C_p contours, computational flowfield schlieren, and Mach number contours for the four nozzle configuration through one complete axial force oscillation cycle ($\alpha = 0°$).

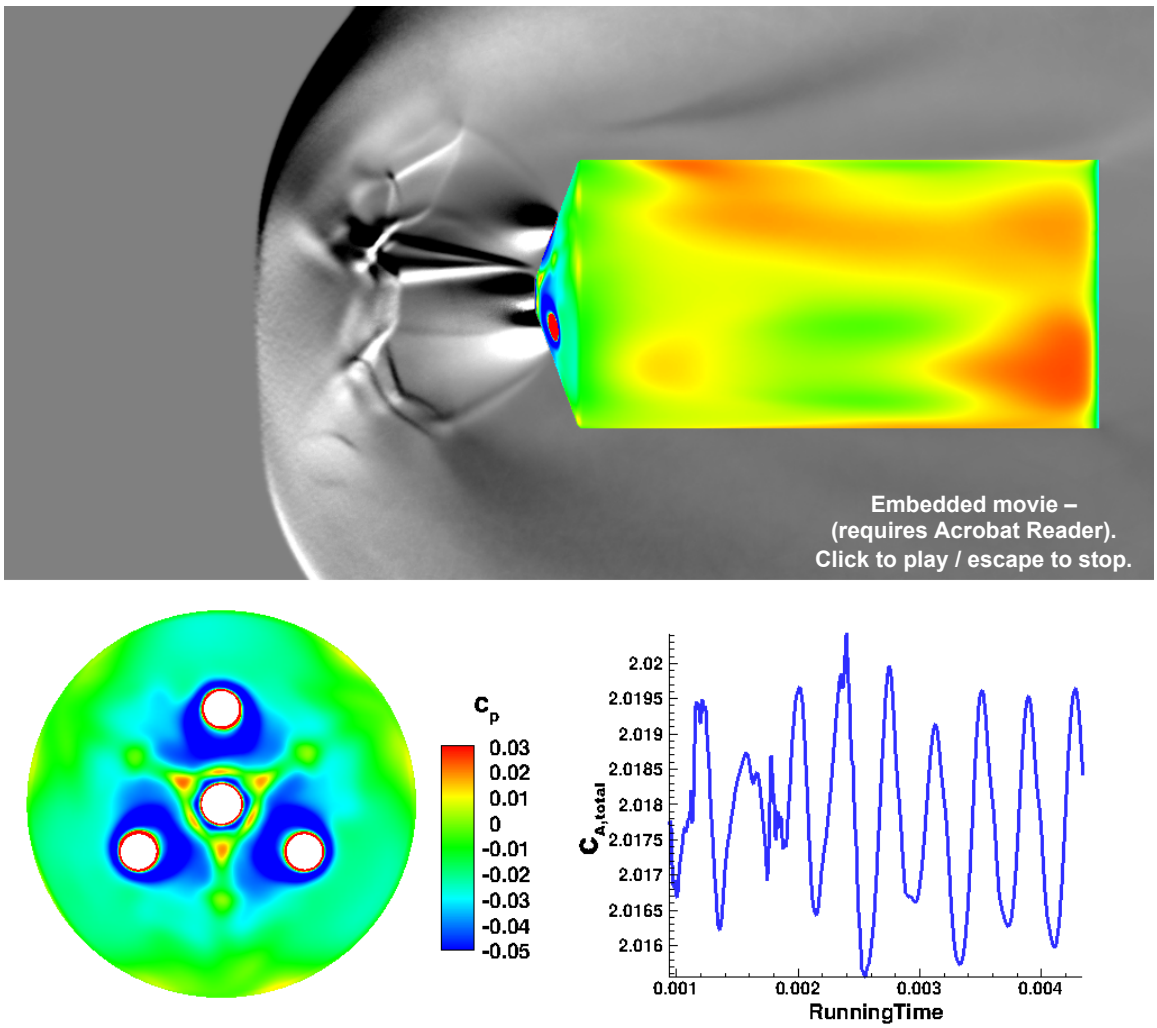

Figure 94: Unsteady flow solution for the four nozzle configuration ($\alpha = 0°$) using computational flowfield schlieren and C_p contours. (Click to play).

energy residuals are given in Fig. 96. The time histories for the forebody axial force coefficient, normal force coefficient, and pitching moment coefficient across 0.01 seconds are given in Fig. 97. The contribution of the jet flow is not included in these results. Note that the y-axis span varies for each coefficient in Fig. 97. The y-axis span for $C_{A,f}$ is two times greater than the y-axis span for $C_{N,f}$, and the y-axis span for C_m is an order of magnitude smaller than the y-axis span for $C_{N,f}$. Periodic, unsteady behavior is visible in the $C_{A,f}$, $C_{N,f}$ and C_m time histories.

Figure 98 shows the experimental C_p data and FUN3D results for the four nozzle

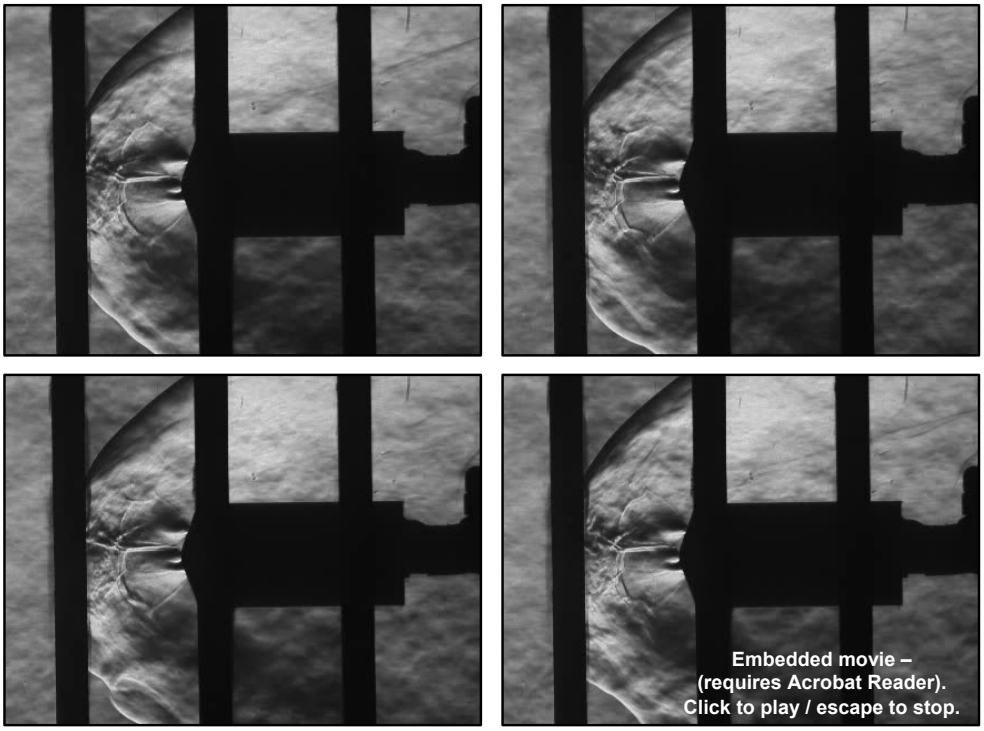

Figure 95: High-speed schlieren test images for Run 307, $\alpha = 0°$. (Click to play, 10,000 frames/sec).

configuration at $\alpha = 0°$ (see Fig. 61 for specification of angular locations on the model). As expected from the flowfield, the forebody pressure data are nearly constant at approximately the freestream static pressure. The pressure rise along the midpoint between nozzles seen for the three nozzle configuration is no longer present with the addition of the center nozzle. The experimental data for the four nozzle configuration is much more symmetric on both the forebody and aftbody than in the other cases, including the baseline.

The FUN3D results compare reasonably well on both the forebody and the aftbody, though the agreement on the aftbody is better than on the forebody. The overall trends in C_p given by FUN3D compare favorably with the given experimental data, though there is an exaggerated decrease in pressure just before and just after the nozzle exits that is seen only as a minimal change in the experimental data. In these regions on the body, the FUN3D results fall outside of the $\pm$ 3σ bounds on

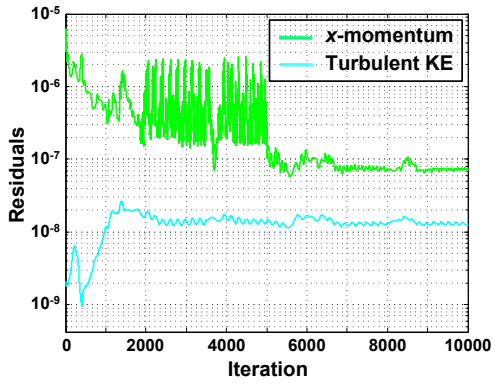

Figure 96: Steady-state histories of x-momentum and turbulent kinetic energy residuals for the four nozzle configuration ($\alpha = 0°$).

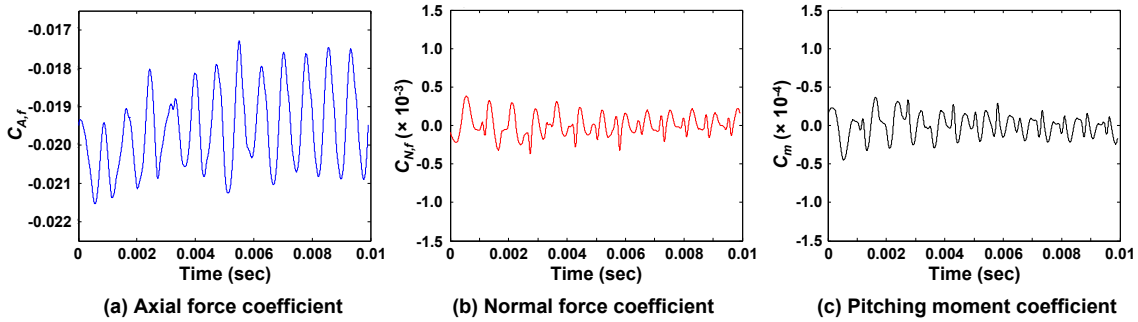

Figure 97: Axial force, normal force, and pitching moment coefficient time histories for the forebody, excluding nozzle surfaces. Four nozzle configuration ($\alpha = 0°$).

the experimental data. A slight pressure rise is observed toward the shoulder in the FUN3D results along the two rays that pass through the midpoint between two nozzles at the half-radius. Overall, FUN3D appears to be under-predicting the forebody surface pressures for this case. The FUN3D results agree well with the experimental data on the aftbody, capturing the slight rise in pressure from the forebody shoulder to the aft end. Along all four rays, FUN3D is slightly under-predicting C_p as compared to the experimental data.

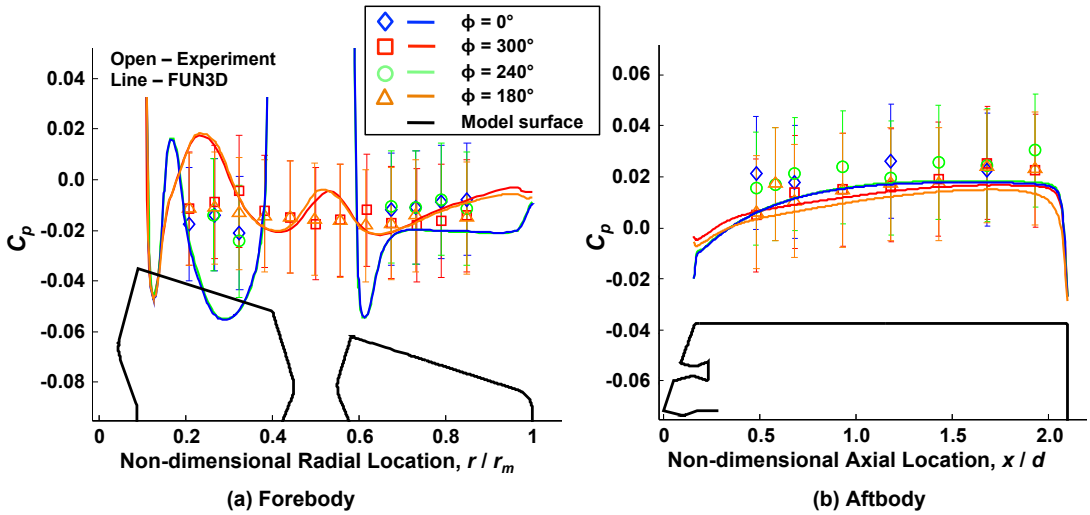

Figure 98: Comparison of C_p for the four nozzle configuration ($\alpha = 0°$).

5.4.4.2 8-deg Angle of Attack

Figure 99 gives forebody C_p contours, computational flowfield schlieren, and Mach number contours with streamlines for the four nozzle configuration at an angle of attack of 8°. The progression of images are for one complete cycle in the axial force history, though no dominant oscillation frequency could be determined for this case. Similar to the four nozzle case at $\alpha = 0°$, the bow shock is displaced upstream by the jet flow and is more normal over a larger area than for the one nozzle cases. In the computational schlieren images in Fig. 99, the bow shock is noticeably disrupted by the windward jets; this disruption is not seen for the same case at $\alpha = 0°$. At these conditions ($C_{T,total} = 1.923$, $M_\infty = 4.6$), even at an angle of attack, the jet structures appear to be symmetric, though the bow shock is no longer symmetric. The annular vortex shedding from the subsonic region seen for the one nozzle cases and four nozzle case at $\alpha = 0°$ is less apparent in this case, though minor variations in the jet structure on the leeward side are visible in the computational schlieren. Figure 100 is a video showing the unsteady behavior for this case using computational schlieren for the flowfield and C_p contours for the body (click to play). No high-speed schlieren test video is available for this case.

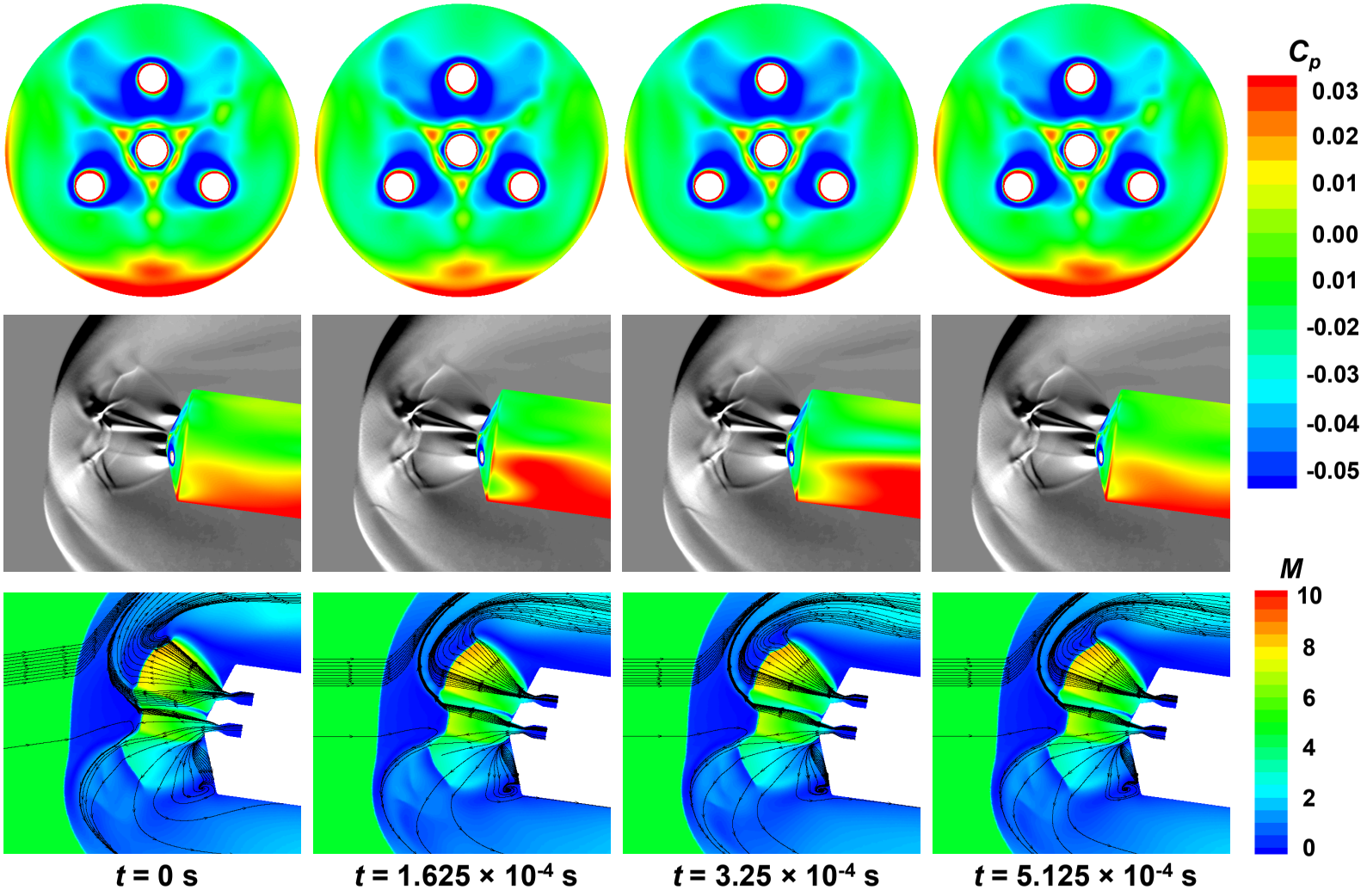

Figure 99: Forebody C_p contours, computational flowfield schlieren, and Mach number contours for the four nozzle configuration through one complete axial force oscillation cycle ($\alpha = 8°$).

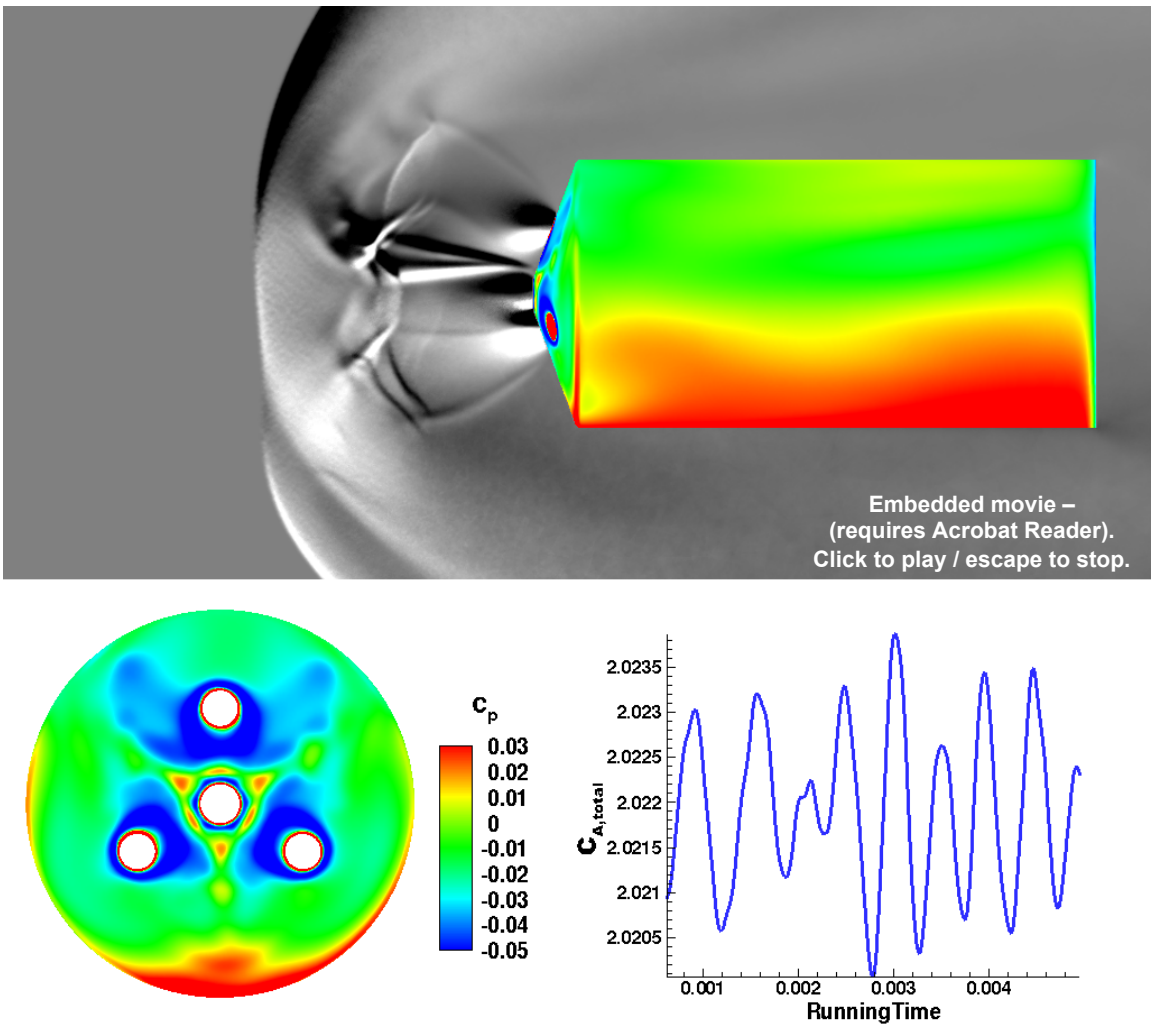

Figure 100: Unsteady flow solution for the four nozzle configuration ($\alpha = 8°$) using computational flowfield schlieren and C_p contours. (Click to play).

The steady-state convergence histories for the x-momentum and turbulent kinetic energy residuals are given in Fig. 101. The time histories for the forebody axial force coefficient, normal force coefficient, and pitching moment coefficient across 0.01 seconds are given in Fig. 102. The contribution of the jet flow is not included in these results. While oscillatory behavior can be seen in the total axial force coefficient history in Fig. 102(a), no dominant frequency could be determined. Running additional time steps for this case may eventually yield a dominant frequency related

to vortex shedding in the subsonic region. However, computational resource considerations limited this case to the current number of time steps. Note that the y-axis span is the same for $C_{A,f}$, $C_{N,f}$ and C_m in Fig. 102. Though less periodic than in the $\alpha = 0°$ case, $C_{A,f}$, $C_{N,f}$ and C_m all exhibit unsteady behavior.

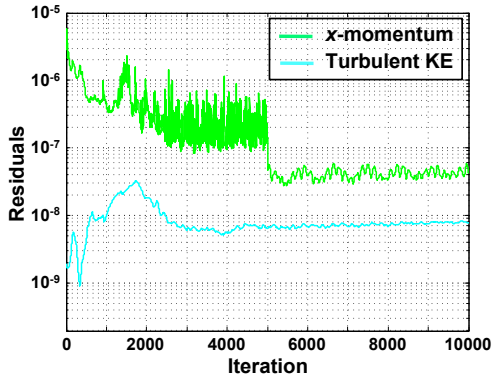

Figure 101: Steady-state histories of x-momentum and turbulent kinetic energy residuals for the four nozzle configuration ($\alpha = 8°$).

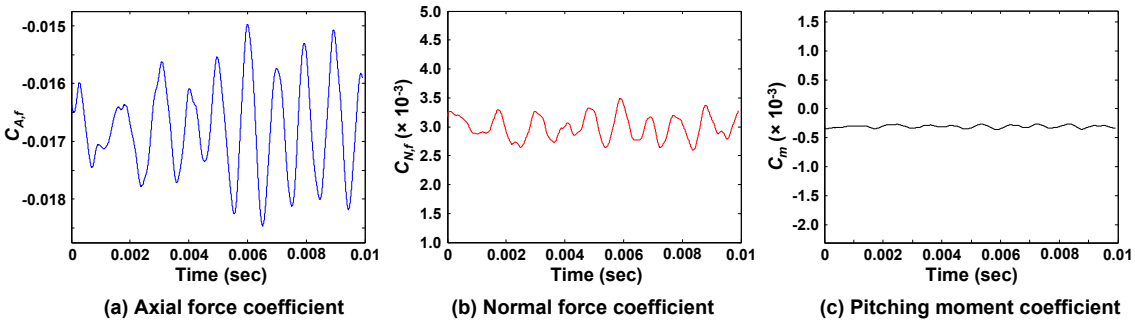

Figure 102: Axial force, normal force, and pitching moment coefficient time histories for the forebody, excluding nozzle surfaces. Four nozzle configuration ($\alpha = 8°$).

Figures 103(a) and 103(b) compare FUN3D results for pressure coefficient with experimental data along rays at four angular positions on the body ($\phi = 0°$, $180°$, $240°$, $300°$). The rays for $\phi = 0°$ and $\phi = 240°$ run directly through nozzles at the half-radius, while the rays for $\phi = 180°$ and $\phi = 300°$ run through the midpoint between two nozzles at the half-radius. With the body pitched to an angle of attack of $8°$, $\phi = 180°$ and $\phi = 240°$ are along windward surfaces, and $\phi = 0°$ and $\phi = 300°$ are along leeward surfaces.

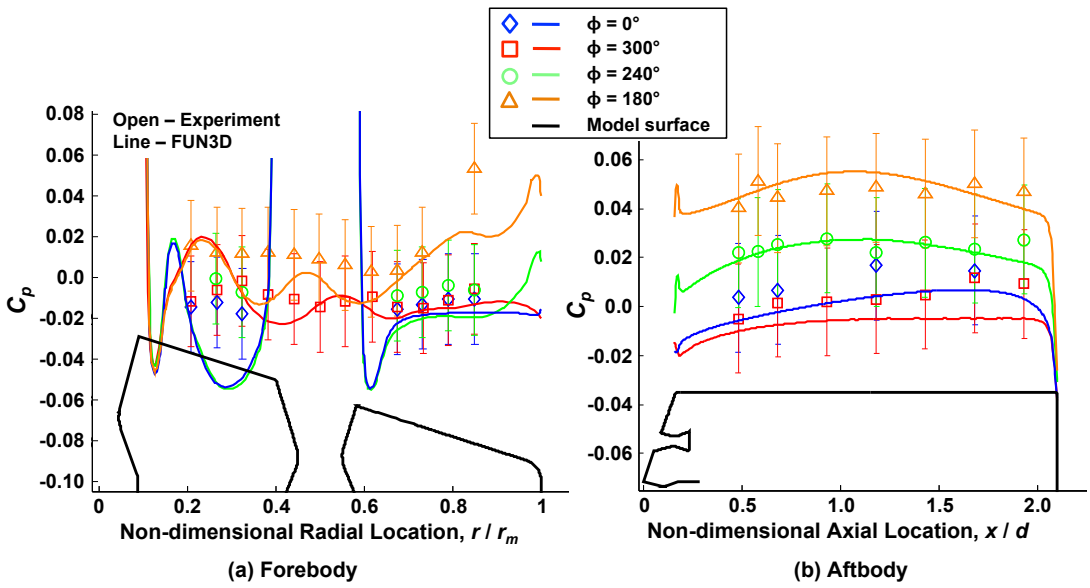

Figure 103: Comparison of C_p for the four nozzle configuration ($\alpha = 8°$).

On the forebody, as seen for the one nozzle configuration, the pressure dropped immediately outside of the center nozzle. The pressures were higher on the windward surfaces than on the leeward surfaces, with pressures over the entire forebody remaining within a C_p range of approximately 0.04. The exception is for the rays along the windward surfaces, which showed a slight increase in pressure toward the shoulder. Similarly, on the aftbody, the highest pressures were on the windward surfaces. Aftbody pressures showed a slight upward trend from the forebody shoulder to the aft end.

In Figs. 103(a) and 103(b), FUN3D is able to capture the general trends in the experimental data on the forebody. However, as in the four nozzle case at $\alpha = 0°$, FUN3D appears to exaggerate pressure changes between the center nozzle and nozzles at the half-radius and also immediately outboard of all nozzle exits. The pressure rise toward the shoulder on the windward surfaces is being captured, though not through strong agreement with the experimental data. Overall, FUN3D is under-predicting the experimentally measured pressures on the forebody. Agreement on the aftbody is much better than on the forebody, though FUN3D is under-predicting leeward surface

pressures. FUN3D is capturing the slight rise in pressure toward the aft end, as well as the higher pressures on the windward surfaces and lower pressures on the leeward surfaces. As discussed for the cases examined for the three nozzle configuration, it is possible that the jet expansion and interaction between the individual jet flows is not being fully captured, contributing to the differences seen in the forebody data comparison.

5.5 Comparison of Steady-State and Time-Accurate Flow Solutions

A comparison of the computational results from all eight cases is given in Table 21. The single nozzle finest grid case from the grid resolution study ($\alpha = 0°$) has also been included to illustrate potential differences arising from grid resolution. All force coefficients are for the forebody only. The one nozzle, three nozzle, and four nozzle cases use time-averaged quantities; the zero nozzle cases use steady-state values. The dominant oscillation frequency for the total axial force and number of steps per cycle are given for the cases exhibiting such behavior. The Strouhal number, St, is also given for these cases, using the model diameter and the freestream velocity.

Table 22 presents a comparison of the computational aerodynamic force results for $C_{D,f}$ and $C_{L,f}$ with the same quantities derived from integration of the experimental static pressure data. As mentioned, no direct force or moment measurements were taken during this test. However, integrated aerodynamic force coefficients were computed. Cruz Ayoroa et al. [107] generated a three-dimensional polar grid of the model forebody, and the C_p distribution was then calculated by interpolation and extrapolation of the averaged C_p data from the test. A bicubic spline was used to create a minimum curvature surface passing through all of the data points.

The aerodynamic force coefficients were determined by integrating the pressure distribution over the forebody surface and subtracting the pressures over the nozzle

areas. In all cases, the computational results agree well with the integrated aerodynamic force coefficients from the test. In looking at the results given in Tables 21 and 22, the effect of SRP on aerodynamic drag at these conditions ($M_\infty = 4.6$, $C_T = 2$) is clear, reducing $C_{D,f}$ from approximately 1.5 to near zero, independent of the configuration. This is consistent with the systems analysis presented in Chapter 3 , which notes that in the case of a high-mass Mars entry trajectory, the aerodynamic drag contribution to the total deceleration required during the SRP phase to safely land on the surface is negligible.

Table 21: Summary of computational results for aerodynamic forces.

	Angle of Attack	$C_{D,f}$	$C_{L,f}$	$C_{D,f}$ oscillation frequency (kHz)	Steps / cycle	St
Zero nozzle	0°	1.482	6.50×10^{-4}	–	–	–
	8°	1.452	-1.82×10^{-1}	–	–	–
One nozzle	0°	0.019	6.46×10^{-4}	1.86	217	0.32
One nozzle (fine)	0°	0.018	3.08×10^{-4}	2.04	198	0.35
	8°	0.016	6.75×10^{-3}	1.80	224	0.31
Three nozzle	0°	0.016	-7.95×10^{-4}	–	–	–
	8°	0.015	8.06×10^{-5}	–	–	–
Four nozzle	0°	0.019	1.17×10^{-4}	2.58	313	0.44
	8°	0.017	3.00×10^{-3}	–	–	–

Table 22: Comparison of computational results with experimental force coefficients (from integrated experimental pressure results).

	Angle of Attack	$C_{D,f}$ CFD	$C_{D,f}$ Exp.	Difference	$C_{L,f}$ CFD	$C_{L,f}$ Exp.	Difference
Zero nozzle	0°	1.482	1.491	0.0087	6.50×10^{-4}	-5.18×10^{-3}	-5.84×10^{-3}
	8°	1.452	1.462	0.0100	-1.82×10^{-1}	-1.85×10^{-1}	-2.50×10^{-3}
One nozzle	0°	0.019	0.018	-0.0008	6.46×10^{-4}	-4.39×10^{-4}	1.09×10^{-3}
	8°	0.016	0.016	0.0001	6.75×10^{-3}	6.62×10^{-3}	-1.30×10^{-4}
Three nozzle	0°	0.016	0.057	0.0414	-7.95×10^{-4}	5.86×10^{-4}	-4.00×10^{-6}
	8°	0.015	0.047	0.0316	8.06×10^{-5}	3.19×10^{-3}	2.87×10^{-3}
Four nozzle	0°	0.019	-0.013	-0.0316	1.17×10^{-4}	1.20×10^{-4}	7.00×10^{-5}
	8°	0.017	-0.001	-0.0176	3.00×10^{-3}	3.68×10^{-3}	-4.00×10^{-6}

The computational expense of each of these cases is significant. All cases were run on Pleiades, part of NASA Advanced Supercomputing High-End Computing Capability resources. Thirty-six Westmere nodes with two six-core Xeon X5670 (Westmere) 2.93 GHz processors per node were used for each case. The steady cases (zero nozzle configuration only) require approximately three hours of wall time, or 1296 CPU hours. The unsteady cases, including the steady solutions used to initialize the unsteady solutions, each require approximately 60 - 70 hours of wall time, or approximately 29,000 CPU hours. The required CPU hours for a single, unsteady FUN3D SRP solution are prohibitive to using such solutions as the primary resource in constructing SRP models and aerodynamic databases for conceptual systems analysis.

All computational solutions for SRP thus far have been with sub-scale models of configurations tested in wind tunnels. The computational cost is likely to increase for cases considering full-scale vehicles and SRP configurations. The grid spacing will scale with the physical size of the vehicle. However, the inclusion of more details of the body geometry, particularly features that are small in comparison to the scale of the vehicle, can increase the total number of grid cells significantly. Accurate and consistent predictions of SRP flowfields and integrated aerodynamics requires the structures in the jet interaction region to be well-resolved, including the jet boundary, barrel shock, Mach disk, shear layers, and bow shock. These structures will also increase in size as Mars-relevant flight conditions are simulated, adding to the computational cost.

Figures 104 and 105 compare steady-state and time-accurate solutions for these wind tunnel test cases to understand the necessity of unsteady CFD solutions in predicting the integrated aerodynamic effects of SRP. In Fig. 104, forebody C_p contours from steady-state solutions are compared with time-averaged solutions. In all six cases, the steady-state C_p distributions compare very favorably with the time-averaged C_p distributions. In Fig. 105, C_p along four rays on the forebody and

aftbody from steady-state solutions (black lines) and time-accurate solutions (colored lines) are compared with experimental data (open symbols). In all cases, the steady-state solutions compare favorably with the time-accurate solutions and also with the experimental data. Any differences between the solutions are over very small ranges in C_p and are likely insignificant from the perspective of vehicle performance.

Two other investigations have compared steady-state and time-accurate solutions for these wind tunnel test cases. Bakhtian et al. [66] computed averages of the variations in flow properties from steady, inviscid solution iteration histories to make quantitative comparisons with the time-averaged results from unsteady, Navier-Stokes solutions. While taking the average of variations in steady solution iteration histories is not equivalent to computing the average of variations in unsteady solution time histories, the magnitudes of the oscillations in flow quantities are small, and for these specific cases, the agreement between the two averages was reasonably good. However, no trends were identified within the cases examined by the NASA ETDD Program that suggested steady-state CFD solutions could be used in place of unsteady CFD solutions for integrated force and moment coefficients to reduce computational cost [68]. In some cases, a steady-state solution compared as well as a time-accurate one with the experimental data, where in other cases, it seemed to matter that unsteady effects were captured, possibly a consequence of variations in the numerical models applied in the analysis. However, similar to the results in this chapter, the surface pressures and coefficient values are very small as a result of the shielding of the body by the SRP interaction structures.

If high-fidelity aerodynamic analysis is desired for the design of SRP systems, steady-state CFD analyses are sufficient for determination of static aerodynamic forces and moments. It remains unknown if and how the unsteadiness observed in SRP flowfields affects the dynamics of the vehicle. Additional unsteady CFD analyses and experimental efforts are needed to address this question.

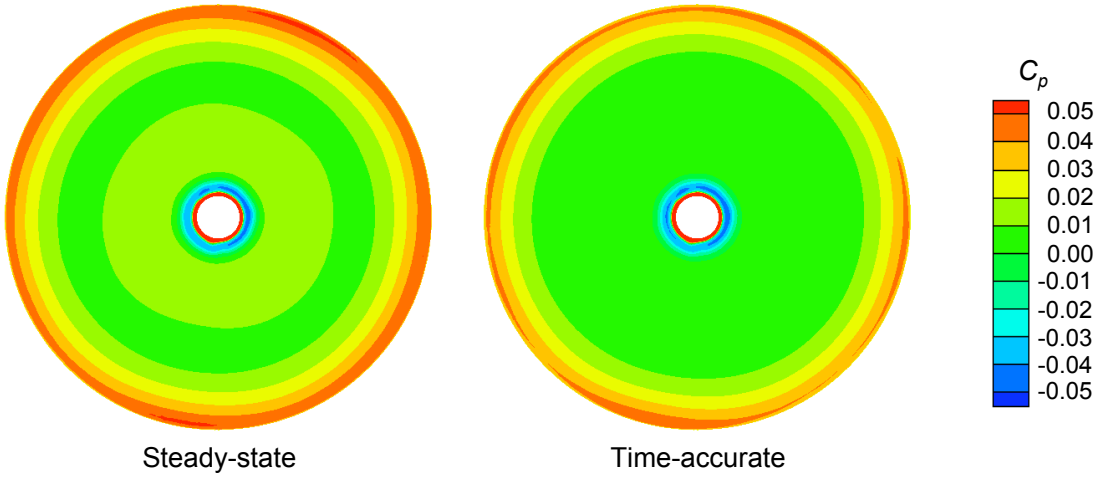

(a) One nozzle configuration, $\alpha = 0°$

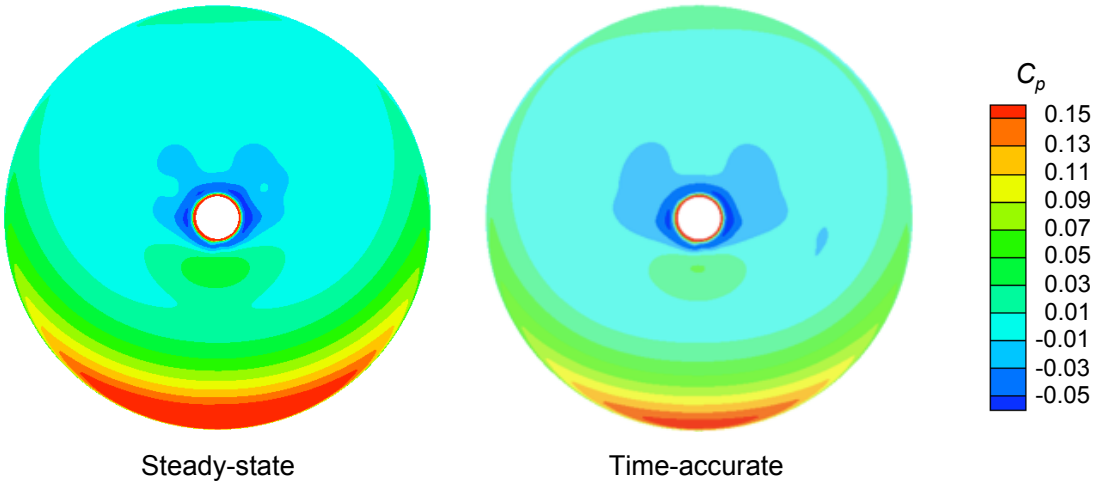

(b) One nozzle configuration, $\alpha = 8°$

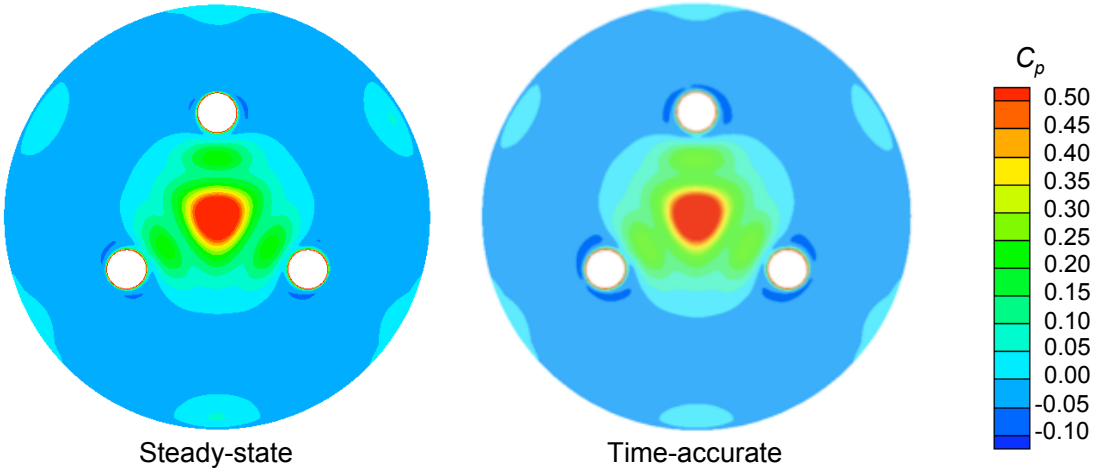

(c) Three nozzle configuration, $\alpha = 0°$

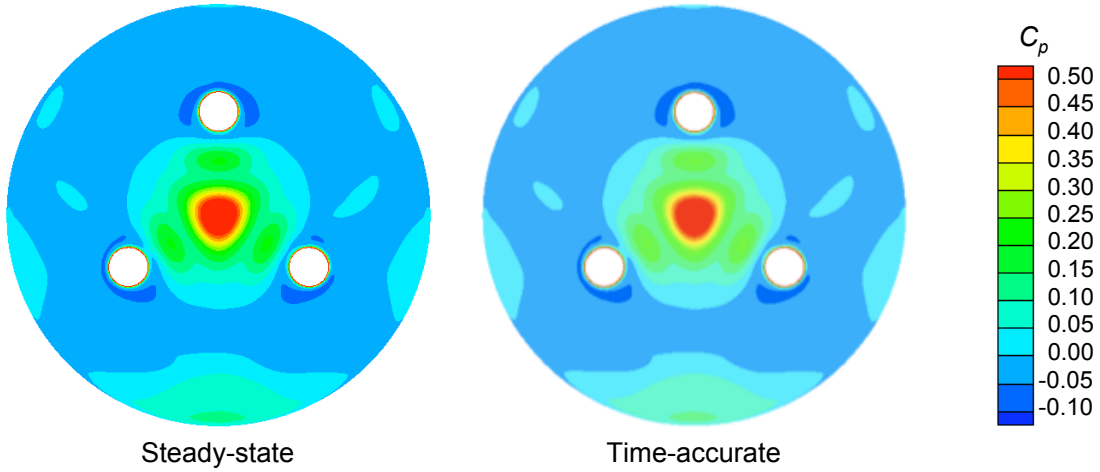

(d) Three nozzle configuration, $\alpha = 8°$

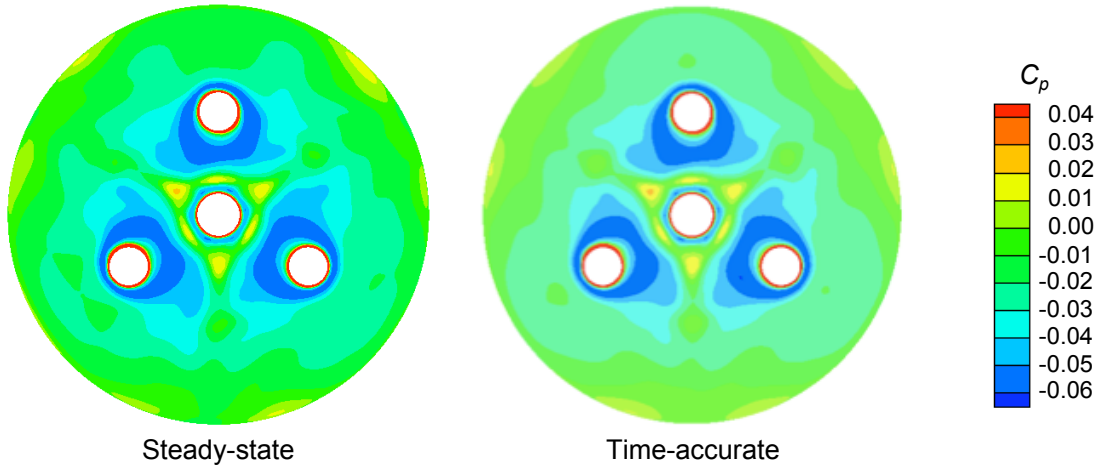

(e) Four nozzle configuration, $\alpha = 0°$

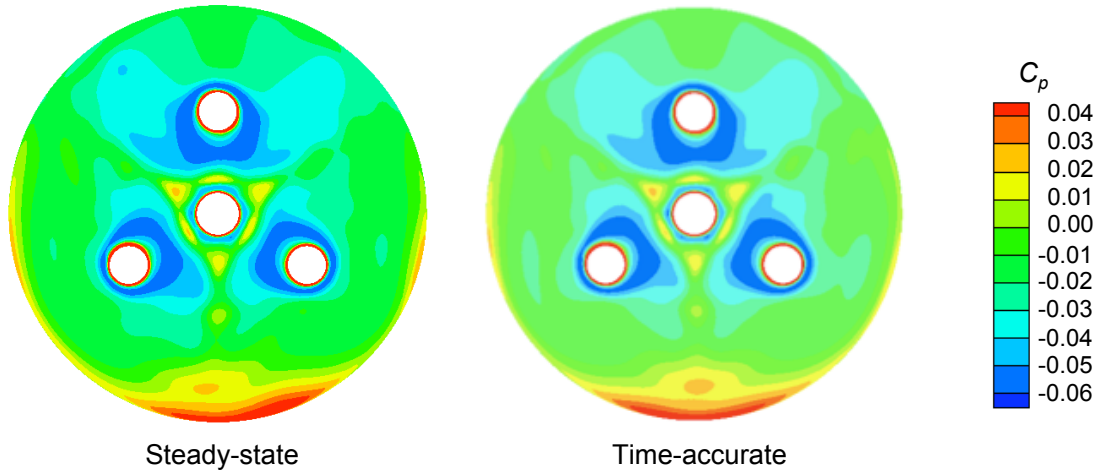

(f) Four nozzle configuration, $\alpha = 8°$

Figure 104: Comparison of forebody C_p contours for steady (left) and unsteady (right) flow solutions.

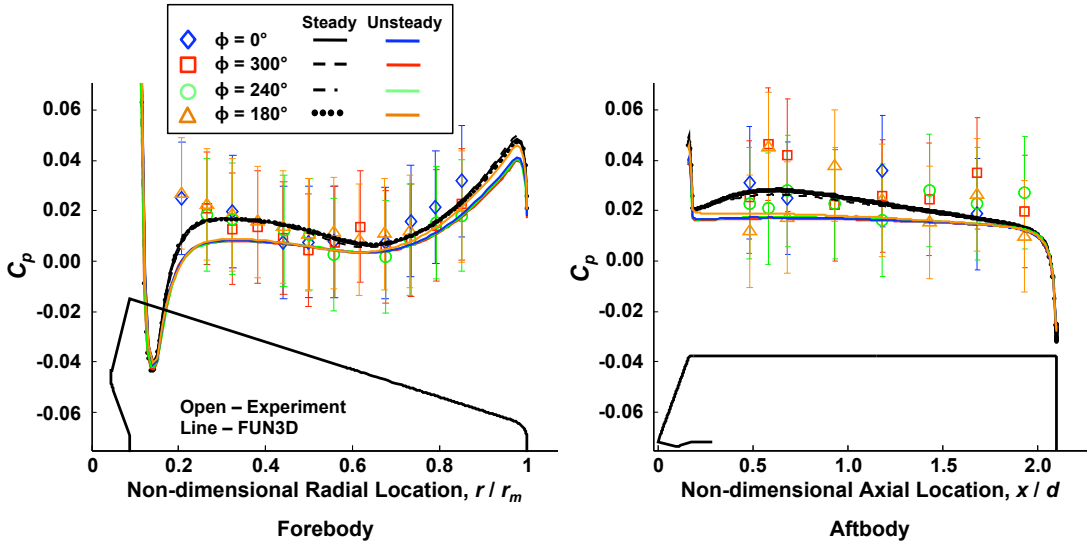

(a) One nozzle configuration, $\alpha = 0°$

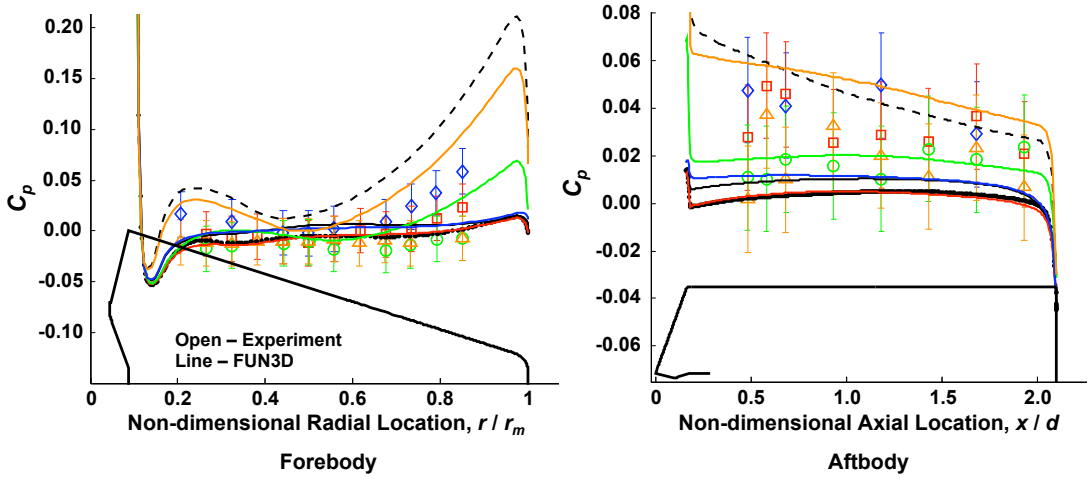

(b) One nozzle configuration, $\alpha = 8°$

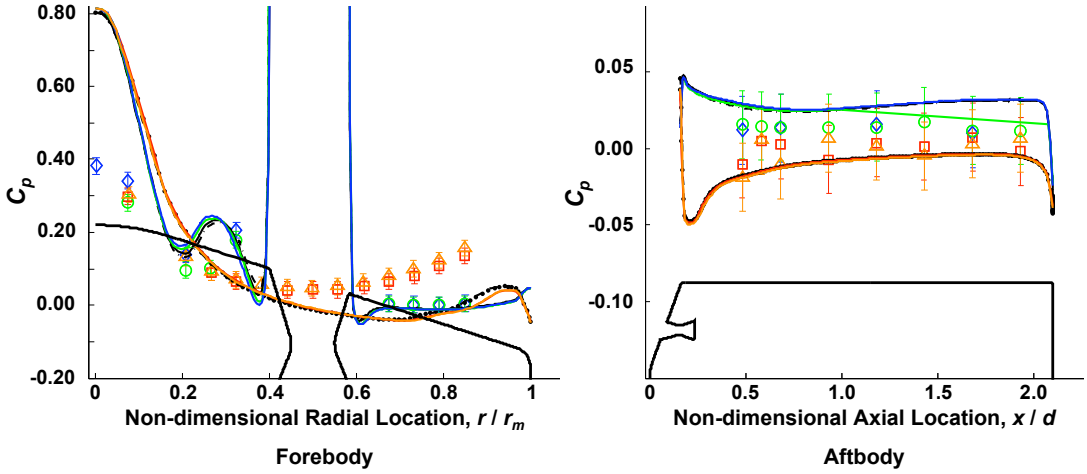

(c) Three nozzle configuration, $\alpha = 0°$

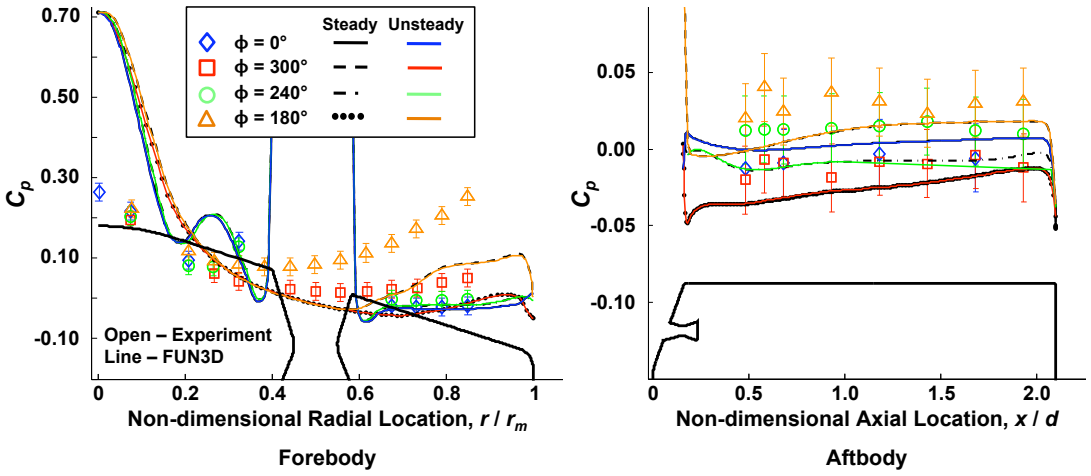

(d) Three nozzle configuration, $\alpha = 8°$

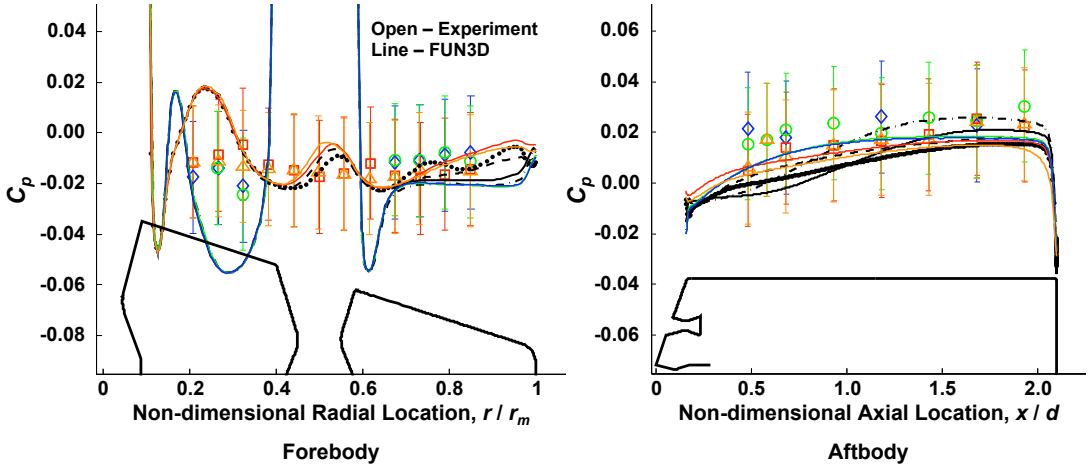

(e) Four nozzle configuration, $\alpha = 0°$

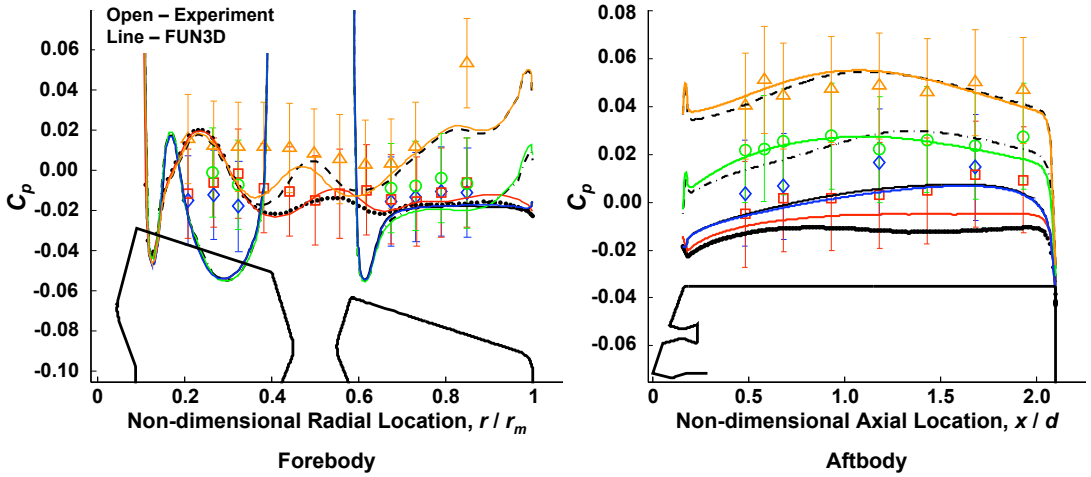

(f) Four nozzle configuration, $\alpha = 8°$

Figure 105: Comparison of C_p for steady and unsteady flow solutions.

5.6 Summary

The work presented in this chapter applied a Reynolds-averaged Navier-Stokes CFD approach to supersonic retropropulsion flowfields. All cases were taken from a recent wind tunnel test of supersonic retropropulsion designed explicitly to provide data for the validation of computational analysis tools. Comparisons of the flowfield structure, flowfield behavior, and static pressure measurements from the test have been made with results generated using FUN3D. Four configurations, two angles of attack, and one test condition ($M_\infty = 4.6$, $C_{T,total} \approx 2$) have been examined using both steady-state and time-accurate approaches.

The general impact of SRP is to severely reduce surface pressures by shielding the body from the freestream flow. Overall, FUN3D and the specific models and approach applied were able to capture the general trends in pressure coefficient on both the forebody and aftbody at angles of attack of 0° and 8°. With the exception of the one nozzle case at $\alpha = 8°$, the computational results showed a consistent, though slight, under-prediction of surface pressures on both the forebody and aftbody, relative to the experimental data set. This is potentially due to the turbulence modeling applied and is an area of further investigation by the CFD community working with supersonic retropropulsion flowfields [16]. An over-prediction of pressures near the nose for the three nozzle configuration was found here and is likely due to not fully capturing the jet expansion and interaction between individual jet flows. Agreement with the experimental data appears to be best for the one nozzle configuration and poorest for the four nozzle configuration, though all disagreements are over very small ranges of C_p.

Unsteady CFD analysis is not needed to determine the quantities of interest in conceptual design. No high-fidelity aerodynamic analyses are needed to determine the boundary conditions and parameters defining nozzle thrust. Empirical models are sufficient for static aerodynamic forces, and steady CFD analysis is sufficient for

determining static aerodynamic moments. Unsteady CFD analyses are only necessary for cases where vehicle dynamics and dynamic SRP interaction effects are of primary interest.

CHAPTER VI

SYSTEM RELEVANCE OF PARAMETERS GOVERNING FLOW INTERACTIONS

Supersonic retropropulsion is just one of many systems within a potential future EDL architecture. Many trades will have to be made before configurations are down-selected, and completion of high-fidelity aerodynamic analyses in support of each trade may be infeasible with current computational capabilities. However, in design, an initial understanding of the significance of SRP configuration on the vehicle's static aerodynamic characteristics and the relation of this configuration to other vehicle performance metrics that traditionally determine vehicle configuration is necessary. Establishing high-level relationships between the flow physics governing SRP and design choices related to vehicle configuration and system performance will also assist in determining the fidelity and effort required to evaluate individual SRP concepts.

Experimental efforts have determined that flowfield structure and flowfield stability for SRP are highly dependent on the retropropulsion configuration, the strength of the retropropulsion exhaust flow relative to the strength of the freestream flow, and the expansion condition of the jet flow. Momentum transfer within the flowfield governs the change in the surface pressure distribution on the vehicle, and accordingly, governs the change in the vehicle's integrated static aerodynamic characteristics. Parameters governing SRP aerodynamics have been identified in this chapter using both experimental trends from the literature and analytical relations of momentum transfer within the SRP flowfield. These analytical relations are specific to highly under-expanded jet flows, contact surfaces, and blunt bodies in supersonic flows.

As discussed in Section 2.1, an expression of the thrust (force) coefficient based on

ideal nozzle thrust can be translated into an expression that is dependent on the ratio of the total pressure of the exhaust flow to the total pressure of the freestream flow, the freestream Mach number, the composition of the freestream and exhaust flows, the nozzle expansion ratio, and the ratio of the nozzle exit area to the reference area of the vehicle. These quantities are directly related to the operating conditions, propulsion system composition, required propulsion system performance, nozzle geometry, and vehicle configuration, all of which are design choices. Investigation into the sensitivities of surface pressures, aerodynamic drag, and total axial force to variation in physical quantities related to vehicle configuration and system performance allows for conclusions to be drawn about the impact of design choices related to system performance on the change in the vehicle's static aerodynamic characteristics.

In this chapter, a momentum-based flow model is developed and then used to assess the relative changes in surface pressure, integrated aerodynamic drag coefficient, and total axial force coefficient. The primary parameters considered are the maximum vehicle T/W, the number of nozzles amongst which the thrust is evenly distributed, and the jet flow composition. The surface pressures and integrated static aerodynamic force coefficients are then determined from the flow model as functions of these design parameters, and the sensitivity of these aerodynamic quantities to design choices is determined.

6.1 Approach

The computational expense of using high-fidelity tools to simulate SRP flowfields prohibits using such tools for high-level trade studies. Development of an approximate model for the SRP aerodynamic - propulsive interaction provides an approach for understanding the relative significance of different design choices. This section discusses the general approach taken to evaluate the sensitivity of aerodynamic drag and total axial force to system-level design choices. Development of the flowfield model used

to obtain these quantities is discussed in Section 6.2.

Design choices to be faced by mission planners include SRP operating conditions (e.g. freestream conditions), the required propulsion system performance (e.g. I_{sp}, $(T/W)_{max}$), propulsion system type (e.g. propellant combination, γ_j), nozzle geometry (e.g. A_e/A^* and potential system packaging impacts), and vehicle configuration (e.g. the number of nozzles distributing thrust). While each of these design choices is related to the others, an effort has been made here to establish a parametric approach to illustrate the significance of specific design choices. Three different physical scales are used to distinguish the effects of SRP and to identify differences arising from vehicle scale and application. These are a human-scale SRP system for a vehicle at Mars, a robotic-scale SRP system for a precursor or technology demonstration mission at Mars, and a sub-scale, cold-gas model for experimentation in a wind tunnel or other Earth-based ground test facility.

The operational envelope for SRP has been defined through analysis determining the optimal trajectories that minimize propulsion system mass (see Chapter 3). The propulsion system performance required to achieve these trajectories is a strong function of the constraints on the analysis. For example, constraining the vehicle $(T/W)_{max}$ to minimize propulsion system mass and volume results in a vehicle $(T/W)_{max}$ approximately three times smaller than constraining the vehicle to a maximum sensed acceleration of 4 (Earth) g's. The smaller $(T/W)_{max}$ results in lower thrust levels and operation at higher freestream Mach numbers. Vehicle $(T/W)_{max}$ is used here as a parameter to represent the operational SRP envelope for a human-scale vehicle, ranging from 3.5 to 10.0 (Mars-relative). This range spans the values of $(T/W)_{max}$ determined in Chapter 3 of this thesis and those used in NASA EDL-SA work [2].

Baseline vehicle concepts utilize multiple nozzle propulsion systems to improve system reliability, provide redundancy, and allow for greater control authority during

powered descent [2]. The results of Chapters 2, 4, and 5 demonstrated that there can be flowfield differences between a single nozzle and multiple nozzles providing the same total thrust. With the dependence of the SRP aerodynamic - propulsive interaction on the relative areas of the nozzle exit and vehicle forebody and the desire to use multiple nozzles on a flight vehicle, the number of nozzles is a design choice. The configuration of multiple nozzles is assumed to consist of equally-spaced nozzles arranged in a ring and aligned parallel with and opposite the freestream flow direction. The change in the vehicle's static aerodynamic performance is explored for cases with the required thrust distributed over 3, 4, 5, and 6 nozzles for a human-scale SRP system. The effect of varying the number of nozzles is also examined for a robotic precursor/technology demonstrator mission.

A full-scale LOX/CH_4 propulsion system capable of satisfying the thrust and throttling requirements defined in NASA mission concepts does not currently exist. However, propulsion system mass and volume for the same ΔV requirement have been shown to be comparable between theoretical LOX/CH_4 systems and existing LOX/RP-1 systems [85]. The differences in SRP flowfield structure are explored for variation in the composition of the exhaust gas. Exhaust gas characteristics representative of different propellant types (LOX/CH_4, LOX/RP-1, and LOX/LH_2) are considered at both full-scale and sub-scale. The emphasis is on changes in the aerodynamic properties of the nozzle flow that would arise as propulsion system types are traded.

6.2 Flowfield Model Development

This section describes the development of an approximate model for the SRP aerodynamic - propulsive interaction. The flow model is derived from a momentum - force balance at the contact surface and the geometry of the jet flow, body, and contact surface. All assumptions about the structure of the SRP flowfield are consistent with

the discussion presented in Chapter 2 (see Section 2.1 and Fig. 8). Elements of the flow model leverage analytical work in the literature. The flow model structure is directly based on analytical and experimental work by Finley [7] in the mid-1960s. Finley's model is strictly limited to hemispherical bodies, sonic nozzles, air as the composition of the freestream and jet flows ($\gamma_\infty = \gamma_j = 1.4$), a single, central nozzle, and small jet structures relative to the diameter of the body. In this section, Finley's original model is re-derived to generalize the flow model to $M_e > 1$, γ_j and γ_∞ other than 1.4, multiple nozzles on the forebody, and forebody shapes other than hemispheres. These modifications extend the applicability of the flow model to the conditions and geometries more relevant to SRP system design.

6.2.1 Overview of Aerodynamic - Propulsive Interaction Model

Figure 106 illustrates the structure and progression of steps for the SRP flow model. Inputs to the model are the freestream conditions (M_∞, γ_∞, $p_{0,\infty}$, $T_{0,\infty}$), nozzle conditions (γ_j, $p_{0,j}$, $T_{0,j}$), nozzle geometry (A_e/A^* or d_e), and body geometry (d_{body}, r_n). Outputs from the model are the surface pressure (excluding the nozzle exit plane), forebody integrated drag coefficient, and forebody axial force coefficient. There are two main elements to the SRP flow model. The first is a control surface analysis for the momentum - force balance at the contact surface. The second is an analysis based on the flowfield geometry to match the contact surface to the body.

Integration of pressures over the control surface yields the force on the control surface. The summation of the jet flow entering the control surface and the flow in the jet layer exiting the control surface yields the total momentum flux out of the control surface. The diameter of the contact surface, $d_{cs,M-F}$, is then determined from the momentum - force balance. The definition of the control surface and additional details and discussion on this element of the flow model are given in Section 6.2.2.

The flowfield geometry analysis establishes the diameter and axial location of the

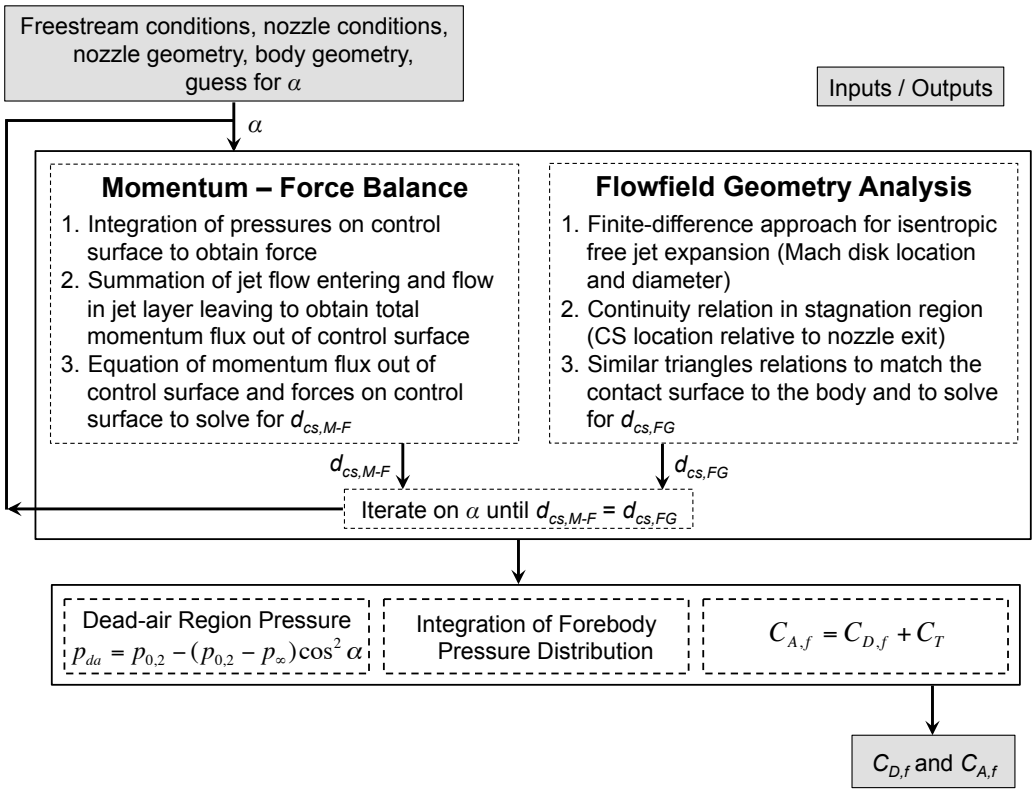

Figure 106: General structure of the flow model for describing the SRP aerodynamic - propulsive interaction.

contact surface from the physics and structure of the jet interaction region. The Mach disk location and diameter are provided by an analytical finite-difference approach developed by Salas [30]. A continuity relation is applied in the stagnation region to determine the location of the contact surface, relative to the nozzle exit. Similar triangles are then used to match the contact surface to the body, yielding the diameter of the contact surface, $d_{cs,FG}$. Additional details and discussion on the flowfield geometry analysis are given in Section 6.2.3.

There are two independent variables in the analysis: P and α. P is specified by the conditions of interest, namely the total pressure of the jet and the freestream conditions ($P = p_{0,j}/p_{0,2}$). The half-angle of the cone partially defining the shape of the contact surface is defined to be the angle α that permits the diameter of the

blunting sphere of the contact surface (determined from conservation of momentum within the flowfield) to be equal to the diameter of the blunting sphere of the contact surface determined from the structure of the jet. The model iterates on α until $d_{cs,M-F}$ matches $d_{cs,FG}$.

The pressure distribution on the contact surface is then determined as a function of α and the pressure in the recirculation region (see Fig. 8) by assuming modified-Newtonian theory. To determine the surface pressure distribution on the body, the pressure in the recirculating region is assumed to be a uniform pressure acting over the entire forebody surface outboard of the nozzle(s) with the exception of the nozzle exit area(s). Following Finley's original notation, this pressure is referred to as the 'dead-air' pressure, p_{da}, and calculated using the equation shown in Fig. 106.

Recalling experimental observations of surface pressures dropping to near-constant values outside of the nozzle and over much of the forebody for moderate to high jet pressure ratios (see Chapters 4 and 5), the pressure distribution across the forebody is assumed to be constant; no model for pressure recovery toward the shoulder has been implemented. The forebody drag coefficient, $C_{D,f}$ is then calculated by integrating the surface pressure distribution, excluding the nozzle exit area(s). With all cases defined to be at zero angle of attack, the total axial force coefficient, $C_{A,f}$, is then determined as the sum of $C_{D,f}$ and C_T.

The flow model has been verified against analytical results from Finley [7] and validated against experimental results from multiple sources, including a recent NASA wind tunnel test [7, 14, 26, 51]. In the development of the model, the flow is assumed to be steady, inviscid, isentropic, and behave as a calorically perfect gas. The flowfield is assumed to be axisymmetric. Sections 6.2.2 - 6.2.4 discuss the flow model in detail, including the historical references on which portions of the analysis are based, modifications made to Finley's original flow model, and the solution process for the surface pressure and integrated aerodynamic drag and total axial force coefficients for

the forebody. A block diagram illustrating the detailed solution process for the flow model is given at the end of Section 6.2.4.

6.2.2 Momentum - Force Balance Analysis

The first portion of the overall flowfield analysis is a momentum - force balance at the contact surface. Figure 107 (reproduced here from Chapter 2) shows the general characteristics of an SRP flowfield with a single nozzle at the center of a blunt body, indicating the locations of the bow shock, contact surface, and Mach disk. Adapted from Finley [7], Fig. 108 shows the control surface (dashed line and labeled) to which the momentum - force balance is applied and illustrates the geometric relationship between the contact surface and the body.

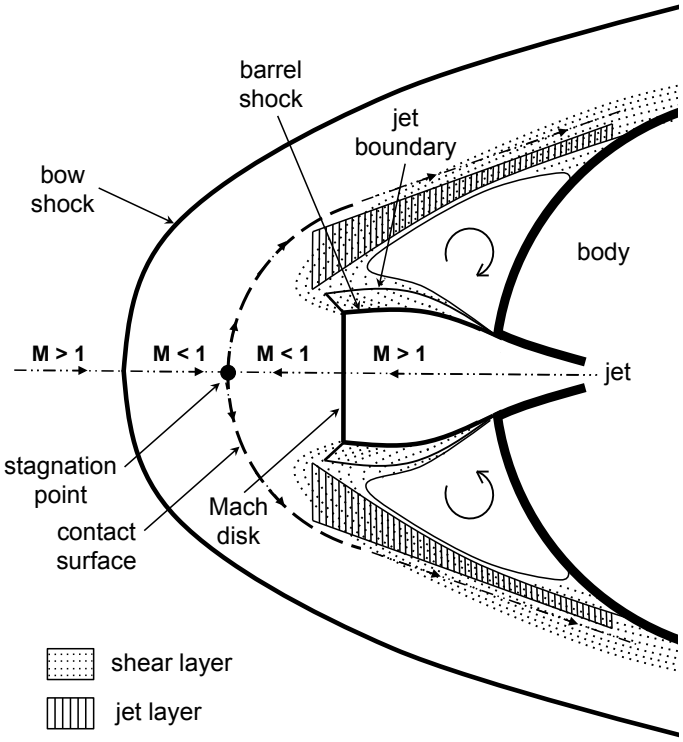

Figure 107: SRP flowfield structure for a single, central jet. (Also shown as Fig. 8 in Chapter 2).

Based on supporting evidence from Van Dyke and Gordon [108] and Finley [7], the contact surface is assumed to be spherical, with a radius of $1/2\ d_{cs}$. The control surface

is defined to be a spherically-blunted cone, including the contact surface and exit plane of the nozzle as well as enclosing the entire jet structure. The pressure everywhere inside of the control surface is defined to be equal to the 'dead-air' pressure, p_{da}. The pressure on the spherical portion of the control surface is the difference between the pressure at the stagnation point, $p_{0,2}$, and p_{da}. The conical portion of the control surface is defined by the cone half-angle, α. The pressure on the conical portion of the control surface is equal to p_{da}, with the exception of the nozzle exit, where the pressure is equal to p_e.

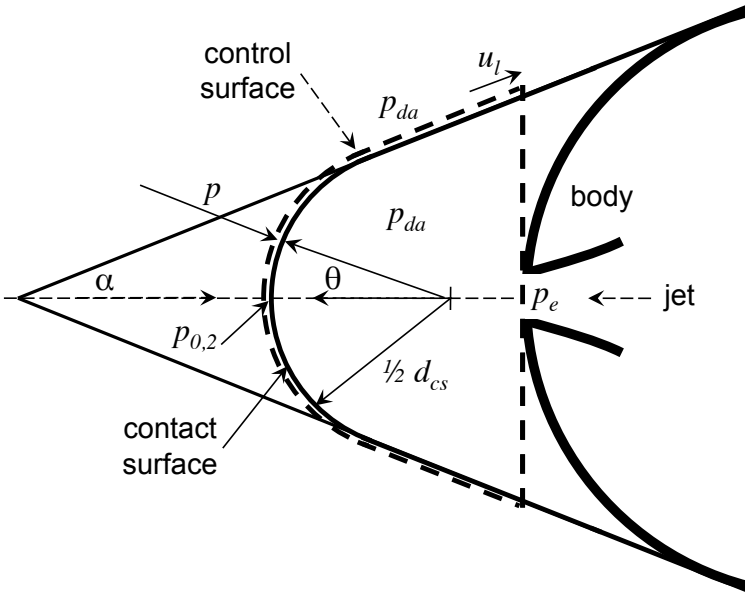

Figure 108: Control surface for the momentum - force balance analysis. (Adapted from [7]).

While not strictly applicable, to allow for closed-form analysis, the pressure distribution on the contact surface is approximated through use of modified-Newtonian theory. For SRP flowfields, the contact surface separates the post-shock freestream flow and the jet flow. The pressure forces on the contact surface must be balanced by the momentum fluxes and pressure forces from multiple sources: the jet flow entering the control surface, the flow in the jet layer exiting the control surface, and the nose of the body.

Integrating the pressure on the control surface yields the force portion of the momentum - force balance:

$$F = \int_0^{90^\circ-\alpha} (p_{0,2} - p_{da}) cos\theta \left[2\pi \left(\frac{d_{cs}}{2}\right) sin\theta\right] \left(\frac{d_{cs}}{2}\right) \mathrm{d}\theta - \left(\frac{\pi}{4}\right) d_e^2 (p_e - p_{da}) \quad (15)$$

If ϕ is the local inclination angle of the spherical portion of the control surface relative to the freestream direction, modified-Newtonian theory gives the following expression, which can be solved for the pressure on a spherical surface:

$$C_p = C_{p,max} sin^2\phi = C_{p,max} sin^2\theta$$

$$C_p = \frac{2}{\gamma M_\infty^2} \left\{ \left[\frac{(\gamma+1)^2 M_\infty^2}{4\gamma M_\infty^2 - 2(\gamma-1)} \right]^{\frac{\gamma}{\gamma-1}} \left(\frac{1-\gamma+2\gamma M_\infty^2}{\gamma+1} \right) - 1 \right\} sin^2(90^\circ - \alpha)$$

$$\begin{aligned} \frac{p_{0,2} - p_{da}}{q_\infty} &= \frac{2}{\gamma M_\infty^2} \left(\frac{p_{0,2}}{p_\infty} - 1 \right) cos^2\alpha \\ &= \frac{2}{p_\infty \gamma M_\infty^2} (p_{0,2} - p_\infty) cos^2\alpha = \frac{p_{0,2} - p_\infty}{q_\infty} cos^2\alpha \quad (16) \\ p_{0,2} - p_{da} &= (p_{0,2} - p_\infty) cos^2\alpha \end{aligned}$$

Substituting the final form of Eq. 16 into Eq. 15:

$$F = \int_0^{90^\circ-\alpha} (p_{0,2} - p_\infty) sin^2\theta cos\theta \left[2\pi \left(\frac{d_{cs}}{2}\right) sin\theta\right] \left(\frac{d_{cs}}{2}\right) \mathrm{d}\theta - \left(\frac{\pi}{4}\right) d_e^2 (p_e - p_{da}) \quad (17)$$

Integrating and rewriting in terms of the cone half-angle, α:

$$F = \left(\frac{\pi d_{cs}^2}{8}\right) (p_{0,2} - p_\infty) cos^4\alpha - \left(\frac{\pi}{4}\right) d_e^2 (p_e - p_{da}) \quad (18)$$

The total momentum flux out of the control surface is the net result of the jet flow entering the control surface and the flow from the jet layer leaving the control surface:

$$\frac{d(mu)}{dt} = \dot{m}_e u_e + \dot{m}_l u_l cos\alpha \quad (19)$$

Combining Eq. 18 and Eq. 19 yields the complete expression for the momentum - force balance on the control surface:

$$\left(\frac{\pi d_{cs}^2}{8}\right) (p_{0,2} - p_\infty) cos^4\alpha - \left(\frac{\pi}{4}\right) d_e^2 (p_e - p_{da}) = \dot{m}_e u_e + \dot{m}_l u_l cos\alpha \quad (20)$$

Recall from Eq. 16 that the assumption of modified-Newtonian theory can be applied to determine the pressure distribution on the contact surface. The 'dead-air' pressure, p_{da}, in terms of α, can be expressed as:

$$p_{da} = p_{0,2} - (p_{0,2} - p_\infty)\, cos^2\alpha \tag{21}$$

The same assumption made by Finley [7] for the total momentum of the flow in the jet layer is also assumed here, namely that the total momentum of the flow in the jet layer is equal to the momentum of the jet mass flow expanded isentropically and uniformly from $p_{0,2}$ to p_{da}. This assumption requires $\dot{m}_e$ to be equal to $\dot{m}_l$ in Eq. 20. Using isentropic relations for the ratio $p_{0,2}/p_{da}$, the Mach number and static temperature of the flow in the jet layer exiting the control surface are determined, assuming all properties of the jet mass flow to be maintained ($T_{0,j}$, R_j, γ_j). This allows for the determination of the velocity of the flow in the jet layer exiting the control surface, u_l. Finally, all of the necessary quantities to determine the diameter of the spherical contact surface, d_{cs}, from Eq. 20 are known. Note that the non-uniformity in the total pressure distributions due to the shock structure in the jet is neglected throughout this analysis.

6.2.3 Flowfield Geometry Analysis

The cone half-angle used in Section 6.2.2 to define the conical section of the control surface cannot be uniquely determined from the momentum - force balance alone. Determination of the distance of the contact surface from the body and matching of the contact surface to the body are also required. Using geometric relationships for the jet structure, contact surface, and body, the diameter of the spherical contact surface, d_{cs}, can be determined separately from the momentum - force balance as a function of the cone half-angle, α. For a given set of conditions, there is one α for which the diameter of the contact surface is the same by both approaches.

6.2.3.1 *Distance of the Contact Surface from the Body*

Figure 109, adapted from Finley [7], shows the generic geometry of the jet structure in relation to the contact surface and the body. As described earlier, the jet flow is assumed to have a structure consistent with highly under-expanded jet flow, terminating with a Mach disk and bounded by a barrel shock.

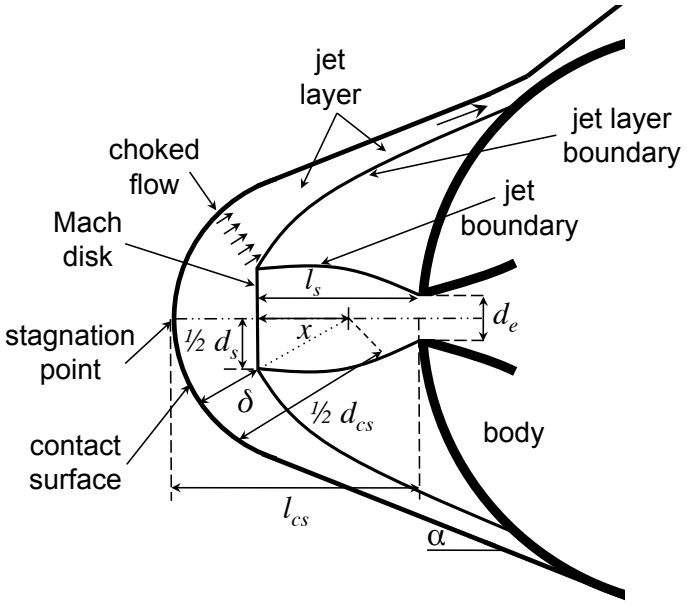

Figure 109: Flowfield geometry used to determine the location of the contact surface. (Adapted from [7]).

In Finley's model, empirical relationships were used for the Mach disk location and diameter. These relationships are valid for sonic jets and $\gamma_j = 1.4$ only. For the analysis in this chapter, these empirical relationships have been replaced with an inviscid, axisymmetric, under-expanded plume solver developed by Salas [30] that is valid for any M_e and γ_j. While most of the analytical work in the literature on the structure of under-expanded jets is based on the method of characteristics, Salas' approach uses a finite-difference, downstream marching technique. Shocks and contact surfaces within the flow are treated explicitly as discontinuities, and the approach is applicable to both uniform and conical nozzle flows [30]. The jet is assumed to

develop as an equivalent free-jet, expanding from $p_{0,j}$ to p_{da} and terminating with a Mach disk. The Mach disk is in the plane that intersects the jet axis at a distance l_s from the nozzle exit plane.

The theory developed by Abbett [31] is applied to determine the location of the Mach disk within Salas' plume solver. Abbett divides the flow into two parts: (1) a quasi-one-dimensional streamtube along the centerline, and (2) the rest of the flow. On the nozzle exit side of the Mach disk, there is a supersonic streamtube that interacts with the supersonic flow outside of the streamtube. On the contact surface side of the Mach disk, there is a subsonic core flow. Abbett's theory requires the subsonic core flow to be accelerated smoothly through a sonic condition with a minimum cross-sectional area to become supersonic.

An iterative procedure using the location of the Mach disk as a parameter is applied to satisfy a sonic condition in solving for the Mach number distribution along the centerline of the jet flowfield [31]. The Mach disk axial location can be used to find initial conditions for the subsonic region in solving for the jet flowfield. In the flow solution, the throat-like region behaves as a saddle-point singularity, and the parameter value resulting in the saddle-point singularity identifies the location of the Mach disk along the centerline [30, 31].

Unlike other theories based strictly on a pressure differential, Abbett's theory allows the Mach disk location to be dependent on the downstream conditions, consistent with the subsonic nature of the flow in the region downstream of the nozzle exit [30]. Salas found Abbett's theory to agree most consistently and most accurately with experimental data, as compared with three alternative theories for the boundary condition necessary to determine the location of the Mach disk [30].

Figure 110 compares the Mach disk location and diameter determined from Salas' approach to experimental data from Love et al. [26] for three different exit Mach numbers. The nozzle flow ($\gamma_j = 1.4$) is exhausting from a contoured nozzle (parallel

exit flow) into an ambient environment at atmospheric pressure. The results from Salas' approach show minor over-predictions for the Mach disk location and diameter as the jet pressure ratio increases, though the overall trends agree well with the experimental data.

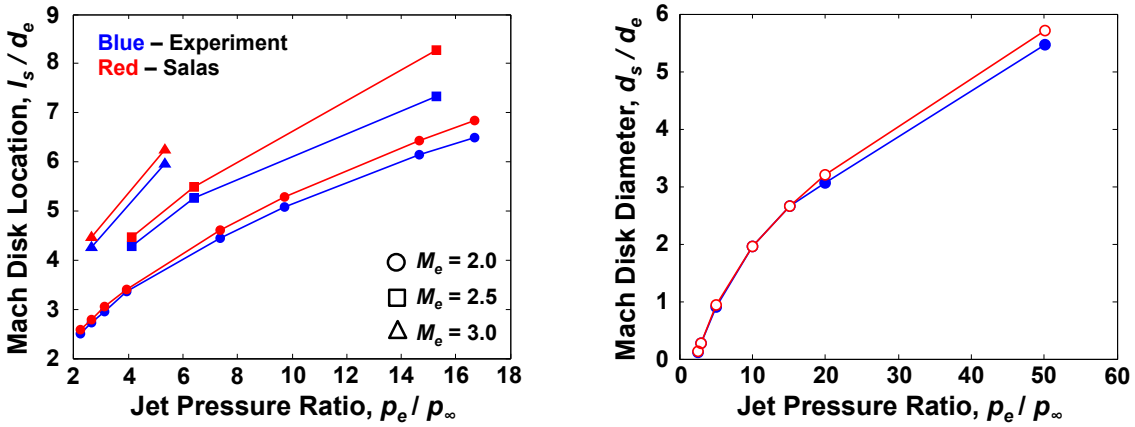

Figure 110: Comparison of the Mach disk location (left) and diameter (right) determined via Salas' approach with experimental data for contoured nozzles exhausting into an atmospheric pressure environment.

Figure 111 compares the integrated drag and axial force coefficient results from the flow model for Salas' analytical approach and Finley's empirical relations in determining the location and diameter of the Mach disk. For reference, Finley's empirical expressions are given in Eq. 22 (based on work by Owen and Thornhill [109] and Ashkenas and Sherman [110]) and Eq. 23 (based on data from Love et al. [26]). The results shown in Fig. 111 assume a hemispherical forebody, $M_e = 1.0$, and $\gamma_j = 1.4$. The behaviors of $C_{D,f}$ and $C_{A,f}$ as C_T increases are very similar, with the curves diverging for only very low C_T. For C_T greater than approximately 0.4, the difference in the integrated results is considered to be negligible.

$$L_s = \frac{l_s}{d_e} = 0.77P^{1/2} \tag{22}$$

$$D_s^2 = \left(\frac{d_s}{d_e}\right)^2 = 0.3 + 0.325P\left(\frac{p_{da}}{p_{0,2}}\right)^{-1} \tag{23}$$

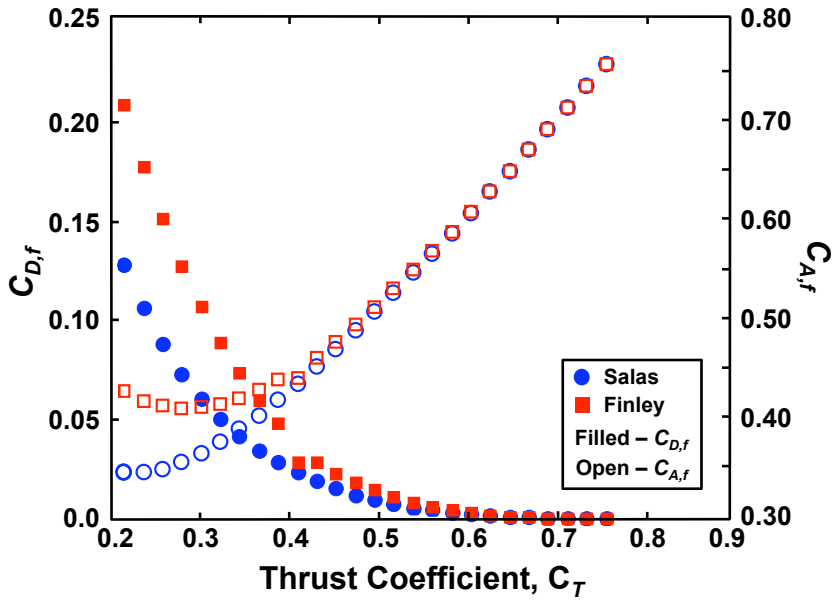

Figure 111: Comparison of the integrated $C_{D,f}$ and $C_{A,f}$ using two different approaches for determining the Mach disk location and diameter. Salas' approach is a higher fidelity under-expanded jet flow solver, and Finley's empirical relations are those given by Eqs. 22 and 23.

The flow exiting the Mach disk in the stagnation region is assumed to be uniform with a total pressure equal to $p_{0,2}$. This flow is then assumed to be choked in an annulus of mean diameter d_s and width δ (see Fig. 109) and uniform in the direction tangent to the contact surface. Recalling the CFD solutions given in Chapters 4 and 5, the jet flow on the subsonic side of the Mach disk turns outboard and accelerates downstream of the stagnation region. As the flow accelerates, it reaches a critical point, and the flow in this annular region becomes choked.

Finley suggests that this behavior is analogous to the behavior in the region between the stagnation point and sonic line for a blunt body in supersonic flow (see Fig. 4 in Chapter 2). In earlier work, Moeckel [111] suggested the flow from the stagnation point to the sonic line to be similar to flow past the throat section of supersonic nozzle. In the case of one-dimensional, isentropic, and non-reacting flow, the location of the maximum constriction (the shoulder of a blunt body or the throat of a supersonic nozzle) coincides with the critical point, either on the body or within a

nozzle. In developing the original flow model, Finley assumed the critical point to be the outer boundary of the annular region, labeled as choked flow in Fig. 109. Under this assumption, a continuity relationship developed originally by Moeckel [111] and trigonometric relations derived by Love [34] are then applied to determine the height of the annular region, δ.

The total pressure and total temperature remain constant between the Mach disk and the critical point under the stated assumptions. In agreement with Finley [7], the annulus of choked flow is assumed to have an average diameter equal to d_s and height equal to δ. The expression for δ (Eq. 25) is generalized here for $M_e > 1.0$ and values of γ_j other than 1.4. The jet flow is assumed to decelerate from M_e to $M = 1.0$ isentropically. The continuity relationship and equation for δ are given in Eqs. 24 and 25, respectively.

$$\begin{aligned} \rho_e u_e A_e &= \rho_l u_l A_l \longrightarrow \\ \frac{A_e}{A_{l,choked}} &= \frac{(\rho_l u_l)_{choked}}{\rho_e u_e} = \left(\frac{p_{0,2}}{p_{0,j}}\right)_{choked} \left[\frac{(\rho u)_{cr}}{\rho_e u_e}\right] \\ &= \left(\frac{p_{0,2}}{p_{0,j}}\right)_{choked} \left(\frac{A_e}{A^*}\right) = \frac{\left(\frac{\pi}{4} d_e^2\right)}{2\pi \left(\frac{d_s}{2}\right) \delta} = \frac{d_e^2}{4 d_s \delta} \end{aligned} \tag{24}$$

$$\delta = \left(\frac{1}{4}\right) \left(\frac{d_e^2}{d_s}\right) \left(\frac{p_{0,j}}{p_{0,2}}\right) \left(\frac{A_e}{A^*}\right)^{-1} \tag{25}$$

The distance x is determined from (by the Pythagorean theorem):

$$\left(\frac{1}{2} d_{cs} - \delta\right)^2 = x^2 + \left(\frac{1}{2} d_s\right)^2 \tag{26}$$

The location of the contact surface, relative to the nozzle exit, is then given by the distance l_{cs}, shown in Fig. 109. This distance can be determined from:

$$l_{cs} = \frac{1}{2} d_{cs} + (l_s - x) \tag{27}$$

6.2.3.2 Matching the Contact Surface to the Body

Assuming the jet layer is thin near reattachment, the contact surface is matched to the body by determining the value of d_{cs} for which the spherical segment of the contact surface is tangent to the conical interface boundary. The cone half-angle, α, then defines the position of the conical interface boundary. For any distance l_{cs}, there will be only one diameter d_{cs} such that the spherical segment of the contact surface is tangent to the conical interface boundary. This geometry is shown in Fig. 112, adapted from Finley [7]. By using similar triangles from the geometry shown in Fig. 112, an expression for d_{body}/d_{cs} can be derived for a spherical body. This expression is given by Eq. 28 and can be directly solved for d_{cs}. Equation 29 is the same relationship as that given in Eq. 28, rewritten in terms of D ($D = d_{body}/d_e$).

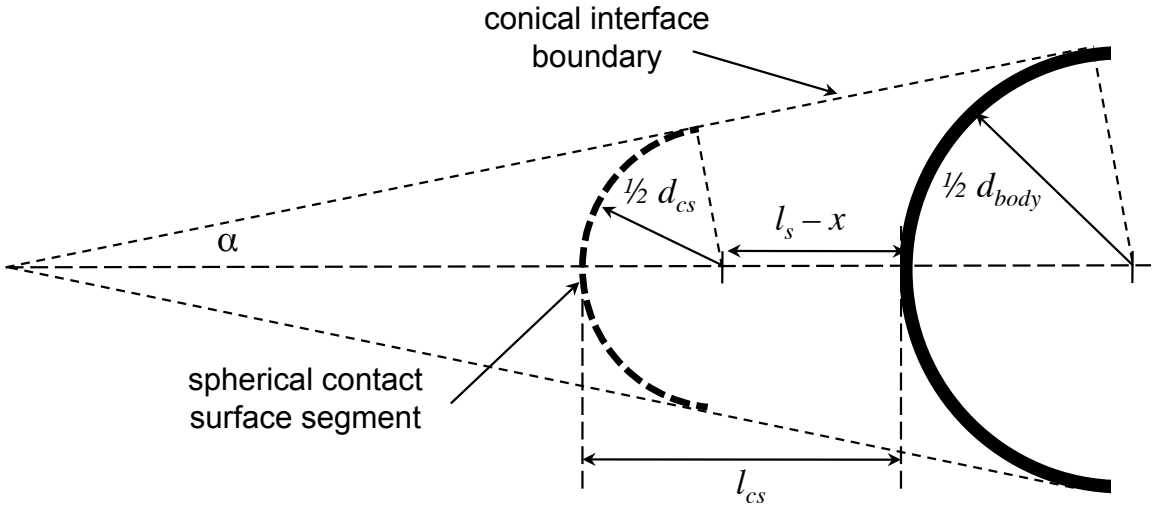

Figure 112: Geometry for matching the contact surface to the body. (Adapted from [7]).

$$\frac{d_{body}}{d_{cs}} = \frac{\left(\frac{d_{cs}}{2sin\alpha} + \frac{1}{2}d_{body} - l_s - x\right)}{\frac{d_{cs}}{2sin\alpha}} \tag{28}$$

The above expression can also be written in terms of D:

$$D = \frac{d_{body}}{d_e} = \frac{\left[\frac{d_{cs}}{d_e} + 2sin\alpha\left(\frac{l_s}{d_e} - \frac{x}{d_e}\right)\right]}{4 - sin\alpha} \tag{29}$$

Equation 28 requires the diameter of the contact surface to be smaller than the diameter of the body (see Fig. 112). As the jet total pressure increases, the diameter of the jet and the diameter of the contact surface increase as well. As this occurs, the body is shielded more and more completely from the freestream. Experimental data has shown that as the total pressure of the jet flow increases, the forebody pressures decrease, eventually reaching and maintaining a minimum as the contact surface completely replaces the body as the freestream flow obstruction. The limit is assumed to be reached in this analysis as $\alpha \rightarrow 0°$.

Recall that P and α are the independent variables in solving for the pressure distribution on the contact surface. P is fixed by the thrust coefficient and freestream conditions of interest. The solution for a particular condition is the value of α resulting in d_{cs}/d_{body} matching for both methods (momentum - force balance and jet - contact surface geometry). The 'dead-air' pressure, p_{da}, is then found from Eq. 21. The aerodynamic drag coefficient, $C_{D,f}$, is calculated by integrating p_{da} over the forebody surface, excluding the nozzle exit area(s). As all cases are at zero angle of attack, the total axial force coefficient, $C_{A,f}$ is given by the sum of $C_{D,f}$ and C_T.

Verification of the flow model for a single jet exhausting from the nose of a hemisphere at zero angle of attack is shown in Fig. 113. The flow model developed in this chapter is consistent with Finley's model in the prediction of the distance of the contact surface from the exit plane of the nozzle. The agreement with the experimental data begins to deteriorate as C_T increases beyond 0.1 for these specific conditions, though the trend appears to be approximately captured. Additional comparisons of results from the flow model developed in this chapter with modern experimental data

are presented in Section 6.2.4.2. Replacing the assumption (known to be inaccurate) of an analogy based on linear sonic lines for the annular stagnation region with a more sophisticated approach using an analogy based on non-linear sonic lines to establish the momentum of the jet flow within the jet layer may improve agreement of the flow model with the experimental data. However, no such modification has been included in this analysis.

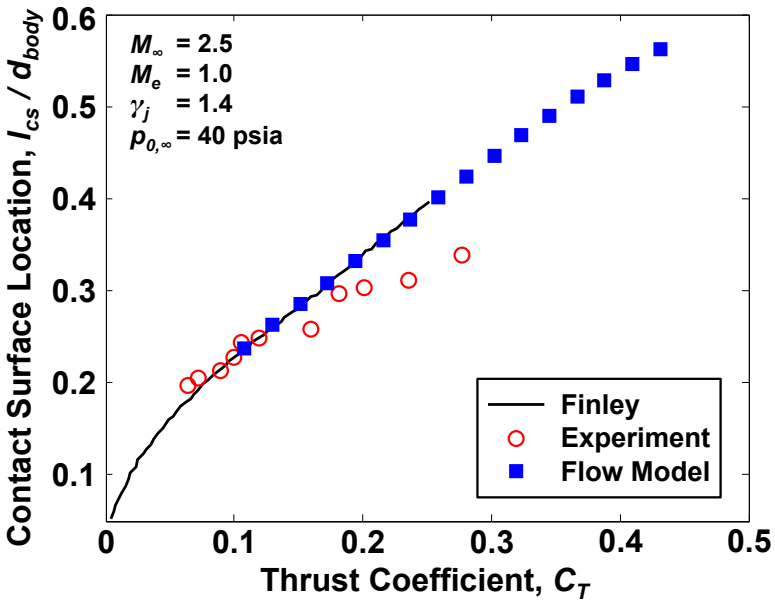

Figure 113: Verification of the flow model through comparison with Finley's original results. Experimental data from [7] are also shown.

Figure 114 shows the comparison of p_{da} as predicted by the flow model and p_{da} as measured experimentally by Finley [7] for a hemisphere with a single, central nozzle. The experimental data points are for the lowest measured pressures on the body [7]. For a range of pressure ratios, $p_{0,j}$ / $p_{0,2} = 1.0$ to 4.0, the 'dead-air' pressure predicted by the flow model is within 0.83 psi of the experimental 'dead-air' pressure, though the flow model is consistently over-predicting p_{da} across these conditions.

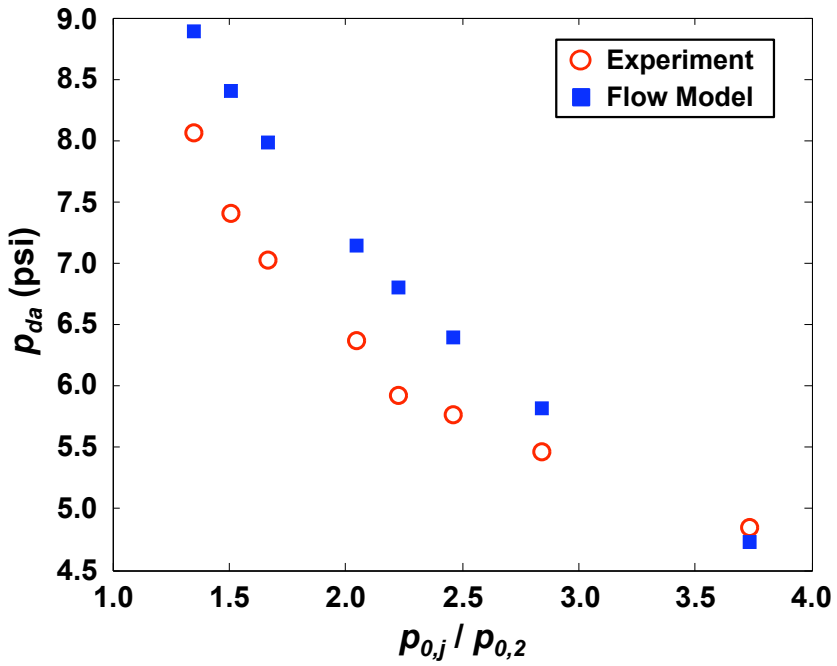

Figure 114: Comparison of p_{da} as predicted by the flow model and as measured via experiment for a configuration with a single, central nozzle. Experimental data are from work by Finley [7] for $M_\infty = 2.5$, $p_{0,\infty} = 40$ psi, $M_e = 1.0$, $\gamma_\infty = \gamma_j = 1.4$.

6.2.4 Additional Modeling

In addition to generalizing Finley's original model to $M_e > 1$ and γ_j other than 1.4, a number of other modifications have been made to extend the flow model's applicability to the design choices of interest. These modifications include the capabilities to use axisymmetric forebody shapes other than hemispheres and to approximate a ring of multiple nozzles on the forebody. A block diagram illustrating the detailed solution process for the complete flow model is given at the end of this section.

6.2.4.1 Additional Forebody Geometries

To consider forebody geometries other than hemispheres, assuming no significant changes in the geometry of the contact surface, Finley [7] provided an expression where a plane projection was applied to the geometry in Fig. 112 for the geometry of interfaces meeting spheroids other than hemispheres. The equivalent bodies must

pass through the same nozzle exit plane and meet a given interface at the same angle. If D_{equiv} is the value of D for a spherical body equivalent to a spheroidal body of D and λ:

$$\frac{D_{equiv}}{D} = \frac{\lambda - (\lambda^2 + \cot^2 \alpha)^{1/2}}{1 - \csc \alpha} \tag{30}$$

The fineness ratio, λ, is the ratio of the elliptical semi-axes parallel and normal to the freestream, respectively. For non-spheroidal bodies, such as sphere-cones, λ is approximated using the axial distance from the nose to the end of the forebody as the parallel axis and the radial distance from the centerline to the shoulder as the normal axis. Flat-faced bodies have a λ of zero.

6.2.4.2 Multiple Nozzles

The flow model described in Sections 6.2.2 and 6.2.3 is nominally for an SRP configuration with a single, centrally-located nozzle on a blunt forebody. More realistic vehicle concepts with SRP generally utilize more than one nozzle. These SRP configurations can be approximated as a cluster or ring of equally-spaced nozzles at some radial distance from the nose. Gilles and Kallis [17] developed a simple modification to the analysis for a single jet that predicts the Mach disk location for a cluster of nozzles, validating their predictions against experimental results with reasonable accuracy. The cluster of jets is converted to an equivalent single jet with the same total mass flow rate. If there are n nozzles in the cluster, then the equivalent single jet has an exit diameter that is $n^{1/2}$ times greater than the exit diameter of a single nozzle in the cluster, or $d_{e,eq} = d_e n^{1/2}$. Given that the physical dimensions of jets with equal nozzle exit conditions scale linearly with nozzle diameter, the location of the Mach disk, $l_{s,eq}$, is then given by $l_s n^{1/2}$. This assumes that the outer jet boundary defined by the cluster of jets is not dependent on the inboard interactions of the individual jet boundaries. Peterson and McKenzie [9] followed an analogous modification with similarly agreeable results. Figure 115 illustrates the simplified flowfield geometry for

this modification.

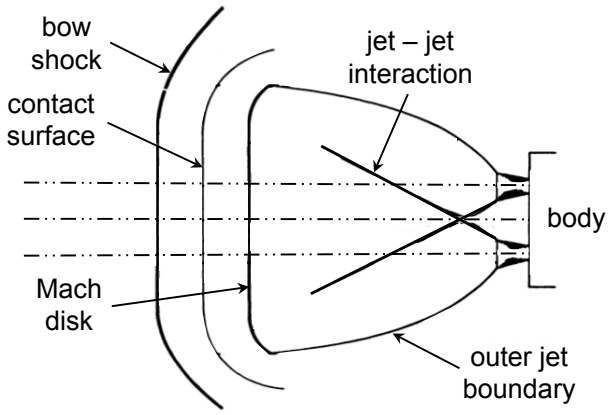

Figure 115: Geometry for modeling a cluster of jets as a single, equivalent jet flow. (Adapted from [17]).

Results from Chapters 2, 4, and 5 demonstrated that configurations with multiple nozzles arranged in a ring can have regions of high pressure preserved inboard of the nozzles under limited conditions. This inboard pressure can be a significant contributor to the aerodynamic drag on the vehicle forebody in these cases. On its own, modeling a cluster of nozzles as a single, equivalent jet does not account for the potential preservation of inboard surface pressures. As such, a simple approximation for the pressure inboard of the nozzles is developed here.

Figure 116 shows the experimental C_p data as a function of non-dimensional radial location on the forebody and C_T for a three nozzle configuration recently tested in the NASA LaRC UPWT [14] (discussed in Chapter 5). Excluding the lowest C_T cases, the highest pressures are inboard of the nozzles, which are at the forebody half-radius. Figure 117 shows the general decrease in C_p at the nose as C_T increases for the same cases shown in Fig. 116. At the lowest thrust coefficients, there is minimal interaction between the individual jets, and a large portion of the "no-jet" pressure at the nose is maintained. For $M_\infty = 2.4$, 3.5, and 4.6, the pressure coefficients at the nose are 1.70, 1.77, and 1.79, respectively.

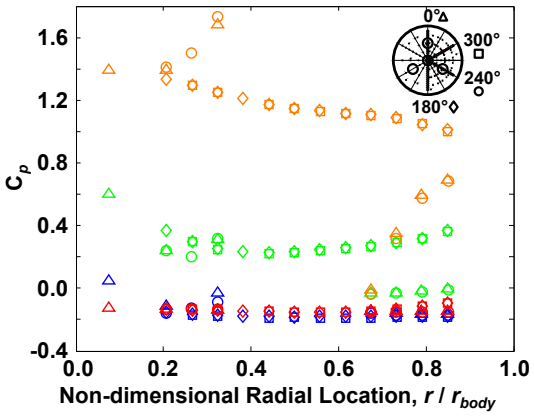

(a) M_∞ = 2.4

C_T	Experimental Run	Color
0.435	Run 206	Orange
0.944	Run 198	Green
1.931	Run 197	Red
2.939	Run 190	Blue

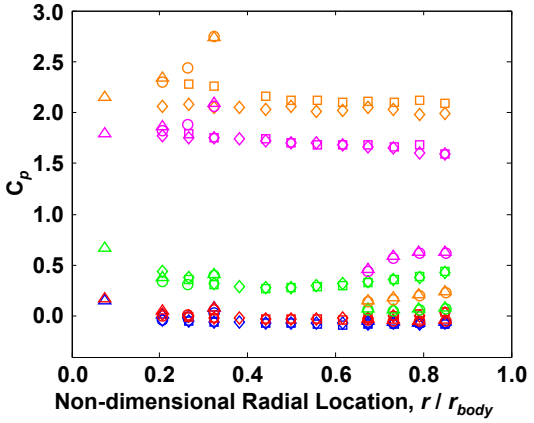

(b) M_∞ = 3.5

C_T	Experimental Run	Color
0.225	Run 241	Magenta
0.462	Run 240	Orange
0.968	Run 234	Green
1.947	Run 229	Red
2.963	Run 222	Blue

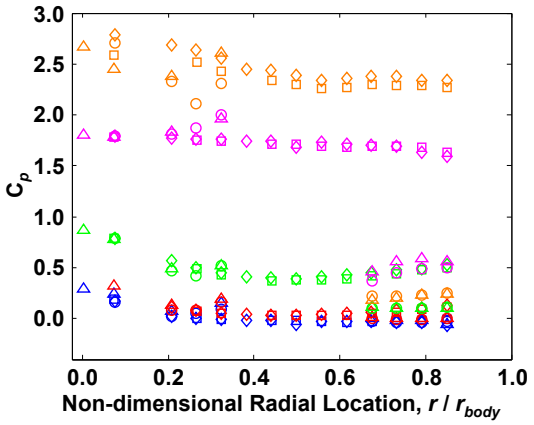

(c) M_∞ = 4.6

C_T	Experimental Run	Color
0.199	Run 257	Magenta
0.428	Run 253	Orange
0.898	Run 252	Green
1.959	Run 242	Red
2.937	Run 262	Blue

Figure 116: Data from the NASA ETDD Program's SRP test in the NASA LaRC UPWT facility for an SRP configuration with three nozzles at the half-radius. The nose is at $r/r_{body} = 0$, and the shoulder is at $r/r_{body} = 1$.

An exponential function with a constant of -0.95 is used to approximate the decrease in C_p at the nose with increasing C_T for all conditions. The initial value is $C_{p,max}$, assuming a perfect gas. At very low C_T, the experimental data show an increase in C_p at the nose above the "no-jet" value. The exponential model does not capture the elevated C_p values for $C_T < 1$. However, the conditions at which such behavior has been observed are well outside of the operational envelope defined for SRP by this thesis and are not considered within the analysis presented in this chapter.

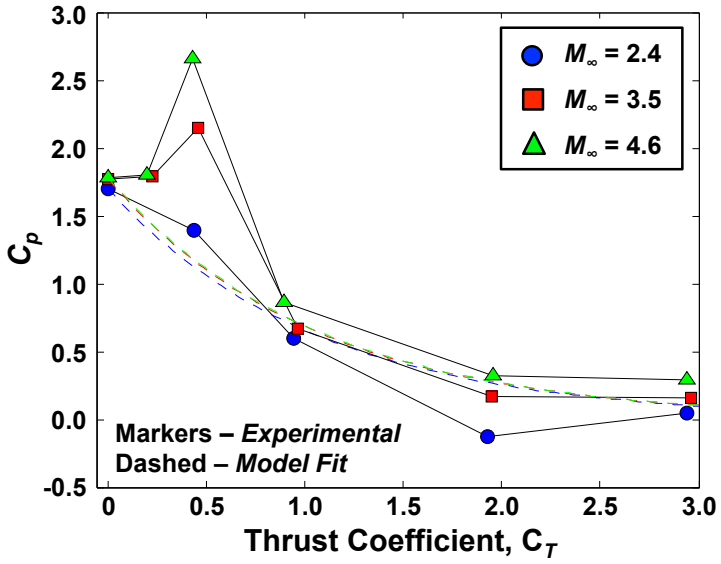

Figure 117: Decrease in C_p at the nose with increasing C_T for the three nozzle SRP configuration tested in the NASA LaRC UPWT facility. The markers represent experimental data points, and the dashed lines represent the approximation of these trends by the exponential model.

Figure 118 compares the integrated $C_{D,f}$ and $C_{A,f}$ results from the flow model to the cases from Figs. 116 and 117. No other data sets are available for comparison. As such, the favorable agreement of the flow model results and experimental data for $C_T > 1$ is not unexpected, even though only C_p inboard of the nozzles is related to the experimental data. It is important to note that the results for $C_{A,f}$ also agree well with the trends observed in prior experimental investigations (see Fig. 16 in Chapter 2). The results differ most at very low C_T (below 1). Recalling Figs. 83

and 87 in Chapter 5, pressures greater than the freestream static pressure exist over portions of the forebody other than just inboard of the nozzles. The flow model does not account for this, using a modified-Newtonian approximation for the inboard regions and integrating C_p from the flow model over the outboard regions. With the inboard regions contributing less than the outboard regions to the integrated drag on the forebody, along with the inaccurate approximation of the individual jet flows as a larger, single jet structure at such low C_T, the flow model significantly under-predicts $C_{D,f}$ and $C_{A,f}$ for $C_T < 1$ and a multiple nozzle configuration. A configuration with a single, central nozzle does not require an additional approximation for pressures inboard of the nozzles. In contrast to a multiple nozzle configuration, the surface pressures predicted by the flow model for such a configuration agree more favorably with experimental data at conditions with aerodynamic drag preservation (see Fig. 114). Again, however, these conditions fall well outside of the envelope of conditions relevant to SRP.

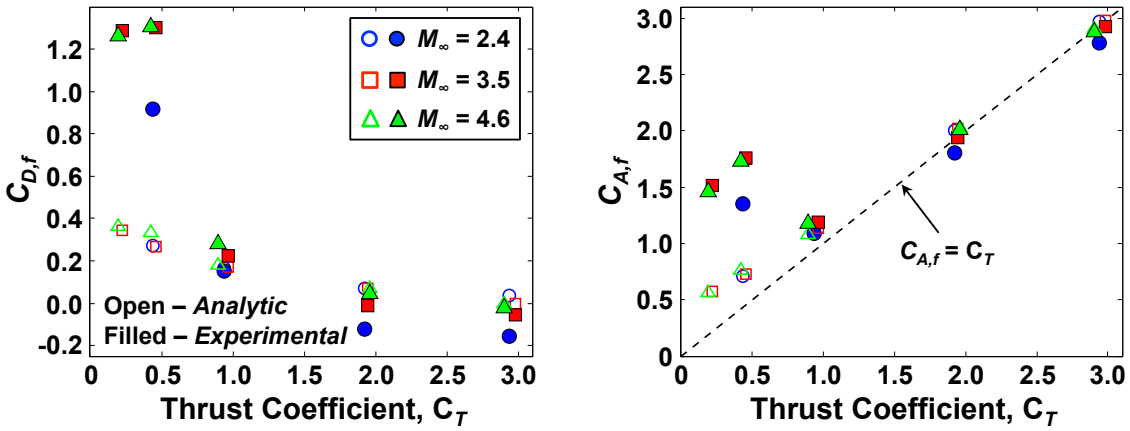

Figure 118: Comparison of $C_{D,f}$ (left) and $C_{A,f}$ (right) as functions of C_T for the analytical flow model and experimental data. The experimental data are for a three nozzle SRP configuration tested in the NASA LaRC UPWT facility. The dashed line in the figure on the right indicates $C_{A,f} = C_T$.

Figure 119 summarizes the detailed solution process for the SRP flow model, using selected equations presented in Sections 6.2.2 - 6.2.4 to obtain C_p, $C_{D,f}$, and $C_{A,f}$.

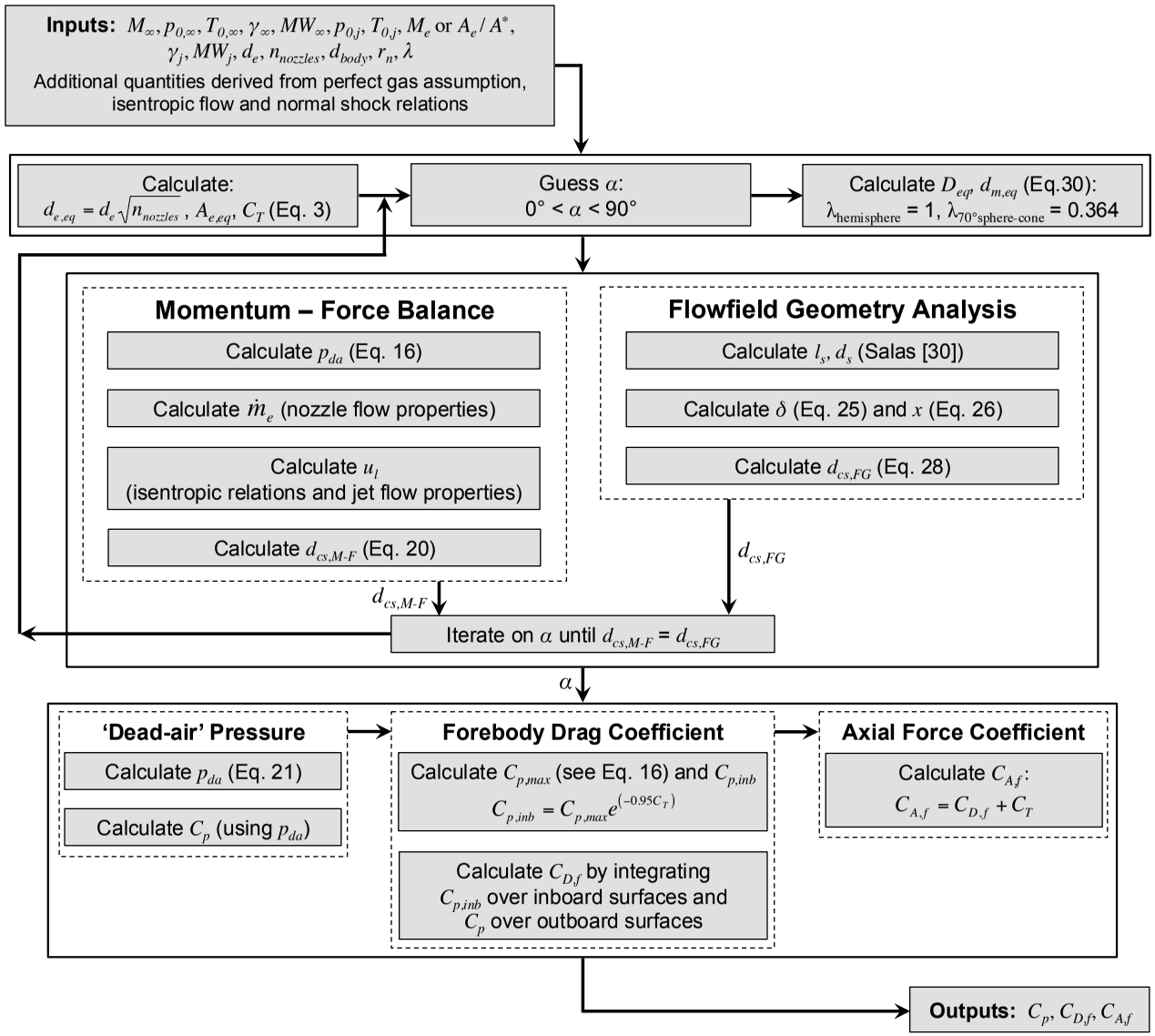

Figure 119: Solution process for the flow model developed in Sections 6.2.2 - 6.2.4.

6.3 Design Sensitivities

This section presents the results of the design choice sensitivities analysis. As discussed in Section 6.1, the primary parameters considered are the maximum vehicle T/W, jet flow composition, and the number of nozzles amongst which the thrust is evenly distributed. These parameters are directly related to the design choices of SRP operating conditions, required propulsion system performance, propulsion system composition, and SRP configuration. The surface pressures and integrated aerodynamic force coefficients are determined from the approximate flow model as a function of these parameters.

The experimental results given in Chapters 2 and 5 demonstrated the dominant effect of SRP on the surface pressure distribution and integrated static aerodynamic characteristics. Even for thrust levels well below those considered to be flight-relevant, surface pressures are reduced far below the post-shock stagnation pressure and in some cases, below the freestream static pressure. This section considers flight-relevant conditions for two mission scales: a vehicle for human exploration and a large, robotic-scale vehicle for a precursor or technology demonstration mission. Conditions for a sub-scale experimental model are also used in examining the impacts of trading propulsion system composition.

The human-scale vehicle concept is defined to be the $\beta = 400$ kg/m^2 vehicle ($m_{entry} \approx 53$ t) evaluated in Chapter 3. The forebody during the SRP phase (not necessarily the same forebody used during the hypersonic phase of the trajectory) is assumed to be a 70° sphere-cone with a 10 m-diameter circular cross-section and a 1.25 m nose radius. This vehicle has 3 LOX/CH_4 engines and operates at an I_{sp} of 350 seconds and a mixture ratio of 3.5, providing a total propulsive ΔV of 509.5 m/s. For a Pareto-optimal $(T/W)_{max}$ of 3.5 ($\tau = 694.4$ kN), the SRP phase begins at $M_\infty = 2.86$ and an altitude of 7.05 km. Where possible, all comparisons are made with the performance of this vehicle concept.

The robotic-scale vehicle concept was developed through NASA's EDL-SA study [112] and is considered to provide a comparison between a human-scale and advanced robotic-scale application of SRP. This concept uses 4 MMH/N_2O_4 engines (based on a modified, pump-fed RS-72 engine) to land a 2.6 t payload on the surface of Mars. The vehicle is designed to maximize the payload capability of a Delta IV-Heavy, though the vehicle diameter is only 2.6 m. For a $(T/W)_{max}$ of 3.7 (τ = 62.4 kN), the SRP phase begins at $M_\infty = 1.69$ and an altitude of 7.60 km.

The sub-scale model is based on experimental work by Finley [7] and is a 2 inch-diameter hemisphere with a single nozzle at the nose ($d_e = 0.0067$ m). The conditions in this section for this model are assumed to be: $M_\infty = 2.5$, $\gamma_\infty = 1.4$, $p_{0,\infty} = 68.95$ kPa, and $A_e/A^* = 4.0$.

6.3.1 Operating Conditions and Required Propulsion System Performance

Section 3.2.2 in Chapter 3 demonstrated mass-optimal SRP operation to favor conditions that maximize available thrust over the minimum time duration required to reach the target terminal state. Extreme degrees of drag preservation are required before deviations from this behavior occur, and such drag characteristics have not been observed in experimental testing or analysis. Therefore, the operating conditions for SRP are a direct function of the maximum thrust available from the propulsion system. The maximum vehicle T/W defines the maximum thrust available.

Figure 120 (left) shows the variation in $C_{D,f}$ and $C_{A,f}$ as $(T/W)_{max}$ increases from the baseline value of 3.5 to 10.0 (relative to Mars). Figure 120 (right) shows the same variation as a function of C_T at initiation. A summary of the conditions and results shown in Fig. 120 is given in Table 23. Note that the baseline value of $(T/W)_{max} = 3.5$ was determined in Chapter 3 to be the value minimizing both propulsion system mass and propulsion system volume. The maximum value considered in this analysis

($(T/W)_{max} = 10.0$) is very close to the value used the exploration class, or human-scale, Mars EDL architectures developed through NASA's EDL-SA efforts [2]. NASA EDL-SA's $(T/W)_{max}$ was determined from a constraint on the trajectory limiting the g-loading experienced by a de-conditioned astronaut crew. The $(T/W)_{max} = 10.0$ case has a lower PMF than the $(T/W)_{max} = 3.5$ case but a higher total propulsion system mass and volume.

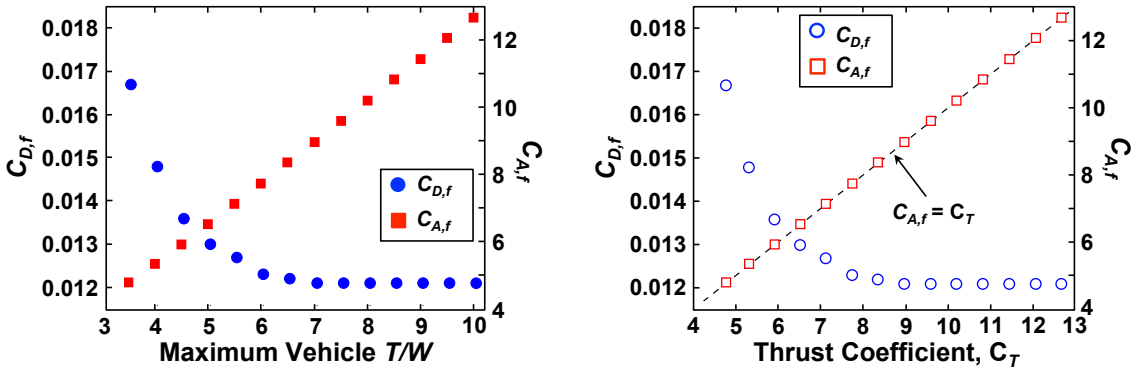

Figure 120: Variation in $C_{D,f}$ and $C_{A,f}$ as functions of $(T/W)_{max}$ (left) and C_T (right). The dashed line in the figure on the right indicates $C_{A,f} = C_T$.

In Fig. 120, the greatest variation in $C_{D,f}$ is seen for $(T/W)_{max}$ less than approximately 5.5. Table 23 shows the corresponding increase in C_T at initiation as $(T/W)_{max}$ increases for each case. As discussed, SRP configurations with multiple nozzles can have regions of higher pressure inboard of the nozzles under limited conditions. However, the degree to which this inboard pressure is preserved decreases as C_T increases. As $(T/W)_{max}$ increases, the individual jet structures become increasingly highly under-expanded. Eventually, as C_T continues to increase, the combined radial expansion of the jets is sufficient to completely shield the vehicle forebody from the oncoming freestream flow. This is reflected in the decrease in $C_{D,f}$ with increasing $(T/W)_{max}$.

Figure 120 shows the expected trend of $C_{A,f} = C_T$ as $(T/W)_{max}$ is increased from 3.5 to 10.0. While some variation in $C_{D,f}$ is seen as $(T/W)_{max}$ is changed, this variation is extremely small in magnitude and has a negligible impact on the vehicle's

overall deceleration performance.

Table 23: Summary of conditions and results for the impact of SRP operating conditions and required propulsion system performance on $C_{D,f}$ and $C_{A,f}$.

$(T/W)_{max}$	$C_{T,total}$	$C_{T,one\ nozzle}$	M_∞	p_e/p_∞	$p_{0,j}/p_{0,\infty}$	$p_{0,j}/p_{0,2}$	$C_{D,f}$	$C_{A,f}$	PMF	$m_{prop\ sys}$
3.5	4.78	1.59	2.81	1.34	139.32	391.07	0.0167	4.80	0.138	16112
4.0	5.33	1.78	2.76	1.44	162.77	434.79	0.0148	5.34	0.133	15970
4.5	5.92	1.97	2.73	1.56	185.77	482.23	0.0136	5.93	0.130	15932
5.0	6.52	2.17	2.71	1.69	208.69	531.15	0.0130	6.53	0.128	15952
5.5	7.12	2.38	2.69	1.83	230.75	579.97	0.0127	7.14	0.126	16107
6.0	7.74	2.58	2.68	1.97	253.14	629.59	0.0123	7.75	0.125	16088
6.5	8.35	2.78	2.67	2.11	275.29	679.08	0.0122	8.36	0.124	16271
7.0	8.96	2.99	2.67	2.26	297.14	729.08	0.0121	8.98	0.123	16273
7.5	9.58	3.19	2.66	2.41	319.02	779.11	0.0121	9.59	0.123	16485
8.0	10.20	3.40	2.66	2.55	340.95	829.25	0.0121	10.21	0.122	16497
8.5	10.82	3.61	2.66	2.70	362.81	879.43	0.0121	10.83	0.122	16716
9.0	11.44	3.81	2.65	2.85	384.68	929.72	0.0121	11.45	0.121	16742
9.5	12.05	4.02	2.65	3.00	405.53	979.40	0.0121	12.06	0.121	16958
10.0	12.65	4.22	2.65	3.13	427.90	1028.05	0.0121	12.66	0.121	16994

It is significant, however, to note the potential effects of the operating conditions within the Martian atmosphere on the structure of the SRP flowfield. The nozzles are assumed to have a nozzle expansion ratio of 180, which yields an exit Mach number of 5.22. By p_e/p_∞, the individual jet flows are under-expanded but not by a significant margin. Comparing p_e with p_2, highly under-expanded jet structures may not occur across the range of conditions considered. A number of works, both experimental and computational, have demonstrated the behavior of SRP flowfields with weakly under-expanded jet flows to be highly unsteady and also to exhibit unstable flow mode transitions [8, 51, 57]. By restricting SRP operation with multiple nozzles to avoid such behaviors, it is likely desirable to operate with fewer engines, lower nozzle expansion ratios, and a higher vehicle T/W.

6.3.2 Supersonic Retropropulsion Configuration

In this investigation, supersonic retropropulsion configuration is represented by the number of nozzles amongst which the required thrust is evenly distributed. Cases with

$(T/W)_{max}$ = 3.5 and 10.0 are examined in this section for the human-scale vehicle concept with 3, 4, 5, and 6 engines. The baseline concept developed through NASA's EDL-SA study is also considered to provide a comparison between a human-scale and advanced robotic-scale (and precursor/technology demonstration) application of SRP. The required thrust is divided evenly, assuming identical engines.

Figure 121 shows the engine arrangements considered for 3 to 6 equally-sized engines for a human-scale vehicle. The exit areas of all of the engines are constrained by the base area of the vehicle. The baseline vehicle has a maximum diameter of 10 m. The maximum exit area for an individual nozzle is determined such that the available area is used efficiently and still allows for gimbaling of the engines. For packaging considerations related to nozzle length, the maximum expansion ratio for an individual nozzle is restricted to 180.

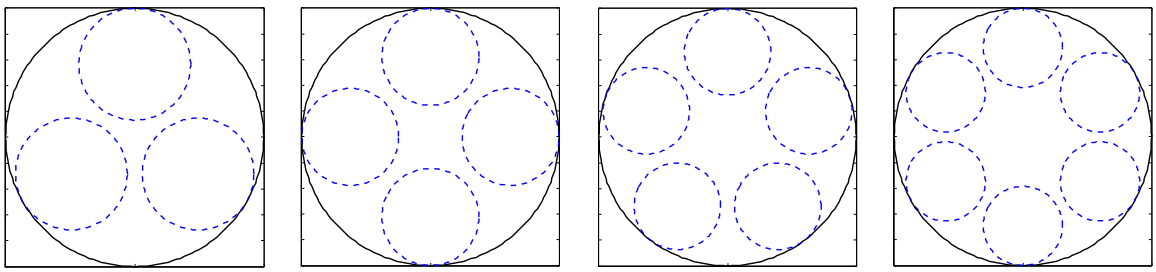

Figure 121: Arrangements of multiple engines showing the maximum allowable exit area for the individual nozzles.

Table 24 summarizes the conditions and results of distributing the required thrust over different numbers of engines during the SRP phase for both mission scales. To first order, distributing the required thrust over different numbers of engines has no discernible effect on the aerodynamic drag and total axial force on the vehicle. While changing the number of nozzles changes the individual jet structures and the amount of surface area over which pressure can potentially be preserved, the thrust requirements and associated operating conditions for both mission scales explored are such that the vehicle forebody is completely shielded from the oncoming freestream

flow. The high-performance rocket engines under consideration for SRP at Mars all operate with large nozzle expansion ratios to maximize efficiency. The resulting vehicle configurations have small ratios of total nozzle exit area to forebody area, leaving little surface area for variation in pressure (due to SRP) to be resolved in the vehicle's static aerodynamic characteristics.

Table 24: Summary of conditions and results for the impact of distributing the required thrust over different numbers of engines on $C_{D,f}$ and $C_{A,f}$.

Human-scale concept (m_{init} = 53 t)								
$(T/W)_{max}$	Number of Nozzles	$C_{T,total}$	$C_{T,one\ nozzle}$	M_∞	p_e/p_∞	$p_{0,j}/p_{0,\infty}$	$C_{D,f}$	$C_{A,f}$
3.5	3	4.78	1.59	2.81	1.34	139.32	0.0167	4.80
3.5	4	4.78	1.59	2.81	1.33	137.76	0.0167	4.80
3.5	5	4.78	1.59	2.81	1.34	138.94	0.0167	4.80
3.5	6	4.78	1.59	2.81	1.33	137.96	0.0167	4.80
10.0	3	12.65	4.22	2.65	3.13	427.90	0.0121	12.66
10.0	4	12.65	4.22	2.65	3.10	423.09	0.0121	12.66
10.0	5	12.65	4.22	2.65	3.13	426.71	0.0121	12.66
10.0	6	12.65	4.22	2.65	3.10	423.72	0.0121	12.66
Robotic-scale concept (m_{init} = 4.6 t)								
$(T/W)_{max}$	Number of Nozzles	$C_{T,total}$	$C_{T,one\ nozzle}$	M_∞	p_e/p_∞	$p_{0,j}/p_{0,\infty}$	$C_{D,f}$	$C_{A,f}$
3.7	3	20.51	6.84	2.66	3.48	5866.2	0.0110	20.52
3.7	4	20.51	5.13	2.66	2.61	4399.7	0.0110	20.52
3.7	5	20.51	4.10	2.66	2.09	3519.7	0.0110	20.52

From a systems-level design perspective, varying the number of nozzles utilized for SRP, i.e. adding redundancy or throttling combinations of engines, is a trade that can be made without requiring significant support from high-fidelity computational analysis. This has been shown to be accurate for SRP configurations with identical nozzles arranged in a ring and directly opposing the freestream flow. For other variations in configuration, it may not be accurate to assume such independence of the integrated vehicle aerodynamics on SRP configuration. As an example, wind tunnel

testing of a sub-scale model by NASA's ETDD Program demonstrated drastic differences in the flowfield structure, behavior, and unsteadiness between a configuration with three nozzles (similar to the configurations explored in this section) and a configuration with the same three nozzles and an additional nozzle in the center of the cluster [14, 52]. Major variations in vehicle configuration will require support from high-fidelity computational analysis, experimental testing, or both. It is important to note, however, that these conclusions apply to static aerodynamic effects in the axial direction only. Supersonic retropropulsion flowfields are inherently unsteady, and the effects of such dynamic behavior on vehicles of any scale remain unknown.

6.3.3 Propulsion System Composition

As mentioned previously, LOX/CH_4 is the propellant combination for the design reference architectures for Mars exploration. However, a flight-proven LOX/CH_4 propulsion system capable of satisfying the thrust and throttling requirements for this application does not currently exist. There are LOX/RP-1 and LOX/LH_2 propulsion systems in the same thrust class that have been flown, and the results from Section 3.2.3 in Chapter 3 show the mass and volume requirements for a LOX/RP-1 system to be comparable to those for a LOX/CH_4 system. Should the primary propulsion system choice be changed or a precursor or technology demonstration mission fly a different propulsion system than that selected for the full-scale mission, the potential differences in the vehicle's aerodynamic performance during SRP need to be understood.

Holding the nozzle expansion ratio fixed, changing the propellant combination changes γ_j. This also changes M_e. Figure 122(a) illustrates the effect of changing γ_j on highly under-expanded jet structure, and Fig. 122(b) illustrates the effect of changing M_e. The initial inclination of the free-jet boundary is greater for smaller values of γ_j. This results in larger jet diameters and the Mach disk located closer

to the nozzle exit as γ_j is reduced. The exit Mach number increases with increasing γ_j. While there is no change in the initial inclination of the free-jet boundary at the nozzle exit, the distance from the nozzle exit plane to the Mach disk increases with increasing M_e as a result of the increased momentum of the jet flow. At conditions where the body is not fully shielded from the freestream flow by the jet interaction structures, cases with a higher γ_j should preserve more surface pressure than cases with a lower γ_j for the same pressure ratio.

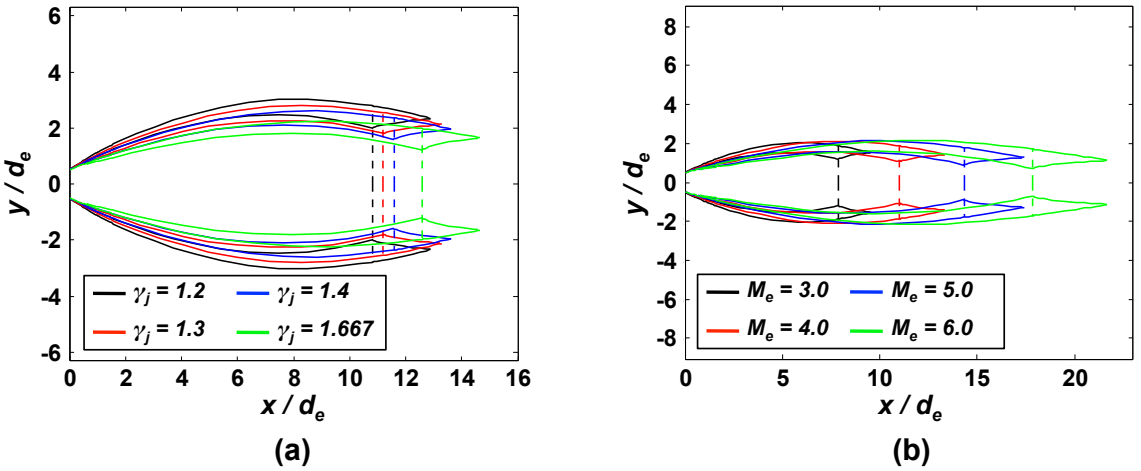

Figure 122: Effect of γ_j (a) and M_e (b) on highly under-expanded jet structure. Conditions for Fig. (a) are: $p_e/p_\infty = 20$, $M_e = 3.0$, $\gamma_\infty = 1.33$, $M_\infty = 0.0$. Conditions for Fig. (b) are: $p_e/p_\infty = 10$, $\gamma_j = 1.20$, $\gamma_\infty = 1.33$, $M_\infty = 0.0$.

Figure 123 shows the effect of changing γ_j on $C_{D,f}$ and $C_{A,f}$ for the sub-scale experimental model. Varying γ_j only has an effect at low pressure ratios ($p_e/p_{da} < 10$), and even then, the change in $C_{D,f}$ is very small. Considering the flight-relevant operating conditions given in Tables 23 and 24, however, these differences may be significant. The baseline propulsion system choice for Mars design reference architectures is LOX/CH_4 ($\gamma_j = 1.19$). Alternatives include LOX/RP-1 ($\gamma_j = 1.24$) and LOX/LH_2 ($\gamma_j = 1.26$). If the expansion ratio of the nozzle is allowed to vary as γ_j changes, these differences can be compensated for, and the same trends for $C_{D,f}$ and $C_{A,f}$ vs. C_T or p_e/p_∞ are preserved.

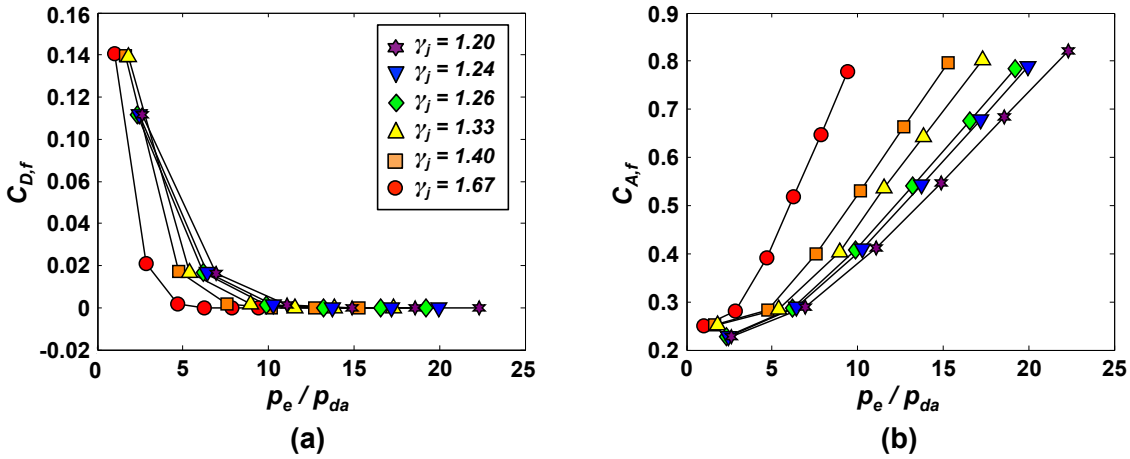

Figure 123: Effect of γ_j on $C_{D,f}$ (a) and $C_{A,f}$ (b) for a 2 inch-diameter hemisphere. Conditions are: $A_e/A^* = 4$, $\gamma_\infty = 1.40$, $M_\infty = 2.5$.

Table 25 summarizes the results from changing the propulsion system from LOX/CH_4 to LOX/RP-1 and LOX/LH_2 for the human-scale vehicle concept. For these operating conditions and vehicle scale, the variations in γ_j and M_e from changing the propulsion system type do not result in any significant change in the integrated $C_{D,f}$ and $C_{A,f}$ of the vehicle. Within the range of SRP operating conditions defined for full-scale vehicles at Mars, trading the propulsion system type can be done without requiring significant additional contributions from high-fidelity computational analyses. However, at this time, very little experimental work has been done using gases other than air or with high-temperature combustion products. When higher-fidelity analysis is required for more detailed design studies of SRP systems, additional experimental work will be required to verify the insensitivity of integrated, static aerodynamic characteristics on exhaust gas composition and any differences in the dynamic behavior of the SRP flowfield.

As discussed in Section 3.2.3, once a propulsion system has been selected, a trade between I_{sp} and nozzle expansion ratio often takes place. Maximizing I_{sp} maximizes propellant efficiency, driving the required propellant mass down. However, doing so also increases A_e/A^*, increasing the length and width of the nozzle and increasing

Table 25: Summary of results for the impact of changing the propulsion system type on $C_{D,f}$ and $C_{A,f}$ for the human-scale vehicle concept.

$(T/W)_{max}$	$C_{T,total}$	Prop Type	p_e/p_∞	$C_{D,f}$	$C_{A,f}$
3.5	4.78	LOX/CH_4	1.34	0.0167	4.80
10.0	12.65	LOX/CH_4	3.13	0.0121	12.66
3.5	4.78	LOX/RP-1	1.07	0.0167	4.80
10.0	12.65	LOX/RP-1	2.50	0.0121	12.66
3.5	4.78	LOX/LH_2	0.98	0.0167	4.80
10.0	12.65	LOX/LH_2	2.29	0.0121	12.66

the mass of the propulsion system hardware. The final choice is often driven by a compromise between available mass margin and the ability to package and operate the system.

Changing the nozzle expansion ratio changes M_e and the distance of the Mach disk from the nozzle exit. It also changes the ratio of the total nozzle exit area to the vehicle forebody (or base) area. These changes do affect the structure of the SRP flowfield. However, significant reduction in the nozzle expansion ratios of the propulsion systems baselined for the full-scale vehicle concepts would be required before any significant change in $C_{D,f}$ and $C_{A,f}$ would occur. The thrust performance would also need to be reduced (thus affecting the operating conditions) for appreciable pressures to be preserved over the increased forebody surface area and substantially contribute to $C_{D,f}$. Based on the results given in this section, the static aerodynamic drag performance of full-scale vehicles utilizing SRP is likely to be insensitive to changes in I_{sp} and A_e/A^* for the conditions defining flight-relevant operation and scale. Note, however, that along with all of the results in this chapter, these conclusions refer strictly to the static aerodynamic drag characteristics of the vehicle. No conclusions can be drawn on the dynamic effects arising from changes in the inherent unsteadiness of SRP flowfields, e.g. frequency and/or amplitude, or any other flow-driven effects on the stability of the vehicle from aftbody pressure variations or reattachment.

6.4 Summary

This chapter developed an approximate SRP flowfield model to assist in evaluating the impact of entry, descent, and landing vehicle design choices on the vehicle's static aerodynamic characteristics for flight-relevant conditions and scales. These design choices included SRP operating conditions, required propulsion system performance, propulsion system composition, and SRP configuration. The model was shown to be capable of capturing trends in integrated aerodynamic drag and axial force characteristics across a broad range of conditions and design parameters within the SRP design space. Relative differences in these quantities and physical changes in flowfield structure were used to identify the fidelity and effort required to support specific design trades.

The SRP flowfield is governed by the quantities describing the composition and conditions of the freestream and nozzle flow(s) and the geometry and configuration of the vehicle. These quantities are: γ_∞, R_∞, M_∞, p_∞, T_∞, γ_j, R_j, $p_{0,j}$, $T_{0,j}$, A_e/A^*, and $A_{e,total}/A_{vehicle}$. The impact of the individual quantities is problem-dependent, but generally, the most significant quantities are those dictating the expansion condition of the nozzle flow and $A_{e,total}/A_{vehicle}$.

The static forebody aerodynamic drag and axial force characteristics of vehicles at two different mission scales were shown to be insensitive to major trades common to conceptual design. Full-scale vehicles operate with high-performance engines, utilizing large nozzle expansion ratios and thrust levels well beyond those examined experimentally or with high-fidelity computational tools. The large variations in $C_{D,f}$ and $C_{A,f}$ observed through experiment, including in recent tests completed through NASA's ETDD Program, are not resolvable as static effects at the conditions and physical scales required for the flight operation of SRP.

The results of this chapter are limited to operation at zero angle of attack, though recent experimental results suggest extensibility of these conclusions to angles of

attack below 8° [51]. Additionally, the applicability of the flow model developed is limited to forebody surface pressures and integrated, static aerodynamic drag effects. No conclusions can be drawn from this analysis on the potential changes in static stability characteristics. Considering the results in Chapter 5, however, the severe reduction in surface pressure likely challenges or prevents the use of aerodynamic surfaces to control vehicle attitude in the SRP flight regime.

In relating flight-relevant operating conditions identified for SRP through systems analysis to parameters governing SRP flowfield structure, it was observed that highly under-expanded jet flow structures may not occur across the range of conditions considered. A number of works, both experimental and computational, have demonstrated the behavior of SRP flowfields with weakly under-expanded jet flows to be highly unsteady and also to exhibit unstable flow mode transitions [8, 51, 57]. To avoid such behaviors by restricting SRP operation to conditions resulting in highly under-expanded jet structures, it is likely desirable to operate with fewer engines and a higher vehicle T/W. For configurations with multiple nozzles, reducing nozzle expansion ratios can provide additional margin for SRP operation with highly under-expanded jet flow structures.

To this point, past systems analysis efforts by NASA have assumed there to be no aerodynamic forces and moments acting on the vehicle during the SRP phase [2, 23, 112]. Provided the conditions are within the range considered to be flight-relevant and the vehicle configurations remain similar to those discussed in this chapter, design trades may be evaluated with simple engineering models or assumptions. However, if the SRP configuration is varied with extreme changes in nozzle expansion ratio, a non-circular or non-uniform arrangement of nozzles is used, or the application of SRP as a thrust-dominated decelerator changes, evaluation likely requires support from both high-fidelity computational analysis and experiment.

Supersonic retropropulsion alone is not likely to drive design choices with mission-level implications. Recent wind tunnel tests completed by NASA's ETDD Program uncovered SRP flowfields to be inherently unsteady. The dynamic effects of this behavior on vehicle stability remain a significant unknown. If there are configurations and conditions that can be identified that minimize the dynamic response of the vehicle to flow interactions, the likelihood of the incorporation of SRP into a flight system would increase further. High-fidelity computational analysis and experimental work are also likely required for SRP analyses focused on vehicle control and stability.

CHAPTER VII

CONTRIBUTIONS AND RECOMMENDATIONS FOR FORWARD WORK

Supersonic retropropulsion has been identified as a critical technology for the human exploration of Mars. While its presence in the historical literature lends some degree of credibility to the concept, the overall immaturity of this technology challenges its evaluation as a decelerator for high-mass Mars entry systems, as well as its comparison with alternative decelerators. The existing computational tools and approaches applied to SRP flow interactions are computationally expensive in accurately and consistently simulating the features and behaviors of SRP flowfields. Experimental investigations are limited by requirements of high pressure flow through a sub-scale model and the general expense of ground testing. This, along with incomplete data sets in the literature, has contributed to a lack of models available for systems analysis.

Work within this thesis has defined and advanced the state of the art for supersonic retropropulsion. This has been achieved through the development and application of systems analysis, computational analysis, and analytical methods.

Chapter 2 described the nature of SRP to substantially alter the aerodynamic characteristics of a vehicle and discussed the experimental data available for model development. The results of Chapter 3 established the minimum fidelity required for SRP static aerodynamics models for systems analysis in support of developing a capability to evaluate and compare a number of SRP concepts against one another and also against alternative decelerator concepts. Existing experimental data from small-scale wind tunnel testing and modern computational fluid dynamics tools were used

to evaluate the potential benefits of SRP as a supersonic decelerator for advanced Mars entry systems. Chapters 4 and 5 then demonstrated the ability of high-fidelity computational analyses to simulate SRP flow behavior and capture changes in the vehicle's aerodynamics. The results, while agreeing well with experimental data, are prohibitively expensive to obtain for more than a limited number of cases. Chapter 6 identified system-relevant parameters governing SRP fluid interactions and illustrated the impacts of design choices on the change in the vehicle's static aerodynamic characteristics through the use of experimental data and analytical modeling of momentum transfer within the SRP flowfield.

An assessment of the required fidelity for SRP aerodynamic databases in conceptual design was approached in two ways: (1) examination of the robustness of SRP performance trends to variation in drag and static stability characteristics, and (2) investigation into the capabilities of computational analysis in simulating SRP flowfields for several configurations across a range of conditions. This chapter summarizes the contributions of this thesis, referencing results and conclusions from Chapters 2 through 6.

7.1 Characterization of System Performance

Chapter 3 characterized the impact of SRP on system performance and identified significant performance trends. The relevant operating conditions for SRP were defined across a range of mission scales as a function of vehicle ballistic coefficient and thrust available. Models for SRP static aerodynamics as functions of M_∞, C_T, and α were developed using experimental data, and the performance analyses presented are the first to use such models.

Past studies have neglected the potential for aerodynamic - propulsive interactions in performance and sizing and considered heavily constrained EDL design spaces. In contrast, this work used a coupled aerodynamic model, developed from experimental

data, to account for interactions where necessary and considered a broader trade space to define mission scales and relevant operating conditions for which SRP may be beneficial. System performance results for a generic, blunt body configuration and a similarly scaled mid-L/D configuration were used to define the operational envelope for SRP and to determine the sensitivity of mass-optimal performance to changes in model fidelity. Included under this contribution are the following:

- Development of an SRP aerodynamics model for C_D and C_m as functions of M_∞, C_T, and α.
- Characterization of mass-optimal performance over ballistic coefficients ranging from 200 to 600 kg/m^2, including definition of the operational envelope for SRP.
- Assessment of the impact of aerodynamic drag on the optimal trajectories and propulsion system performance requirements of vehicles utilizing SRP.
- Determination of the required restoring moment in the pitch plane during the SRP phase.
- Assessment of the sensitivity of SRP performance (optimal trajectories, thrust profiles, operational envelope, SRP PMF) to the aerodynamics model applied in 3-DOF analysis.

Mass-optimal trajectories for vehicles utilizing SRP are characterized by extended phases of near-constant altitude deceleration deep within the atmosphere, shallow flight path angles at SRP initiation to minimize gravity losses, and initiation conditions that minimize the required propulsive ΔV. These conditions generally imply SRP initiation at a minimum altitude boundary defined by the timeline considerations of subsequent EDL events. SRP initiation conditions are a strong function of the thrust available, and for all cases considered in this work, the SRP phase relies on high thrust levels that do not allow for drag preservation.

No conditions were identified in which operation at conditions potentially preserving a portion of the vehicle's aerodynamic drag would result in minimization of the total propulsion system mass. The system T/W required to decelerate the vehicle through the thin Martian atmosphere across all mission scales far exceeds any experimentally observed drag preservation conditions for SRP. In addition, the uncertainty in the stability and inherent unsteadiness of the aerodynamic - propulsive interaction at lower jet pressure ratios are an unfavorable consequence of SRP. As such, a significant benefit in packaging, performance, and control authority would likely need to be realized before the lower thrust levels that allow an aerodynamic drag contribution be considered by mission designers.

Thrust vector control through engine gimbaling was demonstrated to be a feasible and potentially viable strategy for countering pitching moments during the SRP phase of a high-mass Mars EDL trajectory. Moments about the vehicle's center of gravity in the pitch plane are greatest near SRP initiation and rapidly decrease in magnitude as the vehicle decelerates to subsonic conditions, even at small (up to 10°) angles of attack. The required thrust deflection angles to counteract moments about the vehicle's center of gravity in the pitch plane are most sensitive near SRP initiation; however, the actual moments would need to exceed the predicted moments by more than a full order of magnitude before the required thrust deflection angles are greater than those already proven for liquid bipropellant propulsion systems.

Vehicles utilizing SRP across a range of mission scales are, in general, not sensitive to the SRP aerodynamics models applied in systems analyses. The results given in this thesis provide confidence in the present status of systems analyses and SRP modeling, even if there are significant uncertainties in the force and moment coefficients predicted through computational analysis and ground testing. For conceptual design, support from high-fidelity computational analysis is not required; engineering models for aerodynamic forces and moments during the SRP phase based on trends in the

existing experimental database are sufficient.

7.2 Relationship between System Performance and the Aerodynamic - Propulsive Interaction

Building from the flowfield description and experimental data trends presented in Chapter 2, Chapter 6 established relationships between design choices related to vehicle performance and the SRP-induced change in the vehicle's static aerodynamic drag and axial force characteristics. Included under this contribution are:

- A comprehensive review of past literature relevant to SRP flow physics and performance.
- An approximate model for the integrated forebody aerodynamic drag developed by describing momentum transfer within the SRP flowfield.
- Determination of the sensitivity of integrated aerodynamic characteristics to variation in parameters representing common design choices.
- Recommendations for the design trades likely requiring support from high-fidelity analysis.

A general analytical model based on momentum transfer within the flowfield was developed and used to explore the impact of SRP operating conditions, required propulsion system performance, propulsion system composition, and SRP configuration on the integrated aerodynamic drag characteristics of full-scale vehicles for Mars EDL. The SRP flowfield is governed by the quantities describing the composition and conditions of the freestream and nozzle flow(s) and the geometry and configuration of the vehicle. These quantities are: γ_∞, R_∞, M_∞, p_∞, T_∞, γ_j, R_j, $p_{0,j}$, $T_{0,j}$, A_e/A^*, and $A_{e,total}/A_{vehicle}$. The impact of the individual quantities is problem-dependent, but generally, the most significant quantities are those dictating the expansion condition of the nozzle flow and $A_{e,total}/A_{vehicle}$.

The forebody drag and axial force characteristics of vehicles at two different mission scales were found to be insensitive to major trades common to conceptual design. Full-scale vehicles operate with high-performance engines, utilizing large nozzle expansion ratios and thrust levels well beyond those tested in wind tunnels and examined thus far with high-fidelity computational tools. As a result, the variations in $C_{D,f}$ and $C_{A,f}$ observed in small-scale experiments are not resolvable as static effects at the conditions and physical scales required for the flight operation of SRP.

Highly under-expanded jet structures may not be fully developed for flight-relevant operating conditions within the Martian atmosphere. To avoid the large-scale unsteadiness and unstable mode transitions common to weakly under-expanded SRP flows, it is likely desirable to operate with fewer engines and a higher vehicle T/W. For configurations with multiple nozzles, reducing nozzle expansion ratios can provide additional margin for SRP operation with highly under-expanded jet flow structures.

Minimal support from high-fidelity computational analysis is needed for SRP systems analysis trades in the conceptual design phase. Design trades may be evaluated with engineering models, provided the conditions are within the range presently considered to be flight-relevant and the vehicle configurations remain circular and axisymmetric. If the SRP configuration is varied with large changes in nozzle expansion ratio, a non-circular and/or non-uniform arrangement of nozzles is used, or the application of SRP as a thrust-dominated decelerator changes, the evaluation may require support from both high-fidelity computational analysis and experiment.

Supersonic retropropulsion is not likely to drive design choices with mission-level implications. However, if there are configurations and conditions that minimize the dynamic response of the vehicle to SRP flow interactions, SRP may have a role in influencing design choices. High-fidelity computational analysis and experimental work may also be required for systems-level analyses focused on vehicle control and stability.

7.3 Required Fidelity and Computational Cost of Aerodynamic Database Development

To evaluate and compare a number of SRP concepts against one another and also against alternative decelerator concepts, more sophisticated models for systems analysis are required. The development of these models is highly dependent on CFD methods. This work is the first comprehensive study integrating results from systems analysis, CFD analysis, and analytical aerodynamics to understand the fidelity necessary to develop new models and evaluate SRP concepts. This assessment is completed through the following:

- Assessment of the sensitivity of SRP performance (optimal trajectories, thrust profiles, operational envelope, SRP PMF) to the aerodynamics models applied in 3-DOF trajectory analysis to establish a minimum fidelity requirement.
- Evaluation of the performance of a RANS CFD approach in predicting flowfield structure and behavior, surface pressure distributions, and integrated aerodynamics quantities; included are definition of the size of the computational domain, grid resolution, and temporal approach required to achieve this performance.

Moving beyond the conceptual design phase, higher-fidelity aerodynamic models will be needed to evaluate the performance of vehicles utilizing SRP. The expense and complexity of testing SRP in ground-based test facilities and the inability to fully simulate Mars-relevant conditions and configurations substantially increases the reliance on high-fidelity CFD methods. Understanding the relationship between the performance of high fidelity computational approaches in predicting the aerodynamic - propulsive interactions inherent to SRP and the computational cost associated with achieving such performance is critical to defining the computational requirements for progressive phases of development and design.

Chapters 4 and 5 investigated the capability of a high-fidelity CFD approach in simulating the behavior and resulting aerodynamics of SRP. A NASA-developed CFD tool was used to evaluate the ability of a Reynolds-averaged Navier-Stokes approach to predict the flowfield structure, surface pressure distributions, and integrated aerodynamic force coefficients using both historical and modern wind tunnel test cases. Time-accurate solutions were generated to capture the unsteady behaviors observed in recent experimental testing.

Solutions for three different SRP configurations and a baseline case were compared with data from a recent wind tunnel test designed explicitly to provide a validation data set for CFD analyses. Overall, the specific models and approach applied captured the general trends in pressure coefficient on both the forebody and aftbody, including cases at small angles of attack.

With the exception of a one nozzle case at $\alpha = 8°$, the computational results showed a consistent, though slight, under-prediction of surface pressures on both the forebody and aftbody. Pressures at the nose for a configuration with three nozzles equally-spaced at the forebody half-radius were over-predicted by the approach applied in this thesis (and by several other approaches examined through NASA's ETDD Program). The unsteady, viscous, turbulent CFD approach captured most of the surface pressure distributions within $\pm$ 3 times the experimental RMS value of C_p. Discrepancies outside of the immediate nose region on the forebody were limited to very small ranges of C_p and were not resolved in the integrated aerodynamic forces on the model.

SRP cases, in general, require very large computational grids. Large volumes of fine grid resolution are required in the region from the nozzle exit to the bow shock, and this region can extend several body diameters in the upstream and cross-stream directions. Additionally, with a flow obstruction often significantly larger than the actual body, the downstream boundary for the wake flow to fully close

may be tens of body diameters downstream. The unsteady solutions presented in this thesis required, on average, approximately 29,000 CPU hours, or 23x more CPU hours than required for steady solutions. It should be noted, however, that unsteady CFD analysis is not needed to determine the quantities of interest for conceptual design. No high-fidelity aerodynamic analyses are needed to determine the boundary conditions and parameters defining nozzle thrust. Empirical models are sufficient for static aerodynamic forces, and steady CFD analysis is sufficient for determining static aerodynamic moments. Unsteady CFD analyses are only necessary for cases where vehicle dynamics and dynamic SRP interaction effects are of primary interest.

The results in this thesis have defined the aerodynamic modeling fidelity required for SRP during the conceptual design phase. This thesis has also examined the ability of the high-fidelity computational analysis required for more detailed design to capture SRP flowfield behavior and integrated static aerodynamics, including flowfield unsteadiness, and the computational cost associated with generating consistent and accurate flow solutions. The operating conditions, vehicle scales, and application defined for SRP as part of a human Mars exploration mission are such that the vehicle is almost entirely shielded from the freestream flow by the aerodynamic - propulsive interaction. As such, empirical models based on newly available experimental data or the assumption of no aerodynamic forces acting on the vehicle are sufficient for conceptual design. For more detailed design, however, support from high-fidelity CFD analysis is necessary, as may be additional experimental efforts. The computational cost of obtaining consistent and accurate flow solutions using high-fidelity computational tools has been shown to be significant. This may be a challenge for the development of more detailed SRP models.

7.4 Directions for Forward Work

At the present time, supersonic retropropulsion has been assessed by NASA to be at TRL 2, defined to be a level at which the "technology concept and/or application has been formulated". Though the actual missions identified for SRP may be far on the horizon, opportunities for technology demonstration or robotic-scale precursor missions may not be. Recommendations for forward work in the areas of experimental testing, computational analysis, and systems analysis are given in the context of the conclusions of this thesis, the present level of technological maturity for SRP, and the next steps required to develop SRP into a flight-ready system.

7.4.1 Experimental Testing

While two recent wind tunnel tests completed by the NASA ETDD Program have greatly expanded the experimental database for SRP, additional experimental work, through the use of ground-based facilities and sub-scale flight testing, is strongly recommended. Direct measurement of forces and moments has never been attempted in an SRP test and would provide critical data for on-going CFD validation activities and aerodynamic model development for systems analysis. The configurations tested thus far have not been representative of the configurations identified to be flight relevant. It is recommended that the next models developed for wind tunnel testing have the ability to throttle combinations of multiple nozzles and have ratios of the total nozzle exit area to forebody area closer to 1. This will be challenging from a packaging and instrumentation perspective and also limit test facility options due to the required size of the model.

High-speed schlieren video has indicated that all SRP flowfields have some degree of unsteadiness in the flowfield structure. No conclusions were able to be drawn from the two NASA ETDD Program tests on the potential impacts of this unsteadiness on vehicle stability. A test designed to investigate and quantify the effects of this

unsteadiness on the vehicle's stability and possible excitation of structural modes for a full-scale vehicle is needed. Lastly, all wind tunnel testing has been completed using compressed air or other single-component cold gases. It is recommended that a hot-fire test be completed to provide much needed data on the potential aerothermal and gas chemistry implications of SRP for vehicle design. Additionally, such a test would be an opportunity to address concerns about the potential for thrust instabilities at SRP conditions for start-up, throttling, and nominal operation.

It is also recommended that alternative test platforms be considered for gaining data sets unobtainable in wind tunnel facilities, namely ballistic ranges, sounding rockets, and free-flying Viking BLDT-derived flight test vehicles. Vehicle concepts and mission requirements have already been defined for a proof-of-concept flight test of SRP on a sounding rocket platform by NASA's ETDD Program. It is recommended that these concepts be carried through another design iteration and a formal proposal for a proof-of-concept flight test on a sounding rocket developed. As an alternative, a Viking BLDT-derived, free-flying platform would allow for increased degrees of system integration and test complexity, as well as examine systems representative of those intended for the full-scale flight system.

7.4.2 Computational Analysis

Significant advancements have been made in the area of computational analysis for SRP with the availability of new experimental data sets from two wind tunnel tests completed by the NASA ETDD Program. Forward work in this area should include completing the validation of existing CFD tools using all of the data types available in these data sets. Comparisons with the high-frequency pressure measurements and with force and moment coefficients calculated from integrated pressure measurements have not yet been completed. Validation of existing CFD tools in predicting the dynamic effects of SRP will also be needed, once an appropriate test is completed /

data set becomes available.

Additional investigation into the effects of the physical models used in the analysis, e.g. turbulence models, etc., is also recommended. It would be useful for the EDL community to have an explicit statement of the requirements and best practices for the CFD analysis of SRP flowfields and the accuracy of the results obtained with different CFD approaches. The computational expense of generating SRP flow solutions may be prohibitive in using CFD to complete a large number of explorative studies, but additional investigations into the effects of physical scale, variations in gas composition, and the potential for aerothemal effects with realistic systems are recommended. With the current status of SRP development and the understanding that high-fidelity CFD analysis is not necessary for conceptual design, it is recommended that computational aerodynamic analysis be given a lower priority than experimental or systems-level investigations.

7.4.3 Systems Analysis and Design

NASA has expended significant effort to define concepts for the advanced exploration of Mars. Many of these concepts rely on SRP. The results in this thesis are limited to static aerodynamic effects and modeling requirements for conceptual design. For more detailed phases of the design process, the specific models required for higher-fidelity analysis need to be developed.

It is recommended to continue advancing Mars EDL architecture concepts for all relevant mission scales. Past analysis has emphasized flight mechanics, with the same degree of attention not given to some areas of physical modeling and optimization of integrated vehicle performance. The continued development of these concepts will provide more detailed requirements relevant to the mission applications of SRP. The recommendations from these activities can motivate continued investment in SRP technology development.

With such low surface pressures over the vehicle resulting from SRP, aerodynamic surfaces cannot likely be used to control the vehicle's attitude in flight. Systems analysis, computational analysis, and also experimental testing will be necessary to develop an integrated control strategy for the SRP phase. Additional work in all of these areas is recommended to address current unknowns related to static stability, dynamic stability, and potential impacts of the inherent flowfield unsteadiness.

REFERENCES

[1] Braun, R. D. and Manning, R. M., "Mars Exploration Entry, Descent, and Landing Challenges," *Journal of Spacecraft and Rockets*, Vol. 44, No. 2, March-April 2007, pp. 310–323.

[2] Zang, T. A. and Tahmasebi, F., "Entry, Descent and Landing Systems Analysis Study: Phase 1 Report," TM 2010-216720, NASA, July 2010.

[3] Gnoffo, P. A., "Planetary-Entry Gas Dynamics," *Annual Review of Fluid Mechanics*, Vol. 31, 1999, pp. 459–494.

[4] Pai, S., *Fluid Dynamics of Jets*, Van Nostrand, New York, 1st ed., 1954.

[5] Pindzola, M., "Jet Simulation in Ground Test Facilities," AGARDograph 79, November 1963.

[6] Wilkes, J. A., Glass, C. E., Danehy, P. M., and Nowak, R. J., "Fluorescence Imaging of Underexpanded Jets and Comparison with CFD," No. 2006-910, AIAA, January 2006.

[7] Finley, P. J., "The Flow of a Jet from a Body Opposing a Supersonic Free Stream," *Journal of Fluid Mechanics*, Vol. 26, No. 2, October 1966, pp. 337–368.

[8] Daso, E. O., Pritchett, V. E., Wang, T. S., Ota, D. K., Blankson, I. M., and Auslender, A. H., "Dynamics of Shock Dispersion and Interactions in Supersonic Freestreams with Counterflowing Jets," *AIAA Journal*, Vol. 47, No. 6, June 2009, pp. 1313–1326.

[9] Peterson, V. L. and McKenzie, R. L., "Effects of Simulated Retrorockets on the Aerodynamic Characteristics of a Body of Revolution at Mach Numbers from 0.25 to 1.90," TN D-1300, NASA, May 1962.

[10] Korzun, A. M., Braun, R. D., and Cruz, J. R., "Survey of Supersonic Retropropulsion Technology for Mars Entry, Descent, and Landing," *Journal of Spacecraft and Rockets*, Vol. 46, No. 5, September-October 2009, pp. 929–937.

[11] Korzun, A. M., Cordell, C. E., and Braun, R. D., "Comparison of Inviscid and Viscous Aerodynamic Predictions of Supersonic Retropropulsion Flowfields," No. 2010-5048, AIAA, June 2010.

[12] McGhee, R. J., "Effects of a Retronozzle Located at the Apex of a 140-deg Blunt Cone at Mach Numbers of 3.00, 4.50, and 6.00," TN D-6002, NASA, January 1971.

[13] Jarvinen, P. O. and Adams, R. H., "The Aerodynamic Characteristics of Large Angled Cones with Retrorockets," CR NAS 7-576, NASA, February 1970.

[14] Berry, S. A. and Rhode, M. N., "Supersonic Retro-Propulsion Test 1853 in NASA LaRC Unitary Plan Wind Tunnel Test Section 2," Edl-01-tr-9178, NASA, November 2010.

[15] Berry, S. A., Laws, C. T., Kleb, W. L., Rhode, M. N., Spells, C., McCrea, A. C., Trumble, K. A., Schauerhamer, D. G., and Oberkampf, W. L., "Supersonic Retro-Propulsion Experimental Design for Computational Fluid Dynamics Model Validation," No. 1499, IEEE Aerospace Conference, March 2011.

[16] Kleb, W. L., Carlson, J.-R., Buning, P. G., Berry, S. A., Rhode, M. N., Edquist, K. T., Schauerhamer, D. G., Trumble, K. A., and Sozer, E., "Toward Supersonic Retropropulsion CFD Validation," No. 2011-3490, AIAA, June 2011.

[17] Gilles, S. E. and Kallis, J. M., "Penetration Distance of Retrorocket Exhaust Plumes into an Oncoming Stream," CR TDR-269(4181)-2, USAF, 1964.

[18] Edquist, K. T., Dyakonov, A. A., Korzun, A. M., Shidner, J. D., Studak, J. W., Tigges, M. A., Kipp, D. M., Prakash, R., Trumble, K. A., and Dupzyk, I. C., "Development of Supersonic Retro-Propulsion for Future Mars Entry, Descent, and Landing Systems," No. 2010-5046, AIAA, June 2010.

[19] Christian, J. A., Wells, G. W., Lafleur, J. M., Verges, A. M., and Braun, R. D., "Extension of Traditional Entry, Descent, and Landing Technologies for Human Mars Exploration," *Journal of Spacecraft and Rockets*, Vol. 45, No. 1, January-February 2008, pp. 130–141.

[20] Hoffman, S. J. and Kaplan, D. I., "Human Exploration of Mars: The Reference Mission of the NASA Mars Exploration Study Team," SP 6107, NASA, July 1997.

[21] Drake, B. G., "Reference Mission 3.0: Addendum to the Human Exploration of Mars: The Reference Mission of the NASA Mars Exploration Study Team," SP 6107-ADD, NASA, June 1998.

[22] Drake, B. G., "Human Exploration of Mars: Design Reference Architecture 5.0," SP 2009-566, NASA, July 2009.

[23] Cianciolo, A. D., Zang, T. A., Sostaric, R. R., and McGuire, M. K., "Overview of the NASA Entry, Descent and Landing Systems Analysis Exploration Feed-Forward Study," –, Proceedings of the 8th International Planetary Probe Workshop, June 2011.

[24] Adler, M., Wright, M. J., Campbell, C., Clark, I. G., Engelund, W., and Rivellini, T., "Entry, Descent, and Landing Roadmap - Technology Area 09," Tech. rep., NASA, November 2010.

[25] Vick, A. R. and E. H. Andrews, J., "An Investigation of Highly Underexpanded Exhaust Plumes Impinging Upon a Perpendicular Flat Surface," TN D-3269, NASA, February 1966.

[26] Love, E. S., Grigsby, C. E., Lee, L. P., and Woodling, M. J., "Experimental and Theoretical Studies of Axisymmetric Free Jets," TR R-6, NASA, 1959.

[27] Orth, R. C., Schetz, J. A., and Billig, F. S., "The Interaction and Penetration of Gaseous Jets in Supersonic Flow," CR 1386, NASA, July 1969.

[28] Spaid, F. W. and Cassel, L. A., "Aerodynamic Interference Induced by Reaction Controls," AGARDograph 173, December 1973.

[29] Viti, V., Neel, R., and Schetz, J. A., "Detailed Flow Physics of the Supersonic Jet Interaction Flow Field," *Physics of Fluids*, Vol. 21, No. 4, April 2009, pp. 1–16.

[30] Salas, M. D., "The Numerical Calculation of Inviscid Plume Flow Fields," No. 1974-523, AIAA, June 1974.

[31] Abbett, M., "Mach Disk in Underexpanded Exhaust Plumes," *AIAA Journal*, Vol. 9, No. 3, 1970, pp. 512–514.

[32] Huff, R. G. and Abdalla, K. L., "Mixing Characteristics Downstream of Core Region of High-Temperature Axisymmetric Jets Exhausting into Transonic and Supersonic Streams," TM X-151, NASA, March 1960.

[33] Love, E. S., "The Effect of a Small Jet of Air Exhausting from the Nose of a Body of Revolution in Supersonic Flow," RM L52I19a, NACA, November 1952.

[34] Love, E. S., "A Re-Examination of the Use of Simple Concepts for Predicting the Shape and Location of Detached Shock Waves," TN 4170, NACA, 1957.

[35] Moeckel, W. E., "Flow Separation Ahead of a Blunt Axially Symmetric Body at Mach Numbers 1.76 to 2.10," RM E51I25, NACA, December 1951.

[36] Moeckel, W. E., "Flow Separation Ahead of Blunt Bodies at Supersonic Speeds," TN 2418, NACA, July 1951.

[37] Love, E. S. and Grigsby, C. E., "Some Studies of Axisymmetric Free Jets Exhausting from Sonic and Supersonic Nozzles into Still Air and into Supersonic Freestreams," RM L54L31, NACA, May 1955.

[38] Love, E. S., Woodling, M. J., and Lee, L. P., "Boundaries of Supersonic Axisymmetric Free Jets," RM L56G18, NACA, October 1956.

[39] Keyes, J. W. and Hefner, J. N., "Effect of Forward Facing Jets on Aerodynamic Characteristics of Blunt Configurations at Mach 6," *Journal of Spacecraft and Rockets*, Vol. 4, No. 4, April 1967, pp. 533–534.

[40] Jarvinen, P. O. and Adams, R. H., "The Effects of Retrorockets on the Aerodynamic Characteristics of Conical Aeroshell Planetary Entry Vehicles," No. 70-219, AIAA, January 1970.

[41] Charczenko, N. and Hennessey, K. W., "Investigation of a Retrorocket Exhausting from the Nose of a Blunt Body into a Supersonic Free Stream," TN D-151, NASA, September 1961.

[42] Romeo, D. J. and Sterrett, J. R., "Exploratory Investigation of the Effect of a Forward-Facing Jet on the Bow Shock of a Blunt Body in a Mach Number 6 Free Stream," TN D-1605, NASA, February 1963.

[43] Barber, E. A., "An Experimental Investigation of Stagnation-Point Injection," No. 1963-0433, AIAA, August 1963.

[44] Barber, E. A., "An Experimental Investigation of Stagnation-Point Injection," *Journal of Spacecraft and Rockets*, Vol. 2, No. 5, 1965, pp. 770–774.

[45] Grenich, A. F. and Woods, W. C., "Flow Field Investigation of Atmospheric Braking for High Drag Vehicles with Forward Facing Jets," No. 1981-0293, AIAA, January 1981.

[46] Grimaud, J. E. and McRee, L. C., "Experimental Data on Stagnation-Point Gas Injection Cooling on a Hemisphere-Cone in a Hypersonic Arc Tunnel," TM X-983, NASA, July 1964.

[47] Hayashi, K., Aso, S., and Tani, Y., "Numerical Study of Thermal Protection System by Opposing Jet," No. 2005-0188, AIAA, January 2005.

[48] Romeo, D. J. and Sterrett, J. R., "Flow Field for Sonic Jet Exhausting Counter to a Hypersonic Mainstream," *AIAA Journal*, Vol. 3, No. 3, March 1965, pp. 544–546.

[49] Stalder, J. R. and Inouye, M., "A Method of Reducing Heat Transfer to Blunt Bodies by Air Injection," RM A56B27a, NACA, May 1956.

[50] Warren, C. H. E., "An Experimental Investigation of the Effect of Ejecting a Coolant Gas at the Nose of a Bluff Body," *Journal of Fluid Mechanics*, Vol. 8, No. 3, July 1960, pp. 400–417.

[51] Berry, S. A., Rhode, M. N., Edquist, K. T., and Player, C. J., "Supersonic Retropropulsion Experimental Results," No. 2011-3489, AIAA, June 2011.

[52] Berry, S. A., Rhode, M. N., and Edquist, K. T., "Supersonic Retropropulsion Experimental Results from the NASA Ames 9- x 7-Foot Supersonic Wind Tunnel," No. 2012-2704, AIAA, June 2012.

[53] Abramovich, G. N., *The Theory of Turbulent Jets*, M.I.T. Press, Cambridge, Massachusetts, 1963.

[54] Chung, P. M., "Effect of Localized Mass Transfer Near the Stagnation Region of Blunt Bodies in Hypersonic Flight," TN D-141, NASA, May 1960.

[55] Hayashi, K. and Aso, S., "Effect of Pressure Ratio on Aerodynamic Heating due to Opposing Jet," No. 2003-4041, AIAA, June 2003.

[56] Roberts, L., "Mass Transfer Cooling Near the Stagnation Point," TR R-8, NASA, 1959.

[57] Venkatachari, B. S., Ito, Y., Cheng, G. C., and Chang, C.-L., "Numerical Investigation of the Interaction of Counterflowing Jets and Supersonic Capsule Flows," No. 2011-4030, AIAA, June 2011.

[58] Hayman, L. O. and McDearmon, R., "Jet Effects on Cylindrical Afterbodies Housing Sonic and Supersonic Nozzles which Exhaust against a Supersonic Stream at Angles from 90 to 180 Degrees," TN D-1016, NASA, March 1962.

[59] Rhode, M. N. and Oberkampf, W. L., "Estimation of Uncertainties for Supersonic Retropropulsion Test 1853 NASA Langley Research Center Unitary Plan Wind Tunnel," Edl-01-tr-9217, NASA, October 2011.

[60] Chang, C.-L., Venkatachari, B. S., and Cheng, G. C., "Effect of Counterflow Jet on a Supersonic Reentry Capsule," No. 2006-4776, AIAA, July 2006.

[61] Cheng, G. C., Neroorkar, K. D., Chen, Y. S., Wang, T. S., and Daso, E. O., "Numerical Study of Flow Augmented Thermal Management for Entry and Re-Entry Environments," No. 2007-4560, AIAA, June 2007.

[62] Alkandry, H., Boyd, I. D., Reed, E. M., Codoni, J. R., and McDaniel, J. C., "Interactions of Single-Nozzle Supersonic Propulsive Deceleration Jets on Mars Entry Aeroshells," No. 2011-138, AIAA, January 2011.

[63] Codoni, J. R., Reed, E. M., McDaniel, J. C., Alkandry, H., and Boyd, I. D., "Investigations of Peripheral 4-Jet Sonic and Supersonic Propulsive Deceleration Jets on a Mars Science Laboratory Aeroshell," No. 2011-1036, AIAA, January 2011.

[64] Alkandry, H., Boyd, I. D., Codoni, J. R., Reed, E. M., and McDaniel, J. C., "Numerical Investigation of Multi-Nozzle Propulsive Deceleration Jets for Mars Entry Aeroshells," No. 2011-3953, AIAA, June 2011.

[65] Cordell, C. E., Clark, I. G., and Braun, R. D., "CFD Verification of Supersonic Retropropulsion for a Central and Peripheral Configuration," No. 1190, IEEE Aerospace Conference, March 2011.

[66] Bakhtian, N. M. and Aftosmis, M. J., "Analysis of Inviscid Simulations for the Study of Supersonic Retropropulsion," No. 2011-3194, AIAA, June 2011.

[67] Trumble, K. A., Schauerhamer, D. G., Kleb, W. L., Carlson, J.-R., and Edquist, K. T., "Analysis of Navier-Stokes Codes Applied to Supersonic Retro-Propulsion Wind Tunnel Test," No. 1471, IEEE Aerospace Conference, March 2011.

[68] Schauerhamer, D. G., Trumble, K. A., Kleb, W. L., Carlson, J.-R., Edquist, K. T., and Sozer, E., "Continuing Validation of Computational Fluid Dynamics for Supersonic Retropropulsion," No. 2012-0864, AIAA, January 2012.

[69] Alkandry, H., Boyd, I. D., Reed, E. M., Codoni, J. R., and McDaniel, J. C., "Interactions of Single-Nozzle Sonic Propulsive Deceleration Jets on Mars Entry Aeroshells," No. 2010-4888, AIAA, June 2010.

[70] Bakhtian, N. M. and Aftosmis, M. J., "Parametric Study of Peripheral Nozzle Configurations for Supersonic Retropropulsion," *Journal of Spacecraft and Rockets*, Vol. 47, No. 6, November-December 2010, pp. 935–950.

[71] Cheryni, G. G., "Some Recent Results in Aerodynamic Applications of Flows with Localized Energy Addition," No. 99-4819, AIAA, November 1999.

[72] Daso, E. O., Beaulieu, W., and Hager, J. O., "Prediction of Drag Reduction in Supersonic and Hypersonic Flows with Counterflow Jets," No. 2002-5115, AIAA, September-October 2002.

[73] Fomin, V. M., Maslov, A. A., and Malmuth, N. D., "Influence of a Counterflow Plasma Jet on Supersonic Blunt-Body Pressures," *AIAA Journal*, Vol. 40, No. 6, June 2002, pp. 1170–1177.

[74] Nomura, H., Aso, S., and Nishida, M., "Numerical Simulation of Opposing Sonic Jets," *Computers and Fluids*, Vol. 21, No. 2, 1992, pp. 229–233.

[75] Trumble, K. A., Schauerhamer, D. G., Kleb, W. L., Carlson, J.-R., Buning, P. G., Edquist, K. T., and Barnhardt, M. D., "An Initial Assessment of Navier-Stokes Codes Applied to Supersonic Retro-Propulsion," No. 2010-5047, AIAA, June 2010.

[76] Viti, V., Schetz, J. A., and Neel, R., "Comparison of First and Second Order Turbulence Models for a Jet/3D Ramp Combination in Supersonic Flow," No. 2005-1100, AIAA, January 2005.

[77] Streipe, S. A., *Program to Optimize Simulated Trajectories (POST II) - Utilization Manual, Volume II, Version 1.16.G*, NASA Langley Research Center, 2004.

[78] Spencer, D. A., Blanchard, R. C., Braun, R. D., Kallemeyn, P. H., and Thurman, S. W., "Mars Pathfinder Entry, Descent, and Landing Reconstruction," *Journal of Spacecraft and Rockets*, Vol. 36, No. 3, May-June 1999, pp. 357–366.

[79] Marsh, C. L. and Braun, R. D., "Fully-Propulsive Mars Atmospheric Transit Strategies for High-Mass Payload Missions," No. 1219, IEEE Aerospace Conference, March 2009.

[80] Price, H., Hawkins, A. M., and Radcliffe, T. O., "Austere Human Missions to Mars," No. 2009-6685, AIAA, September 2009.

[81] Steinfeldt, B. A., Theisinger, J. E., Korzun, A. M., Clark, I. G., Grant, M. J., and Braun, R. D., "High Mass Mars Entry, Descent, and Landing Architecture Assessment," No. 2009-6684, AIAA, September 2009.

[82] Way, D. W., Powell, R. W., Chen, A., Steltzner, A. D., Martin, A. M. S., Burkhart, P. D., and Mendeck, G. F., "Mars Science Laboratory: Entry, Descent, and Landing System Performance," No. 1467, IEEE Aerospace Conference, March 2006.

[83] Sutton, G. P. and Biblarz, O., *Rocket Propulsion Elements*, Wiley-Interscience, New York, 7th ed., 2001.

[84] Olson, D. L., "Comparison of Weights in TOPSIS Models," *Mathematical and Computer Modeling*, Vol. 0, No. 1, 2004, pp. 1–6.

[85] Korzun, A. M. and Braun, R. D., "Performance Characterization of Supersonic Retropropulsion for High-Mass Mars Systems," *Journal of Spacecraft and Rockets*, Vol. 47, No. 5, September-October 2010, pp. 836–848.

[86] Chapman, D. R., Kuehn, D. M., and Larson, H. K., "Preliminary Report on a Study of Separated Flows in Supersonic and Subsonic Streams," RM A55L14, NACA, June 1956.

[87] Aftosmis, M. J., Berger, M. J., and Adomavicious, G., "A Parallel Multilevel Method for Adaptively Refined Cartesian Grids with Embedded Boundaries," No. 2000-0808, AIAA, January 2000.

[88] Anderson, W. K. and Bonhaus, D. L., "An Implicit Upwind Algorithm for Computing Turbulent Flows on Unstructured Grids," *Computers and Fluids*, Vol. 23, No. 1, January 1994, pp. 1–21.

[89] Anderson, W. K., Rausch, R. D., and Bonhaus, D. L., "Implicit/Multigrid Algorithm for Incompressible Turbulent Flows on Unstructured Grids," *Journal of Computational Physics*, Vol. 128, No. 2, October 1996, pp. 391–408.

[90] NASA Langley Research Center, http://fun3d.larc.nasa.gov/, *FUN3D Manual*, August 2010.

[91] Edwards, J. R., "A Low-Diffusion Flux-Splitting Scheme for Navier-Stokes Calculations," *Computers and Fluids*, Vol. 26, No. 6, July 1997, pp. 653–659.

[92] Albada, G. D. V., Leer, B. V., and Roberts, W. W., "A Comparative Study of Computational Methods in Cosmic Gas Dynamics," *Astronomy and Astrophysics*, Vol. 108, No. 1, April 1982, pp. 76–84.

[93] Menter, F. R., "Two-Equation Eddy-Viscosity Turbulence Models for Engineering Applications," *AIAA Journal*, Vol. 32, No. 8, August 1994, pp. 1598–1605.

[94] Jones, W. T., *GridEx Manual*, NASA Langley Research Center, December 2001.

[95] Garriz, J. A., *VGRID 3.2 Reference Documents*, ViGYAN, Inc., preliminary draft ed., September 1998.

[96] Peñaranda, F. E. and Freda, M. S., "Aeronautical Facilities Catalogue, Vol. 1 - Wind Tunnels," RP 1132, NASA, January 1985.

[97] Oberkampf, W. L. and Roy, C. J., *Verification and Validation in Scientific Computing*, Cambridge University Press, 2010.

[98] Aeschliman, D. P. and Oberkampf, W. L., "Experimental Methodology for Computational Fluid Dynamics Code Validation," *AIAA Journal*, Vol. 36, No. 5, May 1998, pp. 733–741.

[99] *Assessment of Experimental Uncertainty with Application to Wind Tunnel Testing*, AIAA Standards, AIAA, 1999.

[100] Thomas, J. L., Diskin, B., and Rumsey, C. L., "Towards Verification of Unstructured-Grid Solvers," *AIAA Journal*, Vol. 46, No. 12, January 2008, pp. 3070–3079.

[101] American Institute of Aeronautics and Astronautics, *Editorial Policy Statement on Numerical and Experimental Accuracy*, October 2010.

[102] Vatsa, V. N., Carpenter, M. H., and Lockard, D. P., "Re-evaluation of an Optimized Second Order Backward Difference (BDF2OPT) Scheme for Unsteady Flow Applications," No. 2010-0122, AIAA, January 2010.

[103] Roy, C. J., "Grid Convergence Error Analysis for Mixed-Order Numerical Schemes," *AIAA Journal*, Vol. 41, No. 4, April 2003, pp. 595–603.

[104] Tannehill, J. C., Anderson, D. A., and Pletcher, R. H., *Computational Fluid Mechanics and Heat Transfer*, Taylor and Francis, 2nd ed., 1997.

[105] Godunov, S. K., "A Difference Scheme for Numerical Computation of Discontinuous Solution of Hydrodynamic Equations," JPRS 7226, U.S. Joint Publications Research Service, 1969.

[106] Biedron, R. T., Vatsa, V. N., and Atkins, H. L., "Simulation of Unsteady Flows Using an Unstructured Navier-Stokes Solver on Moving and Stationary Grids," No. 2005-5093, AIAA, June 2005.

[107] Ayoroa, J. G. C. and Edquist, K. T., "Post Processing of Test Data for Supersonic Retropropulsion Test 1853 at Langley Research Center's Unitary Plan Wind Tunnel," Final report, NASA LARSS Program, August 2011.

[108] Dyke, M. V. and Gordon, H. D., "Supersonic Flow Past a Family of Blunt Axisymmetric Bodies," TR R-1, NASA, 1959.

[109] Owen, P. R. and Thornhill, C. K., "The Flow in an Axially Symmetric Supersonic Jet from a Nearly Sonic Orifice into a Vacuum," Rep. and Memo 2616, ARC, 1952.

[110] Ashkenas, H. and Sherman, F. S., "Structure and Utilization of Supersonic Free Jets in Low Density Wind Tunnels," CR 60423, NASA, 1965.

[111] Moeckel, W. E., "Approximate Method for Predicting Form and Location of Detached Shock Waves Ahead of Plane or Axially Symmetric Bodies," TN 1921, NACA, July 1949.

[112] Cianciolo, A. D., "Entry, Descent and Landing Systems Analysis: Exploration Feed Forward Internal Peer Review Slide Package," TM 2011-217050, NASA, February 2011.